



ISSN 2959-0663 (Print)
ISSN 2959-0671 (Online)
ISSN-L 2959-0663

EURASIAN JOURNAL OF CHEMISTRY

2025. Vol. 30 No. 2(118)



ISSN 2959-0663 (Print)
ISSN 2959-0671 (Online)
ISSN-L 2959-0663

EURASIAN JOURNAL OF CHEMISTRY

2025

Volume 30, No. 2 (118)

Founded in 1996

Published 4 times a year

Karaganda
2025

Publisher: Karagandy University of the name of academician E.A. Buketov

Postal address: 28, Universitetskaya Str., Karaganda, 100024, Kazakhstan

E-mail: chemistry.vestnik@ksu.kz;
irina.pustolaikina@ksu.kz;
ipustolaikina@gmail.com

Tel./fax: +7(7212) 34-19-40.

Web-site: <https://ejc.buketov.edu.kz>

Editor-in-Chief

Ye.M. Tazhbayev, Doctor of Chemical sciences

Executive Editor

I.A. Pustolaikina, Candidate of Chemical sciences

Editorial board

- Z.M. Muldakhmetov**, Academician of NAS RK, Doctor of chem. sciences, Institute of Organic Synthesis and Coal Chemistry of the Republic of Kazakhstan, Karaganda (Kazakhstan);
- S.M. Adekenov**, Academician of NAS RK, Doctor of chem. sciences, International Research and Production Holding "Phytochemistry", Karaganda (Kazakhstan);
- S.E. Kudaibergenov**, Doctor of chem. sciences, Institute of Polymer Materials and Technologies, Almaty (Kazakhstan);
- V. Khutoryanskiy**, Professor, University of Reading, Reading (United Kingdom);
- Fengyun Ma**, Professor, Xinjiang University, Urumqi (PRC);
- Xintai Su**, Professor, South China University of Technology, Guangzhou (PRC);
- R.R. Rakhimov**, Doctor of chem. sciences, Norfolk State University, Norfolk (USA);
- N. Nuraje**, Associate Professor, Nazarbayev University, Astana (Kazakhstan);
- S.A. Beznosyuk**, Doctor of phys.-math. sciences, Altai State University, Barnaul (Russia);
- B.F. Minaev**, Doctor of chem. sciences, Bohdan Khmelnytsky National University of Cherkasy, Cherkasy (Ukraine);
- I.V. Kulakov**, Doctor of chem. sciences, University of Tyumen (Russia);
- R.P. Bhole**, PhD, Associate Professor, Dr. D.Y. Patil Institute of Pharmaceutical Sciences and Research, Sant Tukaram Nagar, Pimpri, Pune (India);
- S.S. Gurav**, PhD, Professor, Goa College of Pharmacy, Panaji (India);
- A.A. Atakhanov**, Doctor of techn. sciences, Institute of Polymer Chemistry and Physics, Tashkent (Uzbekistan);
- I.V. Korolkov**, PhD, Associated Professor, Astana branch, Institute of Nuclear Physics of the Republic of Kazakhstan, Astana (Kazakhstan);
- A.M. Makasheva**, Doctor of techn. sciences, Zh. Abishev Chemical-Metallurgical Institute, Karaganda (Kazakhstan);
- M.I. Baikenov**, Doctor of chem. sciences, Karagandy University of the name of acad. E.A. Buketov (Kazakhstan);
- L.K. Salkeeva**, Doctor of chem. sciences, Karagandy University of the name of acad. E.A. Buketov (Kazakhstan);
- G.I. Dzhardimalieva**, Doctor of chem. sciences, Federal Research Center of Problems of Chemical Physics and Medicinal Chemistry, Russian Academy of Sciences, Chernogolovka, Moscow Region (Russia);
- S.K. Filippov**, PhD, Project Leader, DWI-Leibniz Institute for Interactive Materials, Aachen, North Rhine-Westphalia, (Germany);
- S.A. Ivashenko**, Doctor of pharm. sciences, Karaganda Medical University (Kazakhstan).

Proofreader I.N. Murtazina

Computer layout V.V. Butyaikin

Eurasian Journal of Chemistry. — 2025. — Vol. 30, No. 2(118). — 127 p.

ISSN 2959-0663 (Print). ISSN 2959-0671 (Online). ISSN-L 2959-0663

Proprietary: NLC "Karagandy University of the name of academician E.A. Buketov".

Registered by the Ministry of Information and Social Development of the Republic of Kazakhstan. Re-registration certificate No. KZ95VPY00063697 dated 30.01.2023.

Signed in print 27.06.2025. Format 60×84 1/8. Offset paper. Volume 15,88 p.sh. Circulation 200 copies. Price upon request. Order № 77.

Printed in the Publishing house of NLC "Karagandy University of the name of academician E.A. Buketov".

28, University Str., Karaganda, 100024, Kazakhstan. Tel.: +7(7212) 35-63-16. E-mail: izd_karu@buketov.edu.kz

© Karagandy University of the name of academician E.A. Buketov, 2025

CONTENTS

ORGANIC CHEMISTRY

- Kukushkin, A.A., Kudashova, E.V., Root, E.V., Kositsyna, A.S., Ponomarev, I.S., Lyubyashkin, A.V., & Pustolaikina, I.A.* Synthesis, Characterization and Computational Study of Novel Copper(II) Chelate Complexes Ligated by Pyridyl-Containing Beta-Diketones 4
- Dubovskaia, P.I., Saeidi, A., Pronchenko, A.A., Drannikova, A.I., Lukoyanov, I.A., Aripova, F.K., Savenko, M.E., Veretennikova, E.A., Pestov, A.V., Litvinova, E.A., & Drannikov, A.A.* Gel-Phase Synthesis and pH-Sensitive Swelling-Structure Relationships of N-Carboxyethylchitosan 19
- Verekar, R.R., Shaikh, Sh.B.M., Rebelo, S., & Gurav, Sh.S.* Double-Loaded Liposomes Encasing Umbelliferone in Hydroxypropyl- β -Cyclodextrin Inclusion Complexes: Formulation, Characterisation and Investigation of Photoprotective Activity 34

PHYSICAL AND ANALYTICAL CHEMISTRY

- Burkeyeva, G.K., Kovaleva, A.K., Muslimova, D.M., Havlicek, D., Zhumabek, N.M. & Nukin, N.A.* Investigation of Physical and Chemical Properties of Thermosetting Copolymers of Polyethylene Glycol Maleate with Acrylic Acid During their "Cold" Curing 52
- Mukhametgazy, N., Temirkulova, K.M., Balgabayeva, B., Khamzin, B.G., Azat, S., Supiyeva, Zh.A., & Abbas, Q.* Effect of Activating Agent and Temperature Conditions on the Electrochemical Performance of Rice Husk-Based Activated Carbon in Supercapacitors 62

INORGANIC CHEMISTRY

- Ivanova, N.M., Muldakhmetov, Z.M., Vissurkhanova, Ya.A., Soboleva Ye.A., & Borsynbayev A.S.* N-Containing Graphene Preparation Using Melamine as a Nitrogen Source 74
- Badaoui, M., Sehil, H., & Lamouri, C.* Synthesis, Characterization, and Photocatalytic Activity of CeBiO₃ and FeBiO₃ Nanoparticles Prepared via the Sol-Gel Process 85

CHEMICAL TECHNOLOGY

- Galiyeva, A.R., Yessentayeva, N.A., Marsel, D.T., Daribay, A.T., Sadyrbekov, D.T., Moustafine, R.I., & Kutulutskaya, T.V.* Polylactide Acid-Based Nanoparticles for Controlled Delivery of Isoniazid and Rifampicin: Synthesis, Characterization, and *In Vitro* Release Study 95
- Mammadov, E.S., Kerimli, F.Sh., Akhmedova, N.F., Mammadov, S.E., & Mirzaliyeva, S.E.* Effect of Solid-Phase Modification of High-Modulus Zeolite TsVM with Cerium Oxide in Conversion of Bioethanol to Hydrocarbons 109
- Borsynbayev, A.S., Mustafin, Ye.S., Omarov, Kh.B. Muratbekova, A.A., Kaykenov, D.A., Sadyrbekov, D.T., Aynabayev, A.A., Bolatbay A.N, Turovets, M.A.* Study of the Phase Composition and Kinetics of the Metal Leaching Process Using Electrohydropulse Discharge on the Waste from the Zhezkazgan Concentrating Plants 119

ORGANIC CHEMISTRY

Article

Received: 23 March 2024 | Revised: 30 April 2025 |
Accepted: 21 May 2025 | Published online: 28 May 2025

UDC 546.65; 547.442

<https://doi.org/10.31489/2959-0663/2-25-5>

Alexey A. Kukushkin^{1*} , Elizaveta V. Kudashova², Evgeny V. Root^{2,3} , Anna S. Kositsyna^{1,2},
Ilya S. Ponomarev⁴ , Alexey V. Lyubyashkin² , Irina A. Pustolaikina⁵ 

¹School of Petroleum and Gas Engineering, Siberian Federal University, Krasnoyarsk, Russia;

²Siberian State University of Science and Technology named after Academician M.F. Reshetneva, Krasnoyarsk, Russia;

³Krasnoyarsk State Medical University named after Professor V.F. Voyno-Yasenetsky University, Krasnoyarsk, Russia;

⁴Institute of Chemistry and Chemical Technology Siberian Branch of the Russian Academy of Sciences, Krasnoyarsk, Russia;

⁵Department of Physical and Analytical Chemistry, Karaganda Buketov University, Karaganda, Kazakhstan

(*Corresponding author's e-mail: alekseykukushkin@bk.ru)

Synthesis, Characterization and Computational Study of Novel Copper(II) Chelate Complexes Ligated by Pyridyl-Containing Beta-Diketonates

Chelate complexes of copper(II) are widely used today in various sectors of the national economy, including medicine and pharmacology, biotechnology and agriculture, catalysis, and materials science. Pyridyl-containing β -diketonates possess unique properties and can act as chelating ligands for metals, making them promising candidates for the development of metal-based pharmaceutical compounds. Therefore, the development and discovery of new copper(II) chelate complexes are of great interest and practical significance. In this work, new copper(II) chelate complexes of pyridyl-containing β -diketonates were synthesized for the first time. Complexation between pyridyl-containing β -diketonates and copper(II) acetate with molar ratio 2:1 was carried out in ethanol at a temperature not exceeding 50 °C for 1 hour, with the yield of products **IIIa-d** ranging from 8.5 % to 31.3 %. The synthesized complexes were characterized using IR spectroscopy, atomic emission spectroscopy, and mass spectrometry, as well as DFT calculations, PASS prediction, and molecular docking. It was shown that all synthesized chelates exhibit biological activity as nicotinic receptor antagonists, with Pa values ranging from 0.821 to 0.915, and as dehydro-L-gulonate decarboxylase inhibitors, with Pa values exceeding 0.75. Molecular docking simulations with the α_2 nicotinic acetylcholine receptor (PDB ID: 5FJV) confirmed high potential of synthesized chelates as nicotinic receptor antagonists and they can be recommended for further evaluation of therapeutic relevance through *in vitro* and *in vivo* studies.

Keywords: complexation, copper, diketone, atomic emission spectroscopy, mass spectrometry, IR spectroscopy, chelate, complex compound

Introduction

Copper chelate complexes are one of the most interesting classes of coordination compounds, since they are used as combustion catalysts for solid and liquid fuels, light stabilizers for various types of synthetic polymers [1], in the practice of gas chromatography [2]. Copper(II) chelate complexes are also known for their superoxide dismutase activity [3], as well as antibacterial, antifungal [4–6], anti-AchE [7], and anti-proliferative effects against cancer cells [8]. It has been observed that interest in the synthesis and investigation of copper chelate complexes has grown significantly in recent years [9–12].

Copper is a crucial trace element involved in hematopoietic processes, the lack of copper exacerbates the lack of iron in iron deficiency anemia, causing additional depression of hemoglobin synthesis. Metal chelates are the most optimal form of a biogenic metal compound for the body. Thus, one study demonstrated the potential of a drug containing copper chelate complexes to stimulate hematopoiesis in animals [13].

Some copper triketone chelates such as diacetyl isovaleryl methane are used as fungicides and insecticides [1]. Also, the chelate form of copper demonstrates enhanced antimicrobial and wound-healing activity in therapeutic preparations compared to inorganic salts.

Chelate complexes of copper (II) showed anticancer activity [14]. Copper readily forms complexes with various bioactive organic ligands and serves as a convenient model for investigating ligand behavior with more expensive metals, such as platinum, palladium, etc. In turn, palladium(II) complexes can also exhibit biological activity [15]. There are a limited number of papers on the complexation of copper with pyridine-containing beta-diketones. Although such ligands are highly intriguing [16] and have potential applications in various fields [17, 18].

Therefore, the aim of this work was the synthesis of new copper chelate complexes of pyridyl-containing β -diketonates, their characterization and computational study using the *in silico* approach. Methods for *in silico* study of the physicochemical properties and potential biological activity of newly synthesized chemical compounds are now widely used due to the speed of implementation and relative low cost compared to *in vivo* and *in vitro* methods [19–21].

Experimental

Copper acetate II was obtained from LLC “JSC REACHIM” (Moscow, Russia). Ethyl alcohol was used as solvent [22].

IR spectra were recorded on an IR-microscope of “*SpecTRA TECH*” model “*InspectIR*” based on the IR-Fourier spectrophotometer “*Impact 400*” (USA). A sample of the substance was deposited onto a gilded plate, spread using a roller knife, positioned on a microscope stage, and analyzed using ATR spectroscopy. Analysis conditions included an MTC/A detector, a “*Si Caplugs*” lens, a wave number range of 400–650 cm^{-1} , a resolution of 1.928 cm^{-1} , 64 scans, and processing using OMNIC 5.1 E.S.P software.

Mass-spectra were recorded on a Shimadzu LC/MS-2020 device (Japan) with a RAPTOR ARC-18 100 column (2.1 mm diameter, 0.1 mm grain, 100 mm length) using a quadrupole Electron Injection Ion Source (ESI) mass spectrometer. The rate of direct injection of the sample and eluate composition was 10 $\mu\text{l}/\text{min}$. The scan range was 20–1000 Da.

The atomic emission spectrum was recorded on the ICAP 7400 instrument (USA).

Synthesis and Characterization

To study the reaction of the complexation of pyridyl-containing beta-diketones with copper, we synthesized β -diketonates with pyridine substituents 1-phenyl-3-(pyridin-3-yl)propane-1,3-dione (***Ia***), 1-phenyl-3-(pyridin-4-yl)propane-1,3-dione (***Ib***), 1-(pyridin-3-yl)butane-1,3-dione (***Ic***) and 1-(pyridin-4-yl)butane-1,3-dione (***Id***) using the Claisen method, following a well-established procedure [23] (Figure 1).

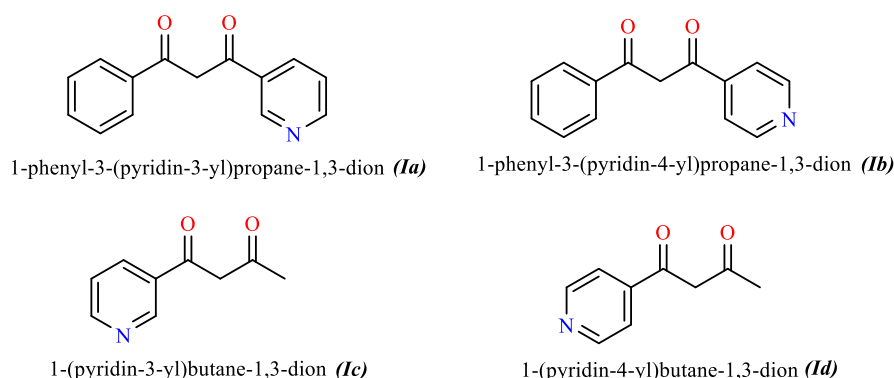


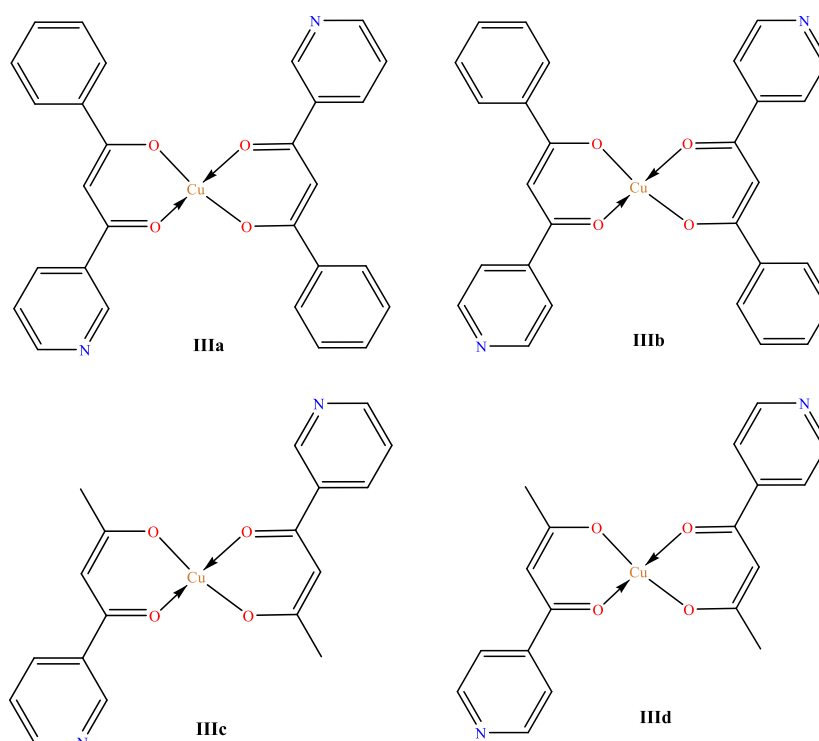
Figure 1 Synthesized pyridyl-containing beta-diketones ***Ia-d***

The complexation of copper(II) acetate with synthesized pyridyl-containing beta-diketones 1-phenyl-3-(pyridin-3-yl)propane-1,3-dione (***a***), 1-phenyl-3-(pyridin-4-yl)propane-1,3-dione (***b***), 1-(pyridin-3-yl)butane-1,3-dione (***c***) and 1-(pyridin-4-yl)butane-1,3-dione (***d***) was studied in various molar ratios of 1:1, 1:2, 2:1 (Table 1). The best results were obtained at a molar ratio of 2:1 [24].

Chelate complexes yields at different molar ratio

Chelate complexes	R ₁	R ₂	Yield (%) at the 1,3- diketone : Cu(II) acetate molar ratio:		
			1:1	1:2	2:1
IIIa	Ph	β-Py	43	25	59
IIIb	Ph	γ-Py	55	27	61
IIIc	Me	β-Py	35	19	36
III d	Me	γ-Py	40	25	43

We hypothesized that the formation of bis(acetylacetonate) complexes was more likely, and the products obtained at a 2:1 ratio of 1,3-diketones to copper(II) acetate were selected as samples (Figure 2). The melting point was used as the comparison parameter. It was found that, for all studied ratios, both the melting point and the mixing sample analysis remained identical. Thus, all studied ratios yielded the same product, with the optimal formation conditions being a 2:1 ratio of 1,3-diketones to copper(II) acetate. Additional confirmation of the obtained samples' identity was achieved through thin-layer chromatography data.

Figure 2. Structures of synthesized chelates **IIIa-d**

Synthesis of Copper Chelate Complexes **IIIa-d**

To 1,3-diketones **Ia-d** (0.004 mol), dissolved in a minimum amount of ethyl alcohol, copper acetate II (0.002 mol) in 70 % ethyl alcohol was added. The mixture was heated 1 hour at a temperature not higher than 50 °C. The color of the solution changed from brown to green during the reaction. The green precipitate was filtered and air-dried. The purity of the resulting product **IIIa-d** was confirmed using thin-layer chromatography with a hexane-ethyl acetate eluent in a 5:1 ratio.

Bis(1-phenyl-3-(pyridin-3-yl)propane-1,3-dionate) Cu (**IIIa**)

Copper acetylacetonate with beta-pyridyl moiety and phenyl substituent (IIIa). Yield 0.6 g (59 %), saturated green powder. IR spectrum, ν , cm^{-1} : 683, 887, 968, 1039, 1149, 1323, 1422, 1595, 1655, 1672, 3250. Mass spectrum, m/z (I, %): 511 (100) $[\text{M}]^+$, 513 (45), 512 (20). AES ICP (Cu) 8.5 %.

Bis(1-phenyl-3-(pyridin-4-yl)propane-1,3-dionate) Cu (IIIb)

Copper acetylacetonate with gama-pyridyl moiety and phenyl substituent (IIIb). Yield 0.62 g (61 %), saturated green powder. IR spectrum, ν , cm^{-1} : 685, 747, 883, 966, 1038, 1149, 1329, 1425, 1597, 1687, 3076. Mass spectrum, m/z (I, %): 511 (100) $[\text{M}]^+$, 513 (45), 512 (20). AES ICP (Cu) 10.4 %.

Bis(1-(pyridin-3-yl)butane-1,3-dionate) Cu (IIIc)

Copper acetylacetonate with beta-pyridyl moiety and methyl substituent (IIIc). Yield 0.28 g (36 %), light green powder. IR spectrum, ν , cm^{-1} : 691, 753, 1024, 1231, 1311, 1393, 1423, 1450, 1472, 1526, 1596, 3089. Mass spectrum, m/z (I, %): 387 (100) $[\text{M}]^+$, 389 (45), 988 (20). AES ICP (Cu) 22 %.

Bis(1-(pyridin-4-yl)butane-1,3-dionate) Cu (III d)

Copper acetylacetonate with gama-pyridyl moiety and methyl substituent (III d). Yield 0.33 g (43 %), light green powder. IR spectrum, ν , cm^{-1} : 544, 643, 698, 725, 765, 1026, 1068, 1228, 1319, 1399, 1421, 1452, 1480, 1521, 1588, 1591, 3085. Mass spectrum, m/z (I, %): 387 (100) $[\text{M}]^+$, 389 (45), 988 (20). AES ICP (Cu) 31.3 %.

*Computational Details**DFT Calculations*

DFT calculations of copper chelate complexes *IIIa-d* were performed at the B3LYP/6-311++G(d, p) on organic (C, H, N, O, P) [25, 26] and LanL2DZ for metal (Cu(II)) [27] part basis set level of theory using Gaussian-16 [28]. In order to get as close as possible to the conditions of biological systems, solvation was taken into account in the calculations within the framework of the macroscopic polarizable continuum model CPCM (water) [29]. Optimization of the geometry of chelate complexes was carried out without any restrictions using the keywords OPT+FREQ; achieving geometry with a minimum of energy on the potential energy surface (PES) was confirmed by the absence of imaginary frequencies.

Based on the results of the DFT optimization of the geometry of the studied copper chelate complexes, HOMO-LUMO frontier orbitals and maps of the distribution of molecular electrostatic potential (MEP) were constructed and analyzed using analytical methods. The obtained values of the energies of the HOMO-LUMO orbitals were then used for calculations of such global descriptors of chemical activity [30], as: the ionization potential (IP), the electron affinity (EA), the energy gap ΔE_{gap} , molecular hardness (η) and softness (σ), the index of electrophilicity (ω) and nucleophilicity (ε), absolute electronegativity (χ) and chemical potential (μ):

$$\text{IP} = -E_{\text{HOMO}}, \quad (1) \quad \text{EA} = -E_{\text{LUMO}}, \quad (2) \quad E_{\text{gap}} = (E_{\text{LUMO}} - E_{\text{HOMO}}), \quad (3)$$

$$\chi = (\text{IP} + \text{EA}) / 2, \quad (4) \quad \mu = -(\text{IP} + \text{EA}) / 2 = -\chi \quad (5) \quad \eta = (\text{IP} - \text{EA}) / 2, \quad (6)$$

$$\omega = \mu^2 / 2\eta, \quad (7) \quad \sigma = 1 / 2\eta, \quad (8) \quad \varepsilon = 1 / \omega. \quad (6)$$

Visualization of DFT optimized molecular structures as well as frontier orbitals and MEPs were performed using GaussView 6.0 software [31].

In silico Study of Biological Activity

PASS (Prediction of Activity Spectra for Substances) program was used to predict useful biological activity of the synthesized copper complexes *IIIa-d* [32–34]. The PASS prediction, based on the molecular structure data, produces a list of probable activities, Pa being the probability of belonging to the “active” class, and Pi being the probability of belonging to the “inactive” class.

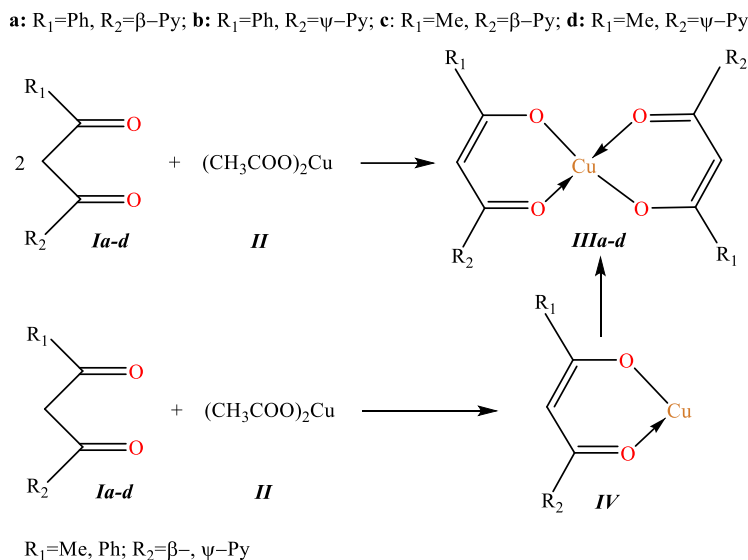
Molecular Docking Simulations

Molecular docking was performed using AutoDock Vina and AutoDock MGL Tools 1.5.7 [35, 36]. The molecular structure of the protein was downloaded from the Protein Data Bank (<https://www.rcsb.org>). Preparation of the protein molecular structure for docking included the steps of removing the native ligand and water molecules, protonation, and specifying the binding site. The position of the binding site was determined based on PDB data, and the following grid coordinates of the receptor active site were used: ($x = 12.881$, $y = 4.486$, $z = -0.184$) for the structure of alpha2 nicotinic acetylcholine receptor (PDB ID: **5FJV**). The docking results were used for comparative analysis of binding affinity and intermolecular interactions between the studied copper chelate complexes and the target protein. The study of intermolecular

interactions between the target protein and ligands was carried out using the BIOVIA Discovery Studio Visualizer 2017 [37] software.

Results and Discussion

We assumed that the resulting chelates have the structure **IIIa-d** (Scheme 1).



Scheme 1. Possible pathways for the copper chelates formation

The structure of the chelates was studied by IR spectroscopy. The IR spectra of chelates **IIIa-d** contain bands corresponding to phenyl and pyridyl fragments, observed in the range of 1680–1440 cm⁻¹.

At the same time, it is known that the ligands of copper acetylacetonate contain a conjugated bond system, –C(O)–CH=C–. The conjugation induces a bathochromic shift, manifesting as three bands at 1575, 1545, 1525 cm⁻¹, characteristic of a quasi-aromatic metallocycle [38]. In our opinion, for compounds **IIIa-d**, the bands of stretching vibrations –C(O)–CH=C– at 1575, 1545, 1525 cm⁻¹ are partially (for compounds **IIIc, III d**) or completely (for compounds **IIIa, III b**) overlapped by stretching vibrations of the pyridine or phenyl fragments.

Indeed, the DFT Calculations performed for all chelates **IIIa-d** showed that with methyl and pyridyl substituents (compounds **IIIc, III d**) the distortion of geometry at the Cu²⁺ ion is minimal. Whereas in the presence of pyridine and phenyl rings (compounds **IIIa** and **III b**) there is a distortion of geometry in one of the ligands. A detailed description of the DFT Calculations results is provided in the Computational Study section of this article.

The next step in elucidating the structure of copper complexes was identifying the number of ligands. Although the reaction proceeded depending on the ratio of 1,3-diketone and copper(II) acetate, the formation of either structure **III** or **IV** remains possible (Scheme 1). To resolve the uncertainty regarding the formation of structure **III** or **IV** in the obtained chelate complexes, a chromato-mass spectrometric study was carried out.

The analysis revealed that the predominant compounds formed contained two molecules of a dicarbonyl compound per copper molecule, with molecular weights of 512 g/mol and 388 g/mol, respectively. Additionally, signals corresponding to compounds with one diketone molecule per copper molecule were observed, with molecular weights of 226 g/mol and 288 g/mol, as presented in Table 2.

Table 2

Results of gas chromatography-mass spectrometry analyses

Complex	R ₁	R ₂	Molecular weight, g/mol	Retention time, min	Peak area, %
IIIa	β-pyridyl	Ph	512	6.32	76.8
IIIb	γ-pyridyl	Ph	512	5.99	83.0
IIIc	β-pyridyl	Me	388	7.30	91.6
III d	γ-pyridyl	Me	388	5.77	98.0

Additionally, sample analysis revealed that, over time, the content of chelates containing one diketone molecule per copper atom, with molecular weights of 226 g/mol and 288 g/mol, decreased. Simultaneously, the peak area of detectable compounds with molecular weights of 512 g/mol and 388 g/mol increased. This indirectly suggests the instability of product **IV** (Scheme 1) and the subsequent formation of product **III** (Scheme 1). Thus, we have demonstrated that chelates preferentially take form **III**.

To confirm the amount of substance that reacted during synthesis, a study was conducted using atomic emission spectroscopy with inductively coupled plasma. The analysis determined the amount of copper that reacted with the original β -diketone. The results of the atomic emission analysis are presented in Table 3.

Table 3

Results of copper content analysis by the atomic emission spectroscopy

Complex	Me	R ₁	R ₂	Copper content, %
IIIa	Cu	β -pyridyl	Ph	8.5
IIIb	Cu	γ -pyridyl	Ph	10.4
IIIc	Cu	β -pyridyl	Me	22.0
III d	Cu	γ -pyridyl	Me	31.3

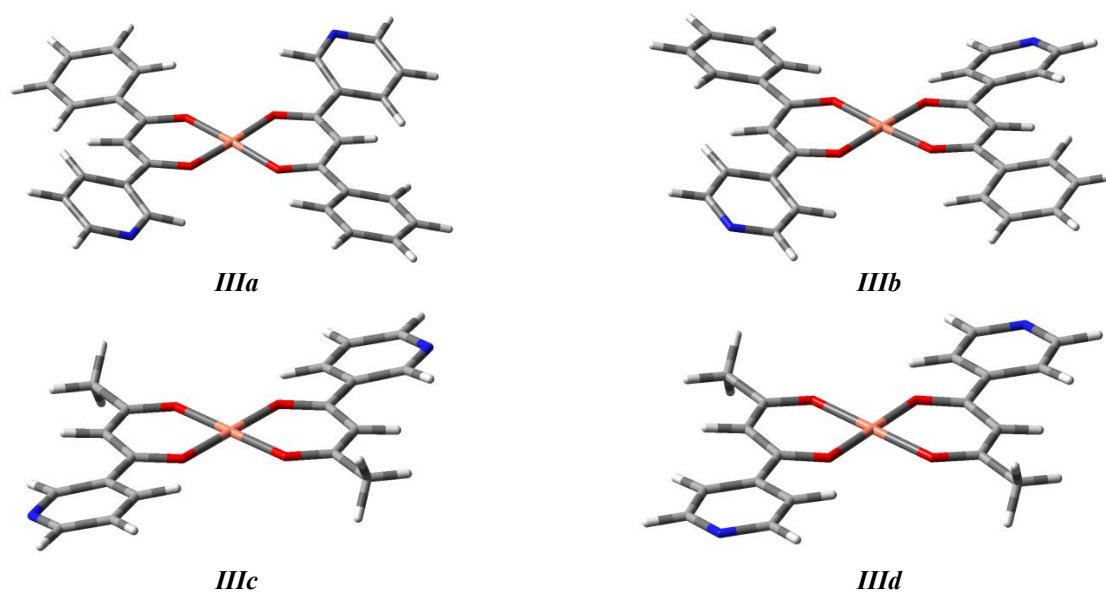
In complex containing pyridine fragment and phenyl substituent amount of copper is 10.4 %, and in complex with methyl substituent and position of nitrogen in γ -position is 31.3 %. This is most likely due to the steric and electron donor properties of the substituents.

In the complex containing a pyridine fragment and a phenyl substituent, the copper content is 10.4 %. In contrast, the complex with a methyl substituent and nitrogen in the γ -position, contains 31.3 % copper. This difference is most likely attributed to the steric and electron-donating properties of the substituents.

Computational Study

DFT Calculations

Since chelate complexes of copper pyridyl-containing beta-diketonates were synthesized for the first time, it was interesting to study their physicochemical properties and biological activity using *in silico* methods. First of all, the geometry of the synthesized copper complexes **IIIa-d** was optimized by the DFT method with the use of the 6-311G++(d, p) and LANL2DZ basis sets for the ligands and its complexes, respectively, in conjunction with the B3LYP hybrid correlation functional taking into account solvation within the framework of the macroscopic solvation CPCM (water) model. Resulting geometry optimization 3D structures are shown in Figures 3 and S1.

Figure 3 Optimized 3D structures of chelate complexes **IIIa-d**

As can be seen in Figures 3 and S1, each copper atom forms a four-center bond with two bidentate diketone ligands in chelate complexes **IIIa-d**. In chelates **IIIc** and **III d**, the central cyclic diketonate fragment with copper is almost planar, while the side pyridyl substituents have deviations from planarity of approximately 10° relative to the plane of the central fragment of the chelate. The structure of chelates **IIIa** and **III b** is more twisted due to the presence of 4 bulky side substituents, while the central cyclic diketonate fragment with copper has small deviations from planarity, while the side pyridyl substituents are rotated at a wider angle of about 17° , and the side benzene rings are rotated at an angle of about 13° relative to the plane of the central fragment of the chelate.

It should be noted that the structure of the resulting chelates is quite symmetrical, as a result of which compounds **IIIa-d** are characterized by small dipole moments of 0.2107, 0.1897, 0.0003 and 0.0004 Debye, respectively, which indicates a homogeneous charge distribution and a low level of polarity of the chelate complexes.

Frontier Molecular Orbitals and Molecular Electrostatic Potential Map (MEP) Analysis

Next, based on the optimized structures of synthesized copper complexes **IIIa-d**, the construction and analysis of the boundary HOMO-LUMO orbitals and Molecular Electrostatic Potential Map (MEPs) were performed (Figures 4, 5).

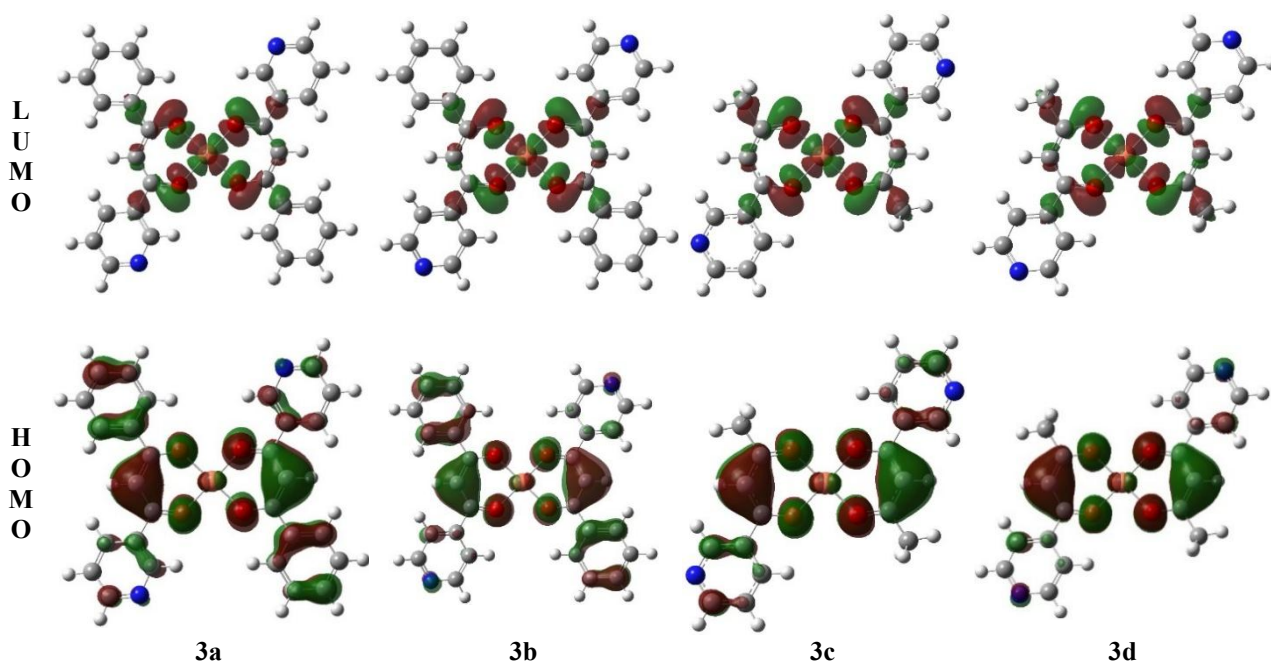
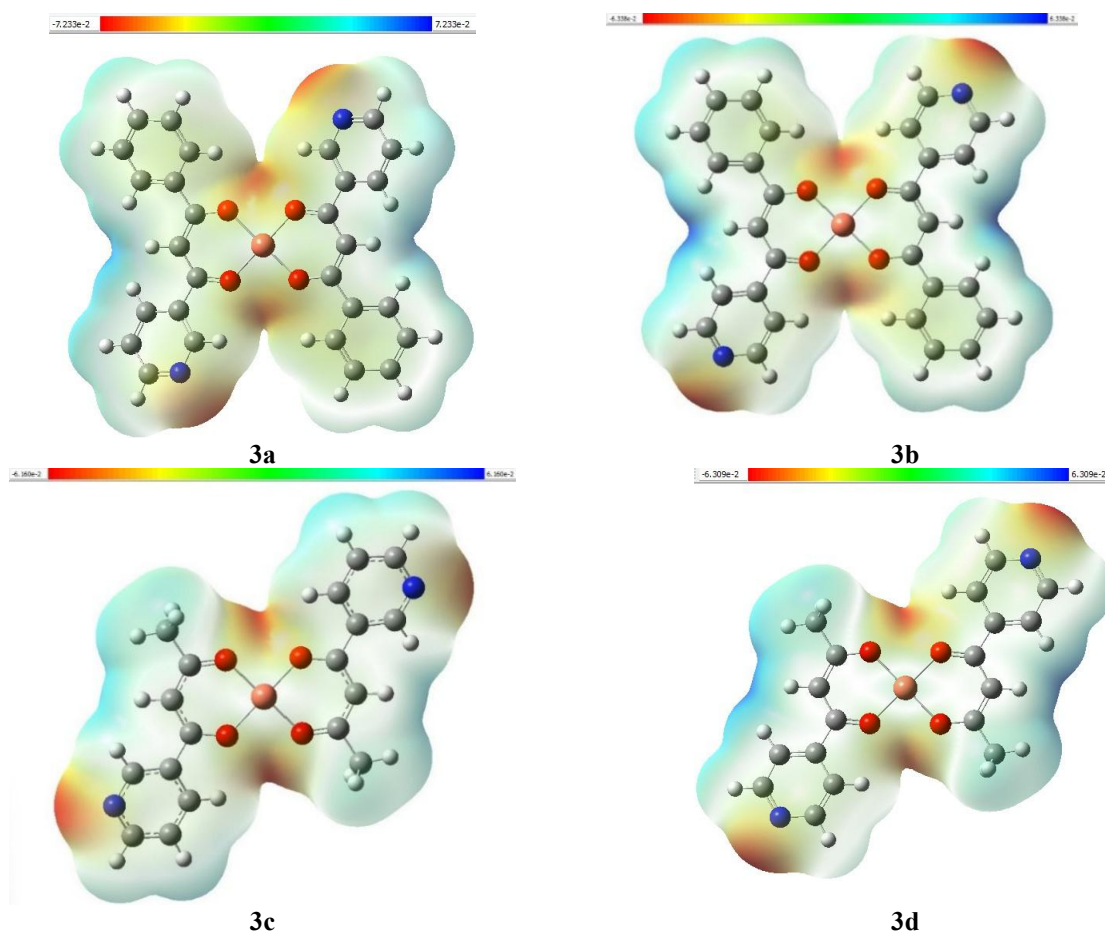


Figure 4. HOMO-LUMO orbital diagrams of chelate complexes **IIIa-d**

As can be seen in Figure 4, the electron density on the HOMO and LUMO orbitals is localized in different places: LUMO is predominantly on the central cyclic diketonate copper containing fragment, while HOMO is more delocalized throughout the entire structure of the complex. Next, the location of electrophilic and nucleophilic centers in the studied complexes **IIIa-d** was assessed based on the analysis of the molecular electrostatic potential (MEP) (Figure 5).

As can be seen in Figure 5, the negative charge in the studied complexes **IIIa-d** is expectedly localized on the oxygens of the central cyclic diketonate fragment, as well as on the nitrogen heteroatoms; the positive charges are concentrated on the complex-forming metal atom, as well as on the hydrogen atoms of the cyclic diketonate fragment. Accordingly, this allows us to assume that the nucleophilic center of the studied copper complexes **IIIa-d** is localized on the oxygen and nitrogen atoms, whereas the electrophilic center can be correlated with the position of the complex-forming copper atom, as well as with the position of the hydrogen atoms of the cyclic diketonate fragment.

Figure 5 Molecular electrostatic potential map (MEP) of chelate complexes *IIIa-d*

Global Reactivity Indexes

An assessment of the studied copper complexes *IIIa-d* global reactivity parameters was performed based on the calculated energy of HOMO-LUMO orbitals. The following global descriptors of chemical activity were assessed: ionization potential (IP), electron affinity (EA), energy gap ΔE_{gap} , molecular hardness (η) and softness (σ), chemical potential (μ), electrophilicity (ω) and nucleophilicity (ε) indexes, absolute electronegativity (χ) (Table 4).

Table 4

Global descriptors of chemical activity

Complex	IP, eV	EA, eV	ΔE_{gap} , eV	η , eV	σ , eV ⁻¹	μ , eV	ω , eV	ε , eV ⁻¹	χ , eV
<i>IIIa</i>	6.5652	3.2904	3.2748	1.6374	0.3053	-4.9278	7.4151	0.1348	4.9278
<i>IIIb</i>	6.6210	3.3344	3.2865	1.6432	0.3042	-4.9777	7.5392	0.1326	4.9777
<i>IIIc</i>	6.6409	3.2735	3.3674	1.6837	0.2969	-4.9572	7.2976	0.1370	4.9572
<i>III d</i>	6.7106	3.3211	3.3894	1.6947	0.2950	-5.0158	7.4227	0.1347	5.0158

As can be seen in Table 4, the studied copper complexes *IIIa-d* are characterized by an electron affinity EA of about 3.2–3.3 eV and a fairly high ionization potential IP in the region of 6.5–6.7 eV, which indicates their low reducing properties. The energy gap ΔE_{gap} at the level of 3.2–3.3 eV indicates the chemical stability of the studied copper complexes *IIIa-d*. The low value of molecular softness σ at the level of 0.3 eV⁻¹, together with the 1.6 eV value of molecular hardness indicates the hard nature of the studied complexes *IIIa-d*. The negative value of the chemical potential μ and its value of (–4.9)–(–5.0) eV confirm the stability of the studied copper complexes. The high level of electrophilicity index ω in the range of 7.2–7.5 eV suggests a predominantly electrophilic nature of the reactivity of the studied complexes. The absolute electronegativity χ of the complexes *IIIa-d* lies in the range from 4.9 to 5.0 eV.

In silico Study of Biological Activity

Next, we used a PASS (Prediction of Activity Spectra for Substances) program to predict useful biological activity of the synthesized copper complexes **IIIa-d**. This tool allows to estimate the probability of various types of biological activity for chemical compounds based on their structural formulas using such indicators as P_a — the probability of being active and P_i — the probability of being inactive. The predicted probabilities of biological activity are presented in the Table 5.

Table 5

PASS predicted biological activity potential of the complexes **IIIa-d**

P_a^*	P_i^*	Type of activity
IIIa		
0.887	0.004	Nicotinic receptor antagonist
0.783	0.011	Dehydro-L-gulonate decarboxylase inhibitor
0.753	0.001	Glutamylendopeptidase II inhibitor
IIIb		
0.890	0.004	Nicotinic receptor antagonist
0.811	0.010	Feruloyl esterase inhibitor
0.787	0.011	Dehydro-L-gulonate decarboxylase inhibitor
IIIc		
0.867	0.005	Gluconate 2-dehydrogenase (acceptor) inhibitor
0.821	0.008	Nicotinic receptor antagonist
0.800	0.009	Dehydro-L-gulonate decarboxylase inhibitor
III d		
0.915	0.003	Gluconate-2-dihydrogenase inhibitor (acceptor)
0.845	0.005	Nicotinic receptor antagonist
0.773	0.013	Dehydro-L-gulonate decarboxylase inhibitor
where: P_a — the probability of being active; P_i — the probability of being inactive.		

As can be seen in Table 5, all complexes **IIIa-d** exhibited biological activity as nicotinic receptor antagonists with P_a values ranging from 0.821 to 0.915, and as dehydro-L-gulonate decarboxylase inhibitors, with P_a values above 0.75. Nicotinic receptor antagonists inhibit acetylcholine activity at nicotinic acetylcholine receptors (nAChRs) and are utilized in the treatment of hypertension, nicotine dependence, neurological disorders, and anesthesia. Gluconate-2-dehydrogenase inhibitor (acceptor) activity is strongly predicted for **IIIc** and **III d** complexes, with high P_a values (0.867–0.915), suggesting a role in carbohydrate metabolism and in the treatment of type 2 diabetes and related cardiovascular diseases.

The analysis of the data presented in Table 5 indicates that complexes **IIIa-d** exhibited the highest biologically active potential as nicotinic receptor antagonists. This biologically active property of complexes **IIIa-d** is potentially very beneficial, as according to WHO data, more than 20 % of the world's population currently uses tobacco, with 8 million people dying each year from the consequences of tobacco use, including 1.3 million passive smokers. Therefore, the search for new nicotinic receptor antagonists is an important area of modern pharmacology, and we further study the inhibitory potential of complexes **IIIa-d** as nicotinic receptor antagonists using the molecular docking approach.

Molecular Docking Simulations

Nicotinic receptor antagonists bind with nicotinic acetylcholine receptors (nAChRs) [39]. These receptors are ion channels that perceive nicotine and acetylcholine, so their action is aimed at regulating the transmission of nerve impulses. Nicotinic acetylcholine receptors (nAChRs) are ligand-gated ion channels that, upon binding nicotine or acetylcholine, open, allowing sodium, potassium, and calcium ions to pass through the cell membrane. This results in depolarization of the cell and initiation of a signal important to the nervous system. nAChR antagonists block this process by preventing binding of nicotine or acetylcholine with the receptor. This results in the prevention of ion channel activation and, accordingly, the suppression of nerve signal transmission. This mechanism is used in pharmacology, for example, in drugs used to treat nicotine addiction or as muscle relaxants during surgery [40]. Target proteins for nicotinic acetylcholine receptor (nAChR) antagonists include receptor subtypes such as: $\alpha 4\beta 2$ receptors are the most common nAChR

subtype in the central nervous system and have been linked to cognitive function and nicotine addiction.; $\alpha 7$ receptors — these receptors are involved in memory, learning and inflammatory processes, and are also a target for the treatment of neurodegenerative diseases [41].

According to the literature [42], alpha2 nicotinic acetylcholine receptor in pentameric assembly (PDB ID: **5FJV** [43]) may act as a target protein for nicotinic acetylcholine receptor antagonists (nAChR), so it was used for molecular docking simulations with synthesized copper complexes **IIIa-d**. Bupropion [44] and the native ligand [43] were used as reference drugs. Molecular docking simulation of the studied copper complexes **IIIa-d** with the target alpha2 nicotinic acetylcholine receptor (PDB ID:**5FJV**) was performed using the AutoDock Vina program; the obtained data on the binding affinity are presented in Table 6.

Table 6

Binding Affinity (kcal·mol⁻¹) of copper complexes *IIIa-d* with alpha2 nicotinic acetylcholine receptor (PDB ID: 5FJV)

Ligand	Binding Affinity, kcal·mol ⁻¹
IIIa	-8.3
IIIb	-8.1
IIIc	-6.9
IIId	-6.6
<i>Reference Drug</i>	
Bupropion	-5.4
Native ligand (1S,2S,4R)-2-(6-chloropyridin-3-yl)-7-azabicyclo[2.2.1]heptane	-5.9

The data presented in Table 4 show that the studied copper complexes **IIIa-d** demonstrate higher binding affinity (-8.3, -8.1, -6.9 and -6.6 kcal·mol⁻¹, respectively) with the alpha2 nicotinic acetylcholine receptor (PDB ID:**5FJV**) compared to the reference drugs Bupropion (-5.4 kcal·mol⁻¹) and the native ligand (-5.9 kcal·mol⁻¹). It should be noted that complexes **IIIa** and **IIIb** interact more effectively (-8.3, -8.1 kcal·mol⁻¹, respectively) with the alpha2 nicotinic acetylcholine receptor (PDB ID:**5FJV**) compared to complexes **IIIc** and **IIId** (-6.9 and -6.6 kcal·mol⁻¹, respectively), which may be due to a larger number of intermolecular interactions (Table 7).

Table 7

Protein 5FJV — Ligand intermolecular interactions

Ligand	Conventional Hydrogen Bond	Carbon Hydrogen Bond	Pi-Pi T-shaped	Pi-Donor	Pi-Sigma	Pi-Sulfur	Pi-alkyl	Pi-Pi-Stacked
IIIa	TRP115	ARG49, ALA48	TRP178	THR179	VAL120	MET134	ALA130	—
IIIb	—	—	TRP178	THR179	ALA130, VAL120	MET134	—	—
IIIc	—	—	—	—	—	—	VAL120, ALA130	PHE129, TRP178
IIId	ARG49	—	—	ALA48	MET134, ALA48	—	—	—
<i>Reference Drug</i>								
Bupropion	GLU128, THR132	—	—	—	—	—	ILE152, TYR153, HIS133, ALA151	—
Native ligand	TYR122, TRP178	—	—	—	—	—	CYS221, CYS222, TYR219, TYR226	—

As can be seen in Table 7, ligand **IIIa** forms 8 bonds with amino acids of the target protein **5FJV**, including one Conventional Hydrogen Bond with TRP115, two Carbon Hydrogen Bond with ARG49, ALA48, one Pi-Pi T-shaped with TRP178, Pi-Donor with THR179, Pi-Sigma with VAL120, Pi-Sulfur with MET134, Pi-alkyl with ALA130. Ligand **IIIb** forms 5 bonds with amino acids of the target protein **5FJV**, including one Pi-Pi T-shaped with TRP178, one Pi-Donor with THR179, two Pi-Sigma with ALA130 and VAL120, one Pi-Sulfur with MET134. Ligand **IIIc** forms four bonds with amino acids of the target protein **5FJV**, including two Pi-alkyl with VAL120 and ALA130, two Pi-Pi-Stacked with PHE129 and TRP178. Ligand **III d** forms 4 bonds with amino acids of the target protein **5FJV**, including one Conventional Hydrogen Bond with ARG49, one Pi-Donor with ALA48, two Pi-Sigma with MET134 and ALA48 (Figures 6, S2-S5).

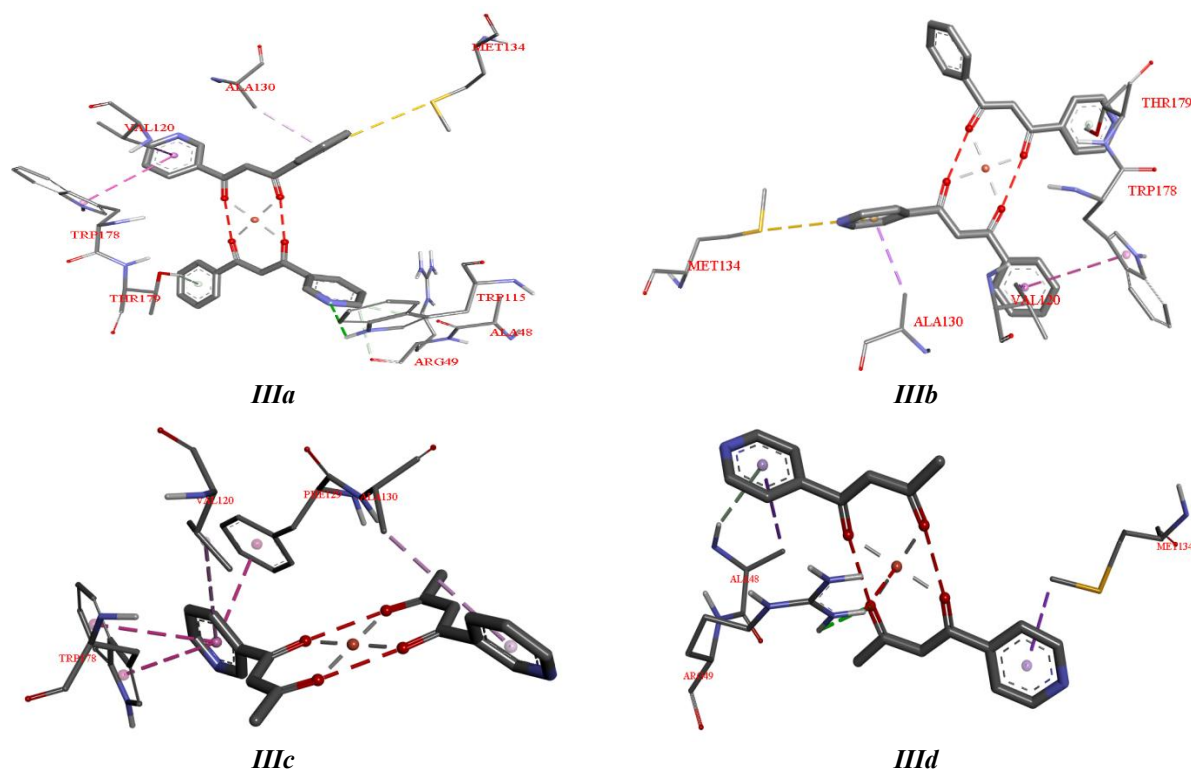


Figure 6 Visualization of protein **5FJV** amino acids — ligand **IIIa-d** interactions

As can be seen in Figures 6, S2-S5, the pi-electron systems of the pyridyl and benzene rings of the studied ligands **IIIa-d** actively participate in intermolecular interactions, therefore their greater number in ligands **IIIa** and **IIIb** leads to a more effective interaction of these compounds with the target protein **5FJV**.

Overall, molecular docking simulations of synthesized copper complexes **IIIa-d** with alpha2 nicotinic acetylcholine receptor (PDB ID:**5FJV**) showed their high potential as nicotinic receptor antagonist. Moreover, compounds **IIIa** and **IIIb** showed a more effective interaction with the **5FJV** protein compared to compounds **IIIc** and **III d**, may be due to the presence of a larger number of substituents with pi-electron systems.

Conclusions

We have obtained previously unknown chelate complexes of copper(II) with pyridyl-containing beta-diketones. The syntheses were carried out with different ratios of reagents, the most successful was the ratio of 2:1 1,3-diketone to copper(II) acetate. Complexation with copper(II) took place at a temperature not exceeding 50 °C for 1 hour, with the yield of products **IIIa-d** ranging from 8.5 % to 31.3 %. The structure of the newly obtained chelates has been proven by IR, atomic emission spectroscopy and mass spectrometry. Based on DFT B3LYP/6-311++G(d, p) /LanL2DZ CPCM (water) calculations, the non-planar structure of the synthesized copper chelate complexes **IIIa-d** was demonstrated, an analysis of the HOMO-LUMO orbitals and molecular electrostatic potential (MEP) was performed, global descriptors of chemical activity were assessed. *In silico* study of biological activity was carried out using the PASS Prediction and AutoDock Vina tools. Molecular docking simulations of synthesized copper complexes **IIIa-d** with alpha2 nicotinic acetylcholine receptor (PDB ID:**5FJV**) showed their high potential as nicotinic receptor antagonist. Moreover,

compounds **IIIa** and **IIIb** showed a more effective interaction with the **5FJV** protein compared to compounds **IIIc** and **IIId**, may be due to the presence of a larger number of substituents with pi-electron systems. Newly synthesized copper complexes **IIIa** and **IIIb** can be recommended for further study of their pharmaceutical potential as nicotinic receptor antagonist via *in vitro* and *in vivo* methods.

Supporting Information

The Supporting Information is available free at <https://ejc.buketov.edu.kz/index.php/ejc/article/view/124/211>

Funding

Authors state no funding involved.

Author Information*

*The authors' names are presented in the following order: First Name, Middle Name and Last Name

Alexey Aleksandrovich Kukushkin (*corresponding author*) — PhD, Associate Professor, School of Petroleum and Gas Engineering, Siberian Federal University, pr. Svobodny, 79, 660041, Krasnoyarsk, Russia; e-mail: alekseykukushkin@bk.ru, <https://orcid.org/0000-0002-2039-5471>

Elizaveta Vitalievna Kudashova — Student, Department of Organic Chemistry and Technology of Organic Compounds, Reshetnev Siberian State University of Science and Technology, Krasnoyarskiy Rabochiy Ave., 31, 660037, Krasnoyarsk, Russia; e-mail: kudasovaelizaveta@gmail.com

Evgeny Vladimirovich Root — PhD, Head of the Department of Organic Chemistry and Technology of Organic Compounds, Reshetnev Siberian State University of Science and Technology, Krasnoyarskiy Rabochiy Ave., 31, 660037, Krasnoyarsk, Russia; Associate Professor of the Department of Pharmacy with PC, State Medical University named after Prof. V.F. Voyno-Yasenetsky, Partizana Zheleznyaka str., 1, 660022, Krasnoyarsk, Russia; e-mail: rootev@mail.ru, <https://orcid.org/0009-0001-7093-4701>

Anna Sergeevna Kositsyna — PhD, Associate Professor, Department of Organic Chemistry and Technology of Organic Compounds, Reshetnev Siberian State University of Science and Technology, Krasnoyarskiy Rabochiy Ave., 31, 660037, Krasnoyarsk, Russia; e-mail: kositsyna-anna@mail.ru

Ilya Sergeevich Ponomarev — Junior Research Assistant, Institute of Chemistry and Chemical Technology Siberian Branch of the Russian Academy of Sciences, Akademgorodok str., 50/24, 660036, Krasnoyarsk, Russia, e-mail: il.ponomarew@yandex.ru, <https://orcid.org/0000-0001-7027-7177>

Alexey Viktorovich Lyubyashkin — Director of the Institute of Chemical Technology, Reshetnev Siberian State University of Science and Technology, Krasnoyarskiy Rabochiy Ave., 31, 660037, Krasnoyarsk, Russia; e-mail: lyubyashkinav@sibsau.ru, <https://orcid.org/0000-0002-0428-5950>

Irina Anatolievna Pustolaikina — Candidate of Chemical Sciences, Associate Professor, Department of Physical and Analytical Chemistry, Karaganda Buketov University, Universitetskaya street, 28, 100024, Karaganda, Kazakhstan; e-mail: pustolaikina_irina@buketov.edu.kz, <https://orcid.org/0000-0001-6319-666X>

Author Contributions

The manuscript was written through contributions of all authors. All authors have given approval to the final version of the manuscript. **CRedit**: **Alexey Aleksandrovich Kukushkin** — investigation, methodology, validation; **Elizaveta Vitalievna Kudashova** — conceptualization, data curation, **Evgeny Vladimirovich Root** — data curation, formal analysis, visualization; **Anna Sergeevna Kositsyna** — validation, writing-original draft; **Ilya Sergeevich Ponomarev** — investigation, methodology; **Alexey Viktorovich Lyubyashkin** — funding acquisition, resources; **Irina Anatolievna Pustolaikina** — computational study, methodology, investigation, data curation, formal analysis, visualization; writing-review & editing.

Acknowledgments

The work was carried out using the equipment of the Krasnoyarsk Regional Center for Collective Use of the Federal Research Center of the KSC SB RAS.

Conflicts of Interest

The authors declare no conflict of interest.

References

- 1 Harwood, J. (1963). *Industrial applications of organometallic compounds*. Chapman&Hall.
- 2 Rykowska I., & Wasiak W. (2002). Gas chromatography silica packings with chemically bonded complexes of Cu (II) and Cr (III). *Analytica Chimica*, 2, 271–278. [https://doi.org/10.1016/S0003-2670\(01\)01404-0](https://doi.org/10.1016/S0003-2670(01)01404-0)
- 3 Patel R.N. et al. (2009). Copper (II) complexes as superoxide dismutase mimics: synthesis, characterization, crystal structure and bioactivity of copper (II) complexes. *Inorganica Chimica*, 14, 4891–4898. <https://doi.org/10.1016/j.ica.2009.07.037>
- 4 Kalarani R. et al. (2020). Synthesis, spectral, DFT calculation, sensor, antimicrobial and DNA binding studies of Co (II), Cu (II) and Zn (II) metal complexes with 2-amino benzimidazole Schiff base. *Journal of Molecular Structure*, 1206, 127725. <https://doi.org/10.1016/j.molstruc.2020.127725>
- 5 Mir, I.A., Ain, Q.U., Singh, I., Carmieli, R., & Sharma, R. (2024). Investigation of biological activity of oxindole semicarbazones based copper (II) complexes: Synthesis, antimicrobial activities and molecular modelling. *Polyhedron*, 263, 117208. <https://doi.org/10.1016/j.poly.2024.117208>
- 6 Hassan, S.S., Aly, S.A., Rizk, N.M.H., Khidr, M.A., Al-Sulami, A.I., Mousa, I.E., Badr, E.E., & Abdalla, E.M. (2024). Synthesis, characterization, antimicrobial, anticancer and the theoretical calculation of a novel N,O-multidentate chelating ligand and its Cu(II) and Fe(III) complexes. *Inorganic Chemistry Communications*, 170, 113279. <https://doi.org/10.1016/j.inoche.2024.113279>
- 7 Karcz D. et al. (2021). Novel coumarin-thiadiazole hybrids and their Cu (II) and Zn (II) complexes as potential antimicrobial agents and acetylcholinesterase inhibitors. *International Journal of Molecular Sciences*, 22(18), 9709. <https://doi.org/10.3390/ijms22189709>
- 8 Stepanenko I. et al. (2021). Coumarin-Based Triapine Derivatives and Their Copper (II) Complexes: Synthesis, Cytotoxicity and mR2 RNR Inhibition Activity. *Biomolecules*, 11(6), 862. <https://doi.org/10.3390/biom11060862>.
- 9 Dey, S.K., Bag, B., Zhou, Z., Chan, A.S., & Mitra, S. (2004). Synthesis, characterization and crystal structure of a monomeric and a macrocyclic copper (II) complex with a large cavity using benzylacetylacetone ligand. *Inorganica chimica acta*, 357(7), 1991–1996. <https://doi.org/10.1016/j.ica.2003.12.014>.
- 10 Pauly, M.A., Erwin, E.M., Powell, D.R., Rowe, G.T., & Yang, L. (2015). A synthetic, spectroscopic and computational study of copper (II) complexes supported by pyridylamide ligands. *Polyhedron*, 102, 722–734. <https://doi.org/10.1016/j.poly.2015.11.015>.
- 11 Walczak, A., Kurpik, G., & Stefankiewicz, A.R. (2020). Intrinsic effect of pyridine-n-position on structural properties of Cu-based low-dimensional coordination frameworks. *International Journal of Molecular Sciences*, 21(17), 6171. <https://doi.org/10.3390/ijms21176171>.
- 12 Dudek, M. et al. (2011). Interaction of Copper (II) with Ditopic Pyridyl- β -diketone Ligands: Dimeric, framework, and metallogel structures. *Crystal growth & design*, 11(5), 1697–1704. <https://doi.org/10.1021/cg101629w>.
- 13 Bendi, A., Jafar Ahamed, A., Kaur, N., Mujafarkani, N., Banu, A.M., & Afshari, M. (2025). Synthesis, Experimental and Computational Evaluation of p-Semidine-p-Phenylenediamine-Formaldehyde (Terpolymer) and Its Copper Complex as Potent Antimicrobial and Anticorrosive Agents. *Journal of Inorganic and Organometallic Polymers and Materials*, 35, 3993–4015. <https://doi.org/10.1007/s10904-024-03507-4>
- 14 Quim Peña et al. (2021). Copper(II) N,N,O-Chelating Complexes as Potential Anticancer Agents. *Inorg. Chem.*, 60, 5, 2939–2952. <https://doi.org/10.1021/acs.inorgchem.0c02932>.
- 15 Gur'eva, Ya.A., Zalevskaya, O.A., & Kuchin, A.V. (2023). Biologically Active Palladium(II), Zinc(II), and Copper(II) Complexes with Terpene Ligands as Potential Pharmaceutical Drugs. *Russian Journal of Coordination Chemistry*, 49(10), 631–651. <https://doi.org/10.1134/s1070328423700665>
- 16 Carlos Martínez-Ceberio et al. (2023). Mesomorphism and luminescence in coordination compounds and ionic salts based on pyridine-functionalized β -diketones. Influence of the pyridine nitrogen position. *Journal of Molecular Liquids*, 385, 1, 122290. <https://doi.org/10.1016/j.molliq.2023.122290>.
- 17 de Gonzalo, G., & Alcántara, A.R. (2021). Recent Developments in the Synthesis of β -Diketones. *Pharmaceuticals*, 14(10), 1043. <https://doi.org/10.3390/ph14101043>
- 18 Kljun, J., & Turel, I. (2017). β -Diketones as Scaffolds for Anticancer Drug Design — From Organic Building Blocks to Natural Products and Metallodrug Components. *European Journal of Inorganic Chemistry*, 2017(12), 1655–1666. Portico. <https://doi.org/10.1002/ejic.201601314>
- 19 Famta, P., et al. (2025). Hydroxypropyl β -cyclodextrin complexes of olaparib: Amalgamation of *in silico*, *in vitro* and *in vivo* approaches for bioavailability enhancement. *Journal of Molecular Structure*, 1336, 142077. <https://doi.org/10.1016/j.molstruc.2025.142077>
- 20 Iqtadar, R., et al. (2025). New halogenated chalcones as potential anti-inflammatory agents: A comprehensive *in silico*, *in vitro*, and *in vivo* study with ADME profiling. *Journal of Molecular Structure*, 1326, 141055. <https://doi.org/10.1016/j.molstruc.2024.141055>.

- 21 Rakhimzhanova, A.S., Muzaparov, R.A., Pustolaikina, I.A., Kurmanova, A.F., Nikolskiy, S.N., Kapishnikova, D.D., Stalinskaya, A.L., & Kulakov, I.V. (2024). Series of Novel Integrastatins Analogues: In silico Study of Physicochemical and Bioactivity Parameters. *Eurasian Journal of Chemistry*, 29(4 (116)), 44–60. <https://doi.org/10.31489/2959-0663/4-24-13>
- 22 Interstate standard (1980). Technical ethyl alcohol. Specifications (GOST 17299-78). <https://docs.cntd.ru/document/120>.
- 23 Levine R., & Sneed J.K. (1951). The relative reactivities of the isomeric methyl pyridinecarboxylates in the acylation of certain ketones. The synthesis of β -diketones containing pyridine rings. *Journal of the American Chemical Society*, 73(12), 5614–5616. <https://doi.org/10.1021/ja01156a035>.
- 24 Rusnac, R., Garbuz, O., Chumakov, Y., Tsapkov, V., Hureau, C., Istrati, D., & Gulea, A. (2023). Synthesis, Characterization, and Biological Properties of the Copper(II) Complexes with Novel Ligand: N-[4-(2-[1-(pyridin-2-yl)ethylidene]hydrazinecarbothioyl)amino]phenyl]acetamide. *Inorganics*, 11(10), 408. <https://doi.org/10.3390/inorganics11100408>
- 25 Kulakov, I.V., Stalinskaya, A.L., Chikunov, S.Y., Pustolaikina, I.A., & Gatilov, Y.V. (2023). Synthesis of New Structural Analogues of Natural Integrastatins with a Basic Epoxybenzo[7,8]oxocine Skeleton: Combined Experimental and Computational Study. *Synthesis*, 56(02), 329–345. CLOCKSS. <https://doi.org/10.1055/s-0042-1751521>
- 26 Stalinskaya, A.L., Chikunov, S.Y., Pustolaikina, I.A., & Kulakov, I.V. (2022). Cyclization Reaction of 3,5-Diacetyl-2,6-dimethylpyridine with Salicylic Aldehyde and Its Derivatives: Quantum-Chemical Study and Molecular Docking. *Russian Journal of General Chemistry*, 92(5), 914–924. <https://doi.org/10.1134/s107036322205022x>
- 27 Alghuwainem, Y.A.A., El-Lateef, H.M.A., Khalaf, M.M., Amer, A.A., Abdelhamid, A.A., Alzharani, A.A., Alfarsi, A., Shaaban, S., Gouda, M., & Abdou, A. (2022). Synthesis, DFT, Biological and Molecular Docking Analysis of Novel Manganese(II), Iron(III), Cobalt(II), Nickel(II), and Copper(II) Chelate Complexes Ligated by 1-(4-Nitrophenylazo)-2-naphthol. *International Journal of Molecular Sciences*, 23(24), 15614. <https://doi.org/10.3390/ijms232415614>
- 28 Gaussian 16, Revision A.03, M.J. Frisch, G.W. Trucks, H.B. Schlegel, G.E. Scuseria, M.A. Robb, J.R. Cheeseman, G. Scalmani, V. Barone, G.A. Petersson, H. Nakatsuji, X. Li, M. Caricato, A.V. Marenich, J. Bloino, B.G. Janesko, R. Gomperts, B. Mennucci, H.P. Hratchian, J.V. Ortiz, A.F. Izmaylov, J.L. Sonnenberg, D. Williams-Young, F. Ding, F. Lipparini, F. Egidi, J. Goings, B. Peng, A. Petrone, T. Henderson, D. Ranasinghe, V.G. Zakrzewski, J. Gao, N. Rega, G. Zheng, W. Liang, M. Hada, M. Ehara, K. Toyota, R. Fukuda, J. Hasegawa, M. Ishida, T. Nakajima, Y. Honda, O. Kitao, H. Nakai, T. Vreven, K. Throssell, J.A. Montgomery, Jr., J.E. Peralta, F. Ogliaro, M.J. Bearpark, J.J. Heyd, E.N. Brothers, K.N. Kudin, V.N. Staroverov, T.A. Keith, R. Kobayashi, J. Normand, K. Raghavachari, A.P. Rendell, J.C. Burant, S.S. Iyengar, J. Tomasi, M. Cossi, J.M. Millam, M. Klene, C. Adamo, R. Cammi, J.W. Ochterski, R.L. Martin, K. Morokuma, O. Farkas, J.B. Foresman, and D.J. Fox, Gaussian, Inc., Wallingford CT, 2016.
- 29 Tomasi, J., Mennucci, B., & Cammi, R. (2005). Quantum mechanical continuum solvation models. *Chemical Reviews*, 105(8), 2999–3094. <https://doi.org/10.1021/cr9904009>
- 30 Molski, M. (2021). Theoretical modeling of structure-toxicity relationship of cyanides. *Toxicology Letters*, 349, 30–39. <https://doi.org/10.1016/j.toxlet.2021.05.011>
- 31 Dennington, R., Keith, T., & Millam, J. GaussView, Version 6. Semichem Inc., Shawnee Mission, KS, 2016. <http://gaussian.com>
- 32 Poroikov, V.V., Filimonov, D.A., Glorizova, T.A., Lagunin, A.A., Druzhilovskiy, D.S., Rudik, A.V., Stolbov, L.A., Dmitriev, A.V., Tarasova, O.A., Ivanov, S.M., & Pogodin, P.V. (2019). Computer-aided prediction of biological activity spectra for organic compounds: the possibilities and limitations. *Russian Chemical Bulletin*, 68(12), 2143–2154. <https://doi.org/10.1007/s11172-019-2683-0>
- 33 Filimonov, D.A., Lagunin, A.A., Glorizova, T.A., Rudik, A.V., Druzhilovskii, D.S., Pogodin, P.V., & Poroikov, V.V. (2014). Prediction of the Biological Activity Spectra of Organic Compounds Using the Pass Online Web Resource. *Chemistry of Heterocyclic Compounds*, 50(3), 444–457. <https://doi.org/10.1007/s10593-014-1496-1>
- 34 Filimonov, D.A., Rudik, A.V., Dmitriev, A.V., & Poroikov, V.V. (2020). Computer-Aided Estimation of Biological Activity Profiles of Drug-Like Compounds Taking into Account Their Metabolism in Human Body. *International Journal of Molecular Sciences*, 21(20), 7492. <https://doi.org/10.3390/ijms21207492>
- 35 Sarkar, A., Concilio, S., Sessa, L., Marraffino, F., & Piotto, S. (2024). Advancements and novel approaches in modified Autodock Vina algorithms for enhanced molecular docking. *Results in Chemistry*, 101319. <https://doi.org/10.1016/j.rechem.2024.101319>
- 36 Forli, S., Huey, R., Pique, M.E., Sanner, M.F., Goodsell, D.S., & Olson, A.J. (2016). Computational protein–ligand docking and virtual drug screening with the AutoDock suite. *Nature Protocols*, 11(5), 905–919. <https://doi.org/10.1038/nprot.2016.051>
- 37 BIOVIA. (2023). BIOVIA Discovery Studio. Dassault Systèmes.
- 38 Kostyuk, N.N., & Dick, T.A. (2020). Synthesis of Ultrapure Copper Chelates. *Russian Journal of General Chemistry*, 90(11), 2141–2146. <https://doi.org/10.1134/s1070363220110195>.
- 39 Rollema, H., Bertrand, D., & Hurst, R.S. (2010). Nicotinic Agonists and Antagonists. In: Stolerman, I.P. (Eds). *Encyclopedia of Psychopharmacology*. Springer, Berlin, Heidelberg. https://doi.org/10.1007/978-3-540-68706-1_304
- 40 Crooks, P.A., Bardo, M.T., & Dwoskin, L.P. (2014). Nicotinic Receptor Antagonists as Treatments for Nicotine Abuse. *Emerging Targets & Therapeutics in the Treatment of Psychostimulant Abuse*, 513–551. <https://doi.org/10.1016/b978-0-12-420118-7.00013-5>
- 41 Wu, C.-H., Lee, C.-H., & Ho, Y.-S. (2011). Nicotinic Acetylcholine Receptor-Based Blockade: Applications of Molecular Targets for Cancer Therapy. *Clinical Cancer Research*, 17(11), 3533–3541. <https://doi.org/10.1158/1078-0432.ccr-10-2434>

42 Kouvatsos, N., Giastas, P., Chroni-Tzartou, D., Pouloupoulou, C., & Tzartos, S. J. (2016). Crystal structure of a human neuronal nAChR extracellular domain in pentameric assembly: Ligand-bound $\alpha 2$ homopentamer. *Proceedings of the National Academy of Sciences*, 113(34), 9635–9640. <https://doi.org/10.1073/pnas.1602619113>

43 Giastas, P., Kouvatsos, N., Chroni-Tzartou, D., & Tzartos, S.J. (2016). *Crystal structure of the extracellular domain of alpha2 nicotinic acetylcholine receptor in pentameric assembly*. <https://doi.org/10.2210/pdb5fjv/pdb>

44 (2025). National Center for Biotechnology Information. PubChem Compound Summary for CID 444, Bupropion. Retrieved from <https://pubchem.ncbi.nlm.nih.gov/compound/Bupropion>

Polina I. Dubovskaia^{1*}, Saeidi Arsalan^{1,2}, Anna A. Pronchenko¹,
Anastasiia I. Drannikova¹, Ivan A. Lukoyanov^{1,3}, Farida K. Aripova^{1,4},
Mariia E. Savenko¹, Elizaveta A. Veretennikova⁵, Alexander V. Pestov⁵,
Ekaterina A. Litvinova¹, Aleksandr A. Drannikov¹

¹*Novosibirsk State Technical University, Novosibirsk, Russia;*

²*Novosibirsk State University, Novosibirsk, Russia;*

³*Boreskov Institute of Catalysis, Siberian Branch of the Russian Academy of Sciences, Novosibirsk, Russia;*

⁴*Novosibirsk State Agrarian University, Novosibirsk, Russia;*

⁵*I. Ya. Postovsky Institute of Organic Synthesis, Ural Branch of the Russian Academy of Sciences, Yekaterinburg, Russia*

(*Corresponding author's e-mail: dubovskaiapolina@gmail.com)

Gel-Phase Synthesis and pH-Sensitive Swelling-Structure Relationships of N-Carboxyethylchitosan

The applicability of native chitosan-based compositions is constrained by their limited solubility in weakly alkaline and neutral media, a consequence of inherent structural features. To overcome this limitation, carboxyalkylation strategies such as the gel-phase Michael synthesis of N-carboxyethylchitosan (N-CEC) were investigated with a focus on optimizing reaction parameters to enhance yield and tailor biopolymer properties. Structural confirmation of the synthesized polymers was performed via FT-IR and SEM, while elemental analysis quantified the degree of substitution (DS), which correlated with temperature in the following way: DS = 0.96–1.10 at 50 °C, 1.07–1.12 at 60 °C and 1.16–1.32 at 70 °C. Porosity measurements indicated pore sizes ranging from 50 to 200 μm in all samples; however, total porosity varied significantly, reaching a maximum of 15 % at 70 °C and decreasing to 4–10 % at lower temperatures. N-CEC exhibited pH-dependent swelling, with minimal expansion (100–150 %) at low pH and a 2–3-fold increase at pH > 7, which was attributed to COO⁻ group formation. These findings position N-CEC as a promising material for pH-responsive applications.

Keywords: carboxyethylchitosan, biopolymer, gel-phase synthesis, derivatization, Michael reaction, pH-sensitive swelling, porosity, green chemistry

1. Introduction

Chitosan is a natural polymer that has garnered significant attention due to its versatile applications in various fields. This aminopolysaccharide is typically derived through the deacetylation of chitin, which is predominantly obtained from crustacean exoskeletons, including those of shrimp and crabs [1–3]. The unique properties of chitosan, such as its biodegradability, low toxicity, and antimicrobial activity, make it an important material for various industries, particularly in biotechnology, medicine, water treatment and agriculture [4–8]. One of chitosan's most notable features is its excellent biocompatibility, enabling its use in various biomedical applications without provoking adverse reactions [4, 9]. This makes chitosan an ideal candidate for drug delivery systems, wound healing, and tissue engineering [10–15]. Its polyelectrolyte properties provide the interaction with negatively charged molecules, such as DNA and RNA, making it a useful material for gene delivery applications [16, 17]. In addition to its primary applications, chitosan exhibits a wide range of other valuable properties, including anti-inflammatory, antioxidant, antimicrobial, antifungal, antihyperglycemic, and antitumor activities. These characteristics make it a highly versatile compound with great potential in the development of novel therapeutic agents and in improving overall quality of life [6, 18–26].

Chitosan-based injectable hydrogels possess high potential for biomedical applications; however, their pH sensitivity limits their application in alkaline and neutral media [27]. To address this, chitosan polymers intended for practical use in vaccine delivery often require chemical modifications to improve their stability and solubility [28]. One of the primary strategies involves structural modification of the chitosan molecule to overcome its poor solubility under neutral and basic conditions [29, 30].

The solubility of chitosan can be improved by introducing various functional groups, such as carboxymethyl, sulfonic, or quaternary ammonium groups [28–34]. In addition to better solubility, chitosan derivatives often demonstrate superior biological activity compared to the native polymer [35]. Chitosan derivatives with substituted functional groups at both the –OH and –NH₂ reactive centers exhibit higher bactericidal activity against both Gram-positive and Gram-negative bacteria [36, 37]. Furthermore, quaternized chitosan derivatives have demonstrated higher antifungal activity than unmodified chitosan [38]. These modifications are particularly significant in applications such as wound dressings, drug delivery systems, and tissue engineering, where robust antimicrobial performance is essential. Additionally, derivatization has been employed to improve the antioxidant capacity of chitosan [39, 40]. The introduction of phenolic groups, for example, has been reported to boost both antioxidant and antitumor activities [41], opening new prospects for their use in cosmetics and food preservation [39, 42].

Another major objective of chitosan derivatization is to improve its drug delivery potential. Under acidic conditions (pH < 6.5), protonated chitosan enhances the paracellular transport of peptide drugs across mucosal epithelia. However, at neutral pH levels — such as those in the intestinal tract — native chitosan loses this absorption-enhancing ability. To overcome this limitation, a variety of chitosan derivatives have been developed and evaluated for performance in such physiological conditions [43, 44]. Moreover, the derivatization of chitosan can introduce stimuli-responsive properties, including pH and temperature sensitivity. These features are especially useful in designing smart drug delivery systems that release therapeutics in response to specific physiological conditions [45–47]. Chitosan is also chemically modified to enhance its biocompatibility and reduce its immunogenicity, making it more suitable for biomedical applications such as tissue scaffolds [30]. Overall, chitosan derivatization significantly expands the polymer's functional versatility and performance across medicine, biotechnology, and environmental science. Figure 1 illustrates the correlation between types of derivatization and the resulting improvements in physicochemical or biological parameters.

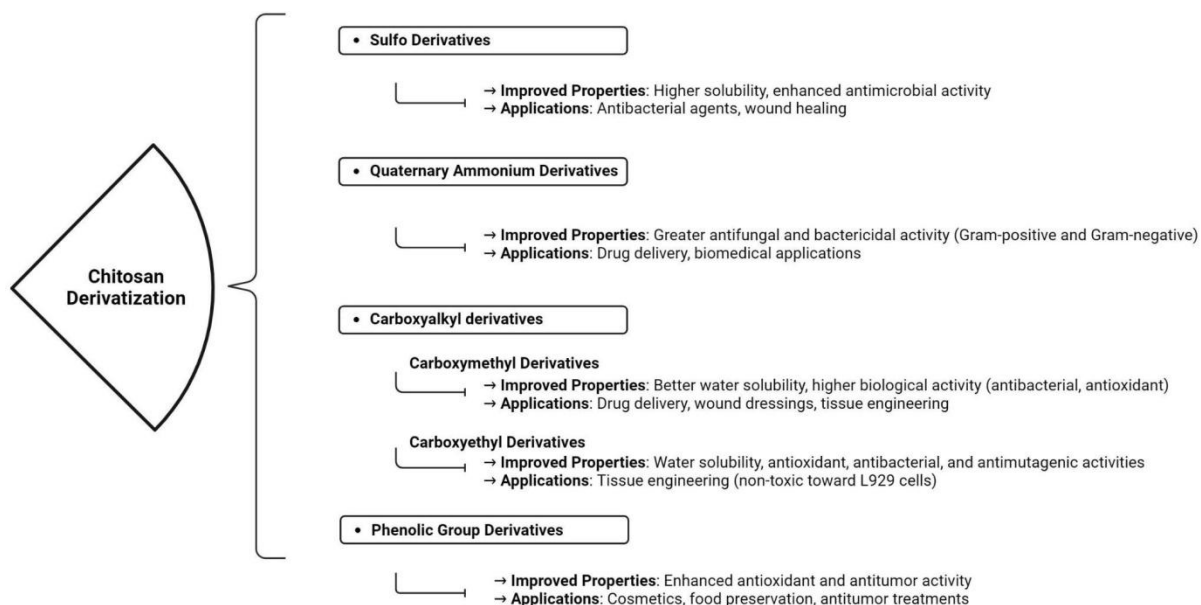


Figure 1. Influence of chitosan derivatization on its properties

Among the carboxyalkyl derivatives carboxyethyl chitosan (CEC) has attracted increasing attention due to its improved characteristics, including enhanced biocompatibility and water solubility [48, 49]. Recent studies have further confirmed the antioxidant and antimutagenic activities of N-(2-carboxyethyl)chitosan (N-CEC) [50], along with its improved antibacterial properties [51]. Additionally, CEC-based fibers have shown great potential as scaffolds for tissue engineering, demonstrating no cytotoxicity toward L929 fibroblast cells [52]. CEC is synthesized through the carboxyethylation of chitosan, in which the hydroxyl and amino groups of chitosan are substituted with carboxyethyl moieties. Based on the substitution sites of the 2-carboxyethyl group, CECs are generally classified into three types: O-CEC, N-CEC, and N,O-CEC [53]. Carboxyalkylation is typically carried out under either heterogeneous or homogeneous conditions through

nucleophilic substitution, addition, and addition-elimination reactions, often followed by reduction. In these reactions, chitosan serves as a nucleophilic polymer substrate [54, 55]. Figure 2 illustrates the synthetic pathways of carboxyethyl chitosan derivatives.

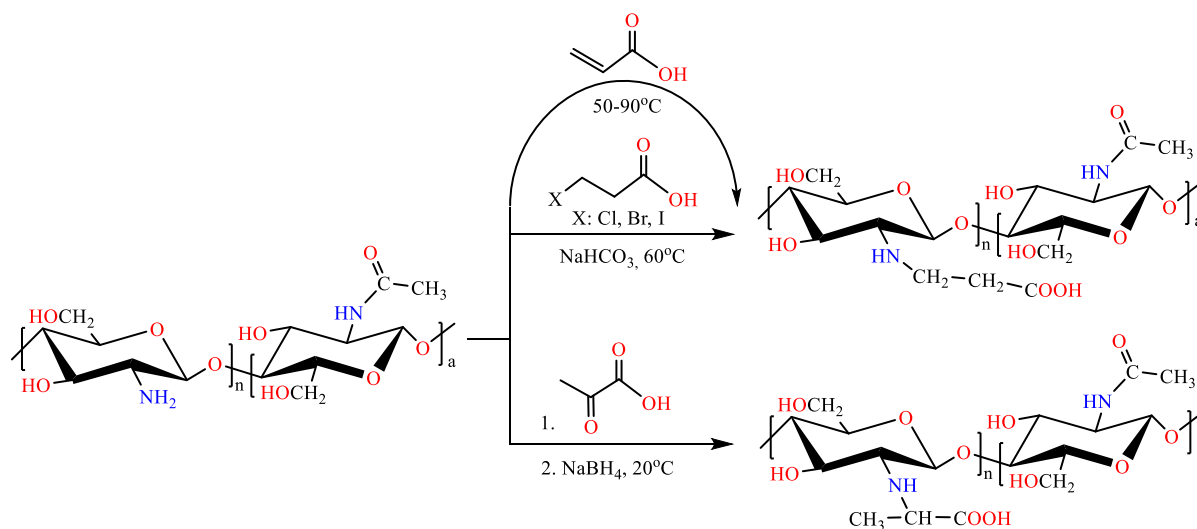


Figure 2. Synthetic routes of carboxyethyl chitosan

Herein, we investigated how gel-phase synthesis of N-CEC, as previously described in [56], influences the biopolymer properties and their relationship with structural features. This approach represents a highly efficient, cost-effective, and environmentally friendly process due to the minimal use of water and the complete absence of organic solvents. Previous studies have demonstrated that temperature and reaction time are the key factors affecting the degree of substitution (DS) of N-CEC [56]. In the present work, we focused on evaluating how variations in DS influence both the yield of N-CEC and its behavior in aqueous environments, particularly in terms of porosity and pH-dependent swelling.

2. Experimental

Chitosan (degree of deacetylation: 85.5 %) was purchased from Orisone Chemicals Limited (China) and used for the gel-phase synthesis of N-CEC without further purification. Acrylic acid (type P) was supplied by SIBUR LLC and was distilled prior to use. The resulting purity of acrylic acid was determined to be 99.4 % by titration.

2.1. Gel-phase synthesis of N-CEC

The synthesis of N-CEC was carried out following the previously reported procedure [56], with modifications to several experimental conditions. Briefly, 1.8 mol of acrylic acid was dissolved in 160 mL of distilled water under stirring using a Scilogex OS20-S Overhead LED Digital Stirrer. Subsequently, 0.9 mol of chitosan was gradually added to the solution to prevent aggregation. After complete dissolution of chitosan, the reaction mixture was stirred for an additional 60 minutes, then transferred to a Kitfort KT-1910 Professional Series oven and incubated under various conditions to complete the carboxyethylation process. The specific parameters used for carboxyethylation are summarized in Table 1.

Table 1

Sample codes

Time, h	Temperature, °C and code		
	50	60	70
24	N-CEC 1	N-CEC 2	N-CEC 3
48	N-CEC 4	N-CEC 5	N-CEC 6
72	N-CEC 7	N-CEC 8	N-CEC 9

After drying, the N-CEC samples were ground into particles approximately 6 mm in size and washed with distilled water until acrylic acid content remained constant at the level of 0.1–0.2 %. The washed

N-CEC was then dried further until the moisture content reached 1-2 %, as measured using a PMB Weighing Moisture Analyzer (Adam Equipment Company, UK). The process yield was calculated according to Equation (1):

$$\eta = \frac{m_{exp}}{m_{calc}} * 100 \%,$$

where m_{exp} is the mass of the product obtained experimentally, g; m_{calc} is the theoretically calculated mass of the product, g.

2.2. Polymer characterization

2.2.1. Fourier-transform infrared spectroscopy

The Fourier-transform infrared (FT-IR) spectroscopy was carried out in triplicate using a Spectrum One spectrometer (PerkinElmer, USA).

2.2.2. Degree of substitution

The degree of substitution (DS) of N-carboxyethylchitosan was determined using a C, H, N, S automated analyzer (PE 2400, Perkin Elmer, US). The resulting DS was calculated according to Equation (2):

$$DS = \frac{\left[\left(\frac{nC}{nN} \right)_{\text{product}} - \left(\frac{nC}{nN} \right)_{\text{chitosan}} \right]}{3},$$

where nC/nN is the atomic ratio of elements in the product and in the initial chitosan, respectively.

2.3. Functional properties evaluation

2.3.1. Swelling studies

The swelling capacity of the samples was measured using a widely accepted gravimetric method, as previously described [57]. Aqueous buffer solutions of varying pH were used as swelling media, including: phosphate buffer solution pH = 3.0, buffered copper sulfate solution pH = 4.0, acetate buffer solution pH = 6.0, phosphate buffer solution pH = 7.0, buffer (phosphate) solution pH = 9.0 and borate buffer solution pH = 10. Prior to testing, the hydrogels were dried to constant weight; the initial dry mass was designated as W_d . The sample was then immersed in 10 mL of distilled water at a temperature of 25 °C. After a specified time, the sample was removed, the excess water on the surface was blotted with tissue paper, and the weight (W_w) was recorded. The swelling percentage (S) was then calculated according to Equation (3):

$$S(\%) = \frac{W_w - W_d}{W_d} * 100.$$

2.3.2. Porosity

The pore volume was determined using the liquid displacement method described in [8]. Ethanol was used as the displacement fluid due to its ability to infiltrate the samples without inducing swelling or structural damage. In summary, the dry sample (initial weight designated as W_d) was immersed in ethanol under vacuum for 30 minutes, and the weight of the sample in ethanol was recorded as W_1 . The sample was then removed, and the surface liquid was blotted with filter paper. The weight of the wetted sample was recorded as W_w . The porosity was calculated according to Equation (4):

$$\varepsilon(\%) = \frac{(W_w - W_d)}{(W_w - W_1)} * 100 \%.$$

Pore size analysis was carried out using scanning electron microscopy (SEM) with an EVO 50 microscope (Zeiss, Germany). For sample preparation, the N-CEC specimens were sputter-coated with a 20 nm layer of copper using a JEOL JFC-1600 sputter coater (Japan) under a pressure not exceeding 8 Pa for 40 seconds.

2.4. Statistics

Data of yield, porosity and swelling are presented as mean \pm standard deviation. The data are visualized using histograms and a scatter plot. Statistical analysis was performed using Past 4.15 statistical software [58]. For data not following a normal distribution, nonparametric statistical methods, including

PERMANOVA, were applied. Comparison between three groups of non-normally distributed samples was performed using the Kruskal-Wallis test.

3. Results and Discussion

Each chitosan carboxyalkylation reaction mechanism strongly depends on reaction conditions, such as pH, temperature, and interaction time. Among these, pH has been shown to be the most critical factor for achieving total conversion. Typically, the reaction is carried out under acidic conditions, as the total reactivity of acrylic acid with the ammonium salt of chitosan exceeds that of acrylate with the free amino groups of chitosan. For instance, a pH of approximately 4.5 promotes the formation of O-carboxymethyl chitosan through a pathway favorable for imine formation; however, lower pH values require higher temperatures — specifically, temperatures sufficient for gel formation [59]. However, under low alkaline conditions (pH = 8), the reaction shifts towards the formation of N-substituted derivatives [60]. The pH parameter is particularly important and more easily controlled when the synthesis is conducted in the liquid phase. However, due to the large volumes of water required for liquid-phase reactions, we opted for the gel-phase synthesis of N-CEC, as previously described in [56]. This method has been reported as a green and efficient approach, with temperature and reaction time identified as the key parameters influencing the quality of the resulting N-CEC. Temperature is a limiting factor for the reaction rate in carboxyethyl chitosan synthesis. It plays a crucial role, with effective reaction temperatures reported at 50 °C [61–64], 60 °C [65–68], and up to 90 °C [56]. The effect of reaction time on the carboxyethylation process remains a matter of debate. Earlier studies showed that extending the reaction duration from 48 h to 240 h increases the DS but significantly reduces the yield by approximately twofold [69]. Other results indicated that 40 h is sufficient to complete the reaction, with only a marginal increase in DS observed beyond this point [70]. To date, it is widely accepted that 48 h represents the optimal reaction time for carboxyethylation of chitosan [71]. In our study, N-CEC samples were synthesized via gel-phase reaction between chitosan and acrylic acid in water under heating. The reaction yield was calculated according to Equation (1), and the obtained results are presented in Figure 3.

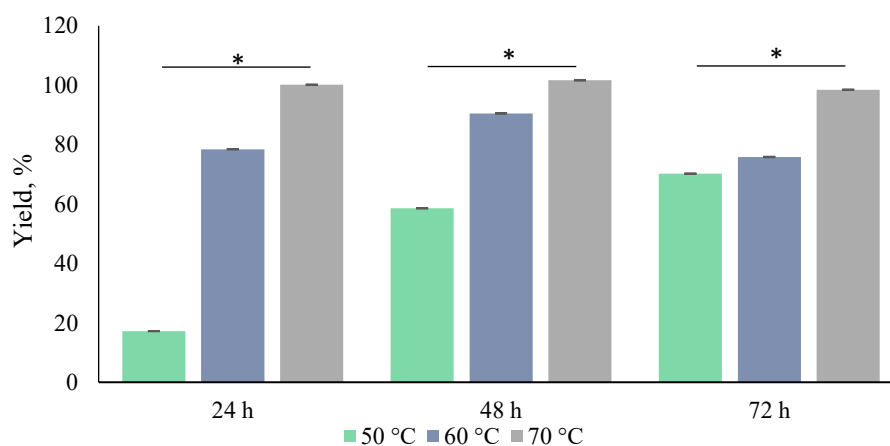


Figure 3. N-CEC yield depending on temperature and reaction time. * $p < 0.05$ Kruskal-Wallis test

A significant effect of both temperature and reaction time on N-CEC yield was observed (two-way PERMANOVA, $F(2, 26) = 866,590$, $p < 0.01$ for temperature; $F(2, 26) = 128,440$, $p < 0.01$ for reaction time). As shown in Figure 3, the yield reaches nearly 100 % at 70 °C after both 48 and 72 hours, with no statistically significant difference between these time points. Nevertheless, we hypothesized that the quality of the resulting N-CEC polymers may also depend on reaction conditions, potentially affecting the structural and functional properties of the final product. For all synthesized samples (coded NCEC-1 to NCEC-9), the FT-IR and SEM analyses yielded consistent results, confirming the successful modification of chitosan.

3.1. Fourier-Transform Infrared Spectroscopy

The FT-IR spectra of chitosan and N-CEC are presented in Figure 4. In the spectrum of N-CEC, absorption bands are observed at 2927, 1775, 1734, 1658, 1561, and 1419 cm^{-1} , which are indicative of successful functionalization of chitosan with 2-carboxyethyl groups.

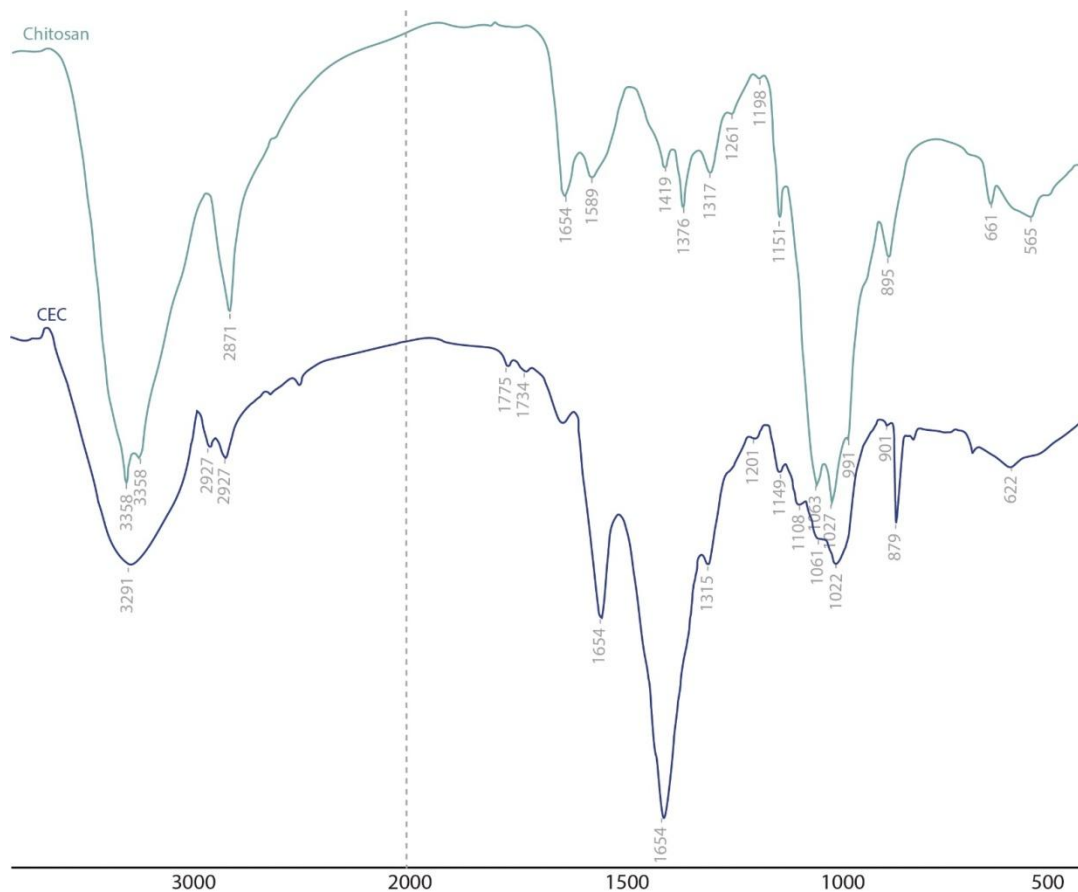


Figure 4. FT-IR spectra of Chitosan and N-CEC

3.2. Degree of substitution

Polysaccharides modification has a high impact on their physicochemical properties, improving solubility, ion-exchange capacity and adsorption [72]. In particular, the introduction of acidic groups into chitosan increases its anionic properties, enabling variable charge density along the biopolymer chain, which in turn leads to pH-dependent behavior [36]. This broadens the diversity of available raw materials and allows for the customization of biopolymer properties according to specific application requirements. Therefore, it is essential to characterize the degree of derivatization, and various analytical approaches have been reported for this purpose including nuclear magnetic resonance [60], elemental analysis [73], ultraviolet-visible and Fourier-transform infrared spectra [74]. In the present study, we investigated the degree of substitution (DS), which reflects the average number of 2-carboxyethyl groups per repeating unit (Table 2).

Table 2

Elemental analysis results

Sample	Element content, %			Degree of substitution
	C	H	N	
N-CEC 1	40.30	6.75	5.04	0.96
N-CEC 2	39.21	6.81	4.70	1.10
N-CEC 3	40.39	6.76	4.99	1.00
N-CEC 4	42.21	6.73	4.74	1.12
N-CEC 5	42.03	6.84	5.06	1.08
N-CEC 6	39.87	6.66	4.82	1.07
N-CEC 7	40.52	6.75	4.66	1.23
N-CEC 8	42.56	6.63	5.00	1.16
N-CEC 9	42.22	6.86	4.73	1.32

The data presented in Table 2 indicate a clear correlation between the DS and the reaction conditions. The DS ranges from 0.96 to 1.10 at 50 °C, from 1.07 to 1.12 at 60 °C and from 1.16 to 1.32 at 70 °C. These values are in agreement with previously reported data, with only minor deviations [56], and confirm the reproducibility of the synthesis, which is critical for future process development.

3.3. Porosity

Modifying porosity allows the improvement of mechanical stability and structure of biopolymers. The distribution of void space within the compositions can be effectively controlled by adjusting the degree of cross-linking, which in turn correlates with the degree of substitution of the starting polymer [75]. An increase in pore size enhances the pH-sensitive properties of chitosan hydrogels [64]. One of the most relevant examples is swelling, a critical factor for hydrogel performance in drug delivery applications [76]. Additionally, high porosity provides a large surface area for drug loading, while the presence of interconnected pores allows for controlled release of therapeutic agents [77]. In tissue engineering, pores and channels formed within the hydrogel matrix facilitate cell migration and proliferation into damaged tissue, ultimately supporting the regeneration or replacement of malfunctioning organs [78]. Proper porosity also contributes to optimal mechanical strength, elasticity, and structural stability of chitosan-based hydrogels [79]. The porosity characteristics of carboxyethylchitosan biopolymers synthesized in the present study are presented in Figure 5.

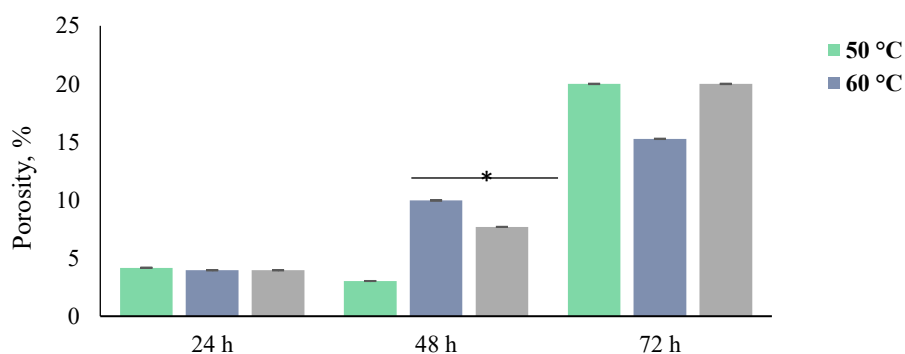


Figure 5. Porosity of N-CEC dependence on the reaction conditions. * $p < 0.05$ Kruskal-Wallis test

Based on the results presented in Figure 5, a significant effect of both temperature and reaction time on the porosity of N-CEC was observed (two-way PERMANOVA, $F(2, 26) = 2,162$, $p < 0.01$ for temperature; $F(2, 26) = 227,360$, $p < 0.01$ for reaction time). The data indicate that reaction temperature exerts a stronger influence on N-CEC porosity than reaction time. Samples synthesized at 70 °C exhibited porosity values exceeding 15 %, whereas those prepared at lower temperatures showed porosity in the range of 4–10 %, with no clear correlation to reaction time. This effect is likely attributed to a higher DS at elevated temperatures, which results in the incorporation of a greater number of $-\text{COOH}$ groups into the biopolymer structure. The increased presence of carboxylic groups enhances the potential for interchain cross-linking, thereby contributing to the formation of a more porous network (Figure 6) [80].

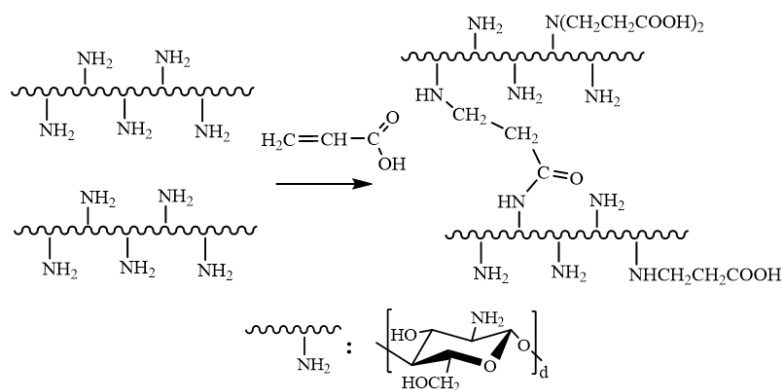


Figure 6. Cross-linking of N-CEC polymer chains occurring within the synthesis

Therefore, mild reaction conditions may lead to the formation of a slightly cross-linked polymer network; however, this assumption requires further comprehensive investigation.

Regarding pore size, N-CEC hydrogels were analyzed in both dried and swollen states. The results, presented in Figures 7a and 7b, respectively, demonstrate that the N-CEC hydrogel exhibits a layered internal structure with distinct porosity, with pore sizes ranging from 50 to 200 μm .

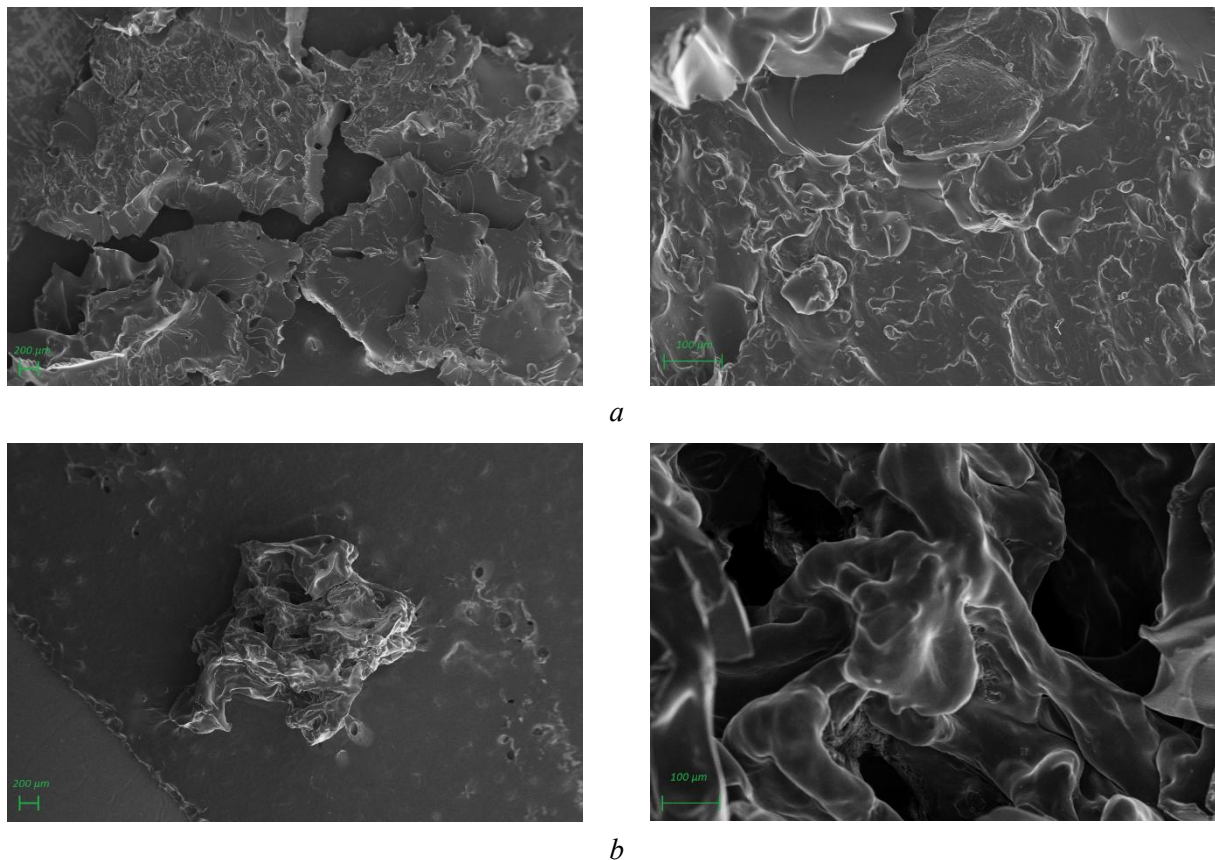


Figure 7. Representative SEM pictures of N-CEC in dried (a) and swollen (b) states

3.4. pH-Sensitive swelling

Swelling behavior is a key characteristic of biopolymers and is influenced not only by their internal structure, but also by external factors such as the pH and ionic strength of the surrounding medium. Previous studies have shown that carboxymethylchitosan (CMC) exhibits good ionic and pH sensitivity in aqueous solution, which has been attributed to the presence of amino groups in its side chains [81]. In addition, temperature-sensitive swelling of CMC-based hydrogels has been reported, with an increase in swelling observed within the temperature range of 5–55 $^{\circ}\text{C}$. This effect has been explained by the formation of additional hydrogen bonds and cross-links at lower temperatures, leading to more rigid and robust structures that are less permeable to water [82]. Overall, swelling is a highly responsive parameter, and understanding its underlying mechanisms is essential for predicting the performance of biopolymers and their compositions. The experimental data on the pH-sensitive swelling of N-CEC biopolymers synthesized under various reaction conditions are presented in Figure 8.

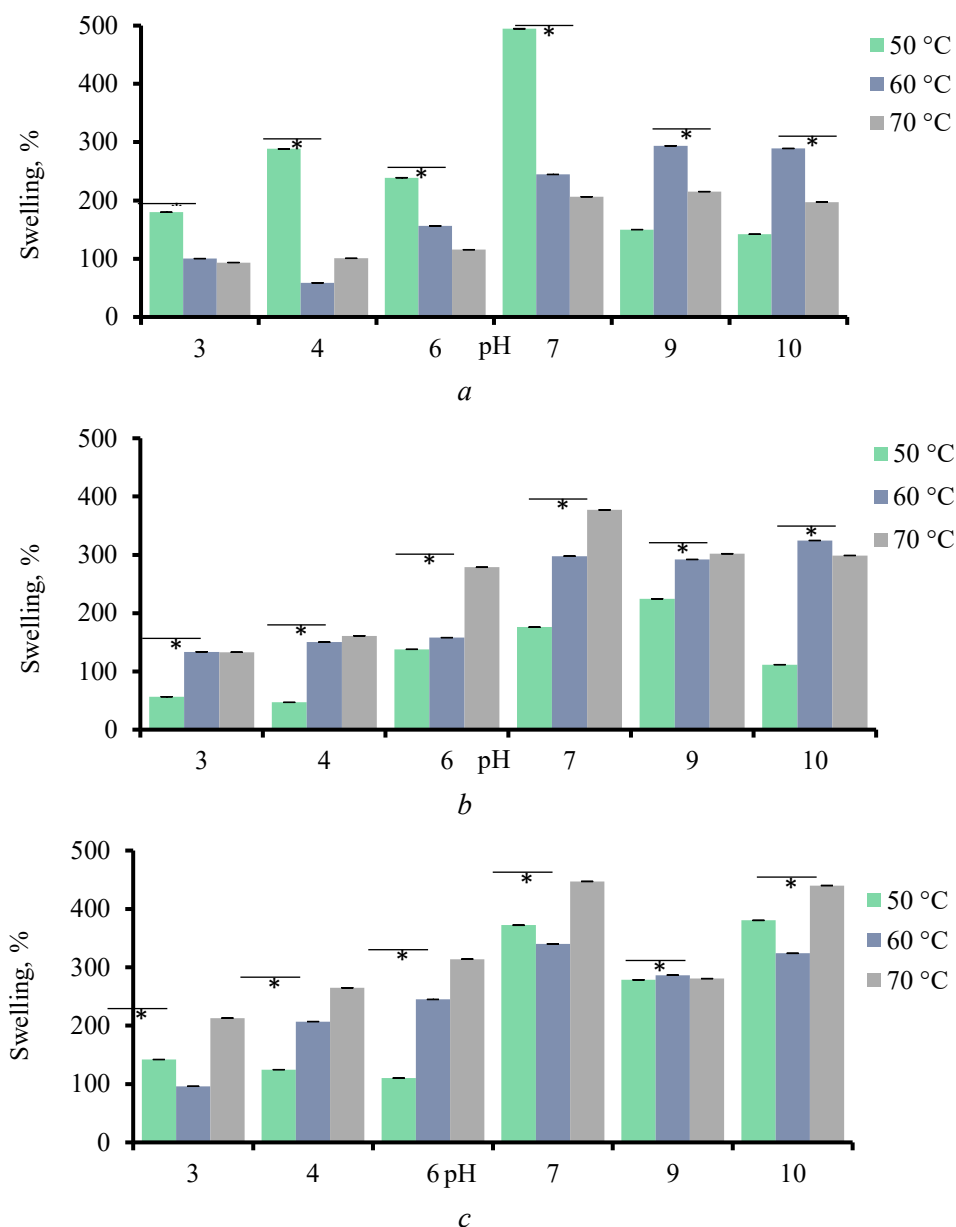


Figure 8. Swelling of N-CEC biopolymers under various pH for the samples synthesized at the temperature of 50 °C, 60 °C and 70 °C, within a). 24 h, b). 48 h, c). 72 h. * $p < 0.05$ Kruskal-Wallis test

Figure 8 demonstrates that the swelling behavior of N-CEC is strongly dependent on the pH of solution. According to two-way PERMANOVA analysis: at 24 hours, $F(2, 53) = 827,360$ $p < 0.01$ and $F(5, 53) = 835,110$ $p < 0.01$, accordingly; at 48 hours, $F(2, 53) = 171,6100$ $p < 0.01$ and $F(5, 53) = 1,049,000$ $p < 0.01$; at 72 hours, $F(2, 53) = 521,560$ $p < 0.01$ and $F(5, 53) = 1,024,200$ $p < 0.01$. All N-CEC samples exhibited limited swelling under acidic conditions, while a notable 2–3-fold increase was observed starting from pH 7, with maximum swelling reaching 450 % for biopolymers synthesized at 70 °C for 72 hours. To better interpret these results, the effects of cross-linking and pH should be considered. Cross-linking is known to significantly influence both swelling behavior and other properties of hydrogels by affecting the molecular weight [83]. In some systems, a lower degree of cross-linking provides greater network flexibility and increased hydrodynamic free volume, allowing the polymer chains to retain more solvent, which leads to increased swelling [84]. However, in our case, the high porosity of the samples synthesized at 70 °C suggests a higher degree of cross-linking, which would typically limit swelling. This apparent contradiction indicates that pH plays a more dominant role in swelling than cross-linking density under these conditions. Similar observations were reported in [85], where enhanced swelling was attributed to the deprotonation of carboxylic acid ($-\text{COOH}$) groups to carboxylate ($-\text{COO}^-$) anions, resulting in electrostatic repulsion between poly-

mer chains. This is consistent with the nature of the gel-phase synthesis, in which amino groups of chitosan are partially substituted by carboxyethyl groups. Interestingly, the unexpectedly high swelling observed for samples synthesized at 50 °C for 24 hours can be explained by a lower DS. This results in a larger number of free amino groups, which are protonated at low pH, allowing the hydrogel to swell. As pH increases, deprotonation of amino groups occurs, reducing repulsion between chains and leading to partial shrinking of the network [86, 87]. In summary, a higher degree of substitution in N-CEC synthesized at 70 °C ensures a combination of enhanced porosity and swelling, compared to mild synthetic conditions.

Conclusions

The present study demonstrates the successful synthesis of N-carboxyethylchitosan via an eco-friendly Michael addition protocol, with systematically varied reaction conditions ranging from 24 h to 72 h and from 50 °C to 70 °C. The resulting yield was strongly dependent on both time and temperature, increasing from 20 % at 50 °C (24 h) and to 98 % under optimized conditions. Structural studies of biopolymer samples were performed using FT-IR, SEM, and elemental analysis, which revealed a direct correlation between reaction temperature and the degree of substitution. Notably, higher synthesis temperatures produced samples with improved porosity (up to 15 %) and a uniform pore size distribution of 50–200 µm. The swelling behavior of N-CEC was found to be highly pH-sensitive. Under acidic conditions, swelling was limited to 100–150 %, whereas under alkaline conditions it increased 2–3-fold, reaching a maximum of 450 % for the sample synthesized at 70 °C for 72 hours. This phenomenon is likely attributable to the deprotonation of –COOH groups to –COO[–] anions, resulting in electrostatic repulsion between polymer chains. These findings highlight the potential of controllable N-CEC synthesis to achieve tunable structural and functional properties, reinforcing its applicability in the design of advanced pH-responsive biomaterials.

Funding

This research was supported by the “Priority-2030” program at Novosibirsk State Technical University (project No. SP-3 Zh-5/1).

Author Information*

**The authors' names are presented in the following order: First Name, Middle Name and Last Name*

Polina Ivanovna Dubovskaia — 3rd-year Bachelor student, Faculty of Business; Laboratory Assistant, Faculty of Physical Engineering, Novosibirsk State Technical University, 20, Prospekt K. Marksa, 630073, Novosibirsk, Russia; e-mail: dubovskaya.2022@stud.nstu.ru; <https://orcid.org/0009-0006-4769-446X>

Saeidi Arsalan — 2nd-year PhD student, Faculty of Natural Sciences, Novosibirsk State University, 1 Pirogova str., 630090, Novosibirsk, Russia; Engineer, Faculty of Physical Engineering, Novosibirsk State Technical University, 20 Prospekt K. Marksa, 630073, Novosibirsk, Russia; e-mail: saeidi@corp.nstu.ru; <https://orcid.org/0009-0006-2395-5127>

Anna Aleksandrovna Pronchenko — Junior Research Fellow, Faculty of Physical Engineering, Novosibirsk State Technical University, 20, Prospekt K. Marksa, 630073, Novosibirsk, Russia; e-mail: belousova2009@corp.nstu.ru; <https://orcid.org/0009-0006-9129-6215>

Anastasiia Ivanovna Drannikova — Engineer, Faculty of Physical Engineering, Novosibirsk State Technical University, 20 Prospekt K. Marksa, 630073, Novosibirsk, Russia; e-mail: drannikova@corp.nstu.ru

Ivan Andreevich Lukoyanov — PhD in Chemistry, Associate Professor, Faculty of Aircraft Engineering, Novosibirsk State Technical University, 20 Prospekt K. Marksa, 630073, Novosibirsk, Russia; e-mail: ivan.lukoyanov@corp.nstu.ru; <https://orcid.org/0000-0002-8706-1222>

Farida Kazbekovna Aripova — 1st-year PhD student, Institute of Fundamental and Applied Agrobiotechnologies, Novosibirsk State Agrarian University, 160 Dobrolyubova st., 630039, Novosibirsk, Russia; Junior Research Fellow, Faculty of Physical Engineering, Novosibirsk State Technical University, 20 Prospekt K. Marksa, 630073, Novosibirsk, Russia; e-mail: aripova@corp.nstu.ru

Mariia Evgenievna Savenko — 3rd-year Bachelor student, Faculty of Mechanical Engineering and Technologies; Laboratory Assistant, Faculty of Physical Engineering, Novosibirsk State Technical University, 20 Prospekt K. Marksa, 630073, Novosibirsk, Russia; e-mail: savenko.2022@stud.nstu.ru

Elizaveta Andreyevna Veretennikova — 3rd-year PhD student, I. Ya. Postovsky Institute of Organic Synthesis, Ural Branch of the Russian Academy of Sciences, 22 Sofya Kovalevskaya St., 620990, Yekaterinburg, Russia; e-mail: lizaveret@yandex.ru; <https://orcid.org/0009-0003-8588-5724>

Alexander Viktorovich Pestov — PhD in Chemistry, Research Fellow, I. Ya. Postovsky Institute of Organic Synthesis, Ural Branch of the Russian Academy of Sciences, 22 Sofya Kovalevskaya St., 620990, Yekaterinburg, Russia; e-mail: pestov@ios.uran.ru; <https://orcid.org/0000-0002-4270-3041>

Ekaterina Anatolyevna Litvinova — PhD in Biology, Research Fellow, Faculty of Physical Engineering, Novosibirsk State Technical University, 20 Prospekt K. Marksa, 630073, Novosibirsk, Russia; e-mail: e.litvinova@corp.nstu.ru; <https://orcid.org/0000-0001-6398-7154>

Aleksandr Alexeyevich Drannikov — PhD in Pharmacy, Junior Research Fellow, Faculty of Physical Engineering, Novosibirsk State Technical University, 20, Prospekt K. Marksa, 630073, Novosibirsk, Russia; e-mail: drannikov@corp.nstu.ru; <https://orcid.org/0000-0002-4839-1667>

Author Contributions

The manuscript was written through contributions of all authors. All authors have given approval to the final version of the manuscript. **CRedit**: **Polina Ivanovna Dubovskaia** investigation, original draft preparation; **Saeidi Arsalan** visualization, original draft preparation; **Anna Aleksandrovna Pronchenko** methodology; **Anastasiia Ivanovna Drannikova** formal analysis, data curation; **Ivan Andreevich Lukoyanov** methodology, resources; **Farida Kazbekovna Aripova** methodology; **Mariia Evgenievna Savenko** methodology; **Elizaveta Andreyevna Veretennikova** methodology; **Alexander Viktorovich Pestov** investigation, methodology, review & editing; **Ekaterina Anatolyevna Litvinova** review & editing, visualization; **Aleksandr Alexeyevich Drannikov** conceptualization, methodology, project Administration, funding acquisition, supervision.

Conflicts of Interest

The authors declare no conflict of interest.

References

- Hisham, F., Maziaty Akmal, M.H., Ahmad, F., Ahmad, K., & Samat, N. (2024). Biopolymer chitosan: Potential sources, extraction methods, and emerging applications. *A in Shams Engineering Journal*, 15(2), 102424. <https://doi.org/10.1016/j.asej.2023.102424>
- Aranaz, I., Alcántara, A.R., Civera, M.C., Arias, C., Elorza, B., Heras Caballero, A., & Acosta, N. (2021). Chitosan: An overview of its properties and applications. *Polymers*, 13(19), 3256. <https://doi.org/10.3390/polym13193256>
- Sharkawy, A., Barreiro, M.F., & Rodrigues, A.E. (2020). Chitosan-based Pickering emulsions and their applications: A review. *Carbohydrate Polymers*, 250(116885), 116885. <https://doi.org/10.1016/j.carbpol.2020.116885>
- Marsili, L., Dal Bo, M., Berti, F., & Toffoli, G. (2021). Chitosan-based biocompatible copolymers for thermoresponsive drug delivery systems: On the development of a standardization system. *Pharmaceutics*, 13(11), 1876. <https://doi.org/10.3390/pharmaceutics13111876>
- Khubiev, O.M., Esakova, V.E., Egorov, A.R., Bely, A.E., Golubev, R.A., Tachaev, M.V., Kirichuk, A.A., Lobanov, N.N., Tskhovrebov, A.G., & Kritchenkov, A.S. (2023). Novel non-toxic highly antibacterial chitosan/Fe(III)-based nanoparticles that contain a deferoxamine — Trojan horse ligands: Combined synthetic and biological studies. *Processes*, 11(3), 870. Basel, Switzerland. <https://doi.org/10.3390/pr11030870>
- Guarnieri, A., Triunfo, M., Scieuzo, C., Ianniciello, D., Tafi, E., Hahn, T., Zibek, S., Salvia, R., De Bonis, A., & Falabella, P. (2022). Antimicrobial properties of chitosan from different developmental stages of the bioconverter insect *Hermetia illucens*. *Scientific Reports*, 12(1). <https://doi.org/10.1038/s41598-022-12150-3>
- Azmana, M., Mahmood, S., Hilles, A.R., Rahman, A., Arifin, M.A.B., & Ahmed, S. (2021). A review on chitosan and chitosan-based bionanocomposites: Promising material for combatting global issues and its applications. *International Journal of Biological Macromolecules*, 185, 832–848. <https://doi.org/10.1016/j.ijbiomac.2021.07.023>

- 8 Drannikov, A.A., Blinova, E.A., Korel, A.V., Samokhin, A.G., Dubovskaya, P.I., Lazurenko, D.V., Zemlyakova, E.O., Pestov, A.V., & Litvinova, E.A. (2024). Novel biosorbents based on carboxyethyl chitosan for Allura Red dye contaminated water treatment *Chimica Techno Acta*, 11(4). <https://doi.org/10.15826/chimtech.2024.11.4.15>
- 9 Ul-Islam, M., Alabbosh, K.F., Manan, S., Khan, S., Ahmad, F., & Ullah, M.W. (2024). Chitosan-based nanostructured biomaterials: Synthesis, properties, and biomedical applications. *Advanced Industrial and Engineering Polymer Research*, 7(1), 79–99. <https://doi.org/10.1016/j.aiepr.2023.07.002>
- 10 Padhi, S., Behera, A., Hasnain, M.S., & Nayak, A.K. (2022). Uses of chitosan in drug delivery. In *Chitosan in Biomedical Applications* (pp 139–162). Elsevier.
- 11 Rajinikanth B., Rajkumar, S., Keerthika, D.S.R., & Vijayaragavan, V. (2024). Chitosan-based biomaterial in wound healing: A review. *Cureus*, 16(2), e55193. <https://doi.org/10.7759/cureus.55193>
- 12 Sultankulov, B., Berillo, D., Sultankulova, K., Tokay, T., & Saparov, A. (2019). Progress in the development of chitosan-based biomaterials for tissue engineering and regenerative medicine. *Biomolecules*, 9(9), 470. <https://doi.org/10.3390/biom9090470>
- 13 Guadarrama-Escobar, O.R., Serrano-Castañeda, P., Anguiano-Almazán, E., Vázquez-Durán, A., Peña-Juárez, M.C., Vera-Graziano, R., Morales-Florido, M.I., Rodríguez-Perez, B., Rodríguez-Cruz, I.M., Miranda-Calderón, J.E., & Escobar-Chávez, J.J. (2023). Chitosan nanoparticles as oral drug carriers. *International Journal of Molecular Sciences*, 24(5), 4289. <https://doi.org/10.3390/ijms24054289>
- 14 Mikušová, V., & Mikuš, P. (2021). Advances in chitosan-based nanoparticles for drug delivery. *International Journal of Molecular Sciences*, 22(17), 9652. <https://doi.org/10.3390/ijms22179652>
- 15 Mura, P., Maestrelli, F., Cirri, M., & Mennini, N. (2022). Multiple roles of chitosan in mucosal drug delivery: An updated review. *Marine Drugs*, 20(5), 335. <https://doi.org/10.3390/md20050335>
- 16 Marques Gonçalves, M., Florencio Maluf, D., Pontarolo, R., Ketzner Saul, C., Almouazen, E., & Chevalier, Y. (2023). Negatively charged chitosan nanoparticles prepared by ionotropic gelation for encapsulation of positively charged proteins. *International Journal of Pharmaceutics*, 642(123164), 123164. <https://doi.org/10.1016/j.ijpharm.2023.123164>
- 17 Chuan, D., Jin, T., Fan, R., Zhou, L., & Guo, G. (2019). Chitosan for gene delivery: Methods for improvement and applications. *Advances in Colloid and Interface Science*, 268, 25–38. <https://doi.org/10.1016/j.cis.2019.03.007>
- 18 Azuma, K., Osaki, T., Minami, S., & Okamoto, Y. (2015). Anticancer and anti-inflammatory properties of chitin and chitosan oligosaccharides. *Journal of Functional Biomaterials*, 6(1), 33–49. <https://doi.org/10.3390/jfb6010033>
- 19 Zosangpuii, & Sudheer, P. (2024). Chitosan a natural anti-inflammatory and wound healing agent: A brief update. *Natural Resources for Human Health*, 4(2), 115–127. <https://doi.org/10.53365/nrfhh/177602>
- 20 Fong, D., & Hoemann, C.D. (2018). Chitosan immunomodulatory properties: Perspectives on the impact of structural properties and dosage. *Future Science OA*, 4(1). <https://doi.org/10.4155/fsoa-2017-0064>
- 21 Chang, S-H, Lin, Y-Y, Wu, G-J, Huang, C-H, & Tsai, G.J. (2019). Effect of chitosan molecular weight on anti-inflammatory activity in the RAW 2647 macrophage model. *International Journal of Biological Macromolecules*, 131, 167–175. <https://doi.org/10.1016/j.ijbiomac.2019.02.066>
- 22 Ivanova, D.G., & Yaneva, Z.L. (2020). Antioxidant properties and redox-modulating activity of chitosan and its derivatives: Biomaterials with application in cancer therapy. *BioResearch Open Access*, 9(1), 64–72. <https://doi.org/10.1089/biores.2019.0028>
- 23 Avelelas, F., Horta, A., Pinto, L.F.V., Cotrim Marques, S., Marques Nunes, P., Pedrosa, R., & Leandro, S.M. (2019). Anti-fungal and antioxidant properties of chitosan polymers obtained from nontraditional *Polybius henslowii* sources. *Marine Drugs*, 17(4), 239. <https://doi.org/10.3390/md17040239>
- 24 Ke, C-L, Deng, F-S, Chuang, C-Y, & Lin, C-H (2021). Antimicrobial actions and applications of chitosan. *Polymers*, 13(6), 904. <https://doi.org/10.3390/polym13060904>
- 25 Sarkar, S., Das, D., Dutta, P., Kalita, J., Wann, S.B., & Manna, P. (2020). Chitosan: A promising therapeutic agent and effective drug delivery system in managing diabetes mellitus. *Carbohydrate Polymers*, 247(116594), 116594. <https://doi.org/10.1016/j.carbpol.2020.116594>
- 26 Ueno, H., Mori, T., & Fujinaga, T. (2001). Topical formulations and wound healing applications of chitosan. *Advanced Drug Delivery Reviews*, 52(2), 105–115. [https://doi.org/10.1016/s0169-409x\(01\)00189-2](https://doi.org/10.1016/s0169-409x(01)00189-2)
- 27 Lavanya, K., Chandran, S.V., Balagangadharan, K., & Selvamurugan, N. (2020). Temperature- and pH-responsive chitosan-based injectable hydrogels for bone tissue engineering. *Materials Science & Engineering C, Materials for Biological Applications*, 111(110862), 110862. <https://doi.org/10.1016/j.msec.2020.110862>
- 28 Xing, L., Fan, Y-T, Shen, L-J, Yang, C-X, Liu, X-Y, Ma, Y-N, Qi, L-Y, Cho, K-H, Cho, C-S, & Jiang, H-L (2019). pH-sensitive and specific ligand-conjugated chitosan nanogels for efficient drug delivery. *International Journal of Biological Macromolecules*, 141, 85–97. <https://doi.org/10.1016/j.ijbiomac.2019.08.237>
- 29 Suryani, S., Chaerunisaa, A., Joni, I.M., Ruslin, R., Aspadiah, V., Anton, A., Sartinah, A., & Ramadhan, L.O.A. (2024). The chemical modification to improve solubility of chitosan and its derivatives application, preparation method, toxicity as a nanoparticles. *Nanotechnology, Science and Applications*, 17, 41–57. <https://doi.org/10.2147/nsa.s450026>
- 30 Desai, N., Rana, D., Salave, S., Gupta, R., Patel, P., Karunakaran, B., Sharma, A., Giri, J., Benival, D., & Kommineni, N. (2023). Chitosan: A potential biopolymer in drug delivery and biomedical applications. *Pharmaceutics*, 15(4), 1313. <https://doi.org/10.3390/pharmaceutics15041313>

- 31 Abourehab, M.A.S., Pramanik, S., Abdelgawad, M.A., Abualsoud, B.M., Kadi, A., Ansari, M.J., & Deepak, A. (2022). Recent advances of chitosan formulations in biomedical applications. *International Journal of Molecular Sciences*, 23(18), 10975. <https://doi.org/10.3390/ijms231810975>
- 32 Holme, K.R., & Perlin, A.S. (1997). Chitosan N-sulfate. A water-soluble polyelectrolyte. *Carbohydrate Research*, 302(1–2), 7–12. [https://doi.org/10.1016/s0008-6215\(97\)00117-1](https://doi.org/10.1016/s0008-6215(97)00117-1)
- 33 Dimassi, S., Tabary, N., Chai, F., Blanchemain, N., & Martel, B. (2018). Sulfonated and sulfated chitosan derivatives for biomedical applications: A review. *Carbohydrate Polymers*, 202, 382–396. <https://doi.org/10.1016/j.carbpol.2018.09.011>
- 34 Fabiano, A., Beconcini, D., Migone, C., Piras, A.M., & Zambito, Y. (2020). Quaternary ammonium chitosans: The importance of the positive fixed charge of the drug delivery systems. *International Journal of Molecular Sciences*, 21(18), 6617. <https://doi.org/10.3390/ijms21186617>
- 35 Harugade, A., Sherje, A.P., & Pethe, A. (2023). Chitosan: A review on properties, biological activities and recent progress in biomedical applications. *Reactive & Functional Polymers*, 191(105634), 105634. <https://doi.org/10.1016/j.reactfunctpolym.2023.105634>
- 36 Ardean, C., Davidescu, C.M., Nemeş, N.S., Negrea, A., Ciopec, M., Duteanu, N., Negrea, P., Duda-Seiman, D., & Musta, V. (2021). Factors influencing the antibacterial activity of chitosan and chitosan modified by functionalization International. *Journal of Molecular Sciences*, 22(14), 7449. <https://doi.org/10.3390/ijms22147449>
- 37 Li, Z., Yang, F., & Yang, R. (2015). Synthesis and characterization of chitosan derivatives with dual-antibacterial functional groups. *International Journal of Biological Macromolecules*, 75, 378–387. <https://doi.org/10.1016/j.ijbiomac.2015.01.056>
- 38 Tan, H., Ma, R., Lin, C., Liu, Z., & Tang, T. (2013). Quaternized chitosan as an antimicrobial agent: Antimicrobial activity, mechanism of action and biomedical applications in orthopedics. *International Journal of Molecular Sciences*, 14(1), 1854–1869. <https://doi.org/10.3390/ijms14011854>
- 39 Fatima, M., Mir, S., Ali, M., Hassan, S., Ul Haq Khan, Z., & Waqar, K. (2024). Synthesis and applications of chitosan derivatives in food preservation — A review. *European Polymer Journal*, 216(113242), 113242. <https://doi.org/10.1016/j.eurpolymj.2024.113242>
- 40 Yang, X., Lan, W., & Sun, X. (2023). Antibacterial and antioxidant properties of phenolic acid grafted chitosan and its application in food preservation: A review. *Food Chemistry*, 428(136788), 136788. <https://doi.org/10.1016/j.foodchem.2023.136788>
- 41 Li, Q., Li, Q., Tan, W., Zhang, J., & Guo, Z. (2020). Phenolic-containing chitosan quaternary ammonium derivatives and their significantly enhanced antioxidant and antitumor properties. *Carbohydrate Research*, 498(108169), 108169. <https://doi.org/10.1016/j.carres.2020.108169>
- 42 Aranaz, I., Acosta, N., Civera, C., Elorza, B., Mingo, J., Castro, C., Gandía, M., & Heras Caballero, A. (2018). Cosmetics and cosmeceutical applications of chitin, chitosan and their derivatives. *Polymers*, 10(2), 213. <https://doi.org/10.3390/polym10020213>
- 43 Thanou, M., Verhoef, J.C., & Junginger, H.E. (2001). Oral drug absorption enhancement by chitosan and its derivatives. *Advanced Drug Delivery Reviews*, 52(2), 117–126. [https://doi.org/10.1016/s0169-409x\(01\)00231-9](https://doi.org/10.1016/s0169-409x(01)00231-9)
- 44 Thanou, M., Verhoef, J.C., & Junginger, H.E. (2001a). Chitosan and its derivatives as intestinal absorption enhancers. *Advanced Drug Delivery Reviews*, 50, S91–S101. [https://doi.org/10.1016/s0169-409x\(01\)00180-6](https://doi.org/10.1016/s0169-409x(01)00180-6)
- 45 McCarthy, P.C., Zhang, Y., & Abebe, F. (2021). Recent applications of dual-stimuli responsive chitosan hydrogel nanocomposites as drug delivery tools. *Molecules (Basel, Switzerland)*, 26(16), 4735. <https://doi.org/10.3390/molecules26164735>
- 46 Zhou, H.Y., Chen, X.G., Kong, M., Liu, C.S., Cha, D.S., & Kennedy, J.F. (2008). Effect of molecular weight and degree of chitosan deacetylation on the preparation and characteristics of chitosan thermosensitive hydrogel as a delivery system. *Carbohydrate Polymers*, 73(2), 265–273. <https://doi.org/10.1016/j.carbpol.2007.11.026>
- 47 Xu, X., Liu, Y., Fu, W., Yao, M., Ding, Z., Xuan, J., Li, D., Wang, S., Xia, Y., & Cao, M. (2020). Poly(N-isopropylacrylamide)-based thermoresponsive composite hydrogels for biomedical applications. *Polymers*, 12(3), 580. <https://doi.org/10.3390/polym12030580>
- 48 Huang, J., Xie, H., Hu, S., Xie, T., Gong, J., Jiang, C., Ge, Q., Wu, Y., Liu, S., Cui, Y., Mao, J., & Mei, L. (2015). Preparation, characterization, and biochemical activities of N-(2-carboxyethyl)chitosan from squid pens. *Journal of Agricultural and Food Chemistry*, 63(9), 2464–2471. <https://doi.org/10.1021/jf505581n>
- 49 Chalitangkoon, J., Ronte, A., & Monvisade, P. (2023). Carboxyethylation of chitosan-based polymeric dyes for potential pH-sensing applications. *Journal of the Taiwan Institute of Chemical Engineers*, 149(105001), 105001. <https://doi.org/10.1016/j.jtice.2023.105001>
- 50 Kogan, G., Skorik, Y., Itanova, I., Krikova, L., Urakova, Z., Gomes, C., Yatluk, Y., & Krajovi, J. (2004). Antioxidant and antimutagenic activity of -(2-carboxyethyl)chitosan. *Toxicology and Applied Pharmacology*, 201(3), 303–310. <https://doi.org/10.1016/j.taap.2004.05.009>
- 51 Ibrahim, H.M., Mostafa, M., & Kandile, N.G. (2020). Potential use of N-carboxyethylchitosan in biomedical applications: Preparation, characterization, biological properties. *International Journal of Biological Macromolecules*, 149, 664–671. <https://doi.org/10.1016/j.ijbiomac.2020.01.299>
- 52 Yang, S., Dong, Q., Yang, H., Liu, X., Gu, S., Zhou, Y., & Xu, W. (2016). N-carboxyethyl chitosan fibers prepared as potential use in tissue engineering. *International Journal of Biological Macromolecules*, 82, 1018–1022. <https://doi.org/10.1016/j.ijbiomac.2015.10.078>

- 53 Huang, J., Xie, H., Ye, H., Xie, T., Lin, Y., Gong, J., Jiang, C., Wu, Y., Liu, S., Cui, Y., Mao, J., & Mei, L. (2016). Effect of carboxyethylation degree on the adsorption capacity of Cu(II) by N-(2-carboxyethyl)chitosan from squid pens. *Carbohydrate Polymers*, 138, 301–308. <https://doi.org/10.1016/j.carbpol.2015.11.037>
- 54 Jayakumar, R., Prabakaran, M., Nair, S.V., Tokura, S., Tamura, H., & Selvamurugan, N. (2010). Novel carboxymethyl derivatives of chitin and chitosan materials and their biomedical applications. *Progress in Materials Science*, 55(7), 675–709. <https://doi.org/10.1016/j.pmatsci.2010.03.001>
- 55 Koshugi, J. (1981). *Carboxyalkylated chitin and derivative* [Patent].
- 56 Pestov, A.V., Zhuravlev, N.A., & Yatluk, Y.G. (2007). Synthesis in a gel as a new procedure for preparing carboxyethyl chitosan. *Russian Journal of Applied Chemistry*, 80(7), 1154–1159. <https://doi.org/10.1134/s1070427207070282>
- 57 Adi Sulianto, A., Adiyaksa, I.P., Wibisono, Y., Khan, E., Ivanov, A., Drannikov, A., Ozaltin, K., & Di Martino, A. (2023). From fruit waste to hydrogels for agricultural applications. *Clean Technologies*, 6(1), 1–17. <https://doi.org/10.3390/cleantechnol6010001>
- 58 Hammer, Ø., Harper, D., & Ryan, P. (2001). Past: Paleontological statistical software package for education and data analysis. *Palaeontologia Electronica*, 4, 1–9.
- 59 Muzzarelli, R.A.A., Tanfani, F., Emanuelli, M., & Mariotti, S. (1982). N-(carboxymethylidene)chitosans and N-(carboxymethyl)chitosans: Novel chelating polyampholytes obtained from chitosan glyoxylate. *Carbohydrate Research*, 107(2), 199–214. [https://doi.org/10.1016/s0008-6215\(00\)80539-x](https://doi.org/10.1016/s0008-6215(00)80539-x)
- 60 Kono, H., & Kato, T. (2021). Elucidation of substituent distribution states for carboxymethyl chitosan by detailed NMR analysis. *Carbohydrate Polymer Technologies and Applications*, 2(100175), 100175. <https://doi.org/10.1016/j.carpta.2021.100175>
- 61 Jiang, H., Wang, Y., Huang, Q., Li, Y., Xu, C., Zhu, K., & Chen, W. (2005). Biodegradable hyaluronic acid/N-carboxyethyl chitosan/protein ternary complexes as implantable carriers for controlled protein release. *Macromolecular Bioscience*, 5(12), 1226–1233. <https://doi.org/10.1002/mabi.200500126>
- 62 Orienti I., & Luppi B. (1999). Chitosan and its N-carboxyethyl and N-aminoethyl derivatives as vehicles for topical formulations. *Journal of cosmetic science*, 50(5), 307–314.
- 63 do N. Ferreira, C.R., de L. Ramos, E.L., Araujo, L.F.S., da S. Sousa, L.M., Feitosa, J.P.A., Cunha, A.F., Oliveira, M.B., Mano, J.F., & da S. Maciel, J. (2021). Synthesis and characterization of scaffolds produced under mild conditions based on oxidized cashew gums and carboxyethyl chitosan. *International Journal of Biological Macromolecules*, 176, 26–36. <https://doi.org/10.1016/j.ijbiomac.2021.01.178>
- 64 Qu, J., Zhao, X., Ma, P.X., & Guo, B. (2017). pH-responsive self-healing injectable hydrogel based on N-carboxyethyl chitosan for hepatocellular carcinoma therapy. *Acta Biomaterialia*, 58, 168–180. <https://doi.org/10.1016/j.actbio.2017.06.001>
- 65 Huang, J., Xie, H., Ye, H., Xie, T., Lin, Y., Gong, J., Jiang, C., Wu, Y., Liu, S., Cui, Y., Mao, J., & Mei, L. (2016). Effect of carboxyethylation degree on the adsorption capacity of Cu(II) by N-(2-carboxyethyl)chitosan from squid pens. *Carbohydrate Polymers*, 138, 301–308. <https://doi.org/10.1016/j.carbpol.2015.11.037>
- 66 Yang, S., Dong, Q., Yang, H., Liu, X., Gu, S., Zhou, Y., & Xu, W. (2016). N-carboxyethyl chitosan fibers prepared as potential use in tissue engineering. *International Journal of Biological Macromolecules*, 82, 1018–1022. <https://doi.org/10.1016/j.ijbiomac.2015.10.078>
- 67 Ibrahim, H.M., Mostafa, M., & Kandile, N.G. (2020). Potential use of N-carboxyethylchitosan in biomedical applications: Preparation, characterization, biological properties. *International Journal of Biological Macromolecules*, 149, 664–671. <https://doi.org/10.1016/j.ijbiomac.2020.01.299>
- 68 Huang, J., Xie, H., Hu, S., Xie, T., Gong, J., Jiang, C., Ge, Q., Wu, Y., Liu, S., Cui, Y., Mao, J., & Mei, L. (2015). Preparation, characterization, and biochemical activities of N-(2-carboxyethyl)chitosan from squid pens. *Journal of Agricultural and Food Chemistry*, 63(9), 2464–2471. <https://doi.org/10.1021/jf505581n>
- 69 Shigemasa, Y., Ishida, A., Sashiwa, H., Saimoto, H., Okamoto, Y., Minami, S., & Matsushashi, A. (1995). Synthesis of a new chitin derivative, (1-carboxyethyl)chitosan. *Chemistry Letters*, 24(8), 623–624. <https://doi.org/10.1246/cl.1995.623>
- 70 Skorik, Y.A., Gomes, C.A.R., Vasconcelos, M.T.S.D., & Yatluk, Y.G. (2003). N-(2-Carboxyethyl)chitosans: regioselective synthesis, characterisation and protolytic equilibria. *Carbohydrate Research*, 338(3), 271–276. [https://doi.org/10.1016/s0008-6215\(02\)00432-9](https://doi.org/10.1016/s0008-6215(02)00432-9)
- 71 Jiang, H., Wang, Y., Huang, Q., Li, Y., Xu, C., Zhu, K., & Chen, W. (2005). Biodegradable hyaluronic acid/N-carboxyethyl chitosan/protein ternary complexes as implantable carriers for controlled protein release. *Macromolecular Bioscience*, 5(12), 1226–1233. <https://doi.org/10.1002/mabi.200500126>
- 72 Liu, X-L, Zhu, C-F, Liu, H-C, & Zhu, J-M (2022). Quantitative analysis of degree of substitution/molar substitution of etherified polysaccharide derivatives. *Designed Monomers and Polymers*, 25(1), 75–88. <https://doi.org/10.1080/15685551.2022.2054118>
- 73 Korel, A., Samokhin, A., Zemlyakova, E., Pestov, A., Blinova, E., Zelikman, M., Tkachenko, V., Bets, V., Kretien, S., Arzhanova, E., & Litvinova, E. (2023). A carboxyethylchitosan gel cross-linked with glutaraldehyde as a candidate carrier for biomedical applications. *Gels (Basel, Switzerland)*, 9(9), 756. <https://doi.org/10.3390/gels9090756>
- 74 Ogawa, K., Hirai, I., Shimasaki, C., Yoshimura, T., Ono, S., Rengakuji, S., Nakamura, Y., & Yamazaki, I. (1999). Simple determination method of degree of substitution for starch acetate. *Bulletin of the Chemical Society of Japan*, 72(12), 2785–2790. <https://doi.org/10.1246/bcsj.72.2785>
- 75 Li, Y., Qiu, Y., Hou, H., Zhang, G., Hao, H., & Bi, J. (2023). The preparation and properties of amino-carboxymethyl chitosan-based antibacterial hydrogel loaded with ϵ -polylysine. *Foods (Basel, Switzerland)*, 12(20), 3807. <https://doi.org/10.3390/foods12203807>

- 76 Craciun, A.M., Morariu, S., & Marin, L. (2022). Self-healing chitosan hydrogels: Preparation and rheological characterization. *Polymers*, *14*(13), 2570. <https://doi.org/10.3390/polym14132570>
- 77 Herdiana, Y., Febrina, E., Nurhasanah, S., Gozali, D., Elamin, K.M., & Wathoni, N. (2024) Drug loading in chitosan-based nanoparticles. *Pharmaceutics*, *16*(8), 1043. <https://doi.org/10.3390/pharmaceutics16081043>
- 78 Fletes-Vargas, G., Espinosa-Andrews, H., Cervantes-Uc, J.M., Limón-Rocha, I., Luna-Bárcenas, G., Vázquez-Lepe, M., Morales-Hernández, N., Jiménez-Ávalos, J.A., Mejía-Torres, D.G., Ramos-Martínez, P., & Rodríguez-Rodríguez, R. (2023) Porous chitosan hydrogels produced by physical crosslinking: Physicochemical, structural, and cytotoxic properties. *Polymers*, *15*(9), 2203. <https://doi.org/10.3390/polym15092203>
- 79 Nayak, S., & Kundu, S.C. (2014). Sericin-carboxymethyl cellulose porous matrices as cellular wound dressing material. *Journal of Biomedical Materials Research Part A*, *102*(6), 1928–1940. <https://doi.org/10.1002/jbma34865>
- 80 Skorik, Y.A., Pestov, A.V., Kodess, M.I., & Yatluk, Y.G. (2012). Carboxyalkylation of chitosan in the gel state. *Carbohydrate Polymers*, *90*(2), 1176–1181. <https://doi.org/10.1016/j.carbpol.2012.06.072>
- 81 Khan, S., & Anwar, N. (2019). Highly porous pH-responsive Carboxymethyl chitosan-grafted-poly (acrylic acid) based smart hydrogels for 5-fluorouracil controlled delivery and colon targeting. *International Journal of Polymer Science*, *2019*, 1–15. <https://doi.org/10.1155/2019/6579239>
- 82 Farasati Far, B., Omrani, M., Naimi Jamal, M.R., & Javanshir, S. (2023). Multi-responsive chitosan-based hydrogels for controlled release of vincristine. *Communications Chemistry*, *6*(1), 1–14. <https://doi.org/10.1038/s42004-023-00829-1>
- 83 Elliott, J.E., Macdonald, M., Nie, J., & Bowman, C.N. (2004). Structure and swelling of poly(acrylic acid) hydrogels: effect of pH, ionic strength, and dilution on the crosslinked polymer structure. *Polymer*, *45*(5), 1503–1510. <https://doi.org/10.1016/j.polymer.2003.12.040>
- 84 Kumar Singh Yadav, H., & Shivakumar, H.G. (2012). in vitro and in vivo evaluation of pH-sensitive hydrogels of carboxymethyl chitosan for intestinal delivery of theophylline. *ISRN Pharmaceutics*, *2012*, 1–9. <https://doi.org/10.5402/2012/763127>
- 85 Nkana, G.R.N., Lajeunesse, A., Chabot, B., & Nguyen-Tri, P. (2024). Design of porous spherical biomaterials from carboxymethyl chitosan for removal of fluoxetine in aqueous medium. *Journal of Environmental Chemical Engineering*, *12*(2), 112228. <https://doi.org/10.1016/j.jece.2024.112228>
- 86 Rohindra, D.R., Nand, A.V., & Khurma, J.R. (2004). Swelling properties of chitosan hydrogels. *The South Pacific Journal of Natural and Applied Sciences*, *22*(1), 32. <https://doi.org/10.1071/sp04005>
- 87 Budianto, E., Muthoharoh, S.P., & Nizado, N.M. (2015). Effect of crosslinking agents, pH and temperature on swelling behavior of cross-linked chitosan hydrogel. *Asian Journal of Applied Sciences*, *3*(5). <https://www.ajouronline.com/index.php/AJAS/article/view/3099>

Ruceera R. Verekar¹, Shamshad Bi M. Shaikh²,
Sarita Rebelo², Shailendra S. Gurav^{1*}

¹Department of Pharmacognosy, Goa College of Pharmacy, Goa University, Goa, India;

²School of Biological Sciences and Biotechnology, Goa University, Taleigao Plateau, Taleigao, Goa, India

(*Corresponding author's email: shailendra.gurav@nic.in)

Double-Loaded Liposomes Encasing Umbelliferone in Hydroxypropyl- β -Cyclodextrin Inclusion Complexes: Formulation, Characterisation and Investigation of Photoprotective Activity

Double-loaded liposomes are a system in which a drug is incorporated in the vesicle lipid layers after aqueous phase inclusion complexation to form a drug-in-cyclodextrin-in phospholipid vesicles complex. Umbelliferone (UMB) is a naturally occurring coumarin used as a photoactive agent because of its UV light absorption ability. In this study, the double loading (DL) technique was used to encapsulate “UMB in hydroxy propyl- β -cyclodextrin (HP- β -CD)-in-liposomes (UMB-CDLP)”. This led to the creation of “double-loaded liposomes encasing UMB in HP- β -CD (DL-UMB-CDLP)”, specifically developed to combine the power of solubilisation of HP- β -CD with the sustained release characteristics of phospholipid vesicles to improve solubility and dissolution profile. HP- β -CD and UMB inclusion complexes prepared by different methods were characterized by FTIR spectroscopy, DSC, saturation solubility, x-ray diffractometry, and scanning electron microscopy. DL-UMB-CDLP was developed using a thin film/lipid hydration method and a Box-Behnken design and was assessed by TEM, *in-vitro* diffusion studies and biological evaluation. The optimized DL-UMB-CDLP formulation demonstrated promising results, indicating the development of a stable composition. Animals treated with the DL-UMB-CDLP gel and exposed to the immediate irradiation protocol proved the UMB's ability to protect against UV-induced oxidative damage based on the amount of antioxidant enzymes estimated to be present in rat skin.

Keywords: Umbelliferone, double-loaded liposome, inclusion complex, photoprotective activity, photoactive agent, irradiation protocol, drug-in-cyclodextrin, drug-in-phospholipid

Introduction

Numerous studies have been established on different plant secondary metabolites for their medicinal properties and general health-promoting potential using phytochemical and phytopharmacological research. However, their limited solubility in lipophilic solvents and hydrolytic instability at various physiological pH levels restrict their topical and oral absorption through the lipoidal biological membrane, which can be overcome by their structural modifications, phospholipid complexation, as well as the use solubility and bioavailability modifiers [1].

Cyclodextrins (CDs) are cyclic oligosaccharides derived from starch and their abridged cone shape with hydrophobic cavity and exterior hydrophilic surface allows them to form inclusion complexes with lipophilic drugs, which is a crucial factor to enhance their solubility and stability. Moreover, modified CDs, such as 2-hydroxypropyl- $\alpha/\beta/\gamma$ CD, enhances drug-binding abilities and solubility [2].

Liposomes, phospholipid vesicles, serve as a drug delivery strategy to enhance loading capacity, stability, sustained-release pattern and encapsulation of hydrophilic and lipophilic molecules resulting in better bioavailability [3]. There are situations where the molecule or molecules to be trapped are incompatible with the vesicles formation, and the addition of lipophilic molecules to vesicle lipid bilayers can negatively affect the bilayer development and ultimately their stability. In therapy, increasing phospholipid levels to support higher drug concentrations may not be possible for obvious reasons [4, 5]. McCormack and Gregoriadis [6] developed a drug-in-cyclodextrin-in phospholipid vesicle system, also known as double-loading (DL) of the drug, by incorporating a drug into the vesicle lipid layers following aqueous phase inclusion complexation [6, 7]. Several reports employing DL of curcumin [2], lycopene [5], paclitaxel [8], quercetin [9], etc., in β -CD have confirmed their enhanced stability and bioavailability.

Acute and long-term inflammatory alterations such as erythema, immunosuppression, photoaging, and carcinogenesis are caused by exposure to ultraviolet (UV) radiation, which also damages the skin clinically and histologically [10–12]. Extrinsic ageing or photoaging (a term describing skin aging caused by cumulative solar UV radiation) is a complex biological process that affects the skin's structural integrity and physiological activity. Long-term exposure of the skin to solar UV radiation increases free radicals and reactive oxygen species (ROS), triggering signaling pathways and facilitating inflammatory reactions through inflammatory cytokines like tumor necrosis factor (TNF- α) and interleukins (IL) of types 1 (IL-1) and 6 (IL-6) [13–15]. Furthermore, oxidative stress is also caused by high levels of ROS. The redox equilibrium cannot be maintained in this situation due to the inadequacy of natural antioxidant defence systems such as the enzymes superoxide dismutase and catalase. Consequently, excess ROS are associated with the skin aging process and have harmful effects on the body [16–18].

The use of dermatological preparations with UV filters is considered the most effective cosmetic strategy to counteract the negative effects of UV radiation [19, 20]. However, they are useless in providing complete protection due to their failure to tackle the biochemical processes leading to UV-induced tissue damage [12]. Furthermore, concerns about the ecological and human safety of filters are pushing the scientific community to look for new options [21, 22]. Plant-derived anti-inflammatory and radical scavengers are proven as promising photoprotective agents against UVA-UVB radiation damage [23, 24].

Umbelliferone (UMB), 7-OH hydroxycoumarin, is a yellowish-white crystalline compound found abundantly in plants, belongs to the Apiaceae family and a few other species, such as *Hieracium pilosella* (Asteraceae) and *Hydrangea macrophylla* (Hydrangeaceae) [25]. A hydroxyl group of UMB interact with phosphatidylcholine's polar choline group to form a UMB-phospholipid complex. Since UMB offers the necessary qualities, the current study formulates it as a UMB-in-cyclodextrin-in phospholipid complex (UMB-CDLP) to enhance its solubility, permeability, antioxidant activity, and decisive photoprotective action. The main goal was to protect UMB from oxidation, heat and light. It has been suggested that this complex formation stabilizes the trapped molecule against various chemical attacks [6, 7]. The aim of this study was to create a UMB-in-CD-in-phospholipid vesicles that would combine the sustained-release pattern of phospholipid vesicles with the solubilizing ability of β -CD. Further, the study extends toward incorporating DL-UMB-CDLP into a semi-solid vehicle to design a final gel formulation for topical application.

Experimental

Materials

UMB was purchased from Tokyo Chemical Industry (TCI), and its purity was >98 %. A gratis sample of Phospholipon@90H (PL90H) was acquired from Lipoid Germany. The cholesterol used was of analytical grade and was supplied by Molychem, Mumbai. The ethanol used was of laboratory grade. The other reagents and chemicals were all analytical grade. The assay kits for antioxidant marker enzyme estimation were purchased from Elabscience USA.

Methodology

Preparation of UMB- β -CD Molecular Inclusion Complexes

Four different methods were used to prepare the UMB- β -CD molecular inclusion complex.

Physical Mixture Method

The necessary molar ratios (1:1, 1:2, and 1:3) of hydroxy propyl- β -cyclodextrin (HP- β -CD) and drug UMB were weighed and combined separately in a mortar by trituration for 5 min. After passing through a #40 sieve, the mixtures were kept in an airtight container until they were needed again [26].

Kneading Method

Precisely weighed molar amounts of each HP- β -CD were mixed with a moistening agent consisting of distilled water and ethanol (1:1). Molar amounts of the drug were added with continuous grinding. The consistency of the pastes was maintained during the 1 hour grinding process using the required amount of moistening agent. Finally, these pastes were dried for 24 hours at 55 °C in a hot air oven. After passing the dried pastes through sieve #40, the leftover mass was gathered and kept in airtight containers until needed again [27, 28].

Solvent Evaporation Method

Distilled water was used in this method to dissolve the drug and HP- β -CD. The resultant mixture was vacuum evaporated at 55 °C stirring for 24 hours to obtain a pure solution. After being dried, the material was pulverised to a powder and run through a sieve #40 [26].

Co-Evaporation Method

To obtain a solid powdered inclusion complex, this technique involves separately dissolving the drug and HP- β -CD in two mutually miscible solvents, such as ethanol and water, respectively, mixing the two solutions to create a molecular dispersion of the drug and complexing agents, and then vacuum evaporating the solvent. After stirring the mixture for an entire day, it was vacuum evaporated at 55 °C. After being pulverised, the dried mass was run through a sieve #40 [2, 27, 28].

Optimization of UMB- β -CD Molecular Inclusion Complex

The percent yield was determined to find the best inclusion complex method and was estimated using the following formula:

$$\text{Percent yield} = \frac{\text{Practical mass}}{\text{Theoretical Mass (Drug + Carrier)}} \times 100\%$$

Drug content was estimated with the help of the reported methods using UV spectrophotometer at 345.5 nm. The detailed procedures are presented in the Supplementary Materials file [29].

Dissolution Studies

Each inclusion complex sample equivalent to 10 mg of UMB was subjected to a dissolution test using Dissolution Test Apparatus USP (Type-II). A comparable dissolution test was performed using 10 mg of pure UMB as a control. The dissolution medium had a volume of 500 mL and consisted of PBS 7.4. The apparatus was operated after adding an inclusion complex equivalent to 10 mg of UMB to the dissolution medium (PBS 7.4). The temperature was held at 37 ± 0.5 °C while the stirring speed was set at 50 rpm. 5 mL aliquots from the dissolution medium were removed using a 0.45 μ m membrane filter (Ustar LB, USA) at 1, 3, 5, 7, 10, 12, 15, 20, 25, 30, 45, and 60 min. An equal volume of the freshly prepared dissolution medium was then added. Spectrophotometric measurements using a UV-visible spectrophotometer (Shimadzu, UV-2700) of UMB concentrations at 324.5 nm were performed using the standard curve's regression equation generated in the same medium. Three duplicates of each experiment were performed and the mean value was determined [28].

Characterisation of Optimized UMB- β -CD Molecular Inclusion Complex

The physicochemical characterisation [5, 28, 30–33] of the plain drug, PL90H, cholesterol, HP- β -CD, physical mixture (PM) and inclusion complex was carried out using various techniques such as FT-IR analyses (FTIR spectrophotometer IR Affinity-1S, Shimadzu), saturation solubility analysis, Differential Scanning Calorimetry (DSC) analysis (TA Instruments, Q20, USA), X-ray diffraction (XRD) analysis (D2 Phaser, Bruker AXS, USA), Scanning electron microscopy (SEM) (JEOL Mode Japan JSM 639OLV) at University Science Instrumentation Center (USIC), Goa University, Goa. The detailed procedures for all the analyses are given in the Supplementary Materials file.

Formulation Development of DL-UMB-CDLP- QbD Approach

DL-UMB-CDLP was prepared using film/lipid hydration methodology and the quality-by-design (QbD) approach. The required lipids (PL90H : cholesterol) were taken in different molar ratios (5:5, 7:3, 9:1) along with C5 complex (Table S3) equivalent to 100 mg of UMB and dissolved in ethanol. The obtained organic solvent was slowly removed using a rotary evaporator at 37 ± 2 °C. The lipid film deposited on the flask's inner walls was hydrated by adding 10 mL of PBS (pH 7.4). The obtained liposome suspension was subjected to stirring on a magnetic stirrer for 3 hours at the required RPM (600, 800, 1000 rpm) and then probe was sonicated for 10s on and 5s off pulse for 5 min at 40 % amplitude. Subsequently, centrifugation (15000 rpm, 4 °C, and 30 min) was performed to separate the pellet from the suspension. The liposomal suspension was stored in glass vials [5].

Coded level and Real values for each factor under study for DL-UMB-CDLP formulations

Variables	Level		
	-1	0	+1
<i>Independent</i>	Real Values		
PL90H : Cholesterol (X1)	5:5	7:3	9:1
Lipid : Drug (X2)	1:1	2:1	3:1
Stirring Speed (X3)	600	800	1000
<i>Dependent: Entrapment Efficiency and Particle Size</i>			

StatEase Inc's Design Expert software (version 10) was used for the design experiments. Three factors and three levels of Box-Behnken design were used to carry out the optimization. This study employed a 3³ randomised full factorial design employing PL90H : Cholesterol ratio (X1), Lipid : Drug ratio (X2), and stirring speed (X3) to determine the effect of those three independent factors on entrapment efficiency and particle size (Table 1). Three levels, numbered +1, 0, and -1, were used to test each component. F-statistics were utilised to assess the response [34]. Variables in the model were deemed significant if their *p*-values were higher than 0.05. The association between the responses and independent variables was ascertained utilising two-dimensional contour plots [5].

Evaluation of the DL-UMB-CDLP

Entrapment Analysis

An indirect method of entrapment analysis was carried out to calculate the entrapment efficiency of a drug. The entrapment efficiency was determined after centrifugation of DL-UMB-CDLP suspension at 15000 rpm, at 4 °C for 30 min. A solvent in which the drug is highly soluble, but the complex is not, was used to separate the untrapped drug fraction. The free drug was estimated by UV analysis. Based on the absorbance range, the formulation batches were dispersed in 10 mL of ethanol; further dilutions were made in PBS 7.4. The UV absorbance was determined at 324.5 nm for DL-UMB-CDLP [25, 35]. The formula given below was used to assess entrapment efficiency:

$$\text{Entrapment Efficiency} = \frac{\text{Total Drug} - \text{Free Drug}}{\text{Total Drug}} \times 100\%$$

Particle Size and Zeta Potential Analysis

The prepared liposomal complex's particle size was determined using photon correlation spectroscopy with dynamic light scattering on a Zetasizer® nano (Malvern, ZSU3100) fitted with a 5 mW Helium-Neon laser with an output wavelength of 633 nm. Measurements were made with a runtime of at least 40 to 80 s, at a 90° angle, and at 25 °C. Smoluchowski's equation was used to determine the zeta potential based on the electrophoretic mobility of liposomes [36].

Differential Scanning Calorimetry (DSC) Analysis

One of the most well-known calorimetric techniques for studying solid-phase interactions of drugs with polymers is DSC. The optimized formulation and pure drug samples were heated in aluminum pans with flat bottoms between 70 °C and 320 °C at a constant rate of 10 °C per minute by employing alumina as a reference standard in a differential scanning calorimeter [28].

Photomicroscopy

A droplet was covered with a cover slip and set on a slide after the formed complex was suspended in distilled water. The photomicrographs were obtained using a microscope (Model: DM 2500, Leica Microsystems, Germany) under 20X magnification. The study was conducted using an optical microscope equipped with a camera [37].

Transmission Electron Microscopy (TEM)

A TECNAI 12 G2 TEM was used for the TEM analysis, a versatile 120 kV TEM suitable for all samples. Surface morphology was determined using TEM. A dilution of 20 µL of the sample in 6 mL distilled water was made, and 2 µL of the sample was coated on a copper-carbon grid and dried under an IR lamp for 5 min. Negative staining was performed with phosphotungstic acid, dried and analysed under TEM [37, 38].

In Vitro Drug Release Study

The *in vitro* drug release was carried out using the dialysis bag technique. To eliminate preservatives, distilled water was used to soak the dialysis membrane at room temperature, rinsed with distilled water once more, and then soaked in phosphate buffer saline (PBS) of pH 7.4. A dialysis bag (dialysis membrane-110, molecular weight cut off 12000) was filled with 1 mL of DL-UMB-CDLP suspension, equivalent to 10 mg of the drug. The bag was then hermetically sealed and submerged in 50 mL of PBS (pH 7.4) and ethanol in a 4:1 ratio. Using a magnetic stirrer, the medium was continuously stirred at 150 rpm while maintaining a temperature of 37 ± 0.5 °C and replacing a 5 mL sample at specified intervals to maintain the sink condition. UV spectrophotometric analysis using a UV-visible spectrophotometer (Shimadzu, UV-2700) at 324.5 nm measured the released drug. Lastly, Zero order, First order, Higuchi's equation, and Peppas-Korsmeyer four models were employed to evaluate the kinetics of the drug release [5].

Preparation of DL-UMB-CDLP Liposomal Gel

Four batches of the gel formulations were prepared by varying the concentration of Carbopol 934 from 1.0 %, 1.5 %, 2.0 % and 2.5 % for batch B1, B2, B3 and B4, respectively. Distilled water was used to soak the proper amount of Carbopol 934 for the entire night. In a beaker, 10 mL of distilled water was utilised to dissolve methyl and propylparaben (0.1 % and 0.01 %, respectively), and Carbopol 934P was added while being constantly stirred. The optimized formulation of DL-UMB-CDLP (1.0 %) was introduced into the mixture. Polyethylene glycol (PEG) 400 (2.5 %) was later added to the dispersion and mixed with triethanolamine to form a gel. Glass ointment bottles were used to hold the prepared gel, which was then kept at room temperature (Table S1 in the Supplementary Materials file) [37].

Evaluation of Gel

pH, Visual Inspection, Homogeneity and Grittiness

The pH of each gel was measured using a pH meter. The results were recorded after two minutes of dipping the electrode in a gel at 27 °C [39]. Visual assessments were conducted on all prepared gel batches to assess their organoleptic qualities, such as color, texture, consistency, and physical appearance [40]. Every gel formulation was tested by rubbing a tiny amount of the gel on the back of the hand and pressing it between the thumb and index finger [41]. Every batch of prepared gel was examined under a microscope to check for the presence of particles [42].

In Vitro Diffusion Study of Gel

The Franz-diffusion cells were used in the *in vitro* release investigation. The dialysis membrane was immersed in phosphate buffer (pH:6.8) for the entire night. 1g of gel was applied to the donor compartment, and 50 mL of phosphate buffer pH 6.8 was added to the receptor compartment. To maintain homogeneity, the mixture was constantly stirred at 150 rpm using a magnetic stirrer at 37 ± 0.5 °C and replenished with a 5 mL sample with an equal amount of freshly prepared buffer to maintain the sink condition, followed by spectrophotometric analysis at 324.5 nm [37].

Stability Studies

Stability assessments in this study were conducted at 4 °C ± 1 °C / 45 %RH, room temperature (25 °C ± 1 °C /65 %RH), and 40 °C ± 1 °C /75 %RH for a specified duration ranging from 0 days to 30 days to 90 days for the optimized formulations. The liposomal suspension was stored in 20 mL sealed vials. Periodically, samples were taken out and examined for zeta potential, polydispersity index (PDI), and particle size. Analysis was done on the optimized DL-UMB-CDLP gel formulation's pH, drug content, drug release, and viscosity. ANOVA was used for statistical analysis and validation of this data [43].

Biological Evaluation

Animals

To evaluate the UV-protective properties of the double-loaded liposomal formulation as a gel, healthy Wistar rats weighing 150–200 g, both male and female, were acquired from the central animal house and housed under standard conditions (20 – 25 °C /55–65 % RH). During the seven days before the experiment, the rats were acclimated to their new surroundings in plastic cages with readily accessible water ad libitum and rat feed. They were also kept at the proper humidity and temperature. All the experiments were conducted per the Institutional Animal Ethical Committee's standard guidelines (Approval no. GCP/IAEC/2023/12) [25, 39].

Ex Vivo Skin Permeation

The rat skin was prepared for *ex vivo* permeation studies using a Franz diffusion cell (Perme Gear Standard Jacketed Franz cell USA) as per the reported method [25]. The rat skin was placed on the Franz diffusion cell in the proper orientation, with the dermal side confronting the receptor compartment filled with buffer and the stratum corneum side towards the donor compartment. Using a magnetic stirrer, the cell was continuously stirred at 37 ± 0.5 °C. Following that, 1 mL of the optimized DL-UMB-CDLP gel preparation and the standard UMB gel (0.1 %) that had been prepared in a similar way were applied evenly to the skin in the donor compartment. After specified intervals, 1 mL sample was withdrawn from the receptor compartment by maintaining the sink condition and analysed spectrophotometrically at 324.5 nm. A comparison was made between the double-loaded liposomal gel's skin penetration and the plain gel [25, 30].

Primary Skin Irritation Studies

Wistar albino rats ($n = 6$) were used in the skin irritation investigation of the prepared formulation. A 4 cm² area was marked after each rat's back hairs were clipped off with a trimmer. Rats ($n = 6$) were allocated at random to one of three categories: Group I: Control (received no drug in gel base), Group II: received UMB treatment in gel base and Group III: treated with optimized DL-UMB-CDLP loaded gel. The control and gel formulations were used for seven days in a row. Before administering each dose, the rat skin was cleansed, and for seven days, it was observed for any reactions, including erythema and edema [39, 44, 45].

Assessment of the Photoprotective Capacity of the Optimized DL-UMB-CDLP Gel Against UV Exposure

The UV lamp (Philips, India; TL 128 W, 315–400 nm; peak radiation at 370 nm) was used. A trimmer shaved a defined region on the rat's dorsal surface (2×3 cm²). To find and eliminate rats exhibiting aberrant hair growth or a reaction to depilation, the rats were monitored for 48 h. Rats in this study were exposed to UVA for 20 min (610 mJ/cm²; 4.42 times MED).

The experimental rats were divided into six groups (G1–G6). The rats' marked shaved area was covered with a thin, even layer of gel formulation. Animals in the control (G1) and UVA-irradiated (G2) groups received a placebo gel formulation. The UMB1 (G3) and UMB2 (G4) groups were given a standard UMB gel that contained 0.1 % medication. DL-UMB-CDLP gel, which includes a liposomal formulation equal to 0.1 % drug, was applied to the DL-UMB-CDLP1 (G5) and DL-UMB-CDLP2 (G6) groups. After topical application, the UVA-irradiated, UMB1 and DL-UMB-CDLP1 groups were immediately exposed to UV radiation for seven consecutive days. Following a 4 hours topical treatment, the G4 and G6 groups were subjected to UV light for 7 days (Table S2 of the Supplementary Materials file). All the rats were sacrificed using the cervical dislocation method on the eighth day. The skin's UV-exposed area was quickly removed in ice-cold saline, followed by homogenate preparation at 0.1 M PBS (pH 7.4) [25].

Estimation of Antioxidant Marker Enzymes in Cutaneous Tissue

The rat skin (2×3 cm²) was cleaned in ice cold saline and sliced into small pieces, followed by immediate homogenisation. Further, a 10 % w/v skin tissue homogenate supernatant was obtained by centrifugation and assayed using kits of Elabscience US per reported methods for the estimation of the antioxidant marker enzymes reduced glutathione (GSH), superoxide dismutase (SOD), thiobarbituric acid reactants (TBARS), lipid peroxidation (LPO) and catalase (CAT) [24, 25].

Statistical Analysis

Except for the estimation of antioxidant enzyme levels in rat skin, which was done using mean \pm standard error of means (SEM), all data were presented as mean \pm standard deviation (SD). GraphPad Prism software was used to conduct the statistical analysis, using a one-way analysis of variance (ANOVA) and Dunnett's post hoc test. The mean differences were deemed significant when the *p*-value was less than 0.05.

Skin Histopathology

After being fixed in 10 % buffered formalin, skin specimens were processed and paraffin-embedded. Additional paraffin sections (7 μ m) were taken and analysed under a microscope after being stained with hematoxylin and eosin to check for skin tissue disfigurement during the experiment [46].

*Results and Discussion**Percent Yield*

The percent yield of an inclusion complex is a useful metric for evaluating the efficiency of the preparation method and the strength of the host-guest interaction. Table S3 of the Supplementary Materials file displays the findings of the percent practical yield studies. It was found that the prepared inclusion complex's

practical yield ranged between 86.67 ± 0.14 and 95.65 ± 0.58 %. In **C5**, a higher yield for the UMB inclusion complex was demonstrated using the kneading method in a 1:2 ratio. The technique used to prepare molecular inclusion complexes is reproducible, as evidenced by low coefficient of variance (CV) values (< 1.0 %) in the percentage yield [47].

Assay or Drug Content Estimation

Determining the amount of drug present in an inclusion complex through assay or drug content estimation is essential for comprehending its characteristics and uses. This is significant because the inclusion complex might exhibit different properties, like enhanced solubility or bioavailability, than the pure drug. All 12 formulations' actual drug contents are displayed in Table S3 of the Supplementary Materials file. It was discovered that the drug content of the prepared inclusion complex ranged from 77.37 ± 0.64 to 98.34 ± 0.40 %, demonstrating the use of current techniques to prepare inclusion complexes with high content uniformity. In **C5**, the highest percentage of drug content was discovered to be 98.34 ± 0.40 %.

In Vitro Dissolution Studies

When a drug forms a complex with another molecule, such as cyclodextrin, *in vitro* dissolution studies of inclusion complexes measure how quickly the drug dissolves compared to the drug itself. These investigations aid to determine whether complexation speeds up the drug's rate of dissolution, which is critical to its efficacy and absorption. Inclusion complexes were prepared successfully, and the perfect combination for increasing the drug dissolution characteristics of the drug in comparison with its pure form was determined. Compared to pure drug, inclusion-complex drug release was faster. After 7 min, the cumulative percentage of drug released for **C5** was 98.9 ± 0.13 %, whereas the cumulative percentage for pure drug UMB was 22.10 ± 0.6 %. The dissolution rate of UMB from all inclusion complexes (apart from **C7** and **C10**) was significantly higher than that of pure UMB, according to the *in vitro* release study in Table S4 of the Supplementary Materials file.

According to the *in vitro* drug release profile, formulation **C5**, which contains HP- β -CD (1:2 ratio), exhibited a higher dissolution rate than the other formulations.

Characterisation of Optimized UMB Inclusion Complex

Saturation Solubility Studies

The solubility of optimized inclusion complex (**C5**) in PBS 7.4 was 33.04 mg/mL, which was approximately 6.5 times higher than pure drug UMB (5.09 mg/mL). UMB entrapment in the HP- β -CD cavity is one aspect of the host-guest interaction that may be responsible for the drug's increased solubility.

Fourier Transform Infrared Analysis (FT-IR)

IR studies are indicative of any interaction between ligand and guest molecules. FT-IR spectrum of optimized inclusion complex **C5** showed major peaks at 3315 cm^{-1} (O-H stretch) and 2922.60 cm^{-1} (C-H stretch) in which the hydroxyl group showed a broad peak along with the absence of the C=O group, indicating the formation of strong bonds between -OH group of HP- β -CD and drug in complex (Figure 1A).

DSC Analysis

It is an effective method for describing inclusion complexes, providing information on their properties and formation. The formation of a complex and the efficiency of the interaction between the host and guest molecules can be ascertained by examining the complex's thermal transitions. When the DSC thermogram of UMB is compared with that of the UMB inclusion complex (Figure 1B, 1C), it was observed that the thermogram of UMB inclusion complex showed a wide peak showing an endothermic peak at $82.68 \text{ }^\circ\text{C}$ and the endothermic peak at $123.13 \text{ }^\circ\text{C}$ corresponding to UMB was not visible indicating complete encapsulation of drug in HP- β -CD.

XRD Analysis

Understanding the structure and formation of an inclusion complex can be gained through XRD analysis. To ascertain the type of inclusion and validate the complex formation, researchers can compare the complex's diffraction patterns to those of the individual host and guest molecules. The XRD patterns of pure UMB and the **C5** are represented in Figures 1D and 1E. The XRD spectra of UMB showed strong reflections at around 11.7° , 15.97° , and 28° , indicating its crystalline nature. However, the peak intensities were somewhat diminished in the XRD spectrum of **C5**. The peak position (angle of diffraction) and the absence of separate, distinct peaks indicate the complex's amorphous nature. A diffractogram of the complex revealed the disappearance of most of the sharp peaks of the drug (crystalline nature), confirming complex formation with a greater amorphous nature of the inclusion complex than the free molecules [25].

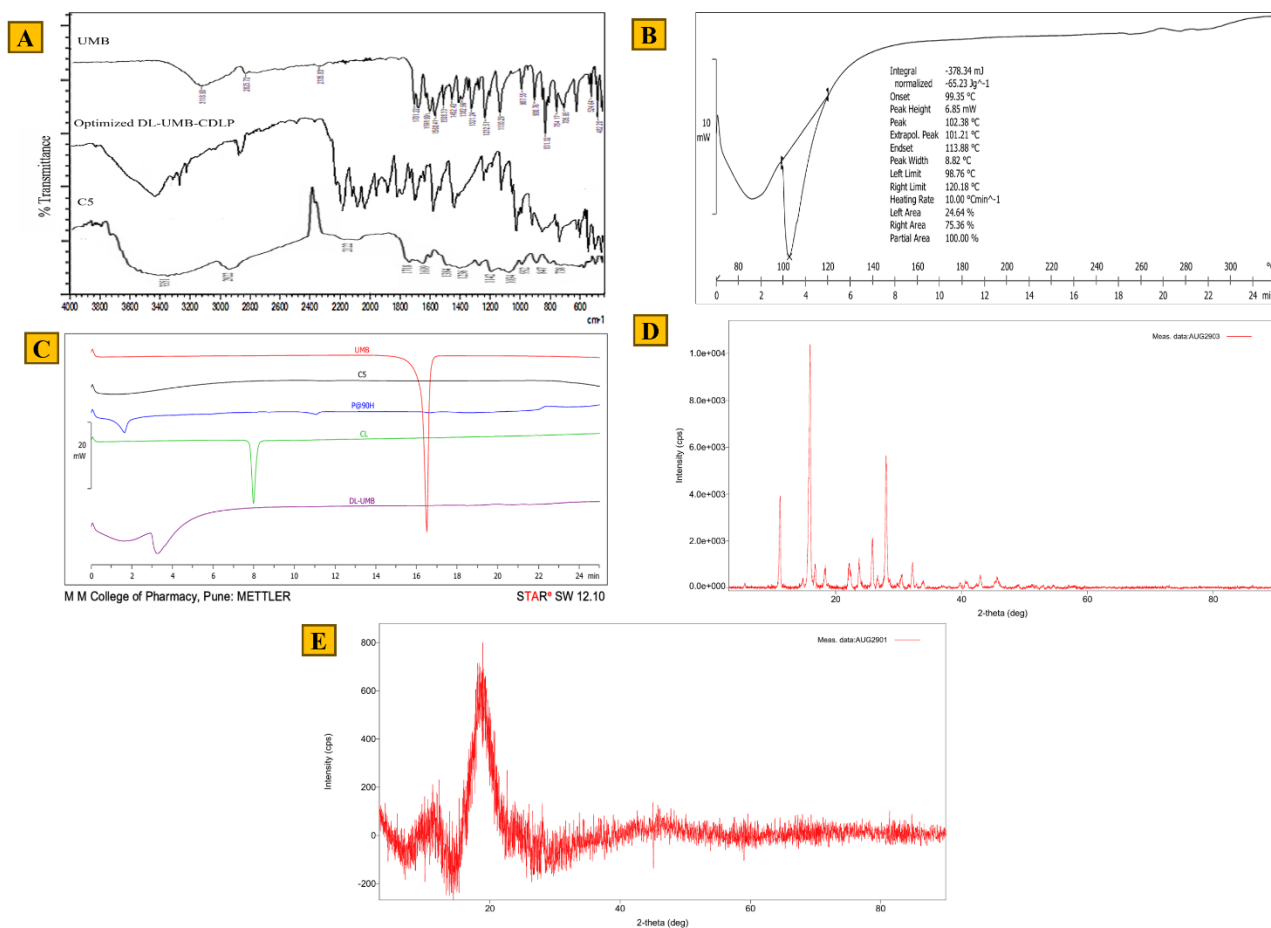


Figure 1. (A) FT-IR Spectra overlay of UMB, optimized batch of DL-UMB-CDLP and C5; (B) DSC thermograph of optimized DL-UMB-CDLP; (C) DSC thermograph overlay of UMB, C5, PL90H, Cholesterol and optimized DL-UMB-CDLP. (D, E) XRD diffractogram of UMB and C5

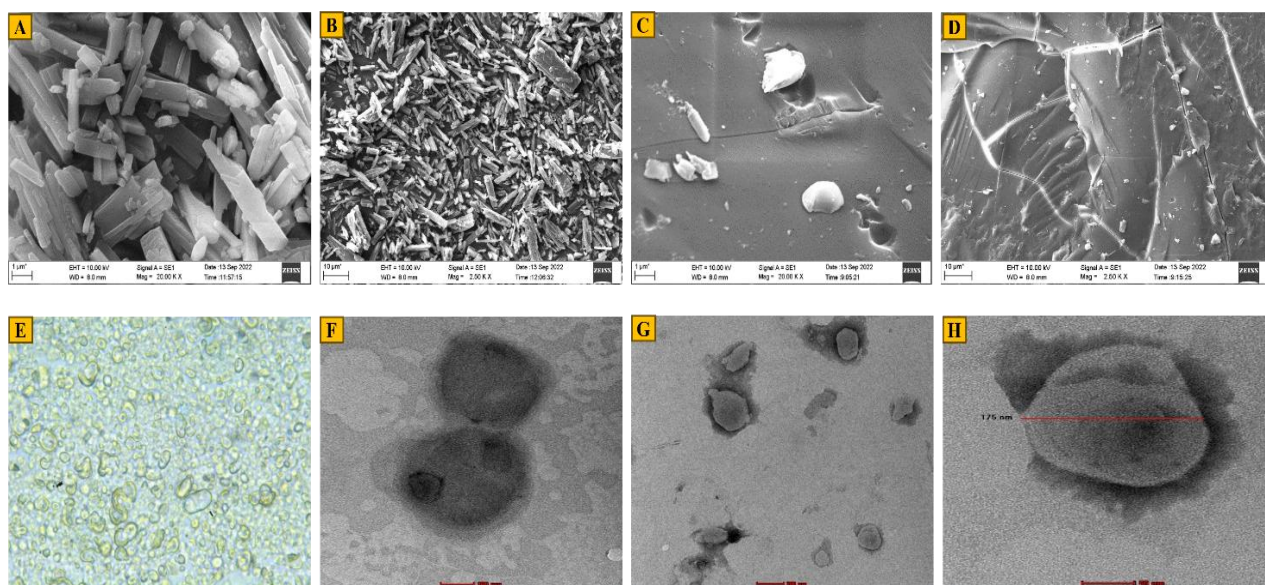


Figure 2. (A, B) SEM images of UMB at 20000 \times and 2500 \times . (C, D) SEM images of C5 at 20000 \times and 2500 \times . (E) Microscopic image of the optimized DL-UMB-CDLP. (F, G, H) TEM images of optimized DL-UMB-CDLP

SEM

This method is applied to the analysis of the surface morphology of inclusion complexes. Observing changes in the particle morphology relative to the individual components makes it possible to ascertain whether the inclusion complex has been successfully formed. The SEM images of the pure drug UMB and C5 at 20000× and 2500× magnification are depicted in Figure 2A–2D. UMB particles were observed to be crystalline individual particles, whereas the C5 complex's irregular shape and rough surface morphology indicated complete conversion into a complex. The drug particles remained dispersed and physically adsorbed on the surface of HP-β-CD and showed homogeneity, signifying the inclusion of complex formation [32].

Formulation Development of DL-UMB-CDLP

The results shown in Table S5 of the Supplementary Materials file were obtained for the formulation development batch for 15 formulations of DL-UMB-CDLP. The batches prepared showed that factors such as PL90H : cholesterol ratio, Lipid : drug ratio and stirring speed significantly affected the formulated double-loaded liposomes' entrapment efficiency.

Use of Design of Experiments (DoE) for Process Optimisation

DoE is a structured and organised way to determine the relationship among various factors that effect the output of a process. A 3³ factorial design was used to understand the effect of three independent variables: PL90H: cholesterol Ratio (A), Lipid: drug ratio (B), and stirring speed (C). Table S5 of the Supplementary Materials file lists the specifics of the 15 batches that were completed in triplicate. It was found that the vesicles' entrapment efficiency elevated as the PL90H: cholesterol ratio shifted from 5:5 to 7:3, and as the concentration of cholesterol increased, the vesicles' particle size reduced. Batches with the greatest PL90H: cholesterol ratio had greater entrapment efficiencies, whereas higher cholesterol levels caused lower entrapment. This may be because cholesterol in the lipid bilayer has displaced UMB [48].

Factorial Design for Entrapment Efficiency

The results show that the *p*-values of the model for entrapment efficiency were less than 0.001, indicating its significance. In this case, A, B, and C represented the formulation's constituent parts, and the equation showed how each of them quantitatively affected the variables. The following equation was obtained:

$$\%EE = 98.90 - 0.7400A - 0.3975B - 0.2025C - 0.5375AB - 1.99AC - 0.3025BC - 1.91A^2 + 0.6511B^2 - 2.75C^2$$

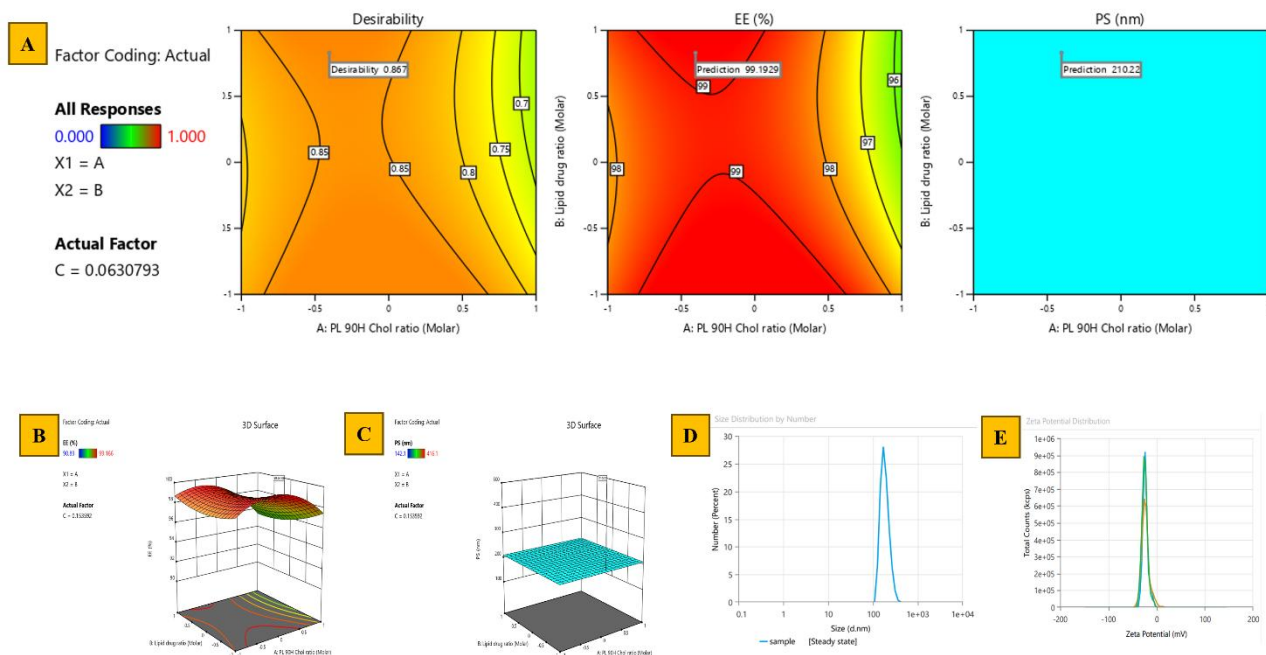


Figure 3. (A) The response surface plot and contour plots based on all the responses for DL-UMB-CDLP. (B, C) Contour plots based on the entrapment efficiency and particle size for DL-UMB-CDLP. (D, E) Particle size and zeta potential analysis of the optimized batch

According to the equation above, the PL90H: cholesterol concentration (A) had a positive coefficient, meaning it had a beneficial effect on the entrapment efficiency, whereas the concentration of cholesterol (B) had a negative coefficient, meaning it had a negative effect. *P* values of 0.05 indicate high significance of the regression coefficients. The contour plots shown in Figures 3A–3C schematically illustrates the response values. By altering the concentrations of the PL90H and cholesterol, these plots can be used to predict the system's entrapment efficiency.

Factorial Design for Particle Size

The results show that the model's *p*-value for particle size was 0.00004, indicating its significance.

Optimization

The formulation was optimized using the desirability function, taking into account PS at the minimum constraint and EE% at the maximum constraint. Numerical optimization predicted an optimal formulation with a lipid to drug ratio of 1.514:1, a PL90H to cholesterol ratio of 6.506:3.494, and a stirring speed of 813.8 rpm (coded values). The anticipated results were a particle size (PS) of 210.22 ± 0.28 nm and an entrapment efficiency (EE) of $99.19 \% \pm 0.39$, with a corresponding desirability of 0.867. The improved formulation was created empirically to validate the model. The measured PS and EE values were 215.45 ± 0.42 nm and $98.75 \pm 0.31 \%$, respectively. The percentage bias for PS and EE was determined to be 2.49 % for PS and 0.51 % for EE. These results confirm that the experimental values closely match the predicted outcomes with minimal bias, indicating the adequacy and reliability of the optimization model.

The optimized batch was DL-UMB-CDLP with an entrapment efficiency of $98.75 \% \pm 0.31 \%$, indicating successful entrapment of UMB into vesicles and a particle size of 215.45 ± 0.42 nm.

Evaluation of the optimized DL-UMB-CDLP Formulation

Zeta Potential Analysis

Zeta potential is another crucial metric frequently used to evaluate the liposomes' stability. The specificity and particle size distribution proved that the preparation method offers good homogeneity to double-loaded nanoparticles, and PL90H concentration plays a crucial role in the stability of formulations. The zeta potential of optimized batch was found to be -23.6 ± 0.49 mV. Thus, the liposomal formulation is considered stable, further restraining the charged particles' aggregation. The particle size and zeta potential analysis results of the optimized formulations of DL-UMB-CDLP are depicted in Figures 3D and 3E.

A polydispersity index (PDI) value of the optimized DL-UMB-CDLP formulation was found to be 0.09 ± 0.02 , confirming monodisperse particles with better homogeneity. Lower PDI values show a better particle size homogeneity.

DSC Analysis

The DSC thermogram of UMB was compared with that of double-loaded liposomal formulations. The optimized formulation of DL-UMB-CDLP thermogram exhibits a single peak at 102.38 °C, which differs from the UMB peak. It is evident that the initially observed UMB peak vanishes from the thermogram of the corresponding liposomal formulation, and the endotherm is seen to be broadened and slightly shifted to a lower temperature. Thus, it can confirm that the liposomal formulation is formed.

Photomicroscopy

This analysis provides a powerful toolkit for visualizing and characterizing double-loaded liposomes. The microscopic images showed the presence of spherical structures of the complex. Figure 2E represents that liposomes are circular or slightly off-circular, with relatively thick edges. Lipid vesicles can be created without cholesterol, but the formed structures will be destroyed easily. Thus, it is quite clear from the images that cholesterol stabilizes the PL90H layers in the liposomes.

TEM

TEM analysis is used to visualise the morphology and size of double-loaded liposomes, revealing their spherical shape and variations in size. Since TEM analysis had a high spatial and atomic resolution, it was utilized to ascertain the internal and structural characteristics. The TEM verified the presence of spherical liposome vesicles (Figure 2F–2H). TEM analysis disclosed the development of homogenous unilamellar, discrete and almost spherical structures of liposomes [49].

In Vitro Drug Release Study

These studies seek to determine the overall effectiveness of the liposomal system, comprehend the release profile of the medications, and evaluate the effect of formulation on drug release kinetics. The drug

release plays a vital role in drug performance. The *in vitro* drug release study of UMB liposomes was carried out in a 4:1 ratio of PBS 7.4: Ethanol at 37 °C using the dialysis method. The release study was carried out for 5 hours. The release rate of the DL-UMB-CDLP was significantly different ($p < 0.05$) compared to UMB. The release profile of free UMB showed 59.65 ± 1.04 % after 5 hours. The release profile of UMB formulations showed 81.64 ± 10.6 % after 5 hours (Figure 4A). The release profile of the liposomal suspension showed a biphasic response with a comparatively significant burst effect followed by a slower release rate. This burst effect and its rate vary depending on the type of liposome and lipid concentration. Sometimes, the addition of cholesterol reduces the initial release rate. Our observation of the sustained manner of drug release is due to the phospholipid complex's slow drug diffusion [50, 51, 52].

Evaluation of Gel

pH, Visual Inspection, Homogeneity, Grittiness

Gel evaluation ensures these formulations' safety, efficacy, and quality, affecting their effectiveness and patient acceptability. Each prepared topical gel formulation ranged between 6.5 and 6.8 (Table S6 of the Supplementary Materials file), a safe range to apply to the skin. The color, texture, consistency, and appearance of the prepared gel formulations were visually inspected. Every prepared formulation had a smooth, viscous texture and a buff color. There was no alteration in the toughness of formulation for all the prepared formulations during application to the skin. No grainy particles and lumps were observed on the slide under microscopic examination.

In Vitro Diffusion Study of Gel

This study gives researchers a better understanding of how a drug will act in the body by simulating drug release and penetration through a barrier, such as the skin, under carefully monitored conditions. This aids in developing and optimising topical gels and other drug delivery systems for increased safety and effectiveness. *In vitro* release profile of optimized DL-UMB-CDLP loaded gels containing different concentrations of Carbopol is shown in Figure 4B; the cumulative release of the control gel was found to be 56.16 ± 0.64 % at the end of 24 hours. Meanwhile, in the liposomal gel, B1, B2, B3, and B4 were found to be 86.29 ± 1.04 %, 118.18 ± 0.77 %, 104.47 ± 0.76 % and 77.23 ± 1.18 %, respectively. A significant difference ($p < 0.05$) was observed between the drug release retardation shown by UMB loaded gel and optimized DL-UMB-CDLP loaded gels. Since formulation B2 demonstrated the highest percentage of cumulative drug release, it was selected as the most optimal.

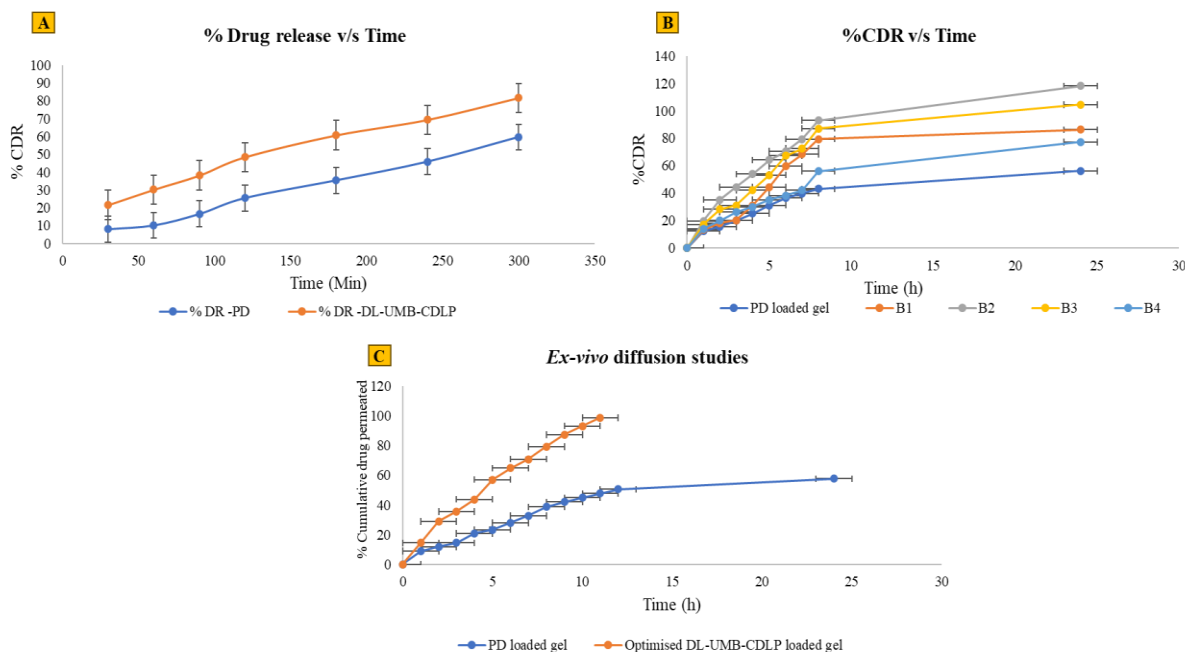


Figure 4. (A) *In vitro* drug release profile of pure drug UMB and optimized DL-UMB-CDLP. (B) *In vitro* drug diffusion profile of optimized DL-UMB-CDLP loaded gel. (C) Graphical representation of % cumulative drug permeation of optimized DL-UMB-CDLP loaded gel formulation and UMB loaded gel using rat skin

Kinetic Modelling of Optimized Gel

Model fitting of the permeation profile of drug from the UMB loaded gel and optimized DL-UMB-CDLP loaded gel was performed using Zero order, First order, Higuchi and Korsmeyer–Peppas models, which exhibited R^2 values of 0.9933, 0.8199, 0.9793 and 0.9962, respectively. Based on the highest coefficient of correlation, the best fit was shown by Korsmeyer–Peppas model ($R^2 = 0.9962$) and the value of permeation coefficient (n) for the drug and complex was obtained to be $0.5 < n < 1$. This indicates a non-Fickian pattern of drug release, i.e. a combination of drug diffusion and matrix erosion. The simple Korsmeyer–Peppas model describes drug release from a polymeric system, also called the “Power law”. Some release mechanisms, including the diffusion of the vehicle into the matrix, the matrix’s swelling, and the matrix’s dissolution, are simultaneously described by the Korsmeyer–Peppas model. The developed liposomal gel has a dual action: ethanol causes skin disruption, and the vesicle action leads to the drug release [31].

Stability Study

Stability study assesses how a pharmaceutical formulation’s efficacy, safety, and quality are preserved over time under various handling and storage conditions. Determining the product’s shelf life, ideal storage conditions, and suitable packaging is an essential step in the process. The study helps ensure that the medication will maintain its potency, purity, and other quality characteristics throughout its anticipated use. The stability studies of the optimum formulation showed that the liposomal formulation’s drug content and entrapment efficiency did not significantly decrease over 30 and 90 days. The results are shown in Tables S7 and S8 of the Supplementary Materials file. Changes in pH were noted, which slightly reduced with time. Maximum changes were observed in formulations stored at room temperature and 40 °C. Therefore, the formulations can be stored at 4 °C.

Biological Evaluation

Ex Vivo Skin Permeation Studies

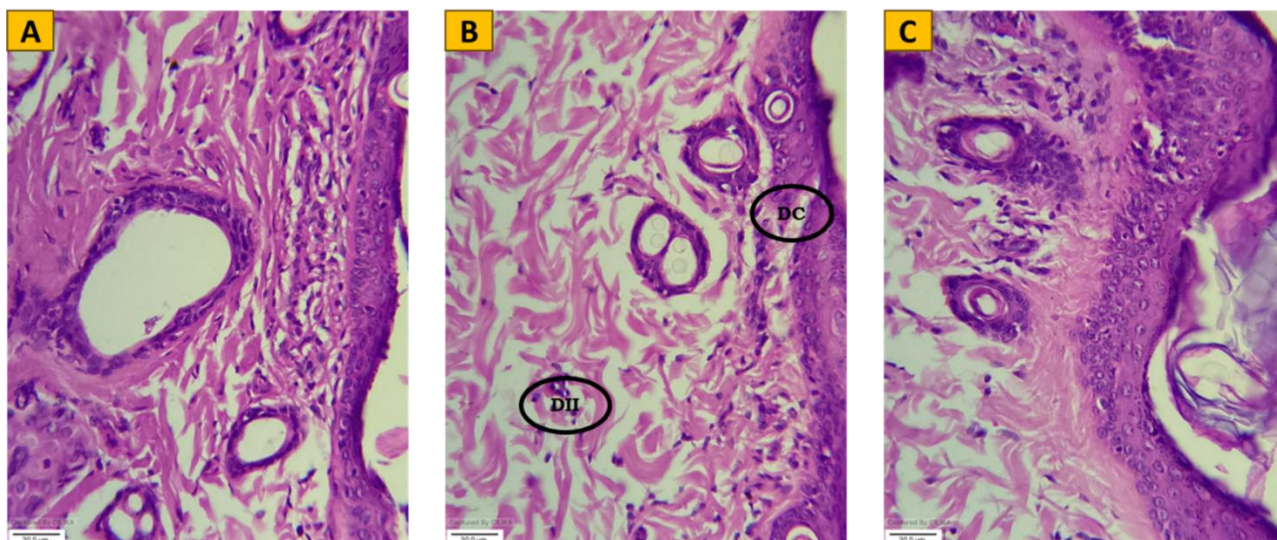
These studies are crucial for understanding drug delivery, evaluating the efficacy of formulations, and predicting how substances will interact with the skin. The comparative results of the cumulative release percentage of the pure drug UMB-loaded gel and the optimized DL-UMB-CDLP gel through the skin are shown in Figure 4C. The cumulative release of the pure drug UMB-loaded gel was 57.76 ± 0.56 % at the end of 24 hours. Meanwhile, in DL-UMB-CDLP gel, the cumulative release was 98.76 ± 0.94 % at the end of 11 hours. When comparing the optimized DL-UMB-CDLP gel to the traditional UMB-loaded gel, the drug release value after 24 hours was significantly higher ($p < 0.05$), indicating a notable improvement in release rate. The presence of phospholipid constituents, which altered the skin layer and improved drug penetration, may have contributed to the enhanced penetration of the optimized DL-UMB-CDLP gel. In contrast, this type of interaction was absent from the conventional UMB-loaded gel. The prepared optimized DL-UMB-CDLP gel was better at facilitating drug penetration and sustained release of UMB, according to this *ex vivo* study conducted for 24 hours [53].

Primary Skin Irritation Studies

This test is crucial for determining the potential of a substance to cause irritation or damage to the skin. The prepared gel formulation was found safe when its skin-irritating effect was assessed. No erythema or edema was seen in any formulation after seven days of study. Additionally, the finer gel matrix mesh of Carbopol 934P prevents droplets from penetrating into the deeper layers of the skin, reducing skin irritation.

Histopathological Analysis of the Skin for Skin Irritancy Testing

A skin irritancy test was done to check vehicle compatibility with the skin and confirm if the DL-UMB-CDLP gel formulation caused any dose toxicity. Figure 5A–5C displays the findings of the skin’s histopathological examination. In this group, 2 (G2), a plain drug-loaded gel, showed mild dermal congestion and inflammatory infiltration. In contrast, gel vehicle (G1) and the optimized gel formulation (G3) showed no histological changes in the skin. Microscopic images show that the vehicle gel base (G1) and the DL-UMB-CDLP gel (G3) are compatible with skin as they do not cause any epidermal changes in the rat skin.



Legend on the figure Bn: (DC) — Microscopy-Dermal Congestion, (DII) — Dermal Inflammatory Infiltratio

Figure 5. Photomicrographs of histological sections of the rat skin for skin irritancy testing. (A) G1 — Gel base. (B) G2 — Placebo. (C) G3 — Optimized DL-UMB-CDLP loaded gel

Assessment of the Photoprotective Capacity of the Optimized DL-UMB-CDLP Gel Against UV Exposure

Rats that underwent this procedure but did not receive UMB treatment (G2 group) exhibited oxidative damage due to the UV irradiation model we used in our study. Decreased activity of CAT, GSH, and SOD indicates depletion of the endogenous antioxidant system, and an increase in the TBARS marker, a marker that sets the lipid peroxidation index, was used to confirm oxidative damage (Figure 6). The effects on individual markers in different groups are depicted in Figure S3 of the Supplementary Materials file. CAT, GSH, and SOD activities significantly recovered in animals that were exposed to the same irradiation protocol and received immediate UV treatment following the application of DL-UMB-CDLP gel formulation. These animals also showed no signs of lipid peroxidation (low TBARS value), comparable to the outcomes of the non-irradiated control (G1) group. These findings demonstrated the UMB’s ability to protect against oxidative damage caused by UV radiation and are associated with its antioxidant activity, which has already been elucidated in previous studies [24, 54, 55].

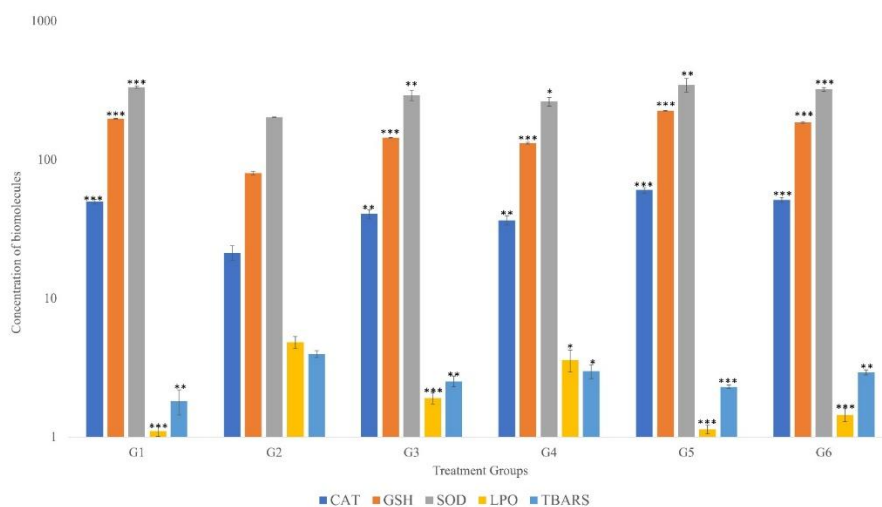
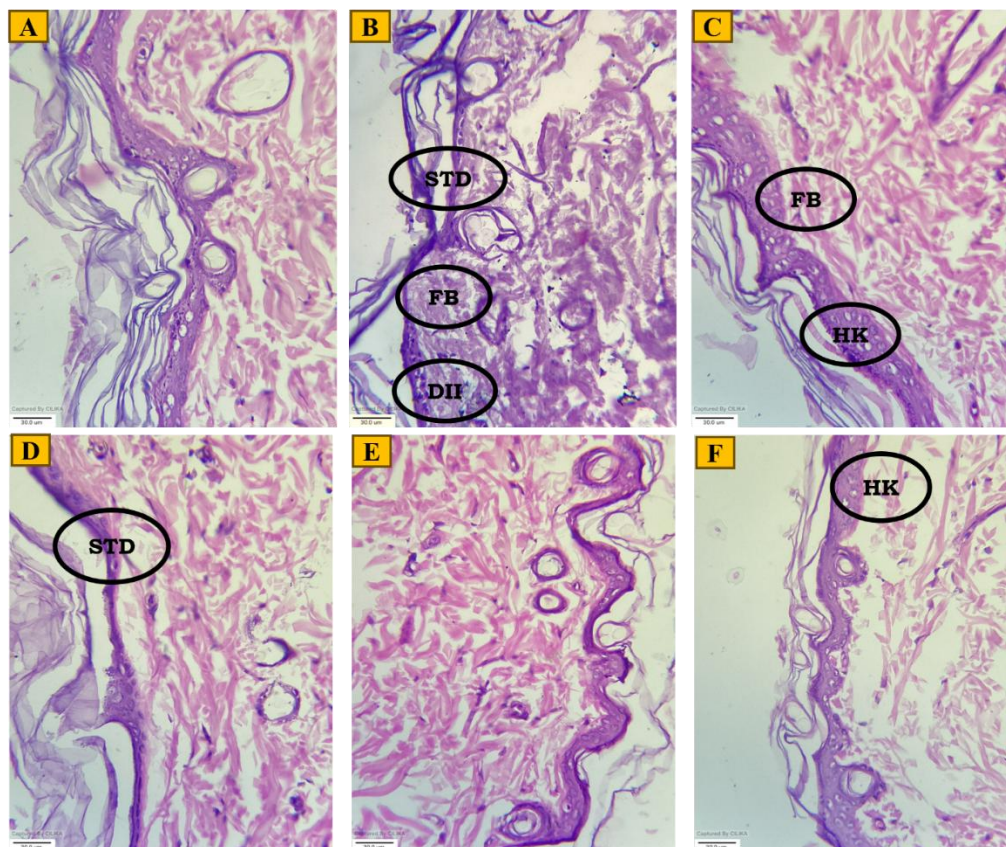


Figure 6. Effect of UV exposure on the antioxidant enzymes CAT, GSH, SOD, LPO and TBARS One-way ANOVA followed by Dunnett’s post hoc test. Data represents mean±SD. (n = 6), *p < 0.01, **p < 0.001, and. ***p < 0.0001 vs G2

Histopathological Analysis of the Skin for Photoprotective Activity

Skin histopathological analysis is important for assessing photoprotective activity because it allows researchers to determine how UV radiation and protective agents affect the cellular and structural integrity of the skin. This analysis helps determine whether a substance or product can reduce or prevent the harmful effects of UV radiation on the skin. The microscopic images are shown in Figure 7. The histopathological analysis of the skin in the UV irradiated control group (G2) showed mild dermal congestion, stratum corneum degeneration, fibrosis and dermal inflammatory infiltration. Fibrosis and hyperkeratosis were observed in the UMB 1 gel group (G3), whereas the UMB 2 gel group (G4) showed stratum corneum degeneration. This study indicates that the vehicle gel base is compatible with the skin, and the DL-UMB-CDLP gel (with immediate UV exposure) did not cause any epidermal changes in the rat skin compared to the UV-irradiated control group [14].



Legend on the microscopy figures: (DC) Dermal Congestion, (DII) Dermal inflammatory infiltration, (STD) Stratum corneum degeneration, (FB) Fibrosis, (HK) Hyperkeratosis

Figure 7. Photomicrographs of histological sections of the rat skin for photoprotective activity: (A) G1- Gel base; (B) G2- UV Irradiated control; (C) G3- UMB 1 gel; (D) G4- UMB 2 gel; (E) G5- DL-UMB-CDLP 1 gel; (F) G6- DL-UMB-CDLP 2 gel

Conclusions

The current work is a novel way to improve UMB's poor bioavailability and low aqueous solubility by complexing it with β -CD and then delivering the drug via liposomal delivery (DL-UMB-CDLP). The UMB- β -CD complex was successfully encapsulated in double-loaded liposomes using the thin-film hydration technique, PL90H, and cholesterol. The impact of independent variables on entrapment efficiency and particle size was examined using the 3^3 full factorial design. The research findings suggest that the DL-UMB-CDLP may be helpful for the sustained release of UMB, a poorly soluble drug. Additionally, it was concluded that the formulation may increase UMB's solubility and prolong its release for improved therapeutic efficacy. In conclusion, the optimized formulation DL-UMB-CDLP loaded gel presented physicochemical characteristics suitable for topical application and shielded the animal's skin from UVA and UVB radiation damage.

UMB's antioxidant and anti-inflammatory qualities and capacity to absorb UV radiation may be linked to the photoprotective effect.

Supporting Information

The Supporting Information is available free at <https://ejc.buketov.edu.kz/index.php/ejc/article/view/341/227>

Author Information*

*The authors' names are presented in the following order: First Name, Middle Name and Last Name

Rucheera Raju Verekar — PhD, Research Scholar, Goa College of Pharmacy, Goa University, 403001, Panaji, Goa, India; e-mail: rucheeraverekar@gmail.com; <https://orcid.org/0000-0003-0197-3325>

Shamshad Bi Mainoddin Shaikh — Assistant Professor, Zoology Discipline, School of Biological Sciences and Biotechnology, Goa University, 403206, Taleigao Plateau Goa, India; e-mail: shamshad.shaikh@unigoa.ac.in; <https://orcid.org/0000-0001-8907-1398>

Sarita Rebelo — PhD, Research Scholar, Zoology Discipline, School of Biological Sciences and Biotechnology, Goa University, 403206, Taleigao Plateau Goa, India; e-mail: zoology.sarita@unigoa.ac.in; <https://orcid.org/0009-0008-1443-4383>

Shailendra Shivaji Gurav (*corresponding author*) — Professor, Department of Pharmacognosy and Phytochemistry, Goa College of Pharmacy, Goa University, 403001, Panaji, Goa, India; e-mail: shailendra.gurav@nic.in; <https://orcid.org/0000-0001-5564-2121>

Author Contributions

The manuscript was written through contributions of all authors. All authors have given approval to the final version of the manuscript. **CRedit: Rucheera Raju Verekar:** Writing — Original draft preparation, Methodology, Software Data analysis; Resources; **Shamshad Bi Mainoddin Shaikh and Sarita Rebelo:** Writing — Review and editing, Methodology, Software Data analysis; Resources; **Shailendra Shivaji Gurav:** Conceptualisation, Methodology, Supervision, Investigation, Project Administration.

Acknowledgement

Authors are grateful to Dr. Madhusudan Joshi (Professor and Head of Pharmacology Department), of Goa College of Pharmacy, Government of Goa; Dr. S.C. Ghadi (Sr. Professor) and Dr. Nitin Sawant (Asst. Professor) of School of Biological Sciences and Biotechnology, Goa University, for providing the facilities to perform the research activities pertaining to animal studies.

Ethics approval and consent to participate

Animal experimentation procedures were followed per CPCSEA guidelines.

Conflicts of interest

The authors declare no conflict of interest.

References

- 1 Usapkar, P., Saoji, S., Jagtap, P., Ayyanar, M., Kalaskar, M., Gurav, N., & Gurav, S. (2024). QbD-guided phospholipid-tagged nanonized boswellic acid naturesomal delivery for effective rheumatoid arthritis treatment. *Int J Pharmaceutics*, *X*, 7, Art. 100257. <https://doi.org/10.1016/j.ijpx.2024.100257>
- 2 Fernández-Romero, A.M., Maestrelli, F., Mura, P.A., Rabasco, A.M., & González-Rodríguez, M.L. (2018). Novel findings about double-loaded Curcumin-in-HP β cyclodextrin-in liposomes: Effects on the lipid bilayer and drug release. *Pharmaceutics*, *10*(4), 256. <https://doi.org/10.3390/pharmaceutics10040256>
- 3 Schnyder, A. & Huwyler, J. (2005). Drug transport to brain with targeted liposomes. *NeuroRX: The Journal of the American Society for Experimental Neurotherapeutics*, *2*(1), 99–107. <https://doi.org/10.1602/neurorx.2.1.99>
- 4 Brandl, M. (2001). Liposomes as drug carriers: a technological approach. *Biotechnology Annual Review*, *7*, 59–85. [https://doi.org/10.1016/s1387-2656\(01\)07033-8](https://doi.org/10.1016/s1387-2656(01)07033-8)
- 5 Jhan, S. & Pethe, A.M. (2020). Double-loaded liposomes encapsulating lycopene β -cyclodextrin complexes: preparation, optimization, and evaluation. *J Liposome Res*, *30*(1), 80–92. <https://doi.org/10.1080/08982104.2019.1593450>

- 6 Mccormack, B. & Gregoriadis, G. (1994). Drugs-in-cyclodextrins-in liposomes: a novel concept in drug delivery. *International Journal of Pharmaceutics*, 112, 249–258. [https://doi.org/10.1016/0378-5173\(94\)90361-1](https://doi.org/10.1016/0378-5173(94)90361-1)
- 7 Gregoriadis, G. & Florence, A.T. (1993). Liposomes in drug delivery. Clinical, diagnostic and ophthalmic potential. *Drugs*, 45(1), 15–28. <https://doi.org/10.2165/00003495-199345010-00003>
- 8 Bhatt, P., Lalani, R., Vhora, I., Patil, S., Amrutiya, J., Misra, A., & Mashru, R. (2018). Liposomes encapsulating native and cyclodextrin enclosed paclitaxel: Enhanced loading efficiency and its pharmacokinetic evaluation. *International journal of pharmaceutics*, 536(1), 95–107. <https://doi.org/10.1016/j.ijpharm.2017.11.048>
- 9 Azzi, J., Jraij, A., Auezova, L., Fourmentin, S., & Greige-Gerges, H. (2018). Novel findings for quercetin encapsulation and preservation with cyclodextrins, liposomes, and drug-in-cyclodextrin-in-liposomes. *Food Hydrocolloids*, 81, 328–340. <https://doi.org/10.1016/j.foodhyd.2018.03.006>
- 10 Baccarin, T., Mitjans, M., Ramos, D., Lemos-Senna, E., & Vinardell, M.P. (2015). Photoprotection by Punica granatum seed oil nanoemulsion entrapping polyphenol-rich ethyl acetate fraction against UVB-induced DNA damage in human keratinocyte (Ha-CaT) cell line. *J Photochem Photobiol B*, 153, 127–136. <https://doi.org/10.1016/j.jphotobiol.2015.09.005>
- 11 Türker, H. (2015). The effect of ultraviolet radiation of pancreatic exocrine cells in mole rats: An ultrastructural study. *J Radiat Res Appl Sci*, 8(1), 49–54. <http://dx.doi.org/10.1016/j.jrras.2014.10.006>
- 12 Batista, C.M., Alves, A.V.F., Queiroz, L.A., Lima, B.S., Filho, R.N.P., Araújo, A.A.S., de Albuquerque Júnior, R.L.C., & Cardoso, J.C. (2018). The photoprotective and anti-inflammatory activity of red propolis extract in rats. *J Photochem Photobiol B*, 180, 198–207. <https://doi.org/10.1016/j.jphotobiol.2018.01.028>
- 13 Gu, Y., Han, J., Jiang, C., & Zhang, Y. (2020). Biomarkers, oxidative stress and autophagy in skin aging. *Ageing Research Reviews*, 59, Art. 101036. <https://doi.org/10.1016/j.arr.2020.101036>
- 14 Serafini, M.R., Detoni, C.B., Menezes, P.D.P., Pereira Filho, R.N., Fortes, V.S., Vieira, M.J.F., Guterres, S.S., Cavalcanti de Albuquerque Junior, R.L., & Araujo, A.A.S. (2014). UVA-UVB photoprotective activity of topical formulations containing morinda citrifolia extract. *Biomed Res Int*, Art. 587819. <http://dx.doi.org/10.1155/2014/587819>
- 15 Nobile, V., Michelotti, A., Cestone, E., Caturla, N., Castillo, J.O., Benavente-García, Pérez-Sánchez, A., & Micol, V. (2016). Skin photoprotective and antiageing effects of a combination of rosemary (*Rosmarinus officinalis*) and grapefruit (*Citrus paradisi*) polyphenols. *Food Nutr Res*, 60. <http://dx.doi.org/10.3402/fnr.v60.31871>
- 16 Liu, X., Zhang, R., Shi, H., Li, X., Li, Y., Taha, A., & Xu, C. (2018). Protective effect of curcumin against ultraviolet A irradiation-induced photoaging in human dermal fibroblasts. *Mol Med Rep*, 17(5), 7227–7237. <https://doi.org/10.3892/mmr.2018.8791>
- 17 Zhou, Y., Yang, W., Li, Z., Luo, D., Li, W., Zhang, Y., Wang, X., Fang, M., Chen, Q., & Jin, X. (2018). Moringa oleifera stem extract protect skin keratinocytes against oxidative stress injury by enhancement of antioxidant defense systems and activation of PPARα. *Biomedicine and Pharmacotherapy*, 107, 44–53. <https://doi.org/10.1016/j.biopha.2018.07.152>
- 18 Cho, B.O., Che, D.N., Shin, J.Y., Kang, H.J., Kim, J.H., Kim, H.Y., Cho, W.G., & Jang, S.I. (2017). Ameliorative effects of Diospyros lotus leaf extract against UVB-induced skin damage in BALB/c mice. *Biomedicine and Pharmacotherapy*, 95, 264–274. <http://dx.doi.org/10.1016/j.biopha.2017.07.159>
- 19 Nery, E.M., Martinez, R.M., Velasco, M.V.R., & Baby, A.R. (2020). A short review of alternative ingredients and technologies of inorganic UV filters. *J Cosmet Dermatol*, 00, 1–5. <https://doi.org/10.1111/jocd.13694>
- 20 Schneider, S.L. & Lim, H.W. (2019). A review of inorganic UV filters zinc oxide and titanium dioxide. *Photodermatol Photoimmunol Photomed*, 35, 442–446. <https://doi.org/10.1111/phpp.12439>
- 21 Schneider, S.L. & Lim, H.W. (2019). Review of environmental effects of oxybenzone and other sunscreen active ingredients. *J Am Acad Dermatol*, 80(1), 266–271. <https://doi.org/10.1016/j.jaad.2018.06.033>
- 22 Narla, S. & Lim, H.W. (2020). Sunscreen: FDA regulation, and environmental and health impact. *Photochem Photobiol Sci*, 19, 66–70. <https://doi.org/10.1039/C9PP00366E>
- 23 Kullavanijaya, P. & Lim, H.W. (2005). Photoprotection. *J Am Acad Dermatol*, 52(6), 937–958. <https://doi.org/10.1016/j.jaad.2004.07.063>
- 24 de Araújo, A.T., Heimfarth, L., dos Santos, D.M., dos Santos, M.R.V., de Albuquerque-Júnior, R.L.C., dos Santos-Neto, A.G., de Araujo, G.R.S., Lira, A.A.M., Matos, S.S., Frank, L.A., Rabelo, T.K., Quintans-Júnior, L.J., de Souza Siqueira Quintans, J., de Souza Araujo, A.A., & Serafini, M.R. (2022). Hesperetin-based hydrogels protect the skin against uv radiation-induced damage. *AAPS PharmSciTech*, 23(6), 170. <https://doi.org/10.1208/s12249-022-02323-8>
- 25 Ittadwar, P.A. & Puranik, P.K. (2016). Novel umbelliferone phytosomes: development and optimization using experimental design approach and evaluation of photoprotective and antioxidant activity. *Int J Pharm Pharm Sci*, 9(1), 218–228. <http://dx.doi.org/10.22159/ijpps.2017v9i1.14635>
- 26 Bhargava, S. & Agrawal, G.P. (2008). Preparation & characterization of solid inclusion complex of cefpodoxime proxetil with beta-cyclodextrin. *Current Drug Delivery*, 5(1), 01–06. <http://dx.doi.org/10.2174/156720108783330998>
- 27 Cid-Samamed, A., Rakmai, J., Mejuto, J.C., Simal-Gandara, J., & Astray, G. (2022). Cyclodextrins inclusion complex: Preparation methods, analytical techniques and food industry applications. *Food Chemistry*, 384, Art. 132467. <https://doi.org/10.1016/j.foodchem.2022.132467>
- 28 Darekar, T., Aithal, K.S., Shirodkar, R., Kumar, L., Attari, Z., & Lewis, S. (2016). Characterization and *in-vivo* evaluation of lacidipine inclusion complexes with β-cyclodextrin and its derivatives. *J Incl Phenom Macrocycl Chem*, 84, 225–235. <https://doi.org/10.1007/s10847-016-0600-9>

- 29 Tan, Q., Liu, S., Chen, X., Wu, M., Wang, H., Yin, H., He, D., Xiong, H., & Zhang, J. (2012). Design and evaluation of a novel evodiamine-phospholipid complex for improved oral bioavailability. *AAPS PharmSciTech*, 13(2), 534–547. <https://doi.org/10.1208/s12249-012-9772-9>
- 30 Bhattacharyya, S., Majhi, S., Saha, B.P., & Mukherjee, P.K. (2014). Chlorogenic acid-phospholipid complex improve protection against UVA induced oxidative stress. *J Photochem Photobiol B*, 130, 293–298. <http://dx.doi.org/10.1016/j.jphotobiol.2013.11.020>
- 31 Gurav, S., Usapkar, P., Gurav, N., Nadaf, S., Ayyanar, M., Verekar, R., & Chikhale, R. (2022). Preparation, characterization, and evaluation (in-vitro, ex-vivo, and in-vivo) of naturosomal nanocarriers for enhanced delivery and therapeutic efficacy of hesperetin. *Plos one*, 17(11), e0274916. <https://doi.org/10.1371/journal.pone.0274916>
- 32 Sapana, B.B. & Shashikant, D.N. (2015). Preparation and characterisation of β -cyclodextrin nebulolol inclusion complex. *Int J Pharm Sci Res*, 6(5), 2205. <http://dx.doi.org/10.13040/IJPSR.0975-8232.6>
- 33 Yue, P.F., Yuan, H.L., Li, X.Y., Yang, M., & Zhu, W.F. (2010). Process optimization, characterization and evaluation *in-vivo* of oxymatrine-phospholipid complex. *Int J Pharm*, 387(1–2), 139–146. <https://doi.org/10.1016/j.ijpharm.2009.12.008>
- 34 Soni, G. & Yadav, K.S. (2014). High encapsulation efficiency of poloxamer-based injectable thermoresponsive hydrogels of etoposide. *Pharm Dev Technol*, 19(6), 651–661. <https://doi.org/10.3109/10837450.2013.819014>
- 35 Galiyeva, A.R., Tazhbayev, Ye.M., Zhumagaliyeva, T.S., Sadyrbekov, D.T., Kaikenov, D.A., Karimova, B.N., & Shokenova, S.S. (2022). Polylactide-co-glycolide nanoparticles immobilized with isoniazid: Optimization using the experimental Taguchi method. *Bulletin of the University of Karaganda — Chemistry*, 105(1), 69–77. <https://doi.org/10.31489/2022Ch1/69-77>
- 36 Saoji, S.D., Rarokar, N.R., Dhore, P.W., Dube, S.O., Gurav, N.S., Gurav, S.S., & Raut, N.A. (2022). Phospholipid based colloidal nanocarriers for enhanced solubility and therapeutic efficacy of withanolides. *J Drug Deliv Sci Technol*, 70, 103251. <https://doi.org/10.1016/j.jddst.2022.103251>
- 37 Metkari, V., Shah, R., Salunkhe, N., & Gurav, S. (2023). QBD approach for the design, optimization, development, and characterization of Naringenin-loaded phytosomes to enhance solubility and oral bioavailability. *J Pharm Innovation*, 18(4), 2083–2097. <https://doi.org/10.1007/s12247-023-09775-w>
- 38 Gracias, S., Ayyanar, M., Peramaiyan, G., Kalaskar, M., Redasani, V., Gurav, N., & Gurav, S. (2023). Fabrication of chitosan nanocomposites loaded with biosynthetic metallic nanoparticles and their therapeutic investigation. *Environ Res*, 234, 116609. <https://doi.org/10.1016/j.envres.2023.116609>
- 39 Rodrigues, K., Nadaf, S., Rarokar, N., Gurav, N., Jagtap, P., Mali, P., Ayyanar, M., Kalaskar, M., & Gurav, S. (2022). QBD approach for the development of hesperetin loaded colloidal nanospheres for sustained delivery: *In-vitro*, *ex-vivo*, and *in-vivo* assessment. *OpenNano*, 7. <https://doi.org/10.1016/j.onano.2022.100045>
- 40 Aiyalu, R., Govindarjan, A., & Ramasamy, A. (2016). Formulation and evaluation of topical herbal gel for the treatment of arthritis in animal model. *Brazilian Journal of Pharmaceutical Sciences*, 52(3), 493–507. <http://dx.doi.org/10.1590/S1984-82502016000300015>
- 41 Chen, M.X., Alexander, K.S., & Baki, G. (2016). Formulation and evaluation of antibacterial creams and gels containing metal ions for topical application. *J Pharm*, 1–10. <http://dx.doi.org/10.1155/2016/5754349>
- 42 Opatha, S.A.T., Titapiwatanakun, V., Boonpisutiinant, K., & Chutoprapat, R. (2022). Preparation, characterization and permeation study of topical gel loaded with transfersomes containing asiatic acid. *Molecules*, 27(15), 4865. <https://doi.org/10.3390/molecules27154865>
- 43 Wasankar, S., Wasankar, S.R., Faizi, S.M., & Deshmuk, A.D. (2012). Formulation and development of liposomal gel for topical drug delivery system. *IJPSR*, 3(11), 4461–4470. [http://dx.doi.org/10.13040/IJPSR.0975-8232.3\(11\).4461-70](http://dx.doi.org/10.13040/IJPSR.0975-8232.3(11).4461-70)
- 44 Wayal, S.R. & Gurav, S.S. (2021). Evaluation of wound healing potential of Bhallatakadi Ghrita — Cow ghee based polyherbal formulation: *In-vivo* excision and incision wound model. *J Complement Integr Med*, 18(3), 507–515. <https://doi.org/10.1515/jcim-2020-0179>
- 45 James, O. (2014). Evaluation of acute dermal irritation and wound contraction by *Gymnema Sylvestre* and *Datura Metel* extracts in rats. *American Journal of Biomedical and Life Sciences*, 2(4), 83–88. <https://doi.org/10.11648/j.ajbls.20140204.14>
- 46 Verekar, R.R., Gurav, S.S., & Bolmal, U. (2020). Thermosensitive mucoadhesive in situ gel for intranasal delivery of Almotriptan malate: Formulation, characterization, and evaluation. *J Drug Deliv Sci Technol*, 58. <https://doi.org/10.1016/j.jddst.2020.101778>
- 47 Dua, K., Pabreja, K., Ramana, M.V., & Lather, V. (2011). Dissolution behavior of β -cyclodextrin molecular inclusion complexes of aceclofenac. *J Pharm Bioallied Sci*, 3(3), 417–425. <https://doi.org/10.4103/0975-7406.84457>
- 48 Yessentayeva, N.A., Galiyeva, A.R., Daribay, A.T., Sadyrbekov, D.T., Moustafine, R.I., & Tazhbayev, Y.M. (2024). Optimization of polylactide-co-glycolide-rifampicin nanoparticle synthesis, *in vitro* study of mucoadhesion and drug release. *Polymers*, 2024, 16, Art. 2466. <https://doi.org/10.3390/polym16172466>
- 49 Meister, A. & Blume, A. (2017). (Cryo) Transmission electron microscopy of phospholipid model membranes interacting with amphiphilic and polyphilic molecules. *Polymers*, 9, 521. <https://doi.org/10.3390/polym9100521>
- 50 Thippeswamy, B.S., Thakker, S.P., Tubachi, S., Kalyani, G.A., Netra, M.K., Patil, U., Desai, S., Gavimath, C.C., & Veerapur, V.P. (2009). Cardioprotective effect of cucumis trigonus roxb on isoproterenol-induced myocardial infarction in rat. *Am J Pharmacol Toxicol*, 4(2), 29–37. <http://dx.doi.org/10.3844/ajptsp.2009.29.37>
- 51 Mishra, R.K. & Singhal, G.S. (1990). Calcium and magnesium induced changes in the relative fluidity of phosphatidylcholine liposomes. *J Biosci*, 15(3), 193–197. <https://doi.org/10.1007/BF02703884>

- 52 Tazhbayev, Ye.M., Galiyeva, A.R., Zhumagaliyeva, T.S., Burkeyev, M.Zh., Kazhuratova, A.T., Zhakupbekova, E.Zh., Zhaparova, L.Zh. & Bakibayev, A.A. (2021). Synthesis and characterization of isoniazid immobilized polylactide-co-glycolide nanoparticles. *Bulletin of the University of Karaganda — Chemistry*, 101(1), 61–70. <https://doi.org/10.31489/2021Ch1/61-70>
- 53 Shah, N. & Patel, K. (2023). Formulation, development and characterization of liposome-based gel of eberconazole nitrate for topical delivery. *Int J Pharm Investig*, 13(3), 485–495. <https://doi.org/10.5530/ijpi.13.3.060>
- 54 Bodduluru, L.N., Kasala, E.R., Barua, C.C., Karnam, K.C., Dahiya, V., & Ellutla, M. (2015). Antiproliferative and antioxidant potential of hesperetin against benzo(a)pyrene-induced lung carcinogenesis in Swiss albino mice. *Chem Biol Interact*, 242, 345–352. <http://dx.doi.org/10.1016/j.cbi.2015.10.020>
- 55 Wang, J., Zhu, H., Yang, Z., & Liu, Z. (2013). Antioxidative effects of hesperetin against lead acetate-induced oxidative stress in rats. *Indian J Pharmacol*, 45(4), 395–398. <https://doi.org/10.4103/0253-7613.115015>

PHYSICAL AND ANALYTICAL CHEMISTRY

Article

Received: 23 February 2025 | Revised: 15 May 2025 |
Accepted: 22 May 2025 | Published online: 28 May 2025

UDC 541.057.17

<https://doi.org/10.31489/2959-0663/2-25-9>

Gulsym K. Burkeyeva¹ , Anna K. Kovaleva^{2*} , Danagul M. Muslimova¹ ,
David Havlicek³ , Nurken M. Zhumabek¹ , Nurlan A. Nukin¹ 

¹Department of Organic Chemistry and Polymers, Karaganda Buketov University, Karaganda, Kazakhstan;

²Research Institute of Chemical Problems, Karaganda Buketov University, Karaganda, Kazakhstan;

³Charles University, Prague, Czech Republic

(*Corresponding author's e-mail: cherry-girl1899@mail.ru)

Investigation of Physical and Chemical Properties of Thermosetting Copolymers of Polyethylene Glycol Maleate with Acrylic Acid During their “Cold” Curing

The paper presents information on the study of physical and chemical properties of solutions of polyethylene glycol maleate in acrylic acid and products of their “cold” curing. The weight-average molecular weight of the initial polyethylene glycol maleate was established using the GPC method. The value of the degree of unsaturation of both the initial unsaturated polyester and copolymers based on it was determined using the bromide-bromate method. The dynamic viscosity of the polymer-monomer mixture of polyester and acrylic acid was established using viscometry. The density of the stock solutions was analyzed using the pycnometric method and the density of the cured products was determined using the hydrostatic method. The total volume shrinkage of the copolymers was calculated from the obtained density values. The composition of the copolymers was analyzed/studied with the help of HPLC. The degree of swelling of the cured products was also calculated by gravimetric method, and their identification was carried out using IR- and ¹H NMR-spectroscopy. The surface topography of cured copolymers was investigated by SEM. The results obtained indicate to the possibility of controlling the properties of cured unsaturated polyester by varying the initial composition of polymer-monomer mixture depending on its purpose and obtaining on its basis the polymer matrix for the manufacture of bulk products with good physical and chemical properties.

Keywords: unsaturated polyester, “cold” curing, density, viscosity, total volumetric shrinkage, hydrophobicity, thermosetting polymers, bulk products

Introduction

Nowadays, thermosetting polyester binders are widely used in various industrial fields due to their good performance properties, including stability and resistance to negative external influences [1–3]. In particular, in the automotive industry the thermosetting polyester binders are used for the production of high-strength composites and coatings, as well as in the production of adhesive compositions that provide strong and durable bonding of various materials [4]. In the aerospace industry, they are used to create lightweight and strong structural materials that must withstand extreme operating conditions such as high temperatures and strong mechanical loads [5, 6].

In addition, thermosetting polyester binders play an important role in the production of construction materials [7, 8]. They are used as polymer binders for bulk products such as concretes [9–11] and construction mixtures to improve their strength properties as well as increase their resistance to environmental influences [12, 13]. Polyester binders are also actively used for the production of modern high-quality insulation materials, which are used in the construction and electrical industries for protection against high temperatures and corrosion [14, 15].

One of the important directions in the development of thermosetting polyester binders is the creation of polymers with unique combinations of properties that can be adapted to specific technological processes. This is achieved by introducing various additives and fillers into the polymer structure, which make it possible to adjust its mechanical, thermal and chemical properties depending on the requirements of the final product. In particular, the addition of minerals, carbon fibers or other materials can significantly increase the strength and resistance of polymers to the negative effects of the external environment [16–18].

Thermosetting polyester binders themselves contain unsaturated bonds in their structure, which provide reactivity and polymerization ability [19]. As a result of the crosslinking reaction, a three-dimensional mesh structure is formed, which significantly increases the mechanical and thermal characteristics of the material and contributes to increasing their resistance to aggressive chemical media. The structure of unsaturated polyesters, consisting of repeating units, allows modifying the properties of polymers by changing the ratio of the monomers and using different curing methods. This opens up opportunities for the creation of the materials with specified characteristics, which is especially important in the context of modern requirements to materials.

The modification of thermosetting polyester materials for improving their properties is great importance. Modern developments in the field of thermosetting binders are aimed at creating polymers with improved resistance to ultraviolet radiation, increased mechanical strength and improved adhesion to various surfaces. This makes it possible to expand the field of application of the materials based on thermosetting polyester binders in such innovative industries as the production of electronic components, biomaterials, and nanocomposites [4, 7, 13, 14].

To date, the most studied are the curing reactions of unsaturated polyesters with styrene [20] and methyl methacrylate to obtain rigid polymeric materials with good performance properties [21]. However, there is no information in literature on the use of unsaturated carboxylic acids as a solvent-curing agent in the curing of polyester binders in order to obtain the filler products based on them.

In our previously published article, we investigated the properties of polyethylene(propylene)glycol-fumarate curing products to determine the possibility of using them as a polymer matrix of hermetic materials [22, 23]. This paper presents data on the study of physicochemical properties of both initial solutions of polyethylene glycol maleate (p-EGM) in acrylic acid (AA) and cured products based on them. The presented studies will allow us to evaluate the suitability of this binary system of p-EGM–AA as thermosetting polyester binders for the production of filler products with minimal inclusion of mineral additives.

Experimental

The following reagents (“Sigma-Aldrich”) were used in this study:

- ethylene glycol and maleic anhydride (co-reagents for the synthesis of initial p-EGM), and zinc chloride (catalyst for the polycondensation reaction) in the first step;
- in the second step, acrylic acid was used as a solvent to prepare solutions of p-EGM in unsaturated carboxylic acid;
- “cold” curing of the above solutions was carried out in the presence of an initiating system consisting of benzene peroxide (BP, initiator) and dimethylaniline (DMA, activator). Dioxane was used as a solvent. All reagents used were purchased from “Sigma-Aldrich”. The purity of the reagents used was 99.95 %, therefore they were used without additional purification.

The initial unsaturated polyester — polyethylene glycol maleate — was obtained by polycondensation of ethylene glycol (dioatomic alcohol) and maleic anhydride (dicarbonic anhydride) with a small excess of the first co-reagent. Zinc chloride was used as a catalyst, which allowed the process to be carried out at a reduced temperature 150–160 °C. The reaction flow was monitored by determining the acid number until the value of 30–40 units was reached, as well as measuring the volume of water released as a result of polycondensation [20]. The molecular weight of the synthesized p-EGM was determined using GPC on a VISCOTEK 270 DUAL DETECTOR MALVERN. The studies were carried out using dust-free dioxane. The measured molecular weight was approximately 1232 Da (M_w). The polyester yield was 98 %.

The degree of unsaturation of the synthesized p-EGM was determined by bromide-bromate method, which was 89 % [20].

Further, solutions of p-EGM in acrylic acid (AA) of different mass composition were prepared: ~60:40 mass.%, ~70:30 mass.%, ~80:20 mass.%, respectively. After preparation of the solutions, their dynamic viscosity at 293 K was determined. The studies were carried out on a vibrating viscometer SV-10. Additionally, the viscometer is equipped with a VT3 liquid thermostat, which allows to maintain the temperature set dur-

ing the experiment. The density of these solutions (ISO 1675:1985 (GOST 18329-2014)) was determined using a pycnometer.

Further, curing was carried out at 293 K in the analyzed solutions after introducing an optimized “cold” curing initiating system (1.0 % : 0.15 % of the polymer-monomer mixture mass) [23]. The obtained p-EGM-AA copolymers were washed with dioxane in order to get rid of the residues of unreacted mixture. The obtained mother liquors were examined by HPLC, from which the actual compositions of the synthesized copolymers were calculated. The yield of the copolymers was also determined gravimetrically [20].

Identification of the curing products was carried out using IR and NMR spectroscopy, in particular to determine the presence of functional groups. The degree of unsaturation of the analyzed copolymers was also determined by bromide-bromate method. For IR study, potassium bromide tablets were fabricated and analyzed on an FSM 1201 spectrometer. NMR analysis was carried out on a DX-90M instrument [21].

The total volumetric shrinkage of the copolymers was calculated on the basis of the obtained values of densities of solutions and cured products, respectively [23].

The surface topography of the cured polymers was studied by SEM on a MIRA 3 high-performance microscope (TESCAN) with a 5.0 kV high-voltage (HV) detector. The SE detector was used to acquire images at 57.6-57.7 kx magnification with composite contrast, which allows imaging with very detailed object structure at the nanometer level. The field of view was 6.00 nm and the image resolution was 1024×1024 pixels [22].

The hydrophobicity of cured products was established by gravimetric method. Studies of the degree of swelling were carried out by keeping a sample (~0.3 g) of the test samples in water (T = 20 °C, pH 7) for 24 hours. The calculation was carried out according to the formula:

$$\alpha = \frac{m - m_0}{m_0} \cdot 100\%$$

where m — the mass of the swollen sample, g; m_0 — mass of dry sample, g.

Results and Discussion

Bulk-type polymer products are becoming increasingly in demand as they are characterized by their versatility and good performance advantages, allowing them to be used in various fields of industries. They are actively used in various spheres, including construction industry, automotive and shipbuilding, electronic industry, consumer products and other industries.

One of the main reasons for their popularity is the possibility of manufacturing the polymer bulk materials on their basis. At the same time, the casting method allows to observe strict parameters when manufacturing such products of non-standard or complex geometry. One of the most promising compounds for the production of bulk goods are the unsaturated polyesters of various compositions, the curing of which in the presence of an initiating system of optimized composition allows to make the process of production of the final product economically profitable. For this purpose, we synthesized an initial unsaturated polyester — polyethylene glycol maleate — by polycondensation reaction. Figure 1 schematically represents the reaction of synthesis:

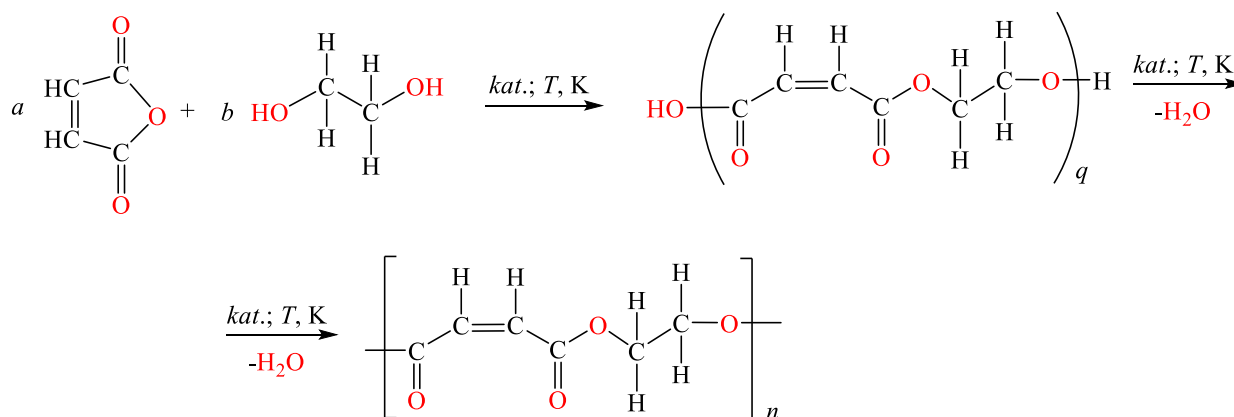


Figure 1. Polyethylene glycol maleate link formation

Solutions of p-EGM with AA of different concentrations were prepared and their density and viscosity were determined. The results obtained are presented in Table 1.

Table 1

Physical and chemical properties of stock solutions of p-EGM (M_1) with AA (M_2), $T = 293\text{K}$

Composition of prepared solution, mass.%		Dynamic viscosity value (η), mPa·s	Solution density value (ρ), g/cm ³
M_1	M_2		
58.48	41.52	294.3±0.1	1.2069±0.060
70.22	29.78	576.5±0.2	1.2202±0.061
79.51	20.49	736.8±0.3	1.2412±0.061

Analyzing the data in Table 1, a good correlation between the content of unsaturated polyester in solution and the values of their dynamic viscosity and density is observed. In particular, at the minimum content of p-EGM (~60 mass.%) in the solution, the minimum values of its dynamic viscosity (294.3 mPa·s) and density (1.2069 g/cm³) are observed. On the contrary, the maximum content of unsaturated polyester (~80 mass.%) corresponds to the maximum value of dynamic viscosity (736.8 mPa·s) and density (1.2412 g/cm³), which is a consequence of high viscosity characteristics of p-EGM. As a result, with increasing p-EGM content in the solution, an increase in such parameters as viscosity and density of this solution is observed.

Figure 2 graphically shows the relationship between the dynamic viscosity and density of these solutions in dependence on the p-EGM content in them.

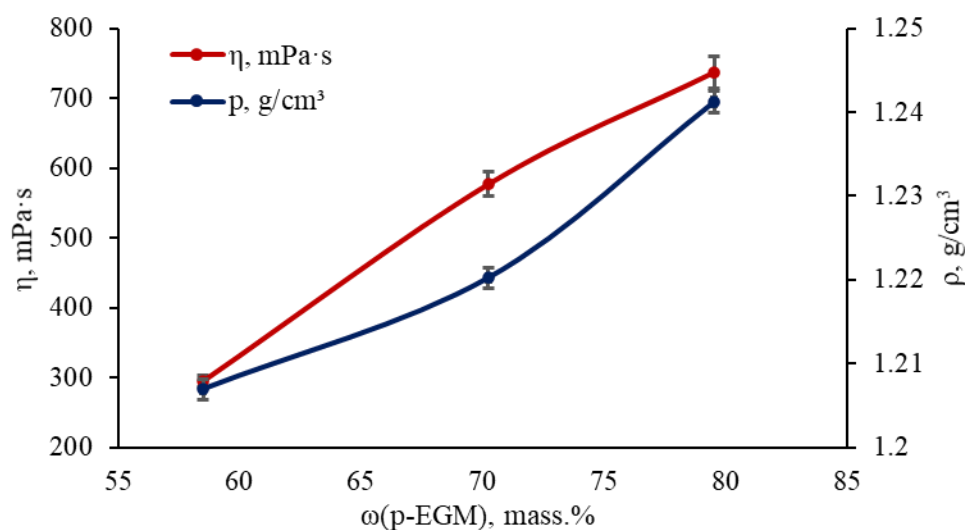
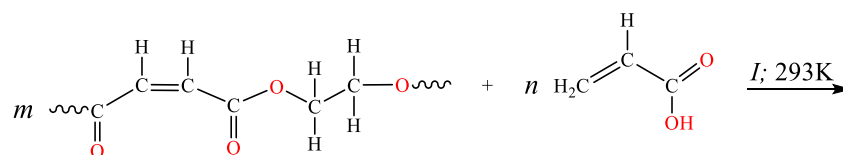


Figure 2. Dependence of dynamic viscosity and density of initial solutions of p-EGM-AA on the content of p-EGM in them

“Cold” curing of the synthesized polyethylene glycol maleate with acrylic acid was carried out in the presence of an initiating system consisting of benzoyl peroxide (initiator) and dimethylaniline (activator). The reaction was carried out at a temperature of 293 K. Schematically, the radical copolymerization reaction is presented in Figure 3.



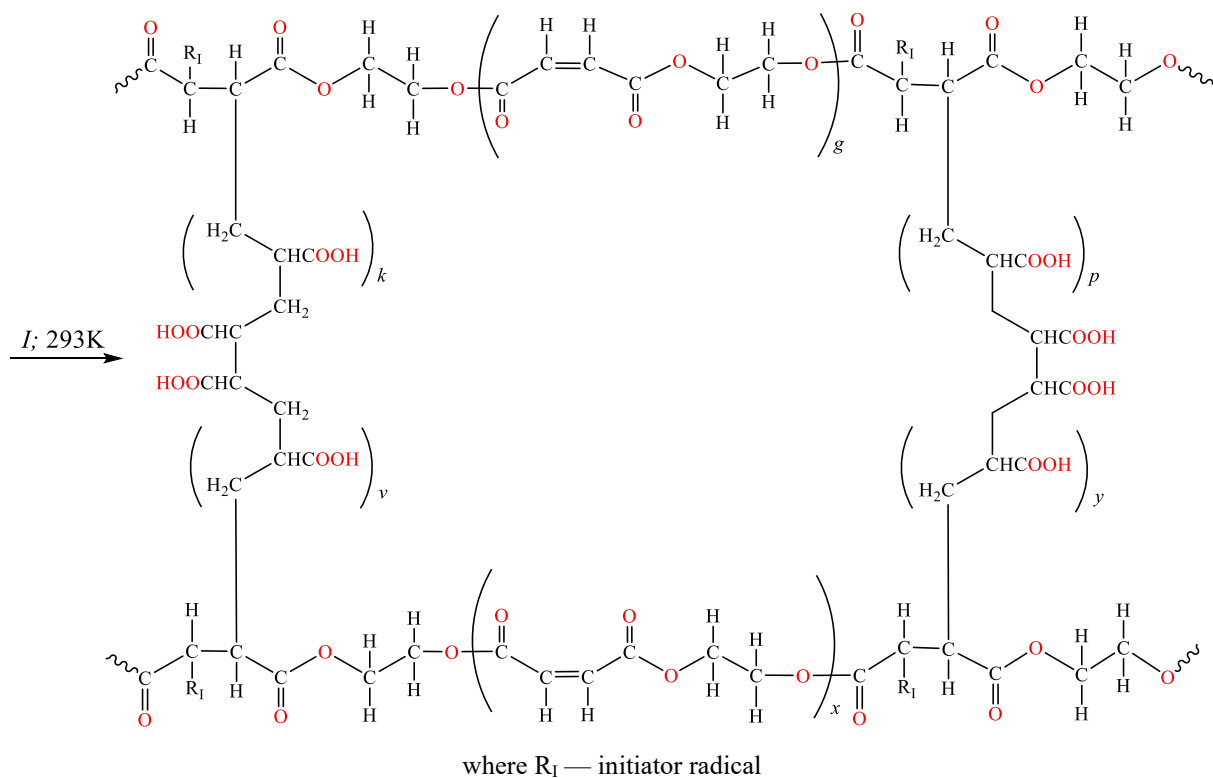


Figure 3. Copolymer structural fragments of the p-EGM-AA

Insoluble net polymers were obtained as a result of the reaction. The obtained solutions in dioxane were analyzed by HPLC, which allowed to establish the true composition of the obtained copolymers. The results of HPLC-analysis are presented in Table 2:

Table 2

**Dependence of copolymer composition and some of their parameters
on the composition of the initial mixtures of p-EGM (M_1) with AA (M_2)**

Composition of the initial solution, mass.%		Composition of the copolymers, mass.%		Yield, %	Degree of unsaturation, %
M_1	M_2	m_1	m_2		
58.48	41.52	57.44	42.56	91.5	37.7
70.22	29.78	68.18	31.82	90.2	42.4
79.51	20.49	77.36	22.64	89.4	54.8

The obtained copolymers were transferred into Petri dishes and dried under vacuum in a desiccator at 30 °C. After establishing constant mass, the yield of the copolymers was calculated. The obtained data is also presented in Table 2. Analysis of the yield values of p-EGM copolymers with AA indicates an increase as the content of unsaturated polyester in the initial solutions decreases. The degree of unsaturation of the cured copolymers was determined by bromatometry, which correlates well with the p-EGM content in the initial reaction mixture. The degree of unsaturation of the cured products is in direct dependence on the content of unsaturated polyester (p-EGM) in the reaction mixture.

The products were identified using IR and NMR spectroscopy. Figure 4 shows the IR spectra of the initial p-EGM and its copolymers with AA of the compositions of 57.44:42.56 mass.% and 77.36:22.64 mass.%. The analysis of the obtained IR spectrum of unsaturated polyester reveals characteristic peaks in the 1570–1590 cm^{-1} range, indicating the presence of unsaturated double bonds in p-EGM. The peaks between 1400–1440 cm^{-1} correspond to the ether group.

Similar absorption bands, but of lower intensity, are present in the IR spectra of the cured products. This confirms the presence of some amount of unsaturated bonds that have not reacted. Also, peaks at

1715 cm^{-1} , 1742 cm^{-1} , 3439 cm^{-1} and 1711 cm^{-1} , 1736 cm^{-1} and 3432 cm^{-1} are present in both IR-spectra of the cured products, respectively, indicating the presence of $-\text{COOH}$ carboxyl groups [24].

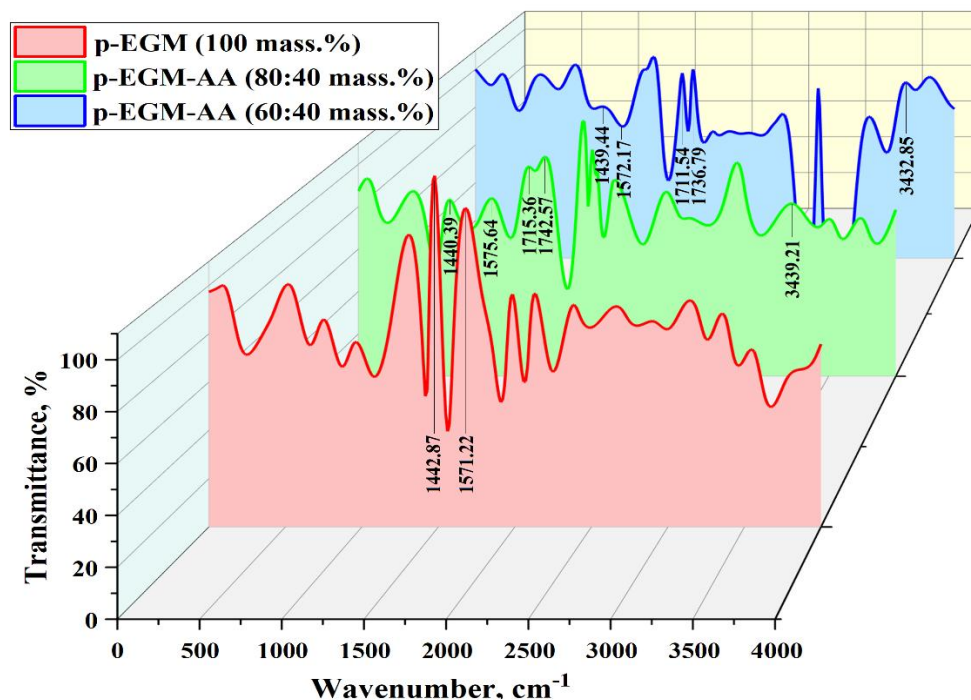


Figure 4. IR spectra of the initial p-EGM and p-EGM-AA copolymers

The ^1H NMR spectrum (Fig. 5) of the p-EGM-AA copolymer shows a pronounced multiplet expressed by signals in the range of 1.14–1.31 ppm. The appearance of the multiplet signal in this range confirms the presence of protons of methylene groups Ha in the polymer linkage, which are bound to oxygen atoms. The presence of multiplet signals in the ranges of 2.94–3.05 ppm and 3.65–4.42 ppm indicates the presence of protons of simple and ester methine and methylene groups of aliphatic series (Hb and Hc). In the range of 5.06–5.23 ppm there is a signal of comparatively lower intensity than in the range of 6.63–6.85 ppm where a signal of high intensity corresponding to a considerable amount of ethylene protons Hd in the copolymer structure appears. The separation of ethylene protons into two multiplet signals is due to their cis- and partially trans-orientation, with neighboring functional groups also having an influence. The high signal intensity in the range of 5.06–5.23 ppm indicates the dominance of cis-isomerism, confirming the structure of p-EGM. Similarly, the ^1H NMR spectrum of the original p-EGM is dominated by ethylene proton signals corresponding to cis-isomerism. The fixation of ethylene protons on the ^1H NMR spectrum, determined at the multiplet in the range of 6.68–6.85 ppm, indicates the presence of more electronegative atoms (neighboring oxygen atoms) in comparison with the protons of the multiplet in the region of 5.06–5.23 ppm [25].

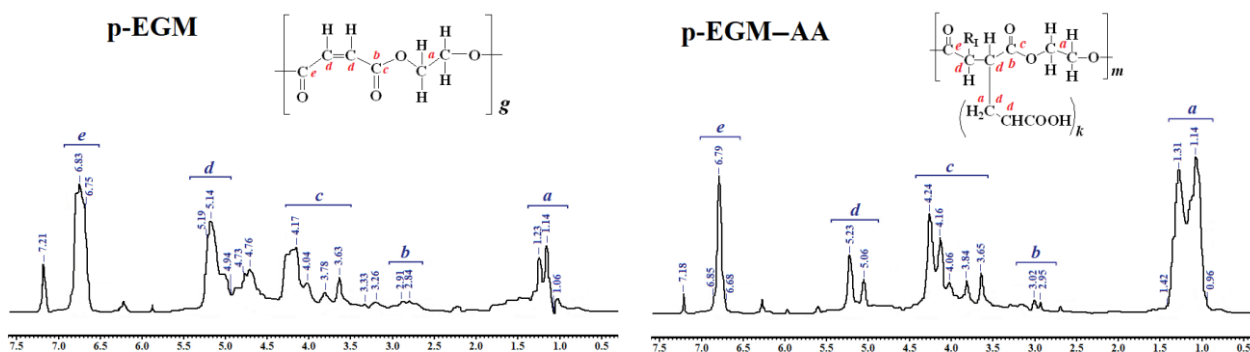


Figure 5. ^1H NMR-spectra of initial p-EGM and p-EGM-AA copolymers (77.36:22.64 mass.%)

“Cold” curing of p-EGM was carried out in mass without solvent, due to which the total volumetric shrinkage of the final product is insignificant. To obtain numerical values of this index, the density of the cured unsaturated polyester was determined using the hydrostatic method. The obtained values of density and, accordingly, the calculated volumetric shrinkage, are given in Table 3.

Table 3

Dependence of copolymer properties on mass composition of p-EGM–AA, PB + DMA (1 % + 0.15 %), T = 293K

Composition of initial solution, mass.%		Density (ρ), g/cm ³	Volume shrinkage, %	Swelling degree, %
p-EGM	AA			
57.44	42.56	1.3195±0.074	9.3	144.6
68.18	31.82	1.3257±0.074	8.6	127.9
77.36	22.64	1.3324±0.075	7.3	78.4
100	0	1.3414±0.075	4.4	12.8

Analysis of the density values of the synthesized p-EGM-AA copolymers and the dynamic viscosity and density values of p-EGM solutions in AA shows their good correlation. Thus, the maximum content of p-EGM (79.51:20.49 mass.%) in the initial solution leads to a cured product (77.36:22.64 mass.%) with a higher density of 1.3489 g/cm³. According to the values of the densities of the solutions of p-EGM in AA and the obtained cured copolymers, their total volume shrinkage indices were calculated depending on the composition of the initial reaction mixture. Based on the data obtained, it was found that this parameter does not exceed 10 %, while the lowest total volume shrinkage is observed for the solution with the maximum p-EGM content (79.51:20.49 mass.%). This parameter, not exceeding 10 %, corresponds to low shrinkage, which characterizes these solutions as suitable raw materials for the production of bulk products [1, 12].

Further, the degree of water sorption by synthesized copolymers was determined by gravimetric method. The results are also presented in Table 3. The data obtained indicate a low moisture absorption index, which defines these compounds as hydrophobic. At the same time, the minimum sorption capacity is observed for the copolymer with the highest unsaturated polyester content.

The surface topography of the initial p-EGM and its copolymers with AA was analyzed using SEM, with the results presented in Figure 6 [26].

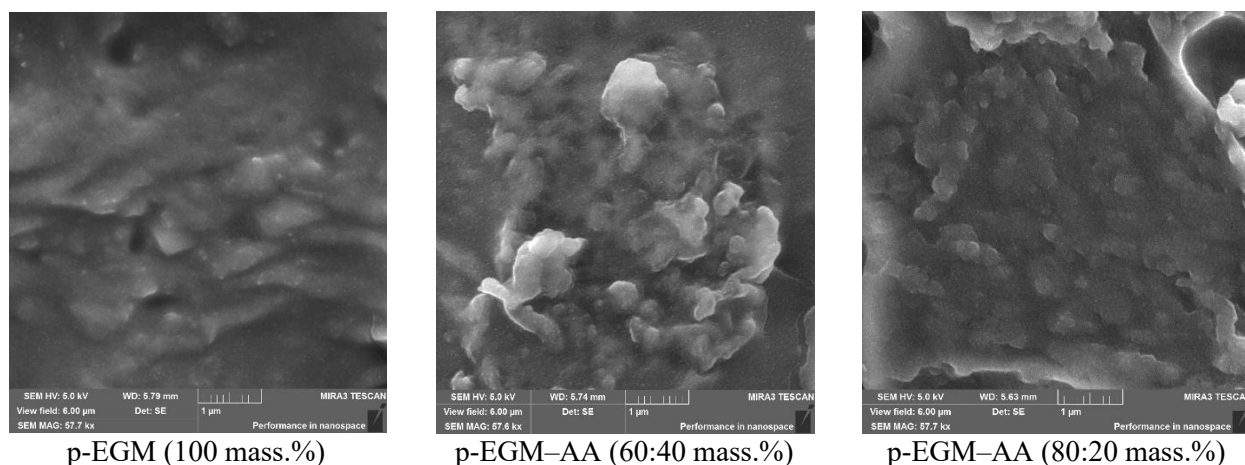


Figure 6. SEM-images of the initial p-EGM and p-EGM-AA copolymers

SEM images of the initial polyether confirm its low porosity. On the contrary, in the SEM images of the p-EGM–AA copolymers, it can be seen that the formation of a porous mesh structure is observed as a result of the curing of the unsaturated polyester with acrylic acid. Comparing SEM images of copolymers with minimum (57.44:42.56 mass.%) and maximum (77.36:22.64 mass.%) content of p-EGM, it should be noted that a greater number of pores and their larger size is observed in the copolymer with a lower content of unsaturated polyether. This correlates well with the results of gravimetric analysis to establish the moisture absorption capacity of the cured copolymers. In particular, the polymers having a more porous structure

(p-EGM–AA composition 57.44:42.56 mass.%) show greater moisture adsorption capacity in contrast to compounds with a high content of unsaturated polyester (the composition of p-EGM–AA is 77.36:22.64 mass.%), which have less pronounced porosity. Regarding the initial unsaturated polyester, it should be noted that this compound is hydrophobic, which is confirmed by the almost complete absence of pores on SEM-images and gravimetric analysis, which showed a swelling degree of 12.8 %.

Conclusions

Analyzing the obtained results of studying the physicochemical properties of solutions of polyethylene glycol maleate in acrylic acid of various composition, as well as cured copolymers on their basis, we can conclude that their use in the manufacture of filler products with a minimum content of mineral bulk fillers is promising. In particular, the dependence of the increase in such indicators as density and viscosity of the analyzed solutions on the content of unsaturated polyester in their composition was demonstrated. Thus, an increase in the unsaturated polyester content in the initial solutions promotes an increase in their dynamic viscosity and density. At the same time, cured products with a high content of p-EGM show higher density and degree of unsaturation.

The analysis of the total volume shrinkage index as well as swelling of cured products shows a similar correlation of these indicators on the content of unsaturated polyester in composition of the copolymers. Thus, the degree of swelling of cured products decreases with increasing p-EGM content. In general, studies of the degree of swelling showed a low moisture sorption capacity of the synthesized copolymers, which allows us to attribute these cured products to hydrophobic polymers. Taking into account that acrylic acid in the initial solution was used simultaneously as a solvent and hardener, the cured solutions had low volumetric shrinkage values (more than 10 %).

Obtained values are important parameters for polymer solutions that can be used to produce fill products for the construction industry. In particular, the production of polymer tiles. Because of this, the most preferable composition with the optimal complex of physical and chemical properties (including high hydrophobicity) for the manufacture of bulk products is the solution of p-EGM–AA (~80:20 mass.%).

Funding

This research is funded by the Science Committee of the Ministry of Science and Higher Education of the Republic of Kazakhstan (Grant No. AP23488036).

Author Information*

**The authors' names are presented in the following order: First Name, Middle Name and Last Name*

Gulsym Kabayevna Burkeyeva — PhD, Associate Professor, Department of Organic Chemistry and Polymers, Karaganda Buketov University, Universitetskaya street, 28, 100024, Karaganda, Kazakhstan; e-mail: guls_b@mail.ru; <https://orcid.org/0000-0003-1993-7648>

Anna Konstantinovna Kovaleva (*corresponding author*) — PhD, Senior Researcher, Karaganda Buketov University, Universitetskaya street, 28, 100024, Karaganda, Kazakhstan; e-mail: cherry-girl1899@mail.ru; <https://orcid.org/0000-0001-9758-648X>

Danagul Magazovna Muslimova — 3rd year PhD Student, Department of Organic Chemistry and Polymers, Karaganda Buketov University, Universitetskaya street, 28, 100024, Karaganda, Kazakhstan; e-mail: m.dana_777@mail.ru; <https://orcid.org/0000-0002-3041-7072>

David Havlicek — Ass. Prof., CSc. Charles University, Opletalova 38, 110 00 Staré Město, Prague, Czech Republic; e-mail: david.havlicek@natur.cuni.cz; <https://orcid.org/0000-0002-8854-6213>

Nurken Meiramuly Zhumabek — 1st year Master Student, Department of Organic Chemistry and Polymers, Karaganda Buketov University, Universitetskaya street, 28, 100024, Karaganda, Kazakhstan; e-mail: zhumabek2003@list.ru; <https://orcid.org/0009-0004-5318-0110>

Nurlan Aleksandrovich Nukin — 1st year Master Student, Department of Organic Chemistry and Polymers, Karaganda Buketov University, Universitetskaya street, 28, 100024, Karaganda, Kazakhstan; e-mail: nukinnurlan3@gmail.com; <https://orcid.org/0009-0004-5468-0846>

Author Contributions

The manuscript was written through contributions of all authors. All authors have given approval to the final version of the manuscript. **CRedit**: **Gulsym Kabayevna Burkeyeva** conceptualization, validation, visualization, supervision & editing; **Anna Konstantinovna Kovaleva** conceptualization, data curation, methodology, validation, visualization, writing-original draft, writing-review & editing; **Danagul Magazovna Muslimova** data curation & methodology; **David Havlicek** supervision & editing; **Nurken Meiramuly Zhumabek** data curation & investigation; **Nurlan Aleksandrovich Nukin** data curation & investigation.

Acknowledgments

Authors thank Karaganda Buketov University for access to library facilities.

Conflicts of Interest

The authors declare no conflict of interest.

References

- Gillela, S., Yadav, S.M., Kelkar, B.U., Sihag, K., Dangtungee, R., Bhuyar, P., Lee, S.H., Fatriasari, W., Wibowo, E.S., & Sinha, A. (2024). Advancing thermoset polymer composites with nanoclay reinforcement: a comprehensive investigation within composite interfaces. *Composite Interfaces*, 31(12), 1615–1657. <https://doi.org/10.1080/09276440.2024.2373486>
- Glogowska, K., Klepka, T., & Dulebova L. (2022). Characteristics of Polymer Materials with New Smart Utilities. *Adv. in Sci. and Tech.-Res. J.*, 14(4), 96–103. <https://doi.org/10.12913/22998624/125581>
- An, W.L., Wang, X.L., Liu, X.H., Wu, G., Xu, S.M., & Wang, Y.Z. (2022). Chemical recovery of thermosetting unsaturated polyester resins. *GREEN CHEM.*, 24(2), 701–712. <https://doi.org/10.1039/d1gc03724b>
- Han, C.Y., Hou, B.N., & Li, Z.Z. (2021). Research progress in functional polymer materials. *Cailiao gongcheng-J. of Mat. Eng.*, 49(6), 55–65. <https://doi.org/10.11868/j.issn.1001-1381.2020.000187>
- Raskutin, A.Ye. (2017). Development strategy for polymer composite materials. *Aviat. Mat and Tech.*, 5, 344–348. <https://doi.org/10.18577/2071-9140-2017-0-S-344-348>
- Lin, C.H. & Yu, J.S. (2022). Research on improving polymer pervious concrete mechanical strength by adding EVA to UP resin binder material. *Const. and Build. Mat.*, 359, Art. 129416. <https://doi.org/10.1016/j.conbuildmat.2022.129416>
- Belhadj, F.A., Belkheir, M., Mokaddem, A. Doumi, B., & Boutaous, A. (2022). Numerical characterization of the humidity effect on the fiber-matrix interface damage of hybrid composite material based on vinyl ester polymer matrix for engineering applications. *Emergent Mat.*, 5(2), 591–600. <https://doi.org/10.1007/s42247-022-00353-3>
- Zhang, Z.P., Liu, H., Ban, X.Y., Liu, X.S., Guo, Y.X., Sun, J., Liu, Y.Q., Zhang, S.Y., & Lei, J.H. (2024). Thermosetting resin modified asphalt: A comprehensive review. *J. of Traffic and Transportation Engineering-Eng. edit.*, 10(6), 1001–1036. <https://doi.org/10.1016/j.jtte.2023.11.002>
- Nodehi, M. (2022). Epoxy, polyester and vinyl ester based polymer concrete: a review. *Inn. Infr. Sol.*, 7(1), Art. 64. <https://doi.org/10.1007/s41062-021-00661-3>
- Jamshidi, M. & Pourkhorshidi, A.R. (2012). Modified polyester resins as an effective binder for polymer concretes. *Mat. and Struct.*, 45(4), 521–527. <https://doi.org/10.1617/s11527-011-9779-9>
- Zhang, H.L., Su, C., Bu, X.D., Zhang, Y.P., Gao, Y., & Huang, M. (2020). Laboratory investigation on the properties of polyurethane/unsaturated polyester resin modified bituminous mixture. *Const. and Build. Mat.*, 260, Art. 119865. <https://doi.org/10.1016/j.conbuildmat.2020.119865>
- Reis, J.M.L. & Jurumenha, M.A.G. (2013). Investigation on the effects of polymer impregnated aggregate on polymer mortars properties. *Mat. and Struct.*, 46(8), 1383–1388. <https://doi.org/10.1617/s11527-012-9980-5>
- Halary, J.L., Avérous, L., & Verney, V. (2010). Polymer materials and sustainable development. *Actualite chimique*, 338, Art. 39, 41–53.
- Fang, Z.M., Wu, X.W., Zhu, X.T., Luo, C., Li, D., Liu, Q.F., & Wang, K. (2024). Curing kinetics study of thermosetting resin material with ultra-low dielectric loss for advanced electronic packaging. *Polymer Testing*, 130, Art. 108312. <https://doi.org/10.1016/j.polymertesting.2023.108312>
- Liu, Y.L., Yu, Z., Wang, B.B., Li, P.Y., Zhu, J., & Ma, S.Q. (2022). Closed-loop chemical recycling of thermosetting polymers and their applications: a review. *Green Chem.*, 24(15), 5691–5708. <https://doi.org/10.1039/d2gc00368f>
- Acikbas, G. & Hindi, H. (2024). The Effect of a Composite Hydrophobic Coating with Zinc Oxide on the Characteristics of Polyester Matrix Composite Surfaces. *J. of Inorg. and Organomet. Polym. and Mat.*, 34(1), 419–429. <https://doi.org/10.1007/s10904-023-02842-2>
- Lubis, M.A.R., Sari, F.P., Laksana, R.P.B., Fatriasari, W., & Hermiati, E. (2006). Ambient curable natural rubber latex adhesive cross-linked with polymeric isocyanate for bonding wood. *Polymer Bulletin*, 79(8), 6745–6757. <https://doi.org/10.1007/s00289-021-03845-0>

- 18 Rajamuneeswaran, S., Vairamuthu, J., & Jayabal, S. (2020). A comparative study on mechanical properties of coir fiber reinforced polymer composites filled with calcium carbonate particles. *Mat. Today — Proceedings*, 33(7), 4790–4792. <https://doi.org/10.1016/j.matpr.2020.08.366>
- 19 Zheng, H. & Song, W. (2019). Hyperbranched unsaturated polyester amide synthesized by two-step method. *Pigment and Resin Tech.*, 48(1), 29–35. <https://doi.org/10.1108/PRT-04-2017-0044>
- 20 Burkeyev, M.Z., Kovaleva, A.K., Plocek, J., Tazhbayev, E.M., Burkeyeva, G.K., Bolatbai, A.N., & Davrenbekov, S.Z. (2018). Synthesis and Properties of Poly(Propylene Glycol Maleate Phthalate) — Styrene Copolymers as a Base of Composite Materials. *Russian J. of Appl. Chem.*, 91(11), 1742–1749. <https://doi.org/10.1134/S1070427218110022>
- 21 Chabros, A. & Gawdzik, B. (2019). Methacrylate monomer as an alternative to styrene in typical polyester–styrene copolymers. *J. of Appl. Polym. Sci.*, 136(27), Art. 47735. <https://doi.org/10.1002/app.47735>
- 22 Burkeyeva, G., Kovaleva, A., Tazhbayev, Y., Ibrayeva, Z., & Zhaparova, L. (2023). Investigation of Curing Process and Thermal Behavior of Copolymers Based on Polypropylene Glycol Fumarate and Acrylic Acid Using the Methods of DSC and TGA. *Polymers.*, 15, Art. 3753. <https://doi.org/10.3390/polym15183753>
- 23 Burkeyeva, G.K., Kovaleva, A.K., Tazhbayev, Ye.M., Ibrayeva, Zh.M., & Plocek, J. Development of Energy-Efficient “Cold” Curing Method for Polypropylene Glycol Fumarate Using an Optimized Initiating System. *Eur. J. of Chem.*, 109(1), 68–77. <https://doi.org/10.31489/2959-0663/1-23-10>
- 24 Lorenz-Fonfina, V.A. (2020). Infrared Difference Spectroscopy of Proteins: From Bands to Bonds. *Chem. Rev.*, 120(7), 3466–3576. <https://doi.org/10.1021/acs.chemrev.9b00449>
- 25 Asakura, K. (2024). NMR Data Processing Software “JASON”, by the NMR Manufacturer, for the NMR Users. *J. of Synth. Org. Chem.*, 82(3), 281–285. <https://doi.org/10.5059/yukigoseikyokaiishi.82.281>
- 26 Wu, H., He, M., Wu, Sh., Cheng, J., Wang, T., Che, Ya., Du, Yo., & Deng, Q. (2024). Effects of binder component and curing regime on compressive strength, capillary water absorption, shrinkage and pore structure of geopolymer mortars. *Const. and Build. Mat.*, 442, Art. 137707. <https://doi.org/10.1016/j.conbuildmat.2024.137707>

Nurbatyr Mukhametgazy¹, Kamila M. Temirkulova^{1,2}, Balausa Balgabayeva^{1,2},
Bekzat G. Khamzin^{1,2}, Seitkhan Azat¹, Zhazira A. Supiyeva^{1,2*}, Qamar Abbas^{3,4}

¹Satbayev University, Almaty, Kazakhstan;

²Al-Farabi Kazakh National University, Almaty, Kazakhstan;

³Graz University of Technology, Graz, Austria;

⁴Poznan University of Technology, Poznan, Poland

(*Corresponding author's e-mail: zhazira.supiyeva@kaznu.kz)

Effect of Activating Agent and Temperature Conditions on the Electrochemical Performance of Rice Husk-Based Activated Carbon in Supercapacitors

This study investigates the electrochemical properties of activated carbon (AC) derived from rice husk, focusing on the influence of activation conditions using NaOH and KOH at temperatures of 650 °C, 750 °C, and 850 °C. The results demonstrate that RH-AC/KOH activated at 750 °C exhibits the highest capacitance retention (159–165 F·g⁻¹) and superior electrochemical performance, attributed to its optimized microporous structure and enhanced electrical conductivity. These properties make it an excellent candidate for electrode material in supercapacitors. Electrochemical evaluations, including cyclic voltammetry (CV), galvanostatic charge-discharge (GCD), and electrochemical impedance spectroscopy (EIS), confirm that RH-AC/KOH activated at 750 °C delivers the highest current density, stable performance across a wide voltage range (0.6–1.5 V), and the longest discharge duration. A comparison of the specific current change (ΔSc) at low potentials (0.6–1.0 V) for the four samples AC/NaOH at 850 °C and RH-AC/KOH at 750 °C, 650 °C, and 850 °C shows the following trend: 281.2 > 269.2 > 267.6 > 190.5 mA·g⁻¹. At higher potentials (1.2–1.5 V), the ΔSc values follow the order: 341.9 \approx 340.0 > 314.6 > 247.8 mA·g⁻¹. These findings identify RH-AC/KOH activated at 750 °C as a highly promising electrode material for next-generation supercapacitors, offering unique energy storage capacity, stability, and long-term durability.

Keywords: activated carbon, rice husk, chemical activation, thermal post-treatment, electrical properties, electrical conductivity, supercapacitors, electrode material, energy storage

Introduction

Activated carbon (AC) is widely used in energy storage applications, particularly in supercapacitors and batteries, due to its high surface area, good electrical conductivity, and relatively low cost [1, 2]. AC can be prepared through several methods, including physical activation (using gases such as CO₂, H₂, or CH₄) and chemical activation (using agents like ZnCl₂, NaOH, KOH, or H₃PO₄). Chemical activation typically involves thermal treatment of a carbon precursor with an activating agent at temperatures ranging from 450 to 900 °C. This method offers distinct benefits compared to physical activation [3]. The resulting porous structure, which includes micro-, meso-, and macropores, makes activated carbon a suitable material for a wide range of industrial and environmental applications [4]. Numerous studies have investigated the influence of processing conditions on the physicochemical properties of AC derived from biowaste sources such as rice husk and walnut shells. Some of these studies have even developed predictive models for estimating AC performance characteristics [5–8]. Nevertheless, there remains significant potential to optimize biowaste-derived AC synthesis methods and explore new applications. Recently, increasing attention has been given to the use of such materials in supercapacitors and hydrogen storage systems. Depending on the energy storage mechanism, supercapacitors (SCs) utilizing AC can be categorized into three main types: electric double-layer capacitors (EDLCs), pseudocapacitors, and hybrid supercapacitors, which combine features of the first two [9]. As research progresses, supercapacitor technology is considered one of the most promising and efficient solutions for next-generation energy storage devices [10, 11].

Despite their advantages, ACs also have certain limitations, including increased internal resistance and reduced power output in energy storage devices [12–14]. Moreover, producing high-quality ACs often requires high-temperature pyrolysis and strong chemical activating agents, such as acids or bases, which can have harmful environmental effects [15, 16]. However, the rapid charging and discharging capacity of super-

capacitors gives them a significant advantage over traditional batteries. From this perspective, one of the key challenges lies in supporting high-speed electric motors, such as those used in electric vehicle engines and specialized equipment. Consequently, biowaste-derived ACs have attracted strong interest from scientists and companies as a promising electrode material for supercapacitor production. In recent years, numerous agricultural by-products have been investigated as sustainable precursors for ACs production, including coconut shells, corn cobs, lignocellulosic biomass, walnut shells, and peanut shells [17–20]. These biomass sources are typically rich in carbon and exhibit a high potential for porosity development, both of which are critical for electrochemical energy storage applications. While abundantly available, walnut shells and corn cobs tend to produce ACs with irregular pore size distributions and limited mesoporosity, restricting ion transport in supercapacitor systems [21, 22]. In contrast, rice husk (RH) is particularly advantageous due to its intrinsic high silica content, which acts as a natural template promoting hierarchical pore formation during activation [23]. Furthermore, RH-derived ACs have consistently demonstrated higher surface areas, better electrical conductivity, and enhanced electrochemical performance compared to other biomass-derived carbons [24]. Importantly, Kazakhstan produces a substantial amount of RH as agricultural waste, especially in rice-producing regions, making it a readily available and cost-effective resource for value-added conversion into energy storage materials [25].

In addition to carbonization temperature and the type of chemical activating agent, several other experimental parameters play an important role in tailoring the structural and electrochemical properties of ACs [26, 27]. Factors, namely activation time, heating rate, precursor particle size, and the atmosphere during carbonization significantly influence porosity, specific surface area, and conductivity, key characteristics that determine ACs performance in applications such as supercapacitors. For instance, prolonged activation time can promote pore development but may also lead to pore collapse if overextended [28]. Similarly, slower heating rates favor more uniform pore structures and higher surface areas [29], while smaller precursor particles have been associated with enhanced textural properties and ion accessibility [30]. Moreover, the carbonization atmosphere (such as nitrogen gas, steam, or CO₂) affects both the physical and chemical properties of the carbon surface, with steam activation often introducing functional groups that improve wettability and electrochemical performance [31, 32]. Therefore, the synergistic optimization of all these conditions is essential to maximize the performance of biomass-derived ACs [33]. This is assessed through rate capability tests (ranging from 0.1 to 10 A·g⁻¹) and long-term stability tests, including voltage floating (100 hours at a cell voltage of 2.7 V) [34]. In our previous studies [35, 36], we compared various thermal treatment methods for synthesizing activated carbon from walnut shells, with the goal of optimizing production processes [5, 7]. To achieve the best electrochemical performance from electrodes, fine-tuning and optimization, especially for activated carbon-based electrodes, are essential. In this study, two activation agents, NaOH and KOH, were used to produce activated carbons at a temperature of 850 °C. After conducting a comparative analysis, it was found that KOH was the more effective agent. As a result, additional tests at 650 °C and 750 °C were performed, and the resulting carbons were evaluated as electrodes in supercapacitors. Ultimately, the comparative analysis revealed that AC activated with KOH at 750 °C delivered the best electrochemical performance among all tested samples.

This study presents a comprehensive investigation into the optimization of rice husk-derived activated carbon for use in supercapacitor electrodes, with a particular focus on the effects of activation temperature (650, 750, and 850 °C) and chemical activating agents (NaOH and KOH). The electrochemical performance of the synthesized carbons was systematically compared across the tested temperatures. The findings provide valuable insights into the optimal activation conditions, demonstrating that activation with KOH at 750 °C yields the most favorable results for enhancing supercapacitor efficiency. Future work will involve cycling stability and capacitance retention testing under extended voltage ranges (beyond 1.5 V), with the goal of further improving the long-term performance and reliability of supercapacitor devices.

Experimental

Materials

Rice husk (RH) was sourced from the Kyzylorda Region, Kazakhstan. The activation agents, sodium hydroxide (NaOH), potassium hydroxide (KOH) with 98 % purity, Carbon black (C₆₅, Timcal C-ENERGY Imerys), and polytetrafluoroethylene (PTFE, 60 % dispersion in water) were purchased from Sigma-Aldrich Chemical Co. (USA) and used without further purification. Nitrogen gas (99.95 wt.% purity, “Ikhsan TechnoGas” Ltd., Almaty, Kazakhstan) was used for the second carbonization step at 500 °C with a heating rate of 7.5–8 °C·min⁻¹. Gas activation was carried out under N₂ atmosphere at a flow rate of 150 mL·min⁻¹. Dis-

tilled water (resistivity $\approx 1\text{--}10\text{ M}\Omega\cdot\text{cm}$) and deionized water (DI, resistivity $\geq 18.2\text{ M}\Omega\cdot\text{cm}$) were prepared in-house and used for washing and synthesis procedures. Ethanol was purchased from “Laborfarma” LLP, Almaty, Kazakhstan.

Methods

Synthesis of RH-Based Activated Carbon

Activated carbon was synthesized from rice husk using NaOH and KOH as activating agents under various high-temperature treatment conditions. Initially, the rice husk was thoroughly washed multiple times with distilled water to remove dirt and surface impurities. After cleaning, it was dried to a constant mass and subjected to preliminary carbonization at $500\text{ }^\circ\text{C}$ ($\pm 10\text{ }^\circ\text{C}$) for 1 hour under a nitrogen atmosphere to prevent oxidation [11, 12]. Chemical activation was carried out at $850\text{ }^\circ\text{C}$ ($\pm 10\text{ }^\circ\text{C}$) for 1 hour under nitrogen flow. For post-thermochemical activation, the carbonized rice husk was mixed with KOH powder and thermally treated in air at $650\text{ }^\circ\text{C}$, $750\text{ }^\circ\text{C}$, and $850\text{ }^\circ\text{C}$ for 5 hours to ensure full impregnation of the carbon structure by molten KOH. Both sodium hydroxide (NaOH) and potassium hydroxide (KOH) were used as activating agents, with a precursor-to-activating agent mass ratio of 1:4. After activation, the resulting samples were washed with hot distilled water until a neutral pH (6-7) was achieved, ensuring the removal of residual alkali. The materials were then dried at $100\text{ }^\circ\text{C}$ for 24 hours. The dried activated carbon was ground and subjected to a second carbonization step at $500\text{ }^\circ\text{C}$ for 90 minutes under an argon atmosphere, with a heating rate of $7.5\text{--}8\text{ }^\circ\text{C}\cdot\text{min}^{-1}$, following the procedure described previously [5, 36]. The resulting RH-AC samples prepared by this method were used in the fabrication of a supercapacitor cell, as described in the next section.

Electrode Fabrication and Electrochemical Tests

A symmetrical two-electrode system was employed, in which both the working and counter electrodes were fabricated from the same activated carbon material derived from rice husk. Additionally, the supercapacitor cell was equipped with an Ag/AgCl reference electrode and a stainless steel current collector. To prepare the activated carbon electrodes (Carbon/C₆₅/PTFE), a composite mixture was formulated consisting of 90 wt.% activated carbon powder, 5 wt.% carbon black (C65) as a conductive additive, and 5 wt.% polytetrafluoroethylene (PTFE, 60 % dispersion in water), resulting in a 90:5:5 weight ratio. The components were thoroughly mixed and ground using an agate mortar and pestle until the solvent fully evaporated. The resulting mixture was dried overnight in a vacuum oven at $120\text{ }^\circ\text{C}$. Afterwards, disc-shaped electrodes (10 mm diameter) were punched from the formed sheet, yielding a final thickness of approximately $100\text{ }\mu\text{m}$ [37].

Table 1

Rice husk-based activated carbon (RH-AC) electrodes

AC	Mass values of AC combinations		
	Carbon, g	C ₆₅ , g	PTFE, g
NaOH — $850\text{ }^\circ\text{C}$	0.2547	0.0151	0.0141
RH — $650\text{ }^\circ\text{C}$	0.2893	0.0163	0.0162
RH — $750\text{ }^\circ\text{C}$	0.2793	0.0155	0.01506
RH — $850\text{ }^\circ\text{C}$	0.2909	0.0161	0.0165

The electrochemical performance of RH-AC in a supercapacitor was evaluated using cyclic voltammetry (CV), galvanostatic charge-discharge (GCD) measurements, and electrochemical impedance spectroscopy (EIS). The CV measurements were carried out within a voltage range of $0.6\text{--}1.5\text{ V}$ at various scan rates. GCD tests were conducted at a constant current of $0.2\text{ A}\cdot\text{g}^{-1}$ to determine specific capacitance and energy density at different current densities, with a potential cutoff of 2 mV . EIS analysis was performed using a VMP-3 multichannel potentiostat/galvanostat (BioLogic Instruments, France) over a frequency range of 100 mHz to 100 kHz to investigate charge transfer resistance and ion diffusion properties [37]. Electrochemical studies were carried out using VSP-300 electrochemical workstations. The CV curves were recorded within a 1 V potential window, while GCD tests were performed at a constant current of $0.2\text{ A}\cdot\text{g}^{-1}$. Impedance measurements were conducted in the $100\text{ kHz}\text{--}10\text{ mHz}$ frequency range with a potential amplitude of 1.5 V . The specific capacitance was calculated from GCD curves using the following equation:

$$C = \frac{4I\Delta t}{m\Delta V}, \quad (1)$$

where C ($\text{F}\cdot\text{g}^{-1}$) is the specific capacitance; I (A) is the discharge current; Δt (s) is the discharge time; ΔV (V) is the potential window; m (mg) is the total mass of two electrodes.

Specific capacitance from the CV curve was calculated using the following equation:

$$C = \frac{2}{mv(V_b - V_a)} \int_{V_a}^{V_b} IdV. \quad (2)$$

Here, C ($\text{F}\cdot\text{g}^{-1}$) represents the specific capacitance, m (mg) denotes the total mass of both electrodes, v ($\text{mV}\cdot\text{s}^{-1}$) is the scan rate, I (A) refer to the discharge current, and V_b and V_a correspond to the upper and lower voltage limits in the cyclic voltammetry (CV) test [38].

Result and Discussion

Characterization of RH-based AC in a Supercapacitor System

The microstructural characteristics of carbon materials derived from rice husks after thermochemical activation were extensively examined in our previous study [35]. The SEM micrographs of RH-AC revealed a well-developed porous architecture within the carbon matrix, formed through carbonization and graphitization at 750°C , followed by KOH-assisted thermochemical activation at 850°C . The resulting material exhibited a uniform distribution of macropores across the surface. The specific surface area of the rice husk-derived activated carbon reached $2290\text{ m}^2\cdot\text{g}^{-1}$, enhancing its suitability for electrochemical applications [36]. Building upon these prior findings, the present study investigates the electrochemical performance of RH-based activated carbons (RH-ACs) in a supercapacitor system, with a particular focus on specific capacitance behavior across a voltage range of $0.6\text{--}1.5\text{ V}$ at varying scan rates. The influence of activation parameters, particularly the choice of chemical activator (KOH vs. NaOH) and activation temperatures (650°C , 750°C , and 850°C), is evaluated using CV, GCD, and EIS to determine the optimal RH-AC materials for use as suitable cathodes in supercapacitors.

Figure 1 presents CV results of two electrodes (2E) in SC systems fabricated using four activated carbon samples: AC/NaOH at 850°C (black), RH-AC/KOH at 650°C (red), RH-AC/KOH at 750°C (blue), and RH-AC/KOH at 850°C (green). Specific capacitance was evaluated across voltage ranges from 0.6 to 1.5 V to assess charge storage efficiency and ion transport properties.

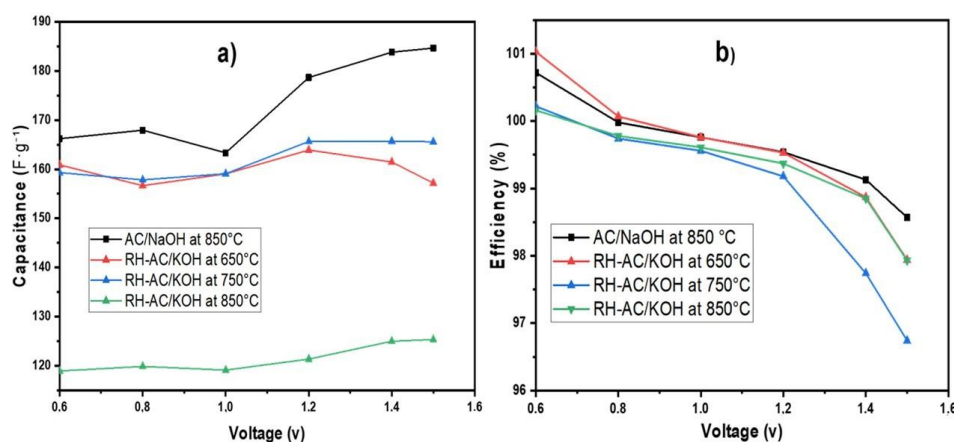


Figure 1. CV results showing (a) specific capacitance and (b) coulombic efficiency of 2E-type electrodes based on AC/NaOH and RH-AC/KOH samples activated at different temperatures, measured across a voltage range of $0.6\text{--}1.5\text{ V}$ at a scan rate of 2 mV/s

Figure 1(a) shows that AC/NaOH sample activated at 850°C exhibited a stable and gradually increasing capacitance, ranging from 166 to $184\text{ F}\cdot\text{g}^{-1}$, except for a slight dip at 1.0 V ($163\text{ F}\cdot\text{g}^{-1}$), suggesting a well-developed pore structure. In contrast, RH-AC/KOH activated at 650°C displayed a sharp decrease in capacitance from 161 to $157\text{ F}\cdot\text{g}^{-1}$, likely due to insufficient activation and poor electrical conductivity. RH-AC/KOH at 850°C showed the lowest capacitance (119 to $125\text{ F}\cdot\text{g}^{-1}$), attributed to excessive pore widening and reduced availability of effective charge storage sites. The RH-AC/KOH at 750°C demonstrated the best capacitance retention (159 to $165\text{ F}\cdot\text{g}^{-1}$), based on the microporosity and conductivity, making it the most effective cathode material for supercapacitor applications. Figure 1(b) illustrates the coulombic efficiency of

four different AC samples in a supercapacitor system. The performance of each sample is analyzed based on capacitance retention as a function of voltage variation within the range of 0.6 to 1.5 V. The efficiency of each sample was evaluated across the voltage range, showing a gradual decline. At the initial voltage of 0.6 V, the efficiencies of AC/NaOH at 850 °C and RH-AC/KOH at 650 °C, 750 °C, and 850 °C were all close to 100 %. By the final voltage of 1.5 V, the efficiency values were approximately 98.6 %, 100 %, 96.7 %, and 100 %, respectively. The RH-AC/KOH at 750 °C displayed slightly lower efficiency compared to the other samples at 1.5 voltage.

The CV curves of two electrode (2E) cells with AC/NaOH at 850 °C and RH-AC/KOH at 650 °C, 750 °C, and 850 °C, measured up to 1.0 V in 1 mol·L⁻¹ Li₂SO₄ electrolyte, are shown in Figure 2 (a, b, c, and d), respectively. As shown in Figure 2(a), the CV curves of AC/NaOH at 850 °C exhibit capacitance traces with a specific current (*Sc*) ranging from -135.6 to 145.6 mA·g⁻¹ in the lower potential region (0.6–1.0 V), while in the higher potential region (1.2–1.5 V), the specific current varies from -157 to 184.9 mA·g⁻¹. The specific current change (ΔSc) at low and high voltages was calculated as 281.2 and 341.9 mA·g⁻¹, respectively. Figure 2(b) presents the CV curves of RH-AC/KOH at 650 °C, showing capacitance traces where the specific current increases from -143.9 to 123.7 mA·g⁻¹ in the low potential region. At higher potentials, the specific current varies from -157 to 184.9 mA·g⁻¹. The corresponding ΔSc values for low and high potentials were determined to be 267.6 and 314.6 mA·g⁻¹, respectively. Similarly, as shown in Figure 2(c), the CV curves of RH-AC/KOH at 750 °C exhibit specific current variations from -135.7 to 133.5 mA·g⁻¹ in the low potential region and from -155.6 to 184.4 mA·g⁻¹ in the higher potential region. The ΔSc values for these voltage ranges were calculated as 269.2 and 340.0 mA·g⁻¹, respectively. In Figure 2(d), the cyclic voltammetry (CV) curves for the RH-AC/KOH sample at 850 °C show that the specific current ranges from -88.4 to 190.5 mA·g⁻¹ at lower potentials and from -106.4 to 141.4 mA·g⁻¹ at higher potentials.

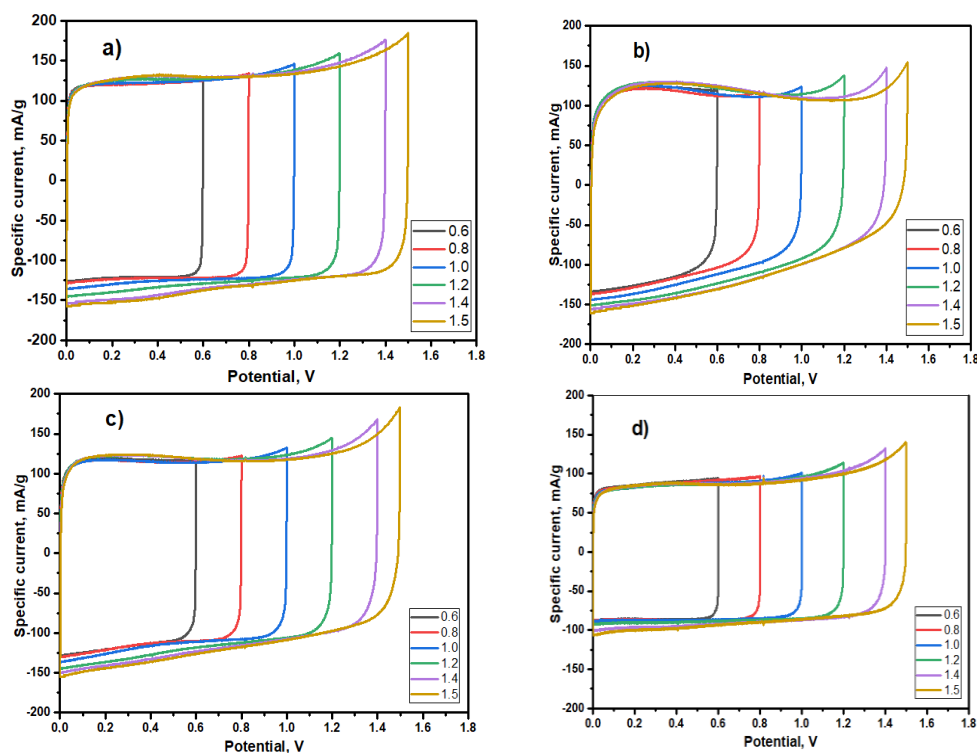


Figure 2. CV curves at 2 mV/s of 2E cell with AC/NaOH at 850 °C (a) and RH-AC/KOH at 650 (b), 750 (c) 850 °C (d) activated electrodes in different voltages

The corresponding changes in specific current (ΔSc) are 190.5 mA·g⁻¹ and 247.8 mA·g⁻¹, respectively. A comparison of ΔSc values at low voltages among the four samples, namely AC/NaOH at 850 °C and RH-AC/KOH at 750 °C, 650 °C, and 850 °C reveals the following trend: 281.2 > 269.2 > 267.6 > 190.5 mA·g⁻¹. Similarly, in the high voltage range, the ΔSc values follow the order: 341.9 \approx 340.0 > 314.6 > 247.8 mA·g⁻¹. From these results, it is evident that the electrode density of AC/NaOH at 850 °C is significantly higher. Among the RH-AC/KOH samples, the one treated at 750 °C exhibits the highest current

density, comparable to that of AC/NaOH at 850 °C. These electrochemical results indicate that RH-AC/KOH at 750 °C achieves the highest current density, signifying superior electrochemical performance.

Figure 3 shows the galvanostatic charge-discharge (*a*), and electrochemical impedance (*b*) of AC/NaOH 2E cell at a current density of 0.2 A·g⁻¹ in different voltage ranges at 850 °C. Figure 3 (*a*) shows a triangular shape within the voltage range of 0.6–1.5 V, which suggests nearly ideal capacitive behavior, as is typical of double-layer capacitors. The initial voltage drop during discharge, which occurs between 259 and 531 seconds, appears minimal. A total discharge duration of 272 seconds indicates low internal resistance and excellent conductivity of the electrode materials. The longest discharge time is observed at 1.5 V, with a maximum discharge time of 671 seconds exhibiting the highest stored charge value between 671 and 1342 seconds. At higher voltages (1.4 V and 1.5 V), the charge-discharge curves remain linear with a right angle, indicating good electrode stability even under elevated voltage conditions. Additionally, the charge-discharge curves are symmetrical and consist of straight lines, showing consistent growth as the voltage increases from 0.6 to 1.5 V. Figure 3(*b*) demonstrates the Nyquist Plot (EIS) at different voltages (0.6–1.5 V). The shift in charge transfer resistance (R_{ct}) at lower voltages 0.6–1.0 shows the same 0.6 Ω and low Equivalent Series Resistance (R_s) 0.27 Ω. The small semicircle at high frequencies corresponds to the charge transfer resistance (R_{ct}) at the electrode/electrolyte interface [36]. According to the specified parameters, the R_{ct} values for the three voltages in 1.2 V, 1.4 V, and 1.5 V gradually increase to 0.73 Ω, 1.21 Ω, and 2.05 Ω, respectively. Correspondingly, the R_s values are 0.32 Ω, 0.41 Ω, and 0.56 Ω, respectively. A larger semicircle at higher voltages (1.4 V and 1.5 V) is attributed to an increase in R_{ct} . The highest change in charge transfer resistance (ΔR_{ct}) is 1.49 Ω, which is possibly due to reduced ionic conductivity at higher voltages compared to lower voltage ranges. The ECI measurement results (Fig. *b*) suggest that the enhanced R_{ct} values of AC/NaOH 2E cells reflect a notable alteration in the porous structure that facilitates easier electrolyte diffusion.

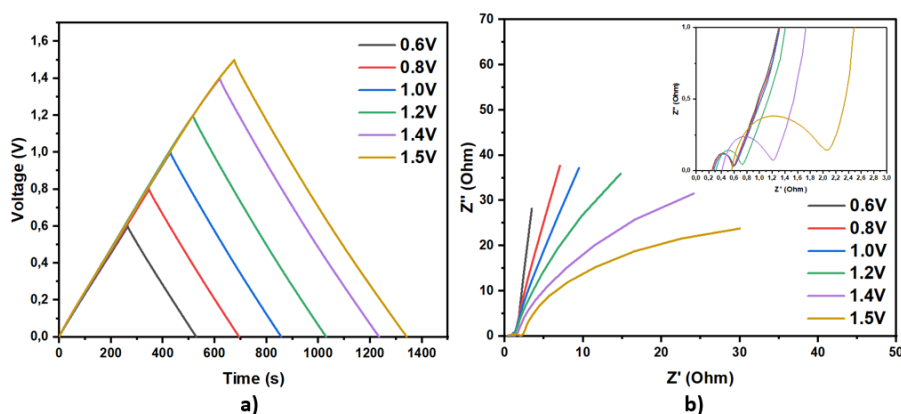


Figure 3. GCD (*a*) and EIS (*b*) curves of the AC/NaOH 2E cell at a current density of 0.2 A·g⁻¹ in different voltage ranges at 850 °C

Figure 4 shows the charge-discharge behavior and electrochemical impedance of a 2E cell with RH-AC treated with KOH at 650 °C, 750 °C, and 850 °C at a current density of 0.2 A·g⁻¹, across various voltage limits. Figure 4(*a*) shows that the initial voltage drop during discharge, occurring between 248 and 498 seconds, is minimal. Moreover, the total discharge duration (ΔT) of 250 seconds suggests low internal resistance and excellent conductivity of the electrode materials. The longest discharge time is notably observed at 1.5 V, ranging from 563 to 1124 seconds, with a maximum duration of (ΔT) 561 seconds, indicating the highest stored charge value. However, the GCD properties of RH-AC/KOH at 650 °C are significantly lower than those of AC/NaOH 2E at 850 °C. Furthermore, at higher voltages (1.4 V and 1.5 V), the charge-discharge curves deviate from linearity; a curved line reduces symmetry rather than a right angle. In contrast, its stability declines as the voltage increases from 1.2 to 1.5 V. Figure 4(*d*) presents the Nyquist plot of RH-AC/KOH at 650 °C. At low voltages (0.6–1.0 V), the charge transfer resistance (R_{ct}) and equivalent series resistance (R_s) remain similar, with values of 2.86 Ω and 0.47 Ω, respectively. As the voltage increases to 1.2 V, 1.4 V, and 1.5 V, the R_{ct} values rise uniformly to 3.5 Ω, 5.2 Ω, and 7.16 Ω, respectively. Similarly, the R_s values increase to 0.56 Ω, 0.72 Ω, and 0.84 Ω. The most significant increase in charge transfer resistance is observed at the highest voltage (1.5 V), reaching 7.16 Ω due to the formation of a large semicircle.

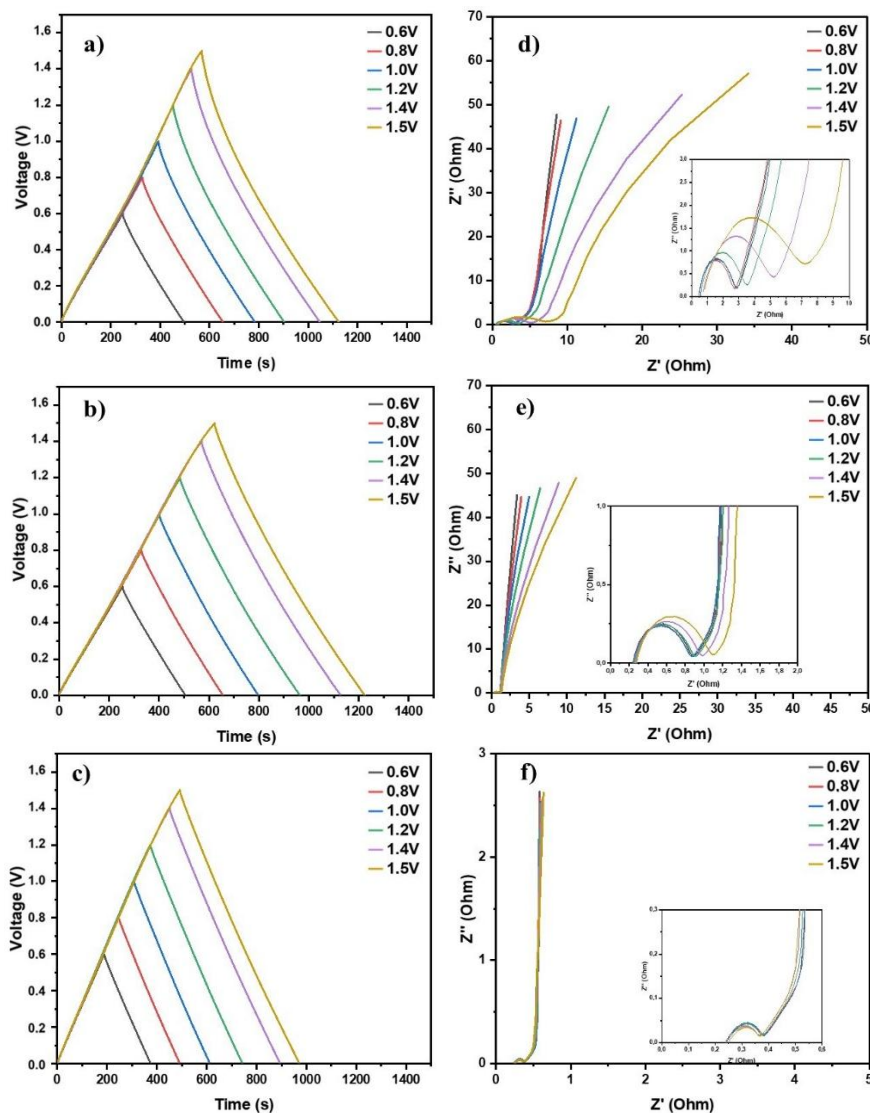


Figure 4. GCD (*a, b, c*), and EIS (*d, e, f*) of the RH-AC/KOH 2E cell at a current density of $0.2 \text{ A} \cdot \text{g}^{-1}$ with different voltages at 650, 750, and 850 °C, respectively

Figure 4(*b*) shows the GCD performance of RH-AC/KOH activated at 750 °C. The initial voltage drop during discharge is minimal and occurs within the time frame of 251 to 505 seconds. Additionally, the total discharge duration (ΔT) of 254 seconds suggests that the electrode materials have low internal resistance and excellent conductivity. Furthermore, the longest discharge time of 604 seconds is recorded at 1.5 V from 620 to 1224 seconds, directly reflecting the highest stored charge. Meanwhile, under comparable conditions, the GCD behavior of RH-AC/KOH activated at 750 °C with KOH remains notably higher than that of the RH-AC/KOH sample activated at 650 °C. Furthermore, at elevated voltages (1.4 V and 1.5 V), the charge-discharge curves exhibit a linear profile, maintaining symmetry between the charge and discharge lines. Figure 4(*e*) presents the Nyquist plot for RH-AC/KOH at 750 °C. At low voltages (0.6–1.2 V), the charge transfer resistance (R_{ct}) and equivalent series resistance (R_s) are similar, with values of 0.89 Ω and 0.26 Ω , respectively. As the voltage increases to 1.4 V and 1.5 V, the R_{ct} values rise slightly to 0.98 Ω and 1.1 Ω , respectively, forming a semicircle with a small radius, indicating that the electrochemical impedance of electrodes does not increase significantly. Meanwhile, the R_s values remain constant at 0.26 Ω throughout the tested voltage range of 0.6–1.5 V. Additionally, the conduction resistance exhibits minimal variation, ranging from 0.89 Ω to 1.1 Ω across the entire voltage range, consistently forming a distinct semicircle. Notably, the maximum change in charge transfer resistance (ΔR_{ct}) is only 0.21 Ω , which further confirms the stability of the system.

As can be seen in Figure 4(c), the initial voltage drop during discharge is minimal and occurs between 188.4 and 490 seconds. Moreover, the total discharge duration (ΔT) of 301.6 seconds indicates low internal resistance and excellent conductivity of the electrode materials. Notably, the longest discharge time is observed at 1.5 V, extending from 490 to 974 seconds. This maximum discharge duration (ΔT) of 484 seconds is directly proportional to the highest charge storage capacity. Furthermore, at higher voltages (1.4 V and 1.5 V), the charge-discharge curves exhibit a linear profile, maintaining symmetry between the charge and discharge lines. Figure 4(f) shows the RH-AC/KOH Nyquist plot at 850 °C. As the voltage increases to 0.6 V and 1.5 V, the equivalent series resistance (R_s) and charge transfer resistance (R_{ct}) values become similar at all six voltages. They increase slightly to 0.24 Ω and 0.38 Ω , respectively, indicating that the electrochemical resistance of the electrodes is very low and forming a semicircle with a very small radius. It is worth noting that the maximum change in charge transfer resistance (ΔR_{ct}) is only 0.14 Ω , confirming that the conductivity of the system is very low.

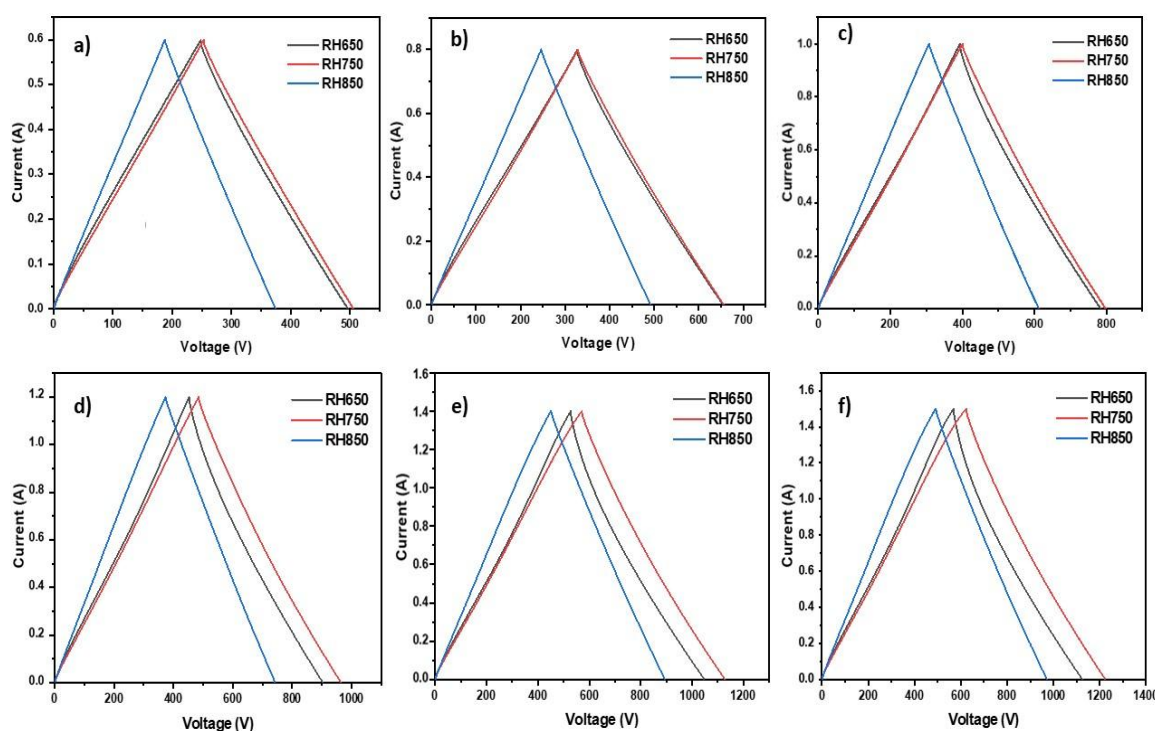


Figure 5. GCD versus 2E cell with RH-AC treated at 650, 750, and 850 °C at a current density of 0.2 A·g⁻¹ versus voltage: (a) 0.6 V, (b) 0.8 V, (c) 1.0 V, (d) 1.2 V, (e) 1.4 V, and (f) 1.5 V

Figure 5 demonstrates the galvanostatic charge-discharge behavior of a 2E cell containing RH-AC treated at 650 °C, 750 °C, and 850 °C at a current density of 0.2 A·g⁻¹ and over a wide range of voltage. Figure 5(a, b and c) shows the charge-discharge voltage variations for the RH/KOH sample treated at 850 °C (blue line) at voltages of 0.6 V, 0.8 V, and 1.0 V, which were 189 V, 246 V, and 306 V, respectively. These values indicate significantly lower capacitance than the other two samples, which were treated at 650 °C and 750 °C. Within the lower voltage range (0.6–1.0 V), the discharge voltage change values (ΔV) for the RH-650 °C and RH-750 °C samples remained consistent across figures a, b, and c. Furthermore, the ΔV values increased in the following order: 247 V < 326 V < 391 V for RH-650 °C and 253 V < 326 V < 400 V for RH-750 °C, respectively. On the other hand, when analyzing the graphs in Figure 5 (d, e, and f), it is evident that at relatively high voltages (1.2 V, 1.4 V, and 1.5 V), the charge-discharge curves are more widely spaced. Specifically, the discharge voltage changes (ΔV) increased in the order of 372 V < 444 V < 525 V for RH-850 °C, 451 V < 520 V < 556 V for RH-650 °C, and 481 V < 558 V < 607 V for RH-750 °C. These results indicate that the ΔV values for RH-850 °C were the lowest across all voltage tests, and the charge-discharge intersection angle formed an acute angle. Meanwhile, the discharge voltage changes (ΔV) for RH-650 °C and RH-750 °C followed a similar increasing trend. Additionally, as the voltage increased from 1.2 V to 1.5 V, the charge-discharge curves for RH-650 °C (brown line) became more arc-shaped, while the discharge voltage gradually decreased. In contrast, the RH-750 °C (red line) displayed the largest discharge

voltage change (ΔV) of $481 \text{ V} < 558 \text{ V} < 607 \text{ V}$, forming larger, symmetrical triangles and maintaining a steady increase.

Figure 6 illustrates the pronounced impact of activation temperature on the pore structure of RH-AC/KOH electrodes. At $650 \text{ }^\circ\text{C}$ (Fig. 6(a)), the RH-AC electrode exhibits a predominantly microporous structure, with micropores (0.35–2 nm) accounting for 62.01 % of the total porosity, along with a notable fraction of small mesopores (2–10 nm) comprising 34.57 %. Figure 6(b) shows that increasing the activation temperature to $750 \text{ }^\circ\text{C}$ leads to a clear shift in pore distribution: microporosity decreases to 52.69 %, while mesoporosity increases to 40.58 %. This trend reflects progressive pore widening, which is attributed to more intense KOH activation at higher temperatures. Furthermore, at $850 \text{ }^\circ\text{C}$ (Fig. 6(c)), the RH-AC/KOH electrode undergoes a dramatic structural transformation, with mesopores dominating at 89.98 % and micropores nearly disappearing to 0.04 %. This suggests that excessive activation at this temperature may lead to overdevelopment of mesopores and potential pore collapse. These results demonstrate the temperature-dependent tunability of the pore network, whereby elevated temperatures promote the formation of mesopores that enhance ion transport. However, this enhancement may come at the expense of a reduced specific surface area. This highlights the importance of optimizing activation conditions to achieve a balanced pore structure for optimal electrochemical performance.

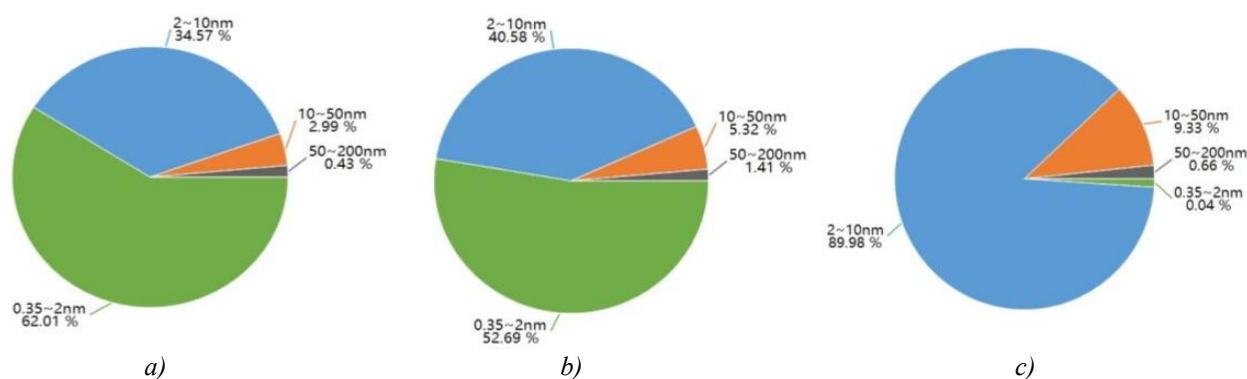


Figure 6. Pore volume distribution maps for RH-AC/KOH at $650 \text{ }^\circ\text{C}$ (a), $750 \text{ }^\circ\text{C}$ (b), and $850 \text{ }^\circ\text{C}$ (c) activated electrodes

This analysis confirms that the RH- $750 \text{ }^\circ\text{C}$ sample exhibits stable and high capacitance across a broad voltage range. Notably, it maintains superior performance at a current density of $0.2 \text{ A}\cdot\text{g}^{-1}$ under voltages higher than 1.5 V , demonstrating superior desirable characteristics for energy storage applications in supercapacitors.

Conclusions

Cyclic voltammetry (CV) tests reveal the electrochemical behavior of activated carbon samples, with RH-AC/KOH synthesized at $750 \text{ }^\circ\text{C}$ demonstrating the highest capacitance retention ($159\text{--}165 \text{ F}\cdot\text{g}^{-1}$). This superior performance is likely due to its optimized microporosity and enhanced conductivity, making it the most effective cathode material for supercapacitors. Electrochemical analysis, including galvanostatic charge-discharge (GCD) and electrochemical impedance spectroscopy (EIS), further confirms that RH-AC/KOH at $750 \text{ }^\circ\text{C}$ achieves the highest current density and maintains stable performance across a voltage range of $0.6\text{--}1.5 \text{ V}$, exhibiting the longest discharge duration. Comparing the specific current change (ΔSc) at low potentials ($0.6\text{--}1.0 \text{ V}$) among four samples of AC/NaOH at $850 \text{ }^\circ\text{C}$ and RH-AC/KOH at $650 \text{ }^\circ\text{C}$, $750 \text{ }^\circ\text{C}$ and $850 \text{ }^\circ\text{C}$ reveals the following trend: $281.2 > 269.2 > 267.6 > 190.5 \text{ mA}\cdot\text{g}^{-1}$. At higher potentials ($1.2\text{--}1.5 \text{ V}$), the ΔSc values follow the order: $341.9 \approx 340.0 > 314.6 > 247.8 \text{ mA}\cdot\text{g}^{-1}$. These results indicate that the AC/NaOH sample at $850 \text{ }^\circ\text{C}$ possesses the highest electrode density. However, the RH-AC/KOH sample treated at $750 \text{ }^\circ\text{C}$ exhibits the highest current density, compared the other RH-AC samples modified at different temperatures. Overall, the electrochemical data highlight the RH-AC/KOH sample treated at $750 \text{ }^\circ\text{C}$ as the most efficient electrode material. It delivers stable, high capacitance across different voltage levels and maintains superior performance at a current density of $0.2 \text{ A}\cdot\text{g}^{-1}$ above 1.5 V . The excellent electrochemical properties of rice husk-derived activated carbon synthesized at $750 \text{ }^\circ\text{C}$ underscore its strong potential as an advanced electrode material for supercapacitor energy storage. Its optimized porosity, improved electrical conductivity, and superior charge retention ensure high capacitance stability

over a broad voltage range. These attributes not only enhance energy storage efficiency but also indicate long-term durability and performance reliability, making it a promising candidate for next-generation supercapacitor applications in sustainable energy systems.

Funding

This research was funded by the Committee of Science of the Ministry of Science and Higher Education of the Republic of Kazakhstan (Grant No. BR27198045).

*Author Information**

**The authors' names are presented in the following order: First Name, Middle Name and Last Name*

Nurbatyr Mukhametgazy — PhD, Satbayev University, 22a Satpaev str., 050013, Almaty, Kazakhstan; e-mail: nurbatyr.kaz@gmail.com; <https://orcid.org/0000-0001-5957-0305>

Kamila Maksatovna Temirkulova — 2nd year Master's Student, al-Farabi Kazakh National University, 71 Al-Farabi Ave., 050040; Satbayev University, 22a Satpaev str., 050013, Almaty, Kazakhstan; e-mail: t.kamila.m@mail.ru; <https://orcid.org/0009-0008-7238-0432>

Balauza Balgabayeva — 1st year Master's Student, al-Farabi Kazakh National University, 71 Al-Farabi Ave., 050040; Satbayev University, 22a Satpaev str., 050013, Almaty, Kazakhstan; e-mail: balauza.balgabayeva002@gmail.com

Bekzat Gadylyuly Khamzin — 1st year Master's Student, al-Farabi Kazakh National University, 050040, 71 Al-Farabi Ave.; Satbayev University, 22a Satpaev str., 050013, Almaty, Kazakhstan; e-mail: bekzatkhamzin@gmail.com; <https://orcid.org/0009-0003-7216-6552>

Seitkhan Azat — PhD, Associate Professor, Satbayev University, 22a Satpaev str., 050013, Almaty, Kazakhstan; e-mail: seytkhan.azat@gmail.com; <https://orcid.org/0000-0002-9705-7438>

Zhazira Asilbekovna Supiyeva (*corresponding author*) — PhD, Acting Associate Professor, al-Farabi Kazakh National University, 71 Al-Farabi Ave., 050040; Satbayev University, 22a Satpaev str., 050013, Almaty, Kazakhstan; e-mail: Zhazira.Supiyeva@kaznu.edu.kz; <https://orcid.org/0000-0002-5221-8605>

Qamar Abbas — Associate Professor, Poznan University of Technology, Poznan 60965, Poland; Graz University of Technology, Stremayrgasse 9, 8010 Graz, Austria; e-mail: qamar.abbas@put.poznan.pl; <https://orcid.org/0000-0002-1169-1906>

Author Contributions

The manuscript was written through contributions of all authors. All authors have given approval to the final version of the manuscript. **CRedit**: **Nurbatyr Mukhametgazy** investigation, formal analysis, visualization, writing-original draft; **Kamila Maksatovna Temirkulova** investigation, formal analysis, visualization; **Balauza Balgabayeva** resources, data curation, validation; **Bekzat Gadylyuly Khamzin** formal analysis, visualization; **Seitkhan Azat** resources, funding acquisition, validation; **Zhazira Asilbekovna Supiyeva** funding acquisition, project administration, supervision, methodology, validation, writing-review & editing; **Qamar Abbas** conceptualization, methodology, writing-review & editing.

Acknowledgments

Authors gratefully acknowledge Satbayev University for providing access to library and research facilities that supported the completion of this work.

Conflicts of Interest

The authors declare no conflict of interest.

References

- Hassan, M.F., Sabri, M.A., Fazal, H., Hafeez, A., Shezad, N., & Hussain, M. (2020). Recent trends in activated carbon fibers production from various precursors and applications — A comparative review. *Journal of Analytical and Applied Pyrolysis*, 145, 104715. <https://doi.org/10.1016/j.jaap.2019.104715>

- 2 Pantrangi, M., Sambasivam, S., & Ran, F. (2022). Recent progress on biomass waste derived activated carbon electrode materials for supercapacitors applications — A review. *Journal of Energy Storage*, 54, 105290. <https://doi.org/10.1016/j.est.2022.105290>
- 3 Sevilla, M., & Mokaya, R. (2014). Energy storage applications of activated carbons: supercapacitors and hydrogen storage. *Energy Environ. Sci.*, 7(4), 1250–1280. <https://doi.org/10.1039/c3ee43525c>
- 4 De, S., Acharya, S., Sahoo, S., & Chandra Nayak, G. (2020). Present status of biomass-derived carbon-based composites for supercapacitor application. *Nanostructured, Functional, and Flexible Materials for Energy Conversion and Storage Systems*, 373–415. <https://doi.org/10.1016/b978-0-12-819552-9.00012-9>
- 5 Pavlenko, V.V., Abbas, Q., Przygocki, P., Kon'kova, T., Supiyeva, Z., Abeykoon, N., Prikhodko, N., Bijsenbayev, Kurbatov, M. A., Lesbayev, B.T., & Mansurov, Z.A. (2018). Temperature dependent characteristics of activated carbons from walnut shells for improved supercapacitor performance. *Eurasian Chemico-Technological Journal*, 20(2), 99–105. <https://doi.org/10.18321/ectj695>
- 6 Yerdauletov, M.S., Nazarov, K., Mukhametuly, B., Yeleuov, M.A., Daulbayev, C., Abdulkarimova, R., Yskakov, A., Napol'skiy, F., & Krivchenko, V. (2023). Characterization of Activated Carbon from Rice Husk for Enhanced Energy Storage Devices. *Molecules*, 28, 5818. <https://doi.org/10.3390/molecules28155818>
- 7 Supiyeva, Zh., Pan, X., & Abbas, Q. (2023). The critical role of nanostructured carbon pores in supercapacitors. *Current Opinion in Electrochemistry*, 39, 101249. <https://doi.org/10.1016/j.coelec.2023.101249>
- 8 Mensah-Darkwa, K., Agyemang, F.O., Akromah, S., Arthur, E. K., Abdallah, F., & Gikunoo, E. (2021). A comparative study on the performance of activated carbon electrodes and activated carbon/titanium dioxide nanotubes hybrid electrodes. *Scientific African*, 12, e00786. <https://doi.org/10.1016/j.sciaf.2021.e00786>
- 9 Reza, M.S., Yun, Ch.S., Afroze, Sh., Radenahmad, N., Abu Bakar, M.S., Saidur, R., Taweekun, J. & Azad, A.K. (2020). Preparation of activated carbon from biomass and its' applications in water and gas purification, a review. *Arab Journal of Basic and Applied Sciences*, 27:1, 208–238. <https://doi.org/10.1080/25765299.2020.1766799>
- 10 Gu, W., & Yushin, G. (2014). Review of nanostructured carbon materials for electrochemical capacitor applications: advantages and limitations of activated carbon, carbide-derived carbon, zeolite-templated carbon, carbon aerogels, carbon nanotubes, onion-like carbon, and graphene. *Wiley Interdisciplinary Reviews: Energy and Environment*, 3(5), 424–473. <https://doi.org/10.1002/wene.102>
- 11 Ntone, E.P.N., Samah, R.A., Wahab, M.S.A., Alsahy, Q.F. & Rahman, S.A. (2025). Review of PPCPs remediation in Asia: the role of agricultural waste in adsorption-membrane hybrid technology. *Chemical Engineering Communications*, 1–35. <https://doi.org/10.1080/00986445.2024.2447843>
- 12 Wu, F.C., Tseng, R.L., Hu, C.C., & Wang, C.C. (2005). Effects of pore structure and electrolyte on the capacitive characteristics of steam-and KOH-activated carbons for supercapacitors. *Journal of Power Sources*, 144(1), 302–309. <https://doi.org/10.1016/j.jpowsour.2004.12.020>
- 13 Liu, P., Verbrugge, M., & Soukiazian, S. (2006). Influence of temperature and electrolyte on the performance of activated-carbon supercapacitors. *Journal of Power Sources*, 156(2), 712–718. <https://doi.org/10.1016/j.jpowsour.2005.05.055>
- 14 Jackel, N., Weingarh, D., Schreiber, A., Krüner, B., Zeiger, M., Tolosa, A., Aslan, M. & Presser, V. (2016). Performance evaluation of conductive additives for activated carbon supercapacitors in organic electrolyte. *Electrochimica Acta*, 191, 284–298. <https://doi.org/10.1016/j.electacta.2016.01.065>
- 15 Du, X., Zhao, W., Wang, Y., Wang, C., Chen, M., Qi, T., etc. & Ma, M. (2013). Preparation of activated carbon hollow fibers from ramie at low temperature for electric double-layer capacitor applications. *Bioresour. Technol.*, 149, 31–37. <https://doi.org/10.1016/j.biortech.2013.09.026>
- 16 Tseng, R.L., Tseng, S.K., Wu, F.C., Hu, C.C., & Wang, C.C. (2013). Effects of micropore development on the physicochemical properties of KOH-activated carbons. *Journal of the Chinese Institute of Chemical Engineers*, 39(1), 37–47. <https://doi.org/10.1016/j.jcice.2007.11.005>
- 17 Lee, Kuan-Ching and Lim, Mitchell and Hong, Zhong-Yun and Chong, Siewhui and Tiong, Joyce and Pan, Guan-Ting and Huang, Chao-Ming (2021). Coconut Shell-Derived Activated Carbon for High-Performance Solid-State Supercapacitors. *Energies*, 14(15), 45–46. <https://doi.org/10.3390/en14154546>
- 18 Ranjeet Kumar Mishra, Bineta Singh, Bishnu Acharya (2024). A comprehensive review on activated carbon from pyrolysis of lignocellulosic biomass: An application for energy and the environment. *Carbon Resources Conversion*, 7(4). 100228. <https://doi.org/10.1016/j.crcon.2024.100228>
- 19 Yang, Juan & Qiu, Keqiang. (2010). Preparation of Activated Carbons from Walnut Shells via Vacuum Chemical Activation and Their Application for Methylene Blue Removal. *Chemical Engineering Journal*, 165, 209–217. <https://doi.org/10.1016/j.cej.2010.09.019>
- 20 Harshal Kulkarni, Chandresh Bari, Sagnik Mukherjee, Prayag Gajera, Govind Sethia (2024). Waste biomass-derived activated carbons for selective oxygen adsorption. *Carbon Trends*, 17, 100398. <https://doi.org/10.1016/j.cartre.2024.100398>
- 21 Smagulova, G., Imash, A., Baltabay, A., Kaidar, B., & Mansurov, Z. (2022). Rice-Husk-Based Materials for Biotechnological and Medical Applications. *MDPI Carbons*, 8(4), 55. <https://doi.org/10.3390/c8040055>
- 22 Azat, S., Korobeinyk, A.V., Moustakas, K., & Inglezakis, V.J. (2019). Sustainable production of pure silica from rice husk waste in Kazakhstan. *Journal of Cleaner Production*, 217, 352–359. <https://doi.org/10.1016/j.jclepro.2019.01.142>
- 23 Kurmanbayeva, I., Mentbayeva, A., Sadykova, A., Adi, A., Mansurov, Z., & Bakenov, Z. (2019). Silica from Kazakhstan Rice Husk as an Anode Material for LIBs. *Eurasian Chemico-Technological Journal*, 1, 75. <https://doi.org/10.18321/ectj794>

- 24 Mansurov, Z.A., Smagulova, G.T., Sultanov, F.R., Kaidar, B.B., Insepov, Z., & Imash, A.A. (2022). Production of activated and Graphene-Like Carbon Materials from rice husk. *Materials Science*, 2210–08352. <https://doi.org/10.48550/arXiv.2210.08352>
- 25 Battalova, A., Ibraeva, Z., Kabdrakhmanova, S., Akatan, K., Shaimardan, E., Demeukhan, A., Tursyngazykyzy, A., Beisebekov, M., & Maussumbayeva, A. (2024). Comparative characteristics of microcrystalline cellulose obtained from the rice waste production of Kazakhstan. *Chemical Bulletin of Kazakh National University*, 113(4), 14–23. <https://doi.org/10.15328/cb1386>
- 26 Zhu, G., Deng, X., Hou, M., Sun, K., Zhang, Y., Li, P., & Liang, F. (2016). Comparative study on characterization and adsorption properties of activated carbons by phosphoric acid activation from corncob and its acid and alkaline hydrolysis residues. *Fuel Processing Technology*, 144, 255–261. <https://doi.org/10.1016/j.fuproc.2016.01.007>
- 27 Kierzek, K., & Gryglewicz, G. (2020). Activated carbons and their evaluation in electric double layer capacitors. *Molecules*, 25(18), 4255. <https://doi.org/10.3390/molecules25184255>
- 28 Song H, Qu Q, Yang Z, Zhang Y, Qiu L, Zhao Y, Li C, Zhu M, & Yang X. (2025). Supercapacitor Performance of Activated Carbon from *Eucommia Ulmoides* Oliver Wood Optimized by the Activation Method. *ACS Omega*, 10(15), 15368–15380. <https://doi.org/10.1021/acsomega.4c11529>
- 29 Bergna, D., Hu, T., Prokkola, H. Prokkola, H., Romar, H., & Lassi, U. (2020). Effect of Some Process Parameters on the Main Properties of Activated Carbon Produced from Peat in a Lab-Scale Process. *Waste Biomass Valor*, 11, 2837–2848. <https://doi.org/10.1007/s12649-019-00584-2>
- 30 Foo, K.Y., & Hameed, B.H. (2012). Preparation and characterization of activated carbon from pistachio nut shells by microwave-induced chemical activation: Application for methylene blue adsorption. *Chemical Engineering Journal*, 180, 66–74. <https://doi.org/10.1016/j.cej.2011.11.044>
- 31 Nahil, M.A., & Williams, P.T. (2012). Characterisation of Activated Carbons with High Surface Area and Variable Porosity Produced from Agricultural Cotton Waste by Chemical Activation and Co-activation. *Waste Biomass Valor* 3, 117–130. <https://doi.org/10.1007/s12649-012-9109-7>
- 32 Jiang, Q., Zhang, Q., Du, B., Zou, R.L., Liu, Y.H., & Zhao, Y. (2008). Effects of activation time on the electrochemical capacitance of activated carbon nanotubes. *Journal of Materials Science: Materials in Electronics*, 19, 241–245. <https://doi.org/10.1007/s10854-007-9291-8>
- 33 Wang, D.W., Li, F., Liu, M., Lu, G. Q., & Cheng, H.M. (2008). 3D aperiodic hierarchical porous graphitic carbon material for high-rate electrochemical capacitive energy storage. *Angewandte Chemie International Edition*, 47(2), 373–376. <https://doi.org/10.1002/anie.200704528>
- 34 Wang, J., & Kaskel, S. (2012). KOH activation of carbon-based materials for energy storage. *Journal of Materials Chemistry*, 22(45), 23710–23725. <https://doi.org/10.1039/c2jm34066f>
- 35 Supiyeva, Zh., Avchukir, Kh., Pavlenko, V., Yeleuov, M., Taurbekov, A., Smagulova, G., & Mansurov, Z. (2020). The investigation of electroreduction of AuCl₄ in the case of gold electroreduction using activated carbon. *Materials Today: Proceedings*, S2214785319336958. <https://doi.org/10.1016/j.matpr.2019.11.013>
- 36 Pavlenko, V., & Supiyeva, Z. (2020). Application of Carbons Produced from Rice Husk in the Process of Capacitive Deionization. *Eurasian Chemico-Technological Journal*, 22(4), 277–284. <https://doi.org/10.18321/ectj996>
- 37 Taurbekov, A., Abdisattar, A., Atamanov, M., Yeleuov, M., Daulbayev, C., Askaruly, K., Kaidar, B., Mansurov, Z., Castro-Gutierrez, J., Celzard, A., et al. (2023). Biomass Derived High Porous Carbon via CO₂ Activation for Supercapacitor Electrodes. *Journal of Composites Science*, 7(10), 444. <https://doi.org/10.3390/jcs7100444>
- 38 Zhang, Z.J., Xie, D.H., Cui, P., & Chen, X.Y. (2014). Conversion of a zinc salicylate complex into porous carbons through a template carbonization process as a superior electrode material for supercapacitors. *RSC advances*, 4(13), 6664–6671. <https://doi.org/10.1039/C3RA44981E>

INORGANIC CHEMISTRY

Article

Received: 25 February 2025 | Revised: 5 May 2025 |
Accepted: 22 May 2025 | Published online: 28 May 2025

UDC 546.26+546.171.1

<https://doi.org/10.31489/2959-0663/2-25-2>

Nina M. Ivanova^{1*}, Zainulla M. Muldakhmetov¹, Yakha A. Vissurkhanova^{1,2},
Yelena A. Soboleva¹, Askhat S. Borsynbayev²

¹LLP "Institute of Organic Synthesis and Coal Chemistry of the Republic of Kazakhstan", Karaganda, Kazakhstan;

²Karaganda Buketov University, Karaganda, Kazakhstan

(*Corresponding author's e-mail: nmiva@mail.ru)

N-Containing Graphene Preparation Using Melamine as a Nitrogen Source

N-doped graphene is not only a promising metal-free catalyst, but also a convenient carrier of metal nanoparticles for the creation of effective catalysts. Graphitic carbon nitride (g-C₃N₄) is used more often in photocatalytic processes and less often as electrocatalysts. This paper describes the preparation of N-containing carbon composites consisting of reduced graphene oxide (rGO) and g-C₃N₄ for the further creation of metal-carbon catalytic systems. These composites were prepared by the heat treating dry mixtures of graphene oxide (GO) and melamine (MA) in the temperature range of 450–550 °C in air. Oxygen-containing groups were identified in the graphene oxide samples synthesized by the modified Hummers method and in its reduced form. The thermogravimetric analysis method was used to determine the ranges of relative thermal stability of the GO + MA mixtures, which were found to be almost identical for the studied compositions with different component ratios. The structure of the graphene oxide and its composites with MA after heat treatment was studied by scanning electron spectroscopy, X-ray diffraction analysis, FTIR spectroscopy and elemental analysis. The effect of the ratio of the initial components on the formation of the heat treatment products was determined. It was shown that to obtain the rGO+g-C₃N₄ composites with a high content of carbon nitride, the ratio of the initial reagents should be taken equal to 1:2, and the heat treatment should be carried out at 550 °C.

Keywords: graphene oxide, oxygen-containing functional groups, melamine, "dry" preparation method, heat treatment, reduced graphene oxide, graphitic carbon nitride, elemental content

Introduction

The incorporation of nitrogen atoms into the structure of the carbon materials diversifies and improves their properties compared to their unmodified analogs. This is excellently confirmed by studies on the use of N-doped graphene as electrocatalysts in the oxygen reduction reaction [1–3]. There are many papers in the literature describing various methods for the synthesis of N-doped graphene, including chemical vapor deposition, thermal annealing, pyrolysis, arc-discharge, plasma treatment, hydrothermal and solvothermal methods, wet chemical synthesis, microwave treatment, and others [4]. The most popular and more accessible method for N-doping of graphene is the thermal treatment of graphene oxide (GO) in the presence of a nitrogen source, which can be ammonia, polyaniline, melamine, urea, polypyrrole or other nitrogen-containing substances. The most common N-precursor used to dope graphene is melamine, in which has at nitrogen content of 66.7 % by weight. For example, by carrying out ultrasonic treatment (UST) and prolonged stirring of a GO suspension in an aqueous solution of melamine, drying and heat treatment at 900 °C in a vacuum, N-doped graphene was prepared with a large surface area and a high percentage of pyridinic and graphitic N sites has been prepared, which determines its effective use in the electrocatalytic reduction of oxygen [5].

Most often, the heat treatment of GO with melamine mixtures is carried out in an inert atmosphere to prevent their rapid oxidation. Therefore, the authors of [6] performed the pyrolysis of GO + melamine samples, prepared from their suspension, at temperatures of 700–1000 °C in an argon environment to produce N-doped graphene. The dry mixtures of GO and melamine were also subjected to heat treatment at 800 °C in an argon atmosphere to form N-G samples, in which the atomic nitrogen content reached 10.1 % [7]. At the same time, in [8], based on thermogravimetric analysis (TGA), it was shown that the mass loss of the GO/melamine mixture when heated in a nitrogen environment and in air is almost the same, and the composition of the TGA products, according to X-ray photoelectron spectroscopy analysis, is the same. It was assumed that melamine can effectively prevent GO oxidation in air.

Due to the presence of various functional groups on the surface and the possibility of their further modification, high surface area, excellent transport, optical properties, and a number of other properties, N-doped graphene finds its application in the purification of wastewater from heavy metal ions, dye molecules and drugs, in the preparation of electrodes for electrochemical capacitors, fuel cells, as well as electrocatalysts, photocatalysts, catalysts and their carriers, in medicine and other fields of science and technology [4, 9–11].

In this paper, the investigations were conducted to prepare N-containing graphene, mainly consisting of reduced graphene oxide and graphitic carbon nitride (rGO + g-C₃N₄), for the further creation of catalysts from metal nanoparticles deposited on the N-modified graphene support. Melamine (MA) was used as a nitrogen source. The mechanically prepared GO+MA mixtures with different ratios of their components were heat-treated in the temperature range of 450–550 °C in closed crucibles in the air atmosphere of a muffle furnace. A detailed study of the structure, phase constitution and morphological characteristics of the products obtained after the thermal treatment was carried out.

Experimental

Materials

In the studies, graphite with a carbon content of ~99 % and particle sizes of 0–50 μm was used as the initial material for the preparation of the chemically modified forms of graphene. The chemical reagents, such as sulfuric acid H₂SO₄, potassium permanganate KMnO₄, hydrochloric acid HCl, and hydrogen peroxide were purchased from “Karagandareactivsbyt” LLP (Karaganda, Kazakhstan). Melamine was purchased from Sigma-Aldrich. Distilled water was used to prepare the required solutions and to wash the prepared carbon samples.

Oxide Graphene Preparation

The oxidation of the graphite was carried out using one of the modified Hummers methods [12]. In a typical synthesis, 100 ml of concentrated sulfuric acid were added to 4 g of graphite. The reaction mixture was stirred for 4 h at room temperature. Then, 12 g of potassium permanganate was added in portions, maintaining the temperature of the mixture below 10 °C. The resulting mixture was stirred for 8 h. As a result, a thick dark brown suspension was formed. Then, 200 ml of distilled water with 20 ml of a 30 % hydrogen peroxide solution were slowly added dropwise. Stirring was continued for another 30 min. The resulting suspension was filtered, and washed with 200 ml of 5 % hydrochloric acid solution and 1000 ml of distilled water to pH 7. The precipitate was dried at 50 °C. As a result, a loose black GO powder weighing 5.5 g was produced.

In order to study the change in the degree of functionalization of graphene oxide prepared by this method, the GO sample was sonicated at a power of 900 W for 1 h.

The presence of oxygen-containing functional groups (hydroxyl, carboxyl and epoxy) and their amount in the synthesized graphene oxide samples were determined by acid-base titration using the Boehm method, which is based on the fact that groups of different types have different acidities and can be neutralized by bases of different strengths [13, 14].

Preparation of the GO + MA mixed compositions and their heat treatment

Samples of mixtures from the synthesized graphene oxide and melamine (GO + MA) were prepared by a “dry” method, which consists of mixing GO and MA powders in mass ratios of 1:1, 1:2 and 1:5 and thoroughly grinding them in a mortar. The resulting dry mixtures of a certain mass were placed in crucibles with closed lids and heat-treated in a muffle furnace at 450, 500 and 550 °C for 3 h.

Characterization

IR spectra were recorded on an FSM 1201 Infrared Fourier spectrometer (LLC “Infraspek”, Russia) for the initial graphite, the prepared graphene oxide samples with and without heat treatment (HT), as well as the heat-treated GO + MA mixtures. Their phase compositions were determined using a D8 ADVANCE ECO diffractometer (Bruker, Germany) in CuK α radiation in the angle range (2θ) 5–90°. The morphological features of the oxide graphene and its mixtures with MA were studied on a TESCAN MIRA 3 (Czech Republic) scanning electron microscope (SEM). Elemental microanalysis of the samples was performed using an X-Act energy dispersive detector (Oxford Instruments), and an Elemental Analyser EA3100 (EuroVector, Italy).

Results and Discussion

The content of oxygen-containing functional groups in the initial graphite and in the graphene oxide samples synthesized three times using the same route was determined by acid-base titration according to the Boehm method [13, 14]. All the obtained GO samples contained the three types of tested functional groups in approximately equal amounts in all three samples (Table 1). Ultrasonic treatment of GO for 1 h resulted in a slight decrease in the total amount of oxygen-containing groups, but the content of hydroxyl groups significantly decreased, while that of carboxyl and epoxy groups, on the contrary, increased. In the reduced graphene oxide prepared by chemical reduction using hydrazine hydrate, hydroxyl and carboxyl groups are absent and the epoxy groups remain in small amounts. In the thermally reduced graphene oxide, all detectable oxygen-containing groups were present, but the amount of epoxy groups increased significantly (Table 1). Partial preservation of the oxygen-containing groups in the reduced graphene samples was also observed in previous studies [15–17]. Surprisingly, the original graphite was also found to contain a small amount of epoxy groups (Table 1).

Table 1

Content of the functional groups in the original graphite and in the synthesized GO and rGO samples

GO samples	Sample weight, g	Total number of groups, mmol/g	Number of hydroxyl groups, mmol/g	Number of carboxyl groups, mmol/g	Number of epoxy groups, mmol/g
G	0.50	0.38	–	–	0.38
GO-1	0.50	5.02	1.54	2.80	0.68
GO-1 + UST	0.50	4.94	0.48	3.18	1.28
GO-2	0.20	5.05	1.56	2.85	0.64
GO-3	0.20	5.00	1.62	2.78	0.60
rGO-1, chem. red.	0.50	0.36	–	–	0.36
rGO, 450°C, 2 h	0.05	3.90	0.60	0.87	2.43

The presence of oxygen-containing groups in the graphene oxide was confirmed by the IR spectra obtained for one of its samples (Figure 1, spectrum 2). The broad band in the region of 3450 cm⁻¹ is attributed to the hydroxyl group, which indicates the presence of adsorbed water in this sample. The band at 1728 cm⁻¹ is related to the deformation vibrations of the C=O bond in the carboxyl or carbonyl groups. The peaks at 1624, 1385, 1227 and 1061 cm⁻¹ can be attributed to the stretching vibrations of the C=C, C–OH, C–O–C and C–O bonds. These results are in good agreement with the descriptions of the IR spectra of graphene oxide in previous studies [15, 18, 19]. Most of these peaks are absent in the structure of the graphite and thermally reduced graphene oxide (Figure 1, spectra 1 and 3).

X-ray diffraction (XRD) analyses were performed for the initial graphite, graphene oxide and chemically reduced graphene oxide. The XRD pattern of graphite (Figure 2) shows a clear diffraction peak at 26.4° with the (002) phase, corresponding to the hexagonal arrangement of atomic layers with an interplanar distance of $d = 3.37$ Å, in agreement with the literature data [15].

In the XRD pattern of graphene oxide GO, the peak for the (002) phase is shifted to the region of smaller angles ($2\theta = 12.5^\circ$) due to an increase in the interplanar distance (7.08 Å) during the oxidation of graphite. This confirms the presence of oxygen-containing functional groups in the GO structure. In the reduced graphene oxide rGO, the interplanar distance decreases again without preserving the crystal structure due to the loss of some of the functional groups. Its XRD pattern shows a broad peak for the (002) phase with a slight shift towards smaller angles ($2\theta = \sim 24.5^\circ$) (Figure 2). The particle sizes of the graphene in this phase, calculated using the Debye-Scherrer method within the diffractometer software, are ~ 17 nm. There is also a low and broadened peak for the (101) phase in the angle range $2\theta = \sim 43\text{--}44^\circ$.

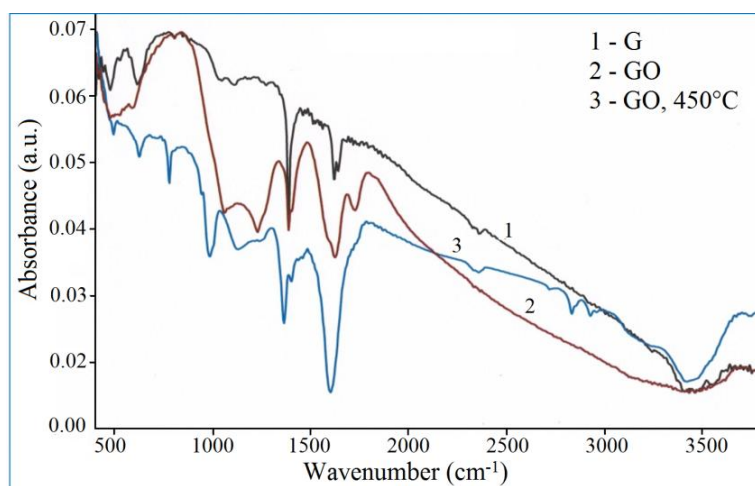


Figure 1. IR spectra of graphite (1), graphene oxide (2), and graphene oxide heated at 450 °C (3)

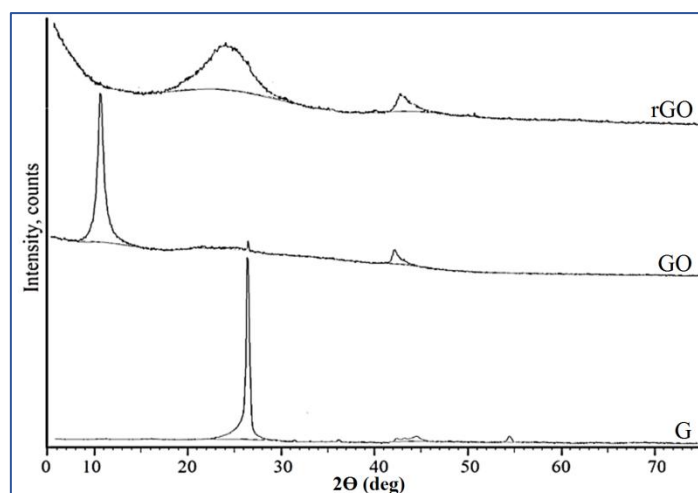


Figure 2. XRD patterns of graphite G, graphene oxide GO and chemically reduced graphene oxide rGO

The morphology of the synthesized graphene oxide has been studied using an electron microscope; its micrographs are shown in Figure 3. As known from the literature, the implantation of functional groups overcomes the van der Waals sheets and increases the distance between the layers, i.e., graphite exfoliation occurs (Figure 3, *a* and *b*). The delaminated layers in synthesized graphene oxide have different thicknesses: ~50–180 nm. When this sample is exposed to ultrasound, its structure changes and becomes curly with thin and light layers (Figure 3, *d*), but denser layers also remain (Figure 3, *c*). According to the energy-dispersive spectroscopy (EDS) analysis, GO contains elements such as carbon (~74 %), oxygen (~24 %) and small amounts of sulfur (due to the use of sulfuric acid in the syntheses). After ultrasound treatment, the oxygen content in GO decreased to 17 %, and the carbon content increased to 81 %, indicating a decrease in the oxygen-containing groups in this sample and confirming the data in Table 1.

To improve the interaction of the metal catalyst particles with the carbon carrier and to enhance the electron transport, N-doping of the graphene carbon layers have been N-doped using various methods. Most often, such modification of graphene is carried out at high temperatures (800–1000 °C) and in an inert atmosphere, which is economically and technically quite expensive. Therefore, attempts are constantly being made to simplify these methods. For example, in paper [8], the possibility of simultaneous reduction and N-doping of graphene in an air environment at a temperature of 430 °C was established and NrGO samples with high catalytic activity in the oxygen reduction reaction were prepared.

In this work, to create N-containing samples of thermally reduced graphene oxide and subsequently produce catalytic systems based on them, melamine was chosen as a nitrogen source that is a chemical compound well enriched with nitrogen and therefore often used to create N-doped carbon materials.

The GO + MA mixtures were prepared using the method of mechanical mixing of graphene oxide and melamine powders with ratios of 1:1, 1:2 and 1:5, and thermogravimetric studies of the thermal stability of these mixtures and their individual components were carried out (Figure 4).

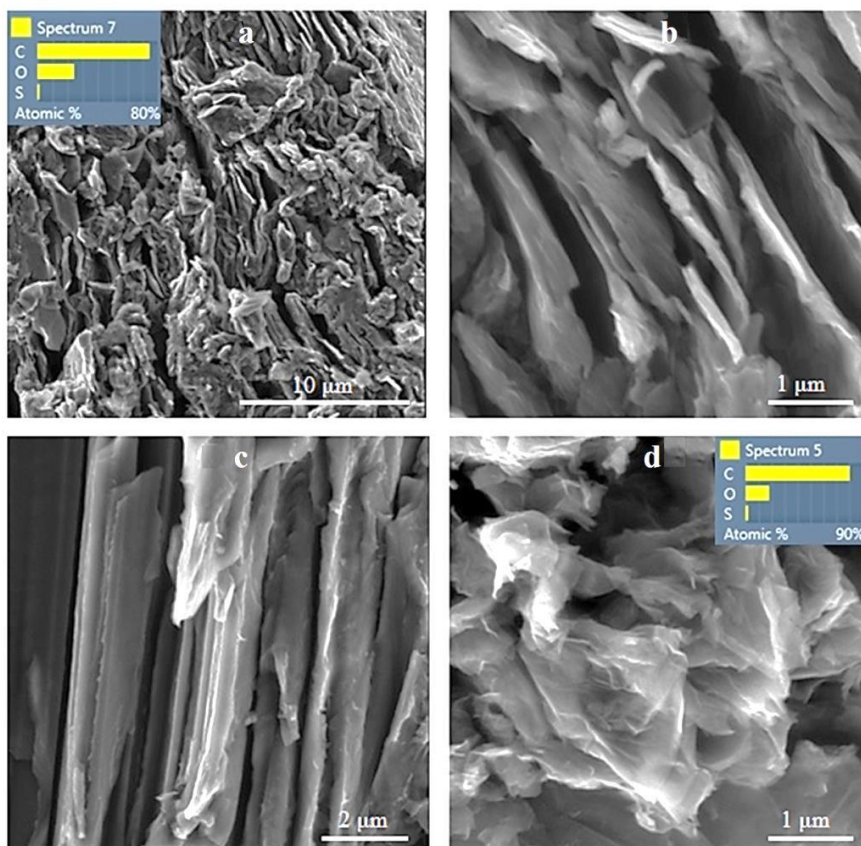


Figure 3. SEM images of synthesized GO (*a, b*) and GO+UST (*c, d*)

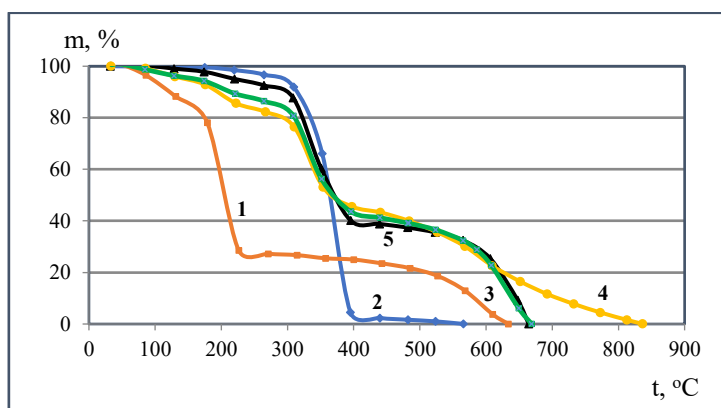


Figure 4. TGA curves for graphene oxide (*1*), melamine (*2*) and their mixtures with ratios (1:1) (*3*), (1:2) (*4*), and (1:5) (*5*)

According to the TGA data, the thermal decomposition of graphene oxide occurs in four temperature ranges with different mass losses (Figure 4, curve 1). The first is in the range of 70–180 °C with a mass loss of ~22 %, mainly due to the evaporation of the adsorbed water. In the second temperature range (~180–203 °C), a strong loss of the GO mass is observed (up to 70 % of the initial one), apparently due to the decomposition of the oxygen-containing groups. The third region (205–495 °C) is relatively stable, with a mass loss of only 10 %. In addition, the fourth region is ~500–630 °C, where the final combustion of carbon residues interacting with oxygen occurs.

Melamine is thermally stable up to almost 300 °C with a mass loss of only 6 % (Figure 4, curve 2). However, during the next 100 °C (up to 400 °C), it decomposes abruptly and completely. Mixtures of GO with melamine behave differently (Figure 4, curves 3–5). When heated to approximately 300 °C, all three GO + MA samples with different component ratios lose from 20 % (1:2 mixture) to 10 % (1:5 mixture) in mass, apparently due to changes in graphene oxide. Then, there is a sharp mass loss (by a further ~ 30 %) up to 400 °C, after which relatively horizontal sections (in the 400–550 °C range) with small mass losses appear on the TGA curves. This is followed their final combustion occurs. As suggested in [8], the presence of melamine in a mixture with graphene oxide prevents its rapid oxidation. The gases released during the decomposition of melamine, and primarily ammonia, create an atmosphere that protects graphene oxide from rapid decomposition in the air and simultaneously have an N-doping effect on graphene.

It is known from the literature [20–22] that melamine (as well as cyanamide, dicyanamide, etc.) undergoes condensation during thermal treatment in an inert atmosphere, first with the formation of melam, melem, then melon, and finally a polymer product is formed — graphitic carbon nitride, $g\text{-C}_3\text{N}_4$ (Figure 5), which is one of the allotropic formations of the polymer with the general formula $(\text{C}_3\text{N}_3\text{H})_n$. It consists of tri-s-triazine rings linked by amino groups (Figure 5). This gives it high thermal stability (600 °C in air) and chemical resistance in both acidic and alkaline environments.

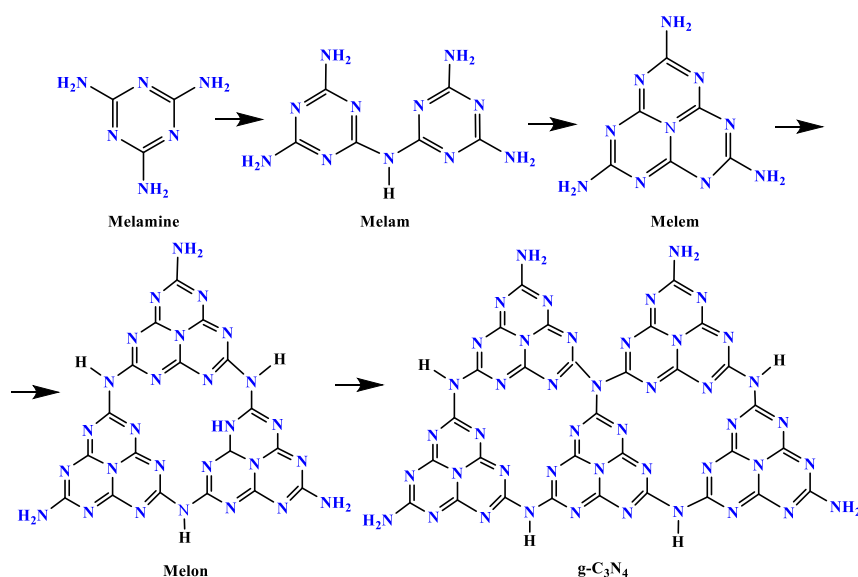


Figure 5. Scheme of the thermal transformation of melamine

In order to produce the samples of reduced graphene containing nitrogen, the mechanical mixtures of GO + MA with mass ratios of 1:1 and 1:2 were subjected to heat treatment (HT). The HT temperature was selected based on the TGA data from the region in which these mixtures retained stable, i.e. 450–550 °C (Figure 4). The powders of both components which had been ground in a mortar were placed in crucibles with closed lids and processed in a muffle furnace at the given temperature for 3 hours.

The IR spectrum of the thermal condensation products of melamine treated at 450 °C (Figure 6, *a*, spectrum 1), shows the characteristic vibrations of triazine cycles are present in the region from 1640 cm^{-1} to 1240 cm^{-1} [21]. The spectra of melamine after HT at 500 and 550 °C are similar and differ significantly from the spectrum of melamine with HT at 450 °C. These spectra show intense bands at 1616 cm^{-1} and 1470 cm^{-1} , which are related to the intermediate condensation products melem and melon (Figure 6, *a*). The first of these bands is also present in the spectrum of the GO + MA (1:1) mixture after heat treatment at 450 °C (Figure 6, *b*, spectrum 1) and overlaps with the band for the stretching vibration of the C=C bond in the benzene rings of graphene and/or for the vibration of the C=N bond in the triazine rings. The absorption bands in the region of 3100–3500 cm^{-1} in the spectra of the thermally treated melamine (Figure 6, *a*) and in the region of 3400–3550 cm^{-1} in the spectra of the GO + MA (1:1) mixture after HT (Figure 6, *b*) indicate the presence of -NH_2 and =NH groups in the resulting products, which indicates the incomplete condensation of the intermediate products and the formation of the $g\text{-C}_3\text{N}_4$ polymer product even at a temperature of 550 °C. The bands at 1362 and 1400 cm^{-1} in the spectrum of the GO + MA (1:1) mixture after heating at 500 and 550 °C may belong to the C–N bond vibrations in the carbon nitride [23].

XRD analyses were performed for the products resulting from the heat treatment of melamine and its mixtures with graphene oxide at ratios 1:1 and 1:2 (Figure 7). These analyses revealed changes in phase constitutions as the heat treatment temperature increased. This is particularly evident in the XRD patterns of both the melamine itself and the GO + MA mixtures with a change in temperature from 450 to 500 °C. The XRD pattern of melamine treated at 450 °C is represented by a set of diffraction peaks that coincide well with the XRD pattern of the intermediate compound melem (2,5,8-triamino-tri-s-triazine) [24] (its structure is shown in Figure 5).

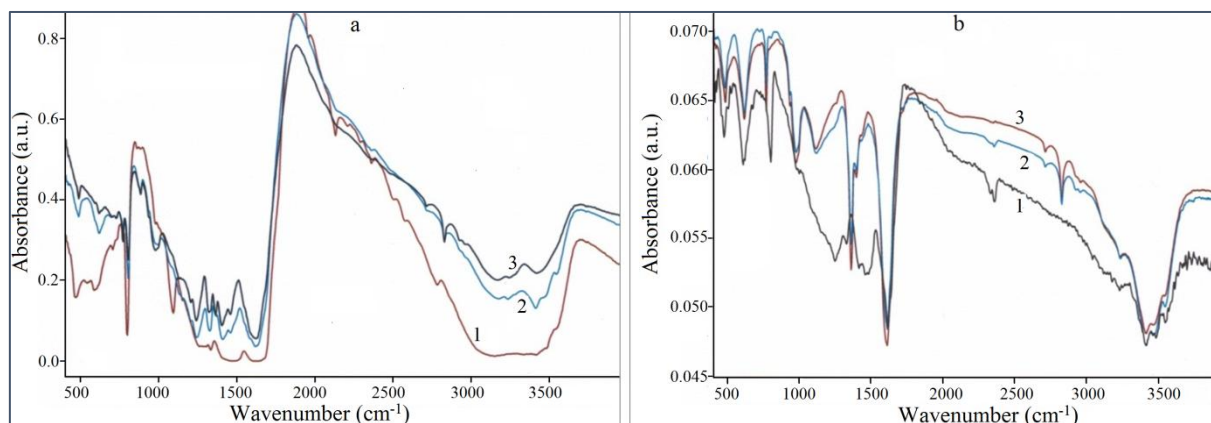


Figure 6. IR spectra of melamine (a) and GO + MA (1:1) mixtures (b) treated at 450 °C (1), 500 °C (2) and 550 °C (3)

The X-ray diffraction patterns for both GO + MA mixtures conditioned at the same temperature have flattened peaks at the same angles with a noticeably weaker intensity (Figure 7, a). When melamine is treated at 500 °C (Figure 7, b), the products formed consist mainly of graphitic carbon nitride, g-C₃N₄ (the main peaks in its standard XRD pattern are located at the angles of 27.46° and 12.93°). There are also insignificant impurities apparently of incompletely reacted melem or melon. According to the XRD pattern in Figure 7, c, the treatment of melamine at 550 °C also leads to the formation of g-C₃N₄.

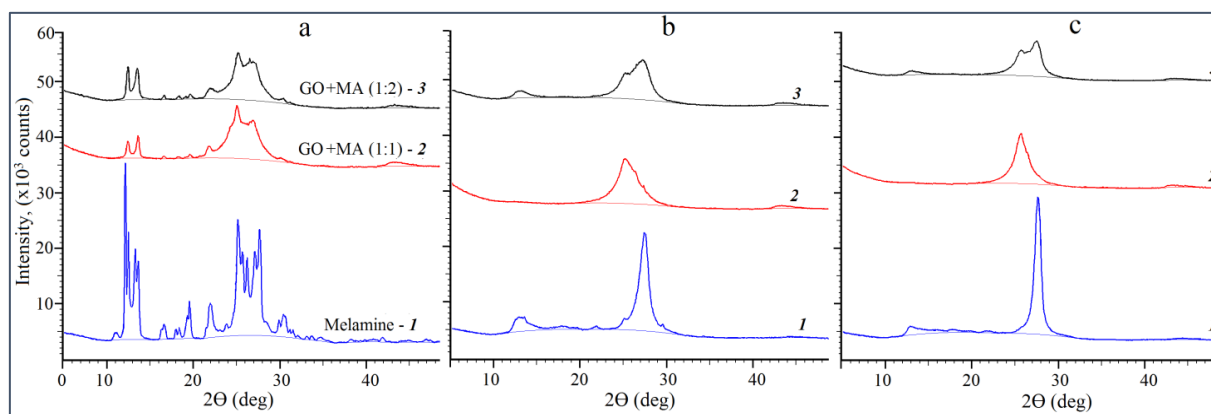


Figure 7. XRD patterns of melamine and its mixtures with graphene oxide after heat treatment at 450 °C (a), 500 °C (b) and 550 °C (c)

The XRD patterns of the GO + MA (1:1) mixture after HT at 500 and 550 °C are represented by one broad peak with a maximum at $2\theta = 25.5^\circ$, which corresponds to the (002) phase of the reduced graphene oxide ($2\theta = 24.5^\circ$, Figure 2), but with a slight shift in the diffraction angle. This peak also covers the peak at $2\theta = 27.37^\circ$, which belongs to the graphitic carbon nitride. The same peaks, but with greater intensity for g-C₃N₄, are also clearly visible in the XRD patterns of the GO + MA mixture with an increased melamine content (the ratio of the initial components was 1:2) which was thermally treated at 550 °C (Figure 7, b and c). It can therefore be concluded that during the heat treatment of the mechanically prepared mixtures of GO and melamine in the temperature range of 500–550 °C, two crystalline phases were formed: reduced graphene oxide and graphitic carbon nitride. As in previous studies [8], it is assumed that, the partial intro-

duction of nitrogen atoms into the graphene structure occurs under the action of released ammonia, resulting in the formation of N-doped reduced graphene oxide, which is most often obtained at higher temperatures and in an inert environment.

Microscopic studies of the GO + MA (1:1) mixture after heat treatment showed that in the products formed both at 450 °C and at 500 °C, the graphene layers are separated (Figure 8), and their thickness ranges from 7 to 45 nm. That is, as a result of heat treatment, multilayer graphene is formed, covered with adsorbed products of the heat-treated melamine, including g-C₃N₄.

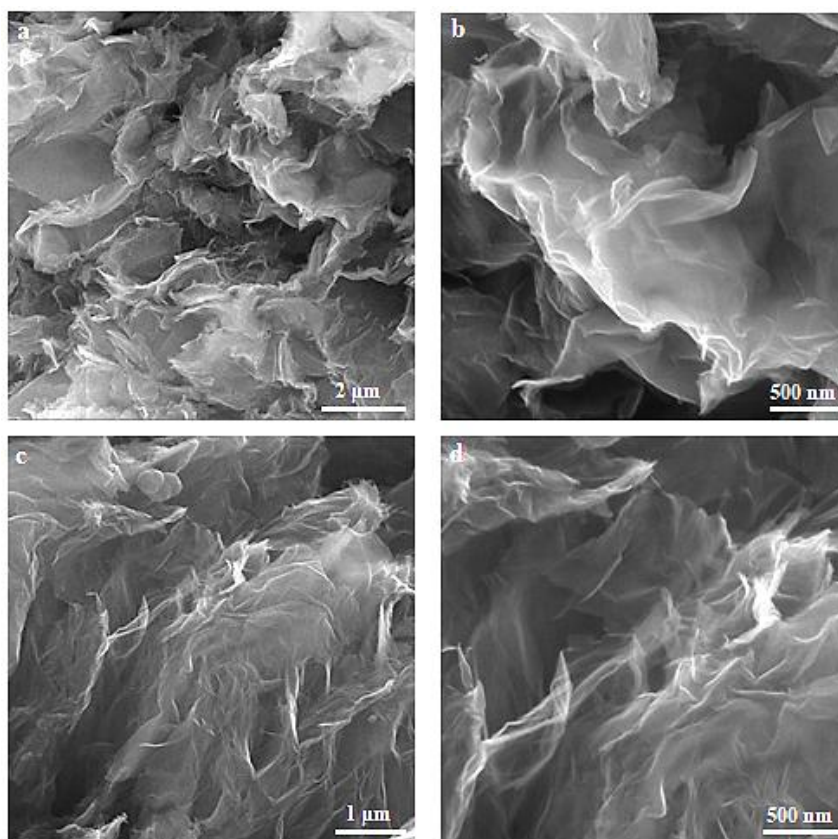


Figure 8. SEM images of the GO + MA (1:1) mixture after heat treatment at 450 °C (*a, b*) and 500 °C (*c, d*)

The distribution of chemical elements (C, N and O) over the surface of the rGO + g-C₃N₄ composite particles prepared by heat treatment of the GO + MA (1:2) mixture at 550 °C is shown in Figure 9. These EDS analyses were performed on a ZepTools ZEM20 microscope (China) using an Oxford AZtec instrument (UK). As can be seen from the images, nitrogen is distributed quite densely across the entire surface of this composite with some localization occurring in certain areas. This confirms the polymerization of intermediate compounds formed during the heat treatment of melamine and the formation of g-C₃N₄.

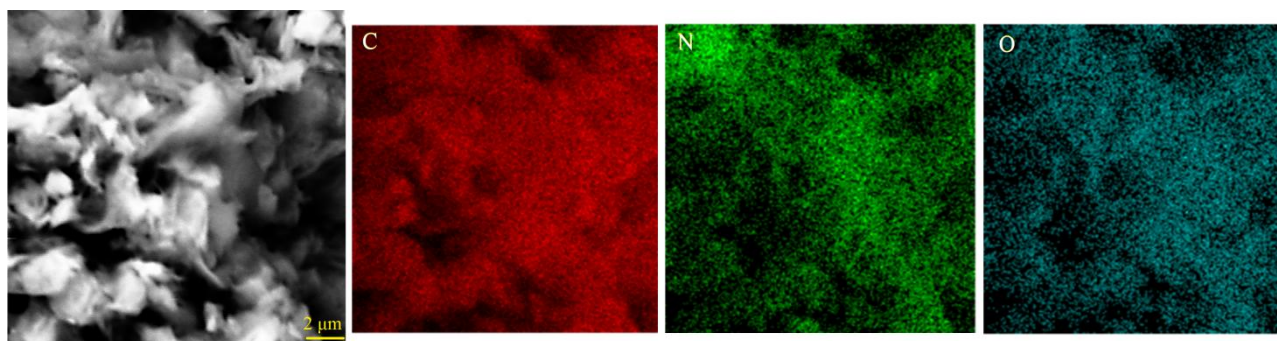


Figure 9. SEM images of the GO + MA (1:2) mixture after heat treatment at 550 °C and distribution of chemical elements in the surface layer of its particles

An elemental analysis was carried out for the products formed after HT of the dry GO + MA mixtures (Table 2). This analysis revealed that the initial amount of melamine in the mixture with GO affects the way it transforms during the thermal treatment.

Table 2

The element contents (C, N, H) in melamine and GO + MA mixtures samples after their heat treatment

Samples	Temperature of HT, °C	Elements Content, %		
		C	N	H
MA	450	33.39	63.97	2.61
MA	500	34.56	63.05	1.89
MA	550	35.00	62.81	1.86
GO + MA (1:1)	450	57.80	33.82	1.68
GO + MA (1:1)	500	76.10	13.00	0.94
GO + MA (1:1)	550	82.18	6.76	–
GO + MA (1:2)	450	49.27	44.21	1.74
GO + MA (1:2)	500	52.44	41.54	1.49
GO + MA (1:2)	550	57.49	35.56	1.52

It follows from the data in Table 2 that the heat treatment of the GO + MA (1:1) mixture in the temperature range of 450–550 °C is accompanied by a sharp decrease in the nitrogen content, which indicates the predominant decomposition of melamine and the formation of a small amount of its condensation product g-C₃N₄. When treating a mixture with a large amount of melamine, i.e., GO + MA (1:2), the nitrogen content also decreased with increasing temperature, but not as significantly as in the case of a mixture with a ratio of 1:1 (Table 2). At the same time, after treating this mixture at 550 °C, graphitic carbon nitride was formed, which was confirmed by XRD analyses (Figure 7, c). For melamine itself, its heat treatment in the studied temperature range led to the formation of the g-C₃N₄ product (Figure 7, c), the decrease in nitrogen in this temperature range was minimal (Table 2), which is in good agreement with the results of the elemental analysis of melamine in [21]. The existence of hydrogen in the studied samples indicates their incomplete deamination and the presence of terminal –NH and –NH₂ groups.

Graphitic carbon nitride, being a polymer semiconductor with a unique electronic structure, is in great demand in various modifications as a photocatalyst for use in processes such as water splitting and organic photosynthesis [25, 26]. Intensive research is being carried out on the creation of metal/g-C₃N₄ composites to improve the semiconductor and photocatalytic properties of carbon nitride and expand the areas of its application [27]. Combining g-C₃N₄ with graphene increases the mechanical strength of their composites, promotes charge transfer and electron-hole separation, which can improve the electrical conductivity and electrocatalytic properties of g-C₃N₄/graphene composites, that has been demonstrated in important electrochemical reactions of oxygen reduction and the formation of hydrogen and oxygen [28]. The products of the heat treatment of the GO and melamine mixtures obtained by us, consisting of reduced graphene and graphitic carbon nitride, as well as partially of N-doped graphene with the incorporation of nitrogen atoms into the graphene structure, will be used as carriers for metal nanoparticles in the creation of catalysts for the electrocatalytic syntheses of organic compounds. It should be noted that the metal-carbon electrocatalysts prepared by us on the basis of pyrolyzed polymers (melamine-formaldehyde and aniline-formaldehyde), as well as carbon nanotubes, showed high electrocatalytic activity in the electrohydrogenation of organic compounds [29, 30].

Conclusions

The performed investigations have shown the possibility of producing N-containing carbon material consisting of reduced graphene oxide and graphitic carbon nitride (rGO + g-C₃N₄) by the heat treatment of mechanical mixtures of graphene oxide powders prepared by the modified Hummers method, and melamine as a nitrogen source. The effect of the ratio of these components on the formation of heat treatment products in an air environment has been established. It has been shown that the GO:MA ratio of 1:2 is more favourable for preparing the carbon base rGO + g-C₃N₄. The prepared samples of N-containing graphene will be used to create metal-carbon catalysts for using them in the electrocatalytic syntheses of organic compounds.

Funding

This research was funded by the Science Committee of the Ministry of Science and Higher Education of the Republic of Kazakhstan (Program No. BR24992921).

Author Information*

*The authors' names are presented in the following order: First Name, Middle Name and Last Name

Nina Mikhailovna Ivanova (*corresponding author*) — Doctor of Chemical Sciences, Full Professor, Head of the Laboratory of Electrocatalysis and Quantum-chemical Research, LLP “Institute of Organic Synthesis and Coal Chemistry of the Republic of Kazakhstan”, Alikhanov Street, 1, 100000, Karaganda, Kazakhstan; e-mail: nmiva@mail.ru; <https://orcid.org/0000-0001-8564-8006>

Zainulla Muldakhmetovich Muldakhmetov — Director of LLP “Institute of Organic Synthesis and Coal Chemistry of the Republic of Kazakhstan”, Alikhanov Street, 1, 100000, Karaganda, Kazakhstan; e-mail: iosu.rk@mail.ru; <https://orcid.org/0000-0001-9497-2545>

Yakha Amkhadovna Vissurkhanova — Researcher, Laboratory of Electrocatalysis and Quantum-chemical Research, LLP “Institute of Organic Synthesis and Coal Chemistry of the Republic of Kazakhstan”, Alikhanov Street, 1, 100000, Karaganda, Kazakhstan; Teacher, Department of Physical and Analytical Chemistry, Karaganda Buketov University, Universitetskaya street, 28, 100024, Karaganda, Kazakhstan; e-mail: yakhavisurkhanova@bk.ru; <https://orcid.org/0000-0001-7279-1145>

Yelena Anatol'evna Soboleva — Candidate of Chemical Sciences, Leading researcher, Laboratory of Electrocatalysis and Quantum-chemical Research, LLP “Institute of Organic Synthesis and Coal Chemistry of the Republic of Kazakhstan”, Alikhanov Street, 1, 100000, Karaganda, Kazakhstan; e-mail: esoboleva-kz@mail.ru; <https://orcid.org/0000-0002-1089-367X>

Askhat Sakenovich Borsynbayev — PhD Doctoral Student, Researcher Laboratory of engineering profile “Physicochemical methods of research”, Karaganda Buketov University, Universitetskaya street, 28, 100028, Karaganda, Kazakhstan; e-mail: askhat.9@mail.ru; <https://orcid.org/0000-0001-7709-5552>

Author Contributions

The manuscript was written through the contributions of all authors. All authors have given approval to the final version of the manuscript. CRediT: **Nina Mikhailovna Ivanova** conceptualization, writing-original draft, methodology, validation, visualization, writing-review & editing; **Zainulla Muldakhmetovich Muldakhmetov** funding acquisition; **Yakha Amkhadovna Vissurkhanova** investigation, methodology, data curation, visualization; **Yelena Anatol'evna Soboleva** investigation, data curation, Figures design, resources, visualization; **Askhat Sakenovich Borsynbayev** conducting spectral analyses.

Conflicts of Interest

The authors declare no conflict of interest.

References

- 1 Shao, Y., Zhang, S., Engelhard, M.H., Li, G., Shao, G., Wang, Y., Liu, J., Aksay, I.A., & Lin, Y. (2010). Nitrogen-doped graphene and its electrochemical applications. *J. Mater. Chem.*, 20(35), 7491–7496. <https://doi.org/10.1039/C0JM00782J>
- 2 Ma, R., Ren, X., Xia, B.Y., Zhou, Y., Sun, C., Liu, Q., Liu, J., & Wang J. (2016). Novel synthesis of N-doped graphene as an efficient electrocatalyst towards oxygen reduction. *Nano Res.*, 9, 808–819. <https://doi.org/10.1007/s12274-015-0960-2>
- 3 Wu, G., Santandreu, A., Kellogg, W., Gupta, S., Ogoke, O., Zhang, H., Wang, H.-L., & Dai, L. (2016). Carbon nanocomposite catalysts for oxygen reduction and evolution reactions: From nitrogen doping to transition-metal addition. *Nano Energy*, 29, 83–110. <https://doi.org/10.1016/j.nanoen.2015.12.032>
- 4 Xu, H., Ma, L., & Jin Z. (2018). Nitrogen-doped graphene: Synthesis, characterizations and energy applications. *J. Energy Chem.*, 27(1), 146–160. <https://doi.org/10.1016/j.jechem.2017.12.006>
- 5 Yang, S.-Y., Chang, K.-H., Huang, Y.-L., Lee, Y.-F., Tien, H.-W., Li, S.-M., Lee, Y.-H., Liu, C.-H., Ma, C.-C. M., & Hu C.-C. (2012). A powerful approach to fabricate nitrogen-doped graphene sheets with high specific surface area. *Electrochem. Comm.*, 14(1), 39–42. <https://doi.org/10.1016/j.elecom.2011.10.028>
- 6 Lin, Z., Song, M., Ding, Y., Liu, Y., Liu, M., & Wong, C. (2012). Facile preparation of nitrogen-doped graphene as a metal-free catalyst for oxygen reduction reaction. *Phys. Chem. Chem. Phys.*, 14(10), 3381–3387. <https://doi.org/10.1039/C2CP00032F>

- 7 Sheng, Z.-H., Shao, L., Chen, J.-J., Bao, W.-J., Wang, F.-B., & Xia, X.-H. (2011). Catalyst-free synthesis of nitrogen-doped graphene via thermal annealing graphite oxide with melamine and its excellent electrocatalysis. *ACS Nano*, *5*(6), 4350–4358. <https://doi.org/10.1021/nn103584t>
- 8 Du, D., Li, P., & Ouyang, J. (2015). Nitrogen-doped reduced graphene oxide prepared by simultaneous thermal reduction and nitrogen-doping of graphene oxide in air and its application as electrocatalyst. *ACS Appl. Mater. & Interfaces*, *7*(48), 26952–26958. <https://doi.org/10.1021/acsami.5b07757>
- 9 Shen, W., & Fan, W. (2013). Nitrogen-containing porous carbons: synthesis and application. *J. Mater. Chem. A*, *1*(4), 999–1013. <https://doi.org/10.1039/C2TA00028H>
- 10 Bie, C., Yu, H., Cheng, B., Ho, W., Fan, J., & Yu J. (2021). Design, fabrication, and mechanism of nitrogen-doped graphene-based photocatalyst. *Adv. Mater.*, *33*(9), 2003521. <https://doi.org/10.1002/adma.202003521>
- 11 Talukder, N., Wang, Y., Nunna, B.B., & Lee, E.S. (2021). Nitrogen-doped graphene nanomaterials for electrochemical catalysis/reactions: A review on chemical structures and stability. *Carbon*, *185*, 198–214. <https://doi.org/10.1016/j.carbon.2021.09.025>
- 12 Adarsh Rag, S., Selvakumar, M., Bhat, S., Chidangil, S., & De, S. (2020). Synthesis and characterization of reduced graphene oxide for supercapacitor application with a biodegradable electrolyte. *J. Electron. Mater.*, *49*, 985–994. <https://doi.org/10.1007/s11664-019-07853-9>
- 13 Schönherr, J., Buchheim, J., Scholz, P., & Adelhelm, P. (2018). Boehm titration revisited (Part I): Practical aspects for achieving a high precision in quantifying oxygen-containing surface groups on carbon materials. *J. Carbon Res.*, *4*(2), 21 (14 pp.). <https://doi.org/10.3390/c4020021>
- 14 Schönherr, J., Buchheim, J., Scholz, P., & Adelhelm, P. (2018). Boehm titration revisited (Part II): A comparison of Boehm titration with other analytical techniques on the quantification of oxygen-containing surface groups for a variety of carbon materials. *J. Carbon Res.*, *4*(2), 22 (17pp.). <https://doi.org/10.3390/c4020022>
- 15 Oliveira, A.E.F., Braga, G.B., Tarley, C.R.T., & Pereira, A.C. (2018). Thermally reduced graphene oxide: Synthesis, studies and characterization. *J. Mater. Sci.*, *53*, 12005–12015. <https://doi.org/10.1007/s10853-018-2473-3>
- 16 Nascimento, J.R., D'Oliveira, M.R., Veiga, A.G., Chagas, C.A., & Schmal, M. (2020). Synthesis of reduced graphene oxide as a support for nano copper and palladium/copper catalysts for selective NO reduction by CO. *ACS Omega*, *5*, 25568–25581. <https://doi.org/10.1021/acsomega.0c02417>
- 17 Banzal, K., Singh, J., & Dhaliwal, A.S. (2022). Synthesis and characterization of graphene oxide and its reduction with different reducing agents. *IOP Conf. Ser.: Mater. Sci. Eng.*, *1225*, 012050. <https://doi.org/10.1088/1757-899X/1225/1/012050>
- 18 Gudyma, T.S., Lapekin, N. I., Popov, M.V., & Bannov, A.G. (2022). Application of ice to the synthesis of graphite oxide: A modified Hummers method. *Solid Fuel Chem.*, *56*, 347–352. <https://doi.org/10.3103/S0361521922050044>
- 19 Wang, R., Wang, Y., Xu, C., Sun, J., & Gao, L. (2013). Facile one-step hydrazine-assisted solvothermal synthesis of nitrogen-doped reduced graphene oxide: reduction effect and mechanisms. *RSC Adv.*, *3*(4), 1194–1200. <https://doi.org/10.1039/C2RA21825A>
- 20 Yang, L., Liu, X., Liu, Z., Wang, C., Liu, G., Li, Q., & Feng, X. (2018). Enhanced photocatalytic activity of g-C₃N₄ 2D nanosheets through thermal exfoliation using dicyandiamide as precursor. *Ceramics Intern.*, *44*(17), 20613–20619. <https://doi.org/10.1016/j.ceramint.2018.06.105>
- 21 Praus, P., Svoboda, L., Ritz, M., Troppova, I., Sihor, M., & Koci, K. (2017). Graphitic carbon nitride: Synthesis, characterization and photocatalytic decomposition of nitrous oxide. *Mater. Chem. Phys.*, *193*, 438–446. <https://doi.org/10.1016/j.matchemphys.2017.03.008>
- 22 Wang, A., Wang, C., Fu, L., Wong-Ng, W., & Lan, Y. (2017). Recent advances of graphitic carbon nitride-based structures and applications in catalyst, sensing, imaging, and LEDs. *Nano-micro Lett.*, *9*, 47. <https://doi.org/10.1007/s10854-021-06508-y>
- 23 Kim, M., Hwang, S., & Yu J.-S. (2007). Novel ordered nanoporous graphitic carbon nitride with C₃N₄ stoichiometry as a support for Pt-Ru anode catalyst in DMFC. *J. Mater. Chem.*, *17*, 1656–1659. <https://doi.org/10.1039/B702213A>
- 24 Jurgens, B., Irran, E., Senker, J., Kroll, P., Muller, H., & Schnick, W. (2003). Melem (2,5,8-triamino-tri-s-triazine), an important intermediate during condensation of melamine rings to graphitic carbon nitride: Synthesis, structure determination by X-ray powder diffractometry, solid-state NMR, and theoretical studies. *J. Am. Chem. Soc.*, *125*(34), 10288–10300. <https://doi.org/10.1021/ja0357689>
- 25 Xing, Y., Wang, X., Hao S., Zhang X., Wang X., Ma W., Zhao H., & Xu X. (2021). Recent advances in the improvement of g-C₃N₄ based photocatalytic materials. *Chinese Chem. Lett.*, *32*(1), 13–20. <https://doi.org/10.1016/j.ccl.2020.11.011>
- 26 Ismael, M. (2020). A review on graphitic carbon nitride (g-C₃N₄) based nanocomposites: Synthesis, categories, and their application in photocatalysis. *J. Alloys Compd.*, *846*, 156446. <https://doi.org/10.1016/j.jallcom.2020.156446>
- 27 Wang, L., Wang, C., Hu, X., Xue, H., & Pang, H. (2016). Metal/graphitic carbon nitride composites: Synthesis, structure, and applications. *Chem. Asian J.*, *11*, 3305–3328. <https://doi.org/10.1002/asia.201601178>
- 28 Zhao, Y., Zhang, J., & Qu, L. (2015). Graphitic carbon nitride/graphene hybrids as new active materials for energy conversion and storage. *ChemNanoMat*, *1*, 298–318. <https://doi.org/10.1002/cnma.201500060>
- 29 Muldakhmetov, Z.M., Ivanova, N.M., Vissurkhanova, Y.A., & Soboleva, E.A. (2022). Preparation and electrocatalytic application of copper- and cobalt-carbon composites based on pyrolyzed polymer. *Catalysts*, *12*(8), 862. <https://doi.org/10.3390/catal12080862>
- 30 Ivanova, N.M., Soboleva, Y.A., & Vissurkhanova Y.A. (2025). Synthesis of copper-carbon nanocomposites and their application as electrocatalysts. *Rus. J. Appl. Chem.*, *98*(1), 10–19. <https://doi.org/10.1134/s1070427225010033>

Mohamed Badaoui^{1*} , Hafida Sehil², Chaimaa Lamouri²

¹*Synthesis and Catalysis Laboratory, University of Tiaret, Tiaret, Algeria;*

²*Department of Chemistry, Faculty of Sciences of the Matter, University of Tiaret, Tiaret, Algeria*

(*Corresponding author's e-mail: mohamed.badaoui@univ-tiaret.dz)

Synthesis, Characterization, and Photocatalytic Activity of CeBiO₃ and FeBiO₃ Nanoparticles Prepared via the Sol-Gel Process

This study investigated the photocatalytic potential of perovskite materials, cerium(III) bismuthate (CeBiO₃) and iron(III) bismuthate (FeBiO₃), for organic dye degradation under visible LED light illumination. The materials were synthesized via the sol-gel method and characterized using X-ray diffraction (XRD), Fourier-transform infrared spectroscopy (FT-IR), diffuse reflectance spectroscopy (DRS), and point of zero charge (PZC) analysis. A rhombohedral structure for FeBiO₃ and a tetragonal structure for CeBiO₃ with band gaps of 2.18 eV and 2.17 eV, respectively were revealed by structural characterization. The kinetic evolution of Methylene Blue (MB) degradation in an aqueous medium was examined. Both catalysts showed remarkable degradation efficiency, and CeBiO₃ demonstrated superior performance. Optimal degradation conditions were achieved at pH 10, with a catalyst concentration of 0.15 g/L, an initial Methylene Blue concentration of 10 mg/L, and a reaction time of 4 hours. Overall, this study highlights the potential of perovskite materials CeBiO₃ and FeBiO₃ to efficiently degrade organic dyes under visible light and contributes to the development of sustainable wastewater treatment solutions.

Keywords: perovskite, nanoparticles, sol-gel, cerium(III) bismuthate, iron(III) bismuthate, photocatalysis, dye degradation, band gap

Introduction

Nanomaterials are increasingly attracting attention across various fields, including environmental remediation, wastewater treatment, energy generation and storage, biomedicine. Their distinctive characteristics and processability into well-defined shapes and dimensions are essential for meeting specific application requirements [1–3]. In this context, perovskite-based materials, discovered in 1839 in the Ural Mountains by Gustave Rose and named after Count Lev Aleksevich von Perovski, have emerged as promising candidates. The earliest identified perovskite compound was CaTiO₃ [4].

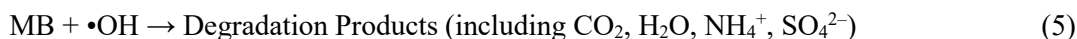
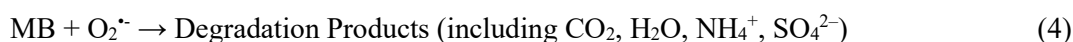
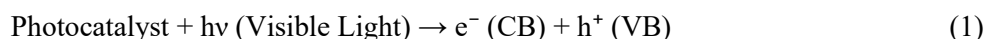
Single perovskites are described by the general formula ABX₃, where A and B are cations, and X is an anion. Alkaline earth metals or lanthanides often occupy the A site, transition metals typically occupy the B site, and X can be oxygen or a halide. When the anion is oxygen, the structure is termed a perovskite oxide; when it is a halide, it is termed a perovskite halide. In single perovskite systems, the coordination number is 6 for the A site, 12 for the B site, and 6 for the O anions. An ideal BO₆ octahedral arrangement leads to a cubic lattice [4, 5].

Perovskite materials have been synthesized using various methods, including co-precipitation, sol-gel processes, microwave-assisted synthesis, hydrothermal and solvothermal methods, microemulsion techniques, and sonochemical routes [6–8]. Sol-gel technology has distinct advantages among these approaches, particularly in terms of its ability to produce solid-state materials from chemically homogeneous precursors. This method is simple and relatively eco-friendly, which makes it very attractive for the synthesis of nanoparticles [9]. Moreover, introducing randomness into the solution state improves the mixing of reactants at the atomic level, which is necessary for the synthesis of ternary and quaternary oxides at lower temperatures and over shorter time periods. The homogeneity and efficiency of the synthesis process is increased by this innovative approach, which in turn leads to a reduction in energy costs and contributes to progress in the production of materials for various industrial applications [10].

Photocatalysis uses a catalyst that absorbs light energy to speed up chemical reactions. The photocatalyst generates electron-hole pairs when irradiated with light, causing surface oxidation-reduction processes. These processes can degrade water pollutants or transform abundant earth elements, such as H₂O, CO₂,

and N₂ [11]. Semiconductor materials with relatively large band gaps, such as TiO₂ (3.2 eV) [12] and ZnO (3.37 eV) [13], are commonly utilized for photocatalytic dye decomposition. More recently, perovskite-type Bismuth Ferrite (BFO) has shown visible-light-driven catalytic activity, with a wide band gap ranging from 2.1 to 2.9 eV [14]. BFO nanoparticles are particularly appealing for dye degradation due to their high charge separation efficiency at room temperature and multiferroic properties. Moreover, materials with relatively lower band gap energies can efficiently support electron transfer to the conduction band under solar irradiation [4].

In the case of Methylene Blue (MB) dye, the initial deep-blue solution becomes colorless after degradation. Photodegradation is an oxidation process through which complex molecules are broken down into simple molecules. Following oxidation, MB decomposes into CO₂, H₂O, NH₄⁺, and SO₄²⁻. Electrons (e⁻) are excited into the conduction band of the catalyst, forming an electron-hole (e⁻, h⁺) pair. Dissolved oxygen from the atmosphere subsequently captures electrons to generate superoxide radicals (O₂^{•-}). Meanwhile, water molecules react with holes (h⁺) in the valence band to form hydroxyl radicals (•OH). These O₂^{•-} and •OH radicals promote MB degradation according to the following equations [4]:



In this study, we investigated the synthesis and characterization of CeBiO₃ and FeBiO₃ nanoparticles via the sol-gel method and examined their photocatalytic activity for organic dye degradation under visible-light irradiation.

Experimental

Materials

Bismuth (III) nitrate (Bi(NO₃)₃·5H₂O), iron nitrate (Fe(NO₃)₃·9H₂O), and cerium (III) nitrate (Ce(NO₃)₃·4H₂O) (Pro analysi MERCK), sodium hydroxide (NaOH), ethanol, citric acid and Methylene Blue were purchased from Sigma Aldrich. Distilled water was used as the solvent to prepare the oxides.

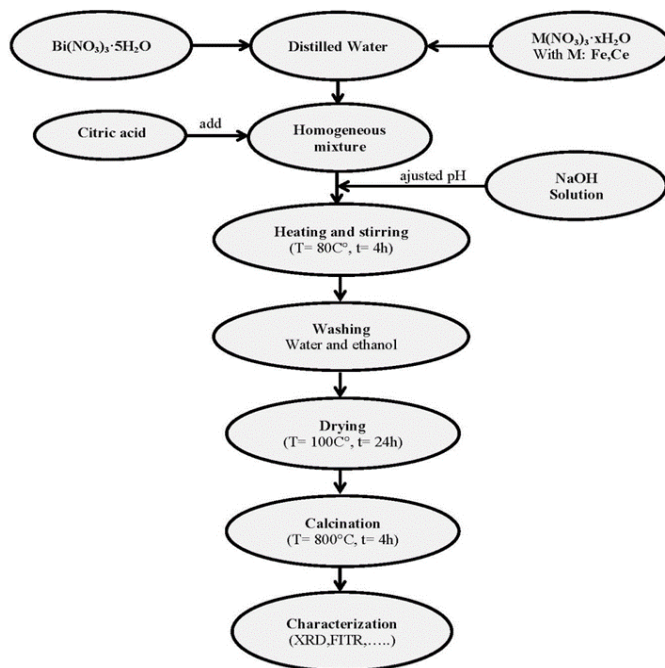
Synthesis Process

CeBiO₃ and FeBiO₃ nanoparticles were synthesized using the sol-gel method (Figure 1). For each compound, 0.1 mol aqueous solutions were prepared using Bi(NO₃)₃·5H₂O, Fe(NO₃)₃·9H₂O, and Ce(NO₃)₃·4H₂O dissolved in double-distilled water. A citric acid solution (1M) was introduced as a chelating agent. The pH was adjusted to 9 using NaOH (2M) under continuous magnetic stirring. The resulting solutions were thermally treated at 80 °C for 4h in a water bath under constant agitation. The obtained precipitates were filtered, washed thoroughly with distilled water and ethanol, and dried at 100 °C for 24 h. Finally, the powders were calcined at 800 °C for 4h in air atmosphere.

Characterization

The CeBiO₃ and FeBiO₃ nanoparticles were characterized using several techniques. X-ray diffraction (XRD) patterns were collected on a Rigaku MINIFLEX 600 diffractometer with monochromatic Cu K α radiation ($\lambda = 1.5418 \text{ \AA}$) over 10–90° at a scanning rate of 5° min⁻¹. Fourier-transform infrared (FT-IR) spectra were recorded in the 500–4000 cm⁻¹ range on a Bruker Alpha-P spectrophotometer. UV-visible diffuse reflectance spectra (DRS) were obtained to investigate the optical properties using a SHIMADZU UV-2600-PC spectrophotometer over 200–800 nm.

The point of zero charge (PZC) was determined using the pH drift method [15]. A series of 50 mL solutions of 0.01 M NaCl were added to closed vials and adjusted to initial pH values between 2 and 12 using (1M) hydrochloric acid (HCl) or sodium hydroxide (NaOH). Subsequently, 0.05 g of oxide was added to each solution and stirred for 48 h. The PZC was identified as the intersection point between the final pH versus initial pH curve and the line $\text{pH}_{\text{final}} = \text{pH}_{\text{initial}}$.

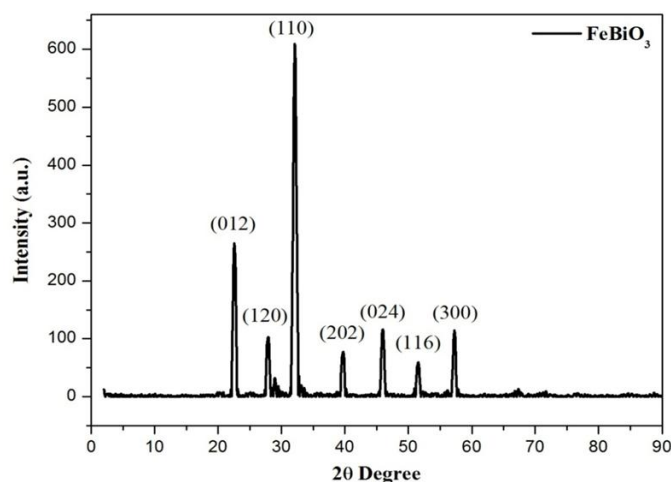
Figure 1. Sol-Gel Synthesis of CeBiO_3 and FeBiO_3 Nanoparticles

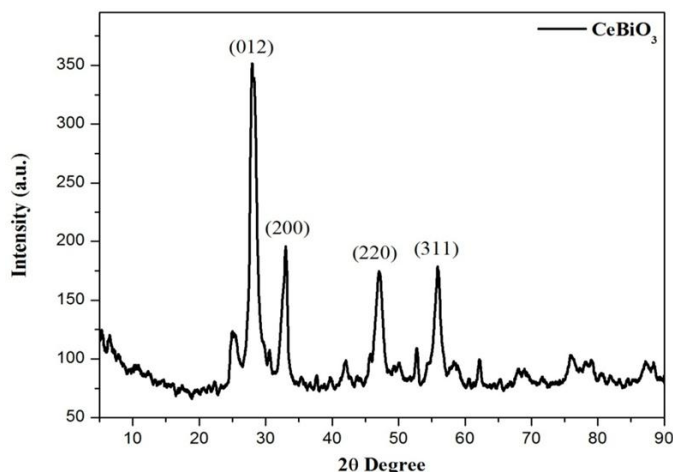
Photocatalytic activity Measurement

The photocatalytic activities of CeBiO_3 and FeBiO_3 were evaluated through MB degradation under visible-light irradiation using a CTRCH LED lamp (13 W). The catalyst (1.0 g/L) was dispersed in MB solution (20 mg/L, 100 mL) under continuous stirring. Prior to irradiation, the suspension was equilibrated in the dark for 30 min. During the degradation process, aliquots were collected at regular intervals and centrifuged (5000 rpm, 10 min) to remove the catalyst. The MB concentration was monitored by measuring the absorbance at 665 nm (the maximum absorption of MB) using a Shimadzu 1650 UV/Visible spectrophotometer.

Results and Discussion

Figure 2 presents the XRD pattern of the synthesized nanoparticles. Diffraction peaks appear at $2\theta = 22.5^\circ$, 32.08° , 39.79° , 45.91° , 51.5° , and 57.35° , which correspond to the (012), (120), (110), (202), (024), and (300) crystal planes of face rhombohedral FeBiO_3 (JCPDS 01-073-0548) [16]. Likewise, Figure 3 exhibits the characteristic CeBiO_3 peaks in the 2θ range of 28.15° , 33.04° , 41.83° , and 55.9° , indexing to the (012), (200), (220), and (311) planes, respectively, and confirming a tetragonal structure in accordance with JCPDS 76-1730 [17].

Figure 2. XRD Pattern of FeBiO_3

Figure 3. XRD Pattern of CeBiO₃

The particle sizes were calculated using the Debye-Scherrer equation [18]:

$$D = (0.9\lambda)/(\beta \cos \theta) \quad (6)$$

Where D is the particle size (nm), λ is the X-ray wavelength (as used in the experiment), θ is the diffraction angle, and β is the full width at half maximum (FWHM), expressed in radians. The calculated sizes are listed in Table 1.

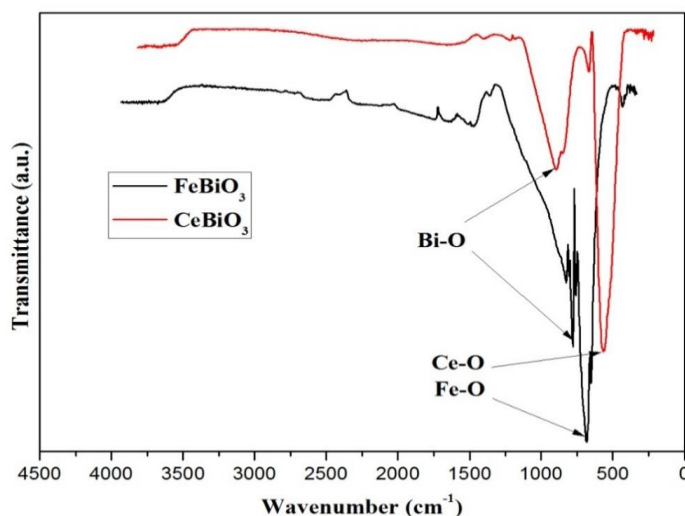
Table 1

Crystallite Size Analysis of the Synthesized Perovskites

Sample	2 θ (°)	(hkl)	D (nm)
FeBiO ₃	32.08	(110)	36.06
CeBiO ₃	28.01	(012)	35.82

The calculated particle sizes for the CeBiO₃ and FeBiO₃ samples calcined at 800 °C were 35.82 nm and 36.06 nm, respectively, which are relatively large and indicate the successful formation of nanoparticles.

The FT-IR spectrum of the synthesized nanoparticles (Figure 4) indicates the presence of adsorption bands at 915 and 809 cm⁻¹, which are attributed to the valence vibration modes of the Bi–O bond in CeBiO₃ and FeBiO₃, respectively [19]. Additionally, the bands at 570 cm⁻¹ and 670 cm⁻¹ correspond to the valence vibration modes of the Ce–O and Fe–O bonds in CeBiO₃ and FeBiO₃, respectively [20, 21].

Figure 4. Fourier-transform infrared spectroscopy (FT-IR) of CeBiO₃ and FeBiO₃

The band gap energies of CeBiO_3 and FeBiO_3 were determined from their diffuse-reflection spectra using the Kubelka–Munk function [22], defined as:

$$F(R) = (1 - R) / (2R) \quad (7)$$

Where R is the observed reflection in the UV/Vis spectrum. The optical band gap was obtained by identifying the intersection point on the $(F(R) hv)^2 - hv$ plot (Figures 5 and 6), where h represents Planck's constant and ν is the photon frequency. By applying this method, the resulting band gaps were 2.18 eV for FeBiO_3 and 2.17 eV for CeBiO_3 [23].

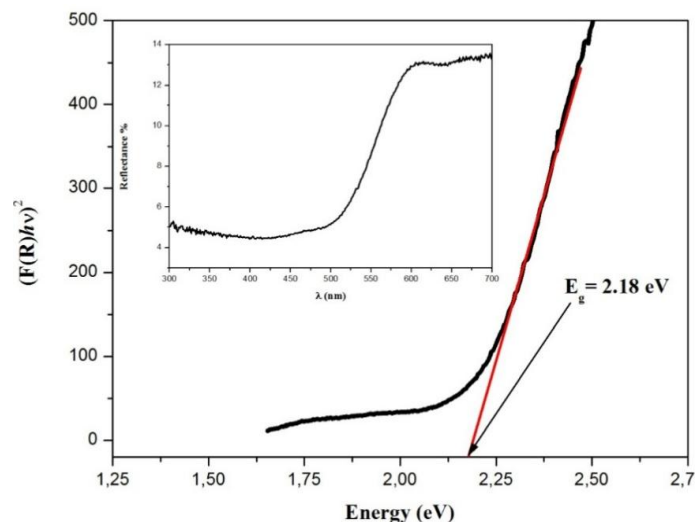


Figure 5. Optical Band Gap Determination of FeBiO_3

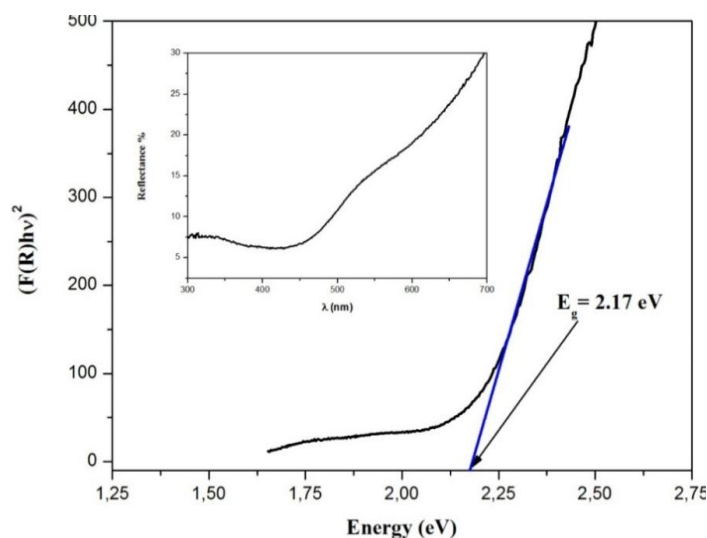


Figure 6. Optical Band Gap Determination of CeBiO_3

The point of zero charge was determined for both materials by plotting the final and initial pH (Figures 7 and 8). The pH_{pzc} values, identified at the intersection of the measurement curve with the bisector line from the data without adding CeBiO_3 and FeBiO_3 , were 6.2 and 5.6 for CeBiO_3 and FeBiO_3 , respectively. These values define the pH-dependent surface charge characteristics of the nanoparticles: the surface becomes negatively charged above pH_{pzc} and positively charged below pH_{pzc} (Figures 9 and 10) [24].

The photocatalytic degradation of MB was monitored under visible-light irradiation (Figure 11). Prior to irradiation, the suspensions were equilibrated in the dark, showing a minimal decrease in the MB concentration due to adsorption. Under visible light, CeBiO_3 demonstrated superior photocatalytic activity, achieving 85 % MB degradation after 4 h, whereas FeBiO_3 reached 48.5 % degradation under identical conditions.

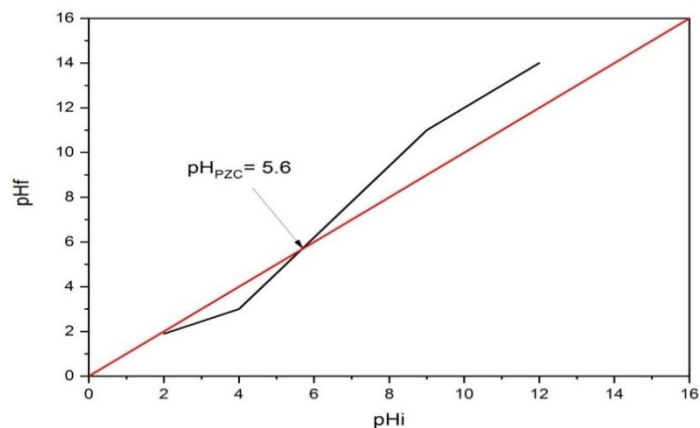


Figure 7. Determination of the pH_{pzc} for $FeBiO_3$

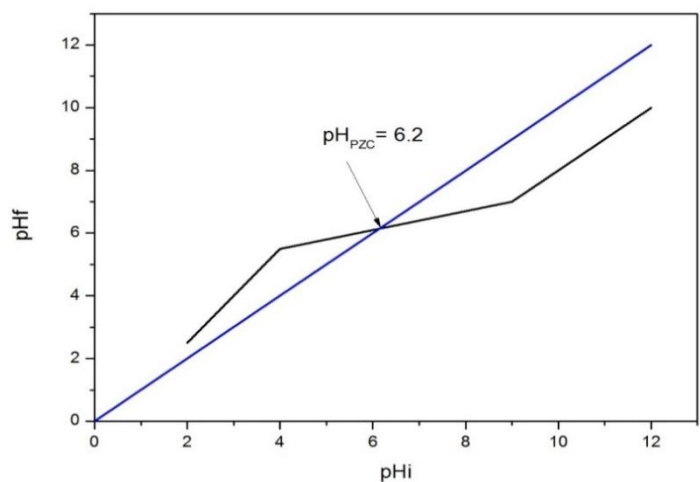


Figure 8. Determination of the pH_{pzc} for $CeBiO_3$

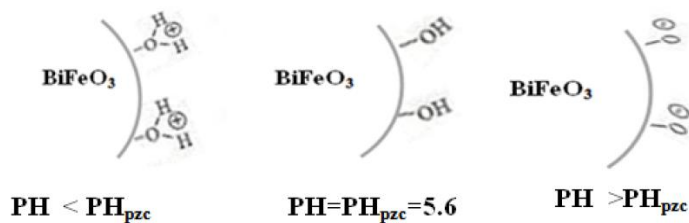


Figure 9. Variation in the Surface Charge of $FeBiO_3$ as a Function of pH

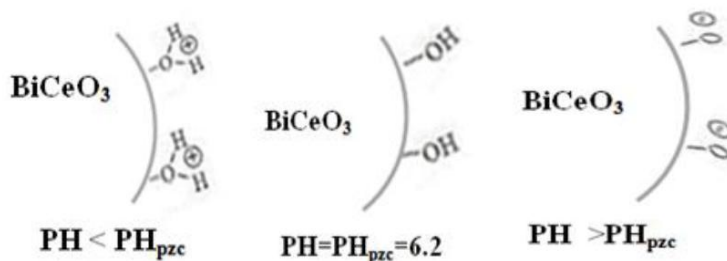


Figure 10. Variation in the Surface Charge of $CeBiO_3$ as a Function of pH

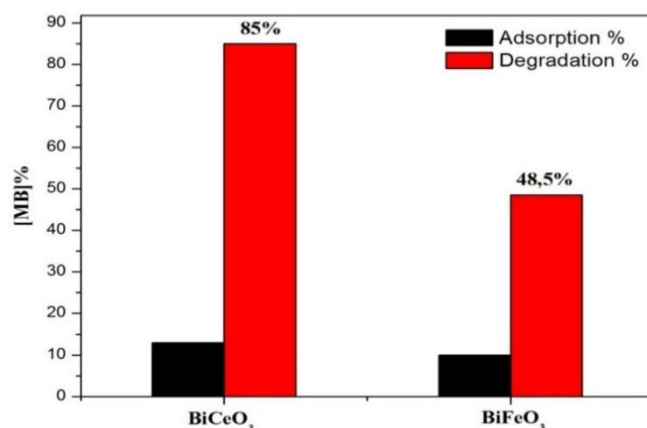


Figure 11. Adsorption and Photocatalytic Degradation of MB ([Catalyst] = 0.1 g; [MB] = 10 mg·L⁻¹; [V] = 100 mL; [T] = 4 h)

The effects of operational parameters, including pH, photocatalyst dosage, and initial MB concentration, on the photocatalytic performance were investigated. The effect of pH was assessed by adjusting the solution pH to 3, 6, and 10 using (1M) HCl and NaOH while maintaining a constant MB concentration (10 mg L⁻¹) and catalyst loading (0.1 g). The results demonstrated that alkaline conditions enhanced the photodegradation efficiency, achieving 91 % removal for both CeBiO₃ and FeBiO₃ catalysts. In contrast, acidic media exhibited substantially lower degradation rates of 46 % and 65 % for CeBiO₃ and FeBiO₃, respectively (Figure 12). These findings are consistent with the previously reported pH-dependent photocatalytic behavior [25, 26].

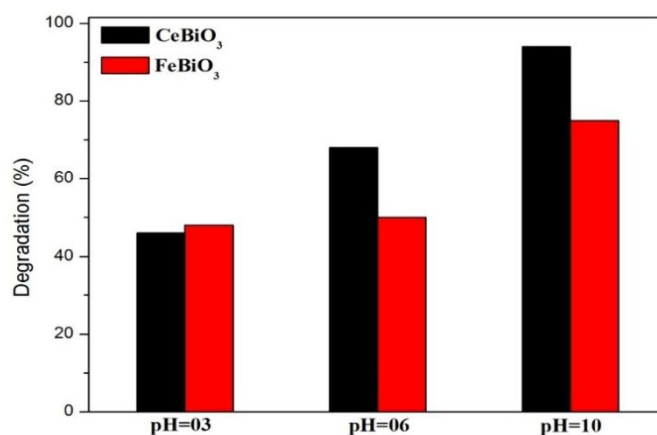


Figure 12. Effect of pH on the Photocatalytic Degradation of MB ([Catalyst] = 1.0 g·L⁻¹; [MB] = 10 mg·L⁻¹)

The impact of pH on MB degradation was investigated under varying pH conditions. The degradation efficiency exhibited minimal activity under acidic conditions (pH = 3) and near-neutral pH (pH = 6). However, alkaline conditions (pH = 10) demonstrated an enhanced photocatalytic performance, with a degradation efficiency of 91 %. This enhancement can be attributed to the increased concentration of hydroxide ions (OH⁻) in the basic medium, which promotes the formation of hydroxyl radicals (•OH) through hole (h⁺) oxidation, as described by the following equation:



This result aligns with previous studies that reported enhanced photocatalytic activity under basic conditions owing to favorable radical formation kinetics [25, 26].

The influence of the photocatalyst dosage on the MB photodegradation efficiency was investigated. Photocatalytic tests were conducted using varying quantities of the catalyst in an aqueous MB solution with an initial 10 mg L⁻¹ concentration under ambient pH conditions. As shown in Figure 13, the photocatalytic degradation performance exhibited an inverse relationship with increasing catalyst concentration. This phe-

nomenon can be attributed to the screening effect manifested at higher catalyst loadings, whereby excessive catalyst particles induce enhanced solution turbidity, consequently diminishing visible light penetration through the reaction medium [25–27]. The optimal photocatalytic performance was achieved within a catalyst dosage range of 0.1–0.15 mg, beyond which a significant reduction in the degradation efficiency was observed.

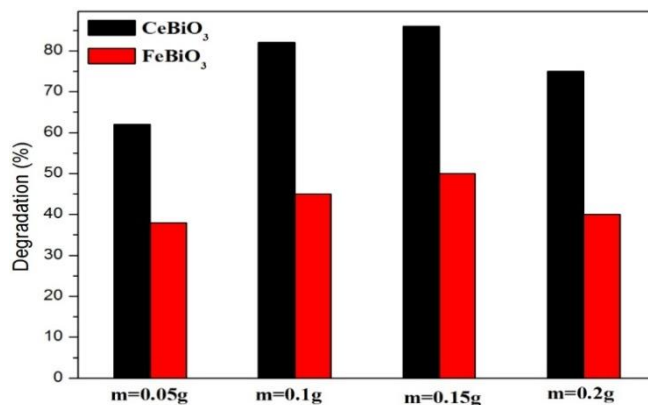


Figure 13. Effect of Catalyst Dosage on the Degradation of MB (10 mg·L⁻¹)

The photocatalytic degradation performance was evaluated as a function of the initial MB concentration, ranging from 5 to 20 mg L⁻¹, utilizing 0.1 g of photocatalyst in 100 mL reaction volume. Figure 14 illustrates the photodegradation efficiencies of CeBiO₃ and FeBiO₃ under varying MB concentrations. The degradation rate was inversely correlated with the MB concentration. This behavior is attributed to the screening effect at elevated MB concentrations, wherein the solution opacity increases, thereby reducing the visible light penetration through the reaction medium. Both synthesized oxide photocatalysts demonstrated comparable concentration-dependent behavior under the investigated conditions [28].

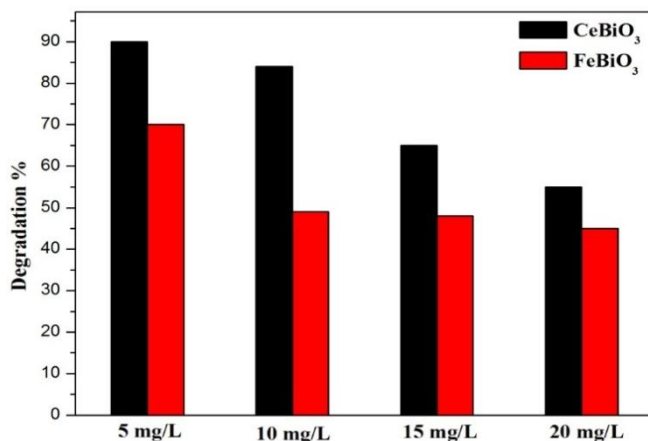


Figure 14. Effect of Initial MB Concentration on Photocatalytic Degradation Efficiency

Conclusions

CeBiO₃ and FeBiO₃ perovskite-structured photocatalysts were synthesized through the sol-gel method followed by calcination at 800 °C and evaluated for MB degradation under visible LED illumination. XRD analysis confirmed the rhombohedral FeBiO₃ and tetragonal CeBiO₃ structures, while FT-IR spectroscopy showed characteristic metal-oxygen bonds at 541/571 cm⁻¹ for the calcined powders and 626/622 cm⁻¹ for Ce–O and Fe–O vibrations. Both materials exhibited comparable band gaps (2.18 eV for FeBiO₃ and 2.17 eV for CeBiO₃) and distinct surface charge characteristics (pH_{pzc} = 5.6 and 6.2, respectively).

CeBiO₃ exhibited enhanced photocatalytic efficiency compared to FeBiO₃, achieving a 91 % degradation efficiency under optimized conditions, including pH 10, a catalyst loading of 0.10–0.15 g/L, and an initial MB concentration of 10 mg/L, within 4 hours of irradiation. An inverse correlation was shown for the

initial degradation rate and MB concentration, which reduced the overall efficiency at higher concentrations due to optical screening effects. The photocatalytic efficiency and visible light absorption properties of these materials, especially CeBiO₃, make them potentially suitable for practical water treatment applications. A sustainable approach for water decontamination is provided by the environmentally benign nature of these materials, combined with visible-light activation.

Author Information*

*The authors' names are presented in the following order: First Name, Middle Name and Last Name

Mohamed Badaoui — Doctor and Researcher, Synthesis and Catalysis Laboratory, University of Tiaret, BP P 78, Zaaroura, Tiaret, Algeria; e-mail: mohamed.badaoui@univ-tiaret.dz; <https://orcid.org/0000-0001-7455-7184>

Hafida Sehil — Doctor and Researcher, Department of Chemistry, Faculty of Sciences of the Matter, University of Tiaret, BP P 78, Zaaroura, Tiaret, Algeria; e-mail: hafida.sehil@univ-tiaret.dz

Chaimaa Lamouri — Master Student, Department of Chemistry, Faculty of Sciences of the Matter, University of Tiaret, BP P 78, Zaaroura, Tiaret, Algeria; e-mail: lamourichaima.38@gmail.com

Author Contributions

The manuscript was written through contributions of all authors. All authors have given approval to the final version of the manuscript. **CRedit**: **Mohamed Badaoui** was responsible for conceptualization, data curation, investigation, methodology, validation, visualization, and writing review and editing. **Hafida Sehil** contributed through data curation, formal analysis, visualization, supervision, drafting the original manuscript and reviewing its content. **Chaimaa Lamouri** was involved in data curation, formal analysis, and resource provision.

Conflicts of Interest

The authors declare no conflicts of interest.

References

- Osman, A.I., et al. (2024). Synthesis of green nanoparticles for energy, biomedical, environmental, agricultural, and food applications: A review. *Environ. Chem. Lett.*, 22, 841–887. <https://doi.org/10.1007/s10311-023-01682-3>
- Rathod, S., Preetam, S., Pandey, C., & Bera, S.P. (2024). Exploring synthesis and applications of green nanoparticles and the role of nanotechnology in wastewater treatment. *Biotechnol. Rep.*, 41, e00830. <https://doi.org/10.1016/j.btre.2024.e00830>
- Attfield, J.P., Lightfoot, P., & Morris, R.E. (2015). Perovskites. *Dalton Trans.*, 44, 10541–10542. <https://doi.org/10.1039/C5DT90083B>
- Irshad, M., et al. (2022). Photocatalysis and perovskite oxide-based materials: A remedy for a clean and sustainable future. *RSC Adv.*, 12, 7009–7039. <https://doi.org/10.1039/D1RA08185C>
- Zhou, D., Zhou, T., Tian, Y., Zhu, X., & Tu, Y. (2018). Perovskite-based solar cells: Materials, methods, and future perspectives. *J. Nanomater.*, 2018, Art. ID 8148072, 1–15. <https://doi.org/10.1155/2018/8148072>
- Ke, H., Wang, W., Wang, Y., Xu, J., Jia, D., Lu, Z., & Zhou, Y. (2011). Factors controlling pure-phase multiferroic BiFeO₃ powders synthesized by chemical co-precipitation. *Journal of Alloys and Compounds*, 509(5), 2192–2197. <https://doi.org/10.1016/j.jallcom.2010.09.213>
- Comyn, T.P., Kanguwe, D.F., He, J., & Brown, A.P. (2008). Synthesis of bismuth ferrite lead titanate nano-powders and ceramics using chemical co-precipitation. *Journal of the European Ceramic Society*, 28(11), 2233–2238. <https://doi.org/10.1016/j.jeurceramsoc.2008.02.013>
- Kim, J.K., Kim, S.S., & Kim, W.-J. (2005). Sol–gel synthesis and properties of multiferroic BiFeO₃. *Materials Letters*, 59(29–30), 4006–4009. <https://doi.org/10.1016/j.matlet.2005.07.050>
- Kakahana, M. (1996). Invited review ‘sol-gel’ preparation of high temperature superconducting oxides. *Journal of Sol-Gel Science and Technology*, 6(1), 7–55. <https://doi.org/10.1007/bf00402588>
- Danks, A.E., Hall, S.R., & Schnepf, Z. (2016). The evolution of ‘sol–gel’ chemistry as a technique for materials synthesis. *Mater. Horiz.*, 3, 91–112. <https://doi.org/10.1039/C5MH00185G>
- Hassaan, M.A., El-Nemr, M.A., Elkatory, M.R., Ragab, S., Niculescu, V.C., & El-Nemr, A. (2023). Principles of photocatalysts and their different applications: A review. *Top Curr. Chem.*, (Z) 381, 31. <https://doi.org/10.1007/s41061-023-00444-7>

- 12 Tasisa, Y.E., Sarma, T.K., Krishnaraj, R., & Sarma, S. (2024). Band gap engineering of titanium dioxide (TiO₂) nanoparticles prepared via green route and its visible-light-driven environmental remediation. *Results Chem.*, *11*, 101850. <https://doi.org/10.1016/j.rechem.2024.101850>
- 13 Jafarova, V.N., & Orudzhev, G.S. (2021). Structural and electronic properties of ZnO: A first-principles DFT study within LDA(GGA) and LDA(GGA)+U methods. *Solid State Commun.*, *325*, 114166. <https://doi.org/10.1016/j.ssc.2020.114166>
- 14 Mandal, G., Goswami, M.N., & Mahapatra, P.K. (2024). Efficient photocatalytic degradation of wastewater solution through Mn-doped BiFeO₃ nanomaterials. *Physica B Condens. Matter*, *695*, 416475. <https://doi.org/10.1016/j.physb.2024.416475>
- 15 López-Ramón, M.V., Stöeckli, F., Moreno-Castilla, C., & Carrasco-Marín, F. (1999). On the characterization of acidic and basic surface sites on carbons by various techniques. *Carbon*, *37*, 1215–1221. [https://doi.org/10.1016/S0008-6223\(98\)00317-0](https://doi.org/10.1016/S0008-6223(98)00317-0)
- 16 Mohd Azmy, H.A., et al. (2017). Visible-light photocatalytic activity of BiFeO₃ nanoparticles for degradation of methylene blue. *J. Phys. Sci.*, *28*, 85–103. <https://doi.org/10.21315/jps2017.28.2.6>
- 17 Das, B.B., & Rao, R.G. (2015). Synthesis, crystal structure, and electronic properties of CeBiO₃ oxide. *Phys. Status Solidi B*, *252*, 2680–2684. <https://doi.org/10.1002/pssb.201451753>
- 18 West, A.R. (2014). *Solid State Chemistry and Its Applications*, 2nd ed.; Wiley: Chichester, West Sussex, UK.
- 19 Meena, P.L., Surela, A.K., Saini, J.K., & Chhachhia, L.K. (2022). Millettia pinnata plant pod extract-mediated synthesis of Bi₂O₃ for degradation of water pollutants. *Environ. Sci. Pollut. Res.*, *29*, 79253–79271. <https://doi.org/10.1007/s11356-022-21435-z>
- 20 Wattanathana, W., et al. (2021). Crystallographic and spectroscopic investigations on oxidative coordination in the heteroleptic mononuclear complex of cerium and benzoxazine dimer. *Molecules*, *26*, 5410. <https://doi.org/10.3390/molecules26175410>
- 21 Hu, Y., Fei, L., Zhang, Y., Yuan, J., Wang, Y., & Gu, H. (2011). Synthesis of bismuth ferrite nanoparticles via a wet chemical route at low temperature. *J. Nanomater.*, *2011*, Art. ID 797639, 1–6. <https://doi.org/10.1155/2011/797639>
- 22 Martins, A.C., et al. (2017). Sol–gel synthesis of new TiO₂/activated carbon photocatalyst and its application for degradation of tetracycline. *Ceram. Int.* *43*, 4411–4418. <https://doi.org/10.1016/j.ceramint.2016.12.088>
- 23 Sonia, A., Kumar, A., & Kumar, P. (2023). Z-scheme ZnFe₂O₄/CeO₂ nanocomposites with enhanced photocatalytic performance under UV light. *Appl. Phys. A*, *129*, 724. <https://doi.org/10.1007/s00339-023-06959-6>
- 24 Subramani, A.K., Byrappa, K., Ananda, S., Lokanatha Rai, K.M., Ranganathaiah, C., & Yoshimura, M. (2007). Photocatalytic degradation of indigo carmine dye using TiO₂-impregnated activated carbon. *Bull. Mater. Sci.*, *30*, 37–41. <https://doi.org/10.1007/s12034-007-0007-8>
- 25 Gupta, V.K., Jain, R., Agarwal, S., Nayak, A., & Shrivastava, M. (2012). Photodegradation of hazardous dye quinoline yellow catalyzed by TiO₂. *J. Colloid Interface Sci.*, *366*, 135–140. <https://doi.org/10.1016/j.jcis.2011.08.059>
- 26 Tsaviv, J.N., Eneji, S.I., Sha'Ato, R., Ahemen, I., Jubu, P.R., & Yusuf, Y. (2024). Photodegradation, kinetics, and non-linear error functions of methylene blue dye using SrZrO₂ perovskite photocatalyst. *Heliyon*, *10*, e34517. <https://doi.org/10.1016/j.heliyon.2024.e34517>
- 27 Yazdanbakhsh, M., Tavakkoli, H., & Hosseini, S.M. (2011). Characterization and evaluation of catalytic efficiency of La_{0.5}Ca_{0.5}NiO₂ nanopowders in removal of reactive blue 5 from aqueous solution. *Desalination*, *281*, 388–395. <https://doi.org/10.1016/j.desal.2011.08.020>
- 28 Fosso-Kankeu, E., Pandey, S., & Ray, S.S. (Eds.). (2020). *Photocatalysts in Advanced Oxidation Processes for Wastewater Treatment*; Scrivener Publishing: Hoboken, NJ. <https://doi.org/10.1002/9781119631422>

CHEMICAL TECHNOLOGY

Article

Received: 28 February 2025 | Revised: 15 May 2025 |
Accepted: 22 May 2025 | Published online: 28 May 2025

UDC 66-971; 620.3

<https://doi.org/10.31489/2959-0663/2-25-12>

Aldana R. Galiyeva*¹, Nazgul A. Yessentayeva¹, Dias T. Marsel¹, Arailym T. Daribay¹,
Daniiyar T. Sadyrbekov¹, Rouslan I. Moustafine², Tatyana V. Kutulutska³

¹Karaganda Buketov University, Karaganda, Kazakhstan;

²Institute of Pharmacy, Kazan State Medical University, Kazan, Russia;

³“Regional Center of Phthisiopulmonology” of the Health Department of Karaganda region, Karaganda, Kazakhstan

(*Corresponding author's e-mail: aldana_karaganda@mail.ru)

Polylactide Acid-Based Nanoparticles for Controlled Delivery of Isoniazid and Rifampicin: Synthesis, Characterization, and *In Vitro* Release Study

The global problem of tuberculosis (TB) requires advanced drug delivery systems that improve treatment efficacy. In this study, polylactic acid (PLA)-based drug carriers were developed for the controlled delivery of the first-line anti-TB drugs isoniazid (INH) and rifampicin (RIF). The main objective of this study is to improve PLA-based NP formulations through optimization to achieve maximum drug content coupled with enhanced stability to improve treatment outcomes. PLA-RIF-INH nanoparticles (NPs) were prepared by double emulsion method using ultrasonic homogenizer, using different surfactants (polyvinyl alcohol, Tween-80 and Pluronic F-127) and with different organic solutions (dichloromethane, dimethyl sulfoxide and ethyl acetate) at different phase ratios. The produced NPs had an average size of 197 ± 8 nm with a polydispersity index of 0.287 ± 0.048 and contained 23 ± 2 % INH and 20 ± 8 % RIF for a NPs yield of 65 ± 2 %. The release of drugs from PLA NPs was investigated using the flow cell method and the vertical diffusion method at different pH values simulating gastrointestinal conditions. It was shown that PLA-RIF-INH NPs have pronounced antimycobacterial activity against *Mycobacterium tuberculosis* H37Rv and isoniazid-resistant strain, which confirms the prospect of their use in tuberculosis therapy.

Keywords: drug delivery systems, nanoparticles, polylactic acid, anti-tuberculosis drugs, double emulsion, flow cell method, vertical diffusion method, *Mycobacterium tuberculosis*, ultrasonic homogenization

Introduction

The development of advanced drug delivery systems becomes a crucial focus of pharmaceutical research, as they address infectious diseases, particularly tuberculosis (TB). The current standard formulations of drugs face multiple drawbacks when they are not properly absorbed in the body and are eliminated quickly, while causing unwanted side effects [1]. Colloidal drug delivery systems have become important due to their ability to improve drug solubility together with their protective effect on active pharmaceutical ingredients and controlled release capabilities. PLA serves as an outstanding biodegradable material for drug delivery applications due to its ability to create stable nanostructures and its notable properties of biocompatibility and biodegradability [2-3]. PLA-based colloidal systems maintain drug circulation times effectively while targeting delivery and reducing toxicity which makes them ideal to encapsulate anti-TB drugs [4].

This study investigates the synthesis and stability aspects of PLA-based colloids and presents the methods for incorporating essential tuberculosis drugs such as isoniazid and rifampicin. Rifampicin together with isoniazid operates as front-line tuberculosis drugs for widespread medical use in tuberculosis therapy [5]. The drugs provide effective tuberculosis treatment by restraining both *Mycobacterium tuberculosis* (MTB)

growth and multiplication. Despite their high success rate in treatment there exists a possible resistance development against these drugs, primarily because of inadequate treatment adherence and improper dosing schedule [6]. Multiple drugs are combined for treatment purposes when resistance emerges against one agent to control resistant bacterial strains effectively [7-8].

This investigation examines double emulsion techniques to develop precise drug delivery methods for anti-TB medications that focus on delivering these agents effectively to bacterial cells. The optimization procedure involved testing multiple factors which included selecting different organic solvents, various stabilizing surfactant concentrations, defining the ratio of organic to aqueous phase and using different molecular weights of polymers during nanoparticle formation. The drug release profiles alongside size and stability of nanoparticles depend strongly upon these particular factors. The study analyzes how PLA-based nanoparticles perform physically through size distribution assessments and surface morphology inspections and investigations of their stability in simulated body fluids. Scanning electron microscopy (SEM) was used to study morphological properties and additional characterization involved infrared spectroscopy (IR), thermogravimetric analysis (TGA), and differential scanning calorimetry (DSC) of the nanoparticles. In vitro experiments evaluated how drug substances released from polymer matrices at various time points. The study analyzes these characteristics to improve the PLA-based nanoparticle system with a more controlled drug release profile for better TB treatment results with drug-resistant strains.

Experimental

Materials

Poly (D,L-lactide) molecular weight (MW) 10,000, 15,000 and 20,000; Pluronic F-127 powder, Polyvinyl alcohol (PVA) (MW 9000–10,000, 80 % hydrolyzed); isoniazid with an in-medical purity of over 99 %, rifampicin with indicated purity over 99 %; dimethyl sulfoxide (DMSO) (≥ 99.5); ethyl acetate (EA) (≥ 99.5); dichloromethane (DCM) (≥ 99.5) were purchased from Sigma Aldrich (St. Louis, MO, USA). Tween 80 solution was purchased from CJSC “Kupavnareaktiv” (Russia, Old Kupavna city).

Preparation of PLA-RIF-INH NPs

Nanoparticles of PLA-RIF-INH were prepared by double emulsion method [9–11]. A solution of INH drug substance (at a concentration of 2–10 mg/mL) dissolved in 1 mL water was combined with 5 mL of PLA solution in organic solvent for the synthesis. The hydrophobic RIF (at a concentration of 2–10 mg/mL) substance needed separate dissolution in an organic solvent and water mixture before addition to PLA solution in the same organic solvent. A primary emulsion formed due to mixing those components after which an ultrasonic homogenizer (Bandelin Sonopuls HD 2070, Bandelin Elec., Germany) ran the mixture continuously for two minutes. A primary emulsion received 10 mL of aqueous phase which included stabilizer (PVA, Tween-80, Pluronic F-127) as a surfactant through droplet addition. An ultrasonic homogenizer stabilized a secondary emulsion from the combined solution. A magnetic stirrer operated at room temperature under stirring for 6 hours to evaporate the solvent from this emulsion. The separation of RIF and INH-loaded PLA nanoparticles occurred through a centrifugation process at 14000 rpm for 30 minutes.

Determination of Particle Size, Polydispersity and ζ -potential of PLA-RIF-INH NPs

The Zetasizer Nano S90 (Malvern Instruments Ltd., Malvern, UK) measured the nanoparticle size distribution and polydispersity index through Dynamic Light Scattering (DLS) examinations. The nanoparticle size examination required 5–8 drops of nanoparticles added to 1.5–2 mL of distilled water. The measurement of the samples took place at 25 °C while using a 90° scattering angle for detection. The ζ -potential was measured with a ζ -potential analyser (NanoBrook ZetaPALS, Holtsville, NY, USA) using electrophoretic laser Doppler anemometry. The analysis with scanning electron microscopy (SEM) evaluated the dimensions together with surface structures and shapes of the nanoparticles. A MIRA 3 LM TESCAN (Brno, Czech Republic, EU) served for SEM analysis.

Evaluation of Drug Loading Efficiency and Nanoparticles' Yield

The determination of drug loading in polymer matrices relied on drug detection from unincorporated drug concentrations in the supernatant. The quantification method used HPLC along with a Shimadzu LC-20 Prominence system featuring a Shimadzu Scientific Instruments UV/VIS detector. Acetonitrile and water (60:40) formed the mobile phase which ran at 0.8 mL/min through the system. The Promosil C18 column from Agilent Technologies (Tokyo, Japan) operated for component separation with a 5 μm sorbent grain size

and 100 Å pore size within 4.6 × 150 mm dimensions. Raising the column temperature to 40 °C served as the maintenance condition. The injection used 10 µL sample with loop injection. The calculations for drug loading efficiency were made using the following formula:

$$\text{Loading efficiency}(LE, \%) = \frac{\text{Total mass of drug} - \text{mass of free drug}}{\text{Mass of NPs}} \times 100 \%;$$

$$\text{Nanoparticles yield}(\%) = \frac{\text{Mass of NPs}}{\text{Total mass of drug} + \text{mass of PLA}} \times 100 \%.$$

In Vitro Drug Release from PLA-RIF-INH NPs

For the investigation of in vitro drug release two analytical approaches were applied: the Flow-Through Cell apparatus with CE 7Smart technology from Sotax (Aesch, Switzerland) and vertical delivery through Franz PHOENIX™ DB-6 cells from Telodyne Hanson Research (Chatsworth, GA, USA) [9, 10]. The investigation applied phosphate buffer solutions at three pH values to replicate physiological conditions: pH 1.2 for gastric conditions and pH 6.8 for intestinal conditions alongside pH 7.4 for blood plasma conditions. Each solution operated at 37 ± 0.5 °C during testing.

The CE 7Smart instrument operated at a continuous flow rate of 2 mL/min during Flow-Through Cell method testing. The experiments employed Float-A-Lyzer® G2 nanoadapters (Merck KGaA, Darmstadt, Germany) as the dialysis membrane with known pore sizes within the range of 8000 to 10,000 Da. The experiment lasted for 24 hours.

In the vertical diffusion method using the Franz cell employed dialysis membranes (MWCO = 8000 Da, Medicell International Ltd., London, UK) were placed the polymeric nanoparticles loaded anti-tuberculosis drugs at 200 rpm stirring. The experimental duration spanned across 48 hours. The collected release medium samples underwent UV/V is spectrophotometer (Lambda 25, PerkinElmer, Waltham, MA, USA) analysis at 475 nm wavelength for RIF and 254 nm wavelength for INH at predefined measurement times of 0.5, 1, 2, 4, 8, 24 and 48 hours. Fresh medium replaced the withdrawn samples at each measurement point. A calibration curve containing drug solutions at specific concentrations served as the comparison standard for analyzing the collected data. A mathematical formula served to calculate the drug release speed in this experiment:

$$\text{Drug release}(\%) = \frac{\text{Mass of released drug}}{\text{Mass of total drug in nanoparticles}} \times 100 \%.$$

Thermal Analysis Using Thermogravimetry and Differential Scanning Calorimetry

TGA and DSC measurements were carried out on a LabSYS evo TGA/DTA/DSC analyzer (Setaram, Caluire France) [12–14]. The experiment took place between 30 °C and 550 °C. A controlled heating process at 10 °C/min was performed while the samples were put inside an aluminum oxide crucible. Under a nitrogen atmosphere the analysis proceeded with a continuous gas flow of 30 mL/min.

Infrared Spectroscopic Analysis of PLA-RIF-INH NPs

The FSM 1202 spectrometer (Infraspek Ltd., Russia) determined the characteristics of the prepared nanoparticle samples through IR spectroscopy tests [15, 16]. The potassium bromide (KBr) pellet technique recorded the Fourier-transform infrared (FTIR) spectrum data. A pellet was made from blending 3 mg of the sample with 100 mg of KBr using pellet formation methods. A spectral analysis covered the wavelength span from 4000 to 400 cm⁻¹.

In vitro Evaluation of Antimycobacterial Activity of PLA-RIF-INH Nanoparticles

In vitro tests were conducted under sterile conditions using Airstream AC2-4E8 biosafety cabinets (Esco Micro Pte. Ltd., Singapore), which ensured a contamination-free environment through negative pressure and HEPA filtration. The antimycobacterial efficacy of PLA-RIF-INH nanoparticles was assessed using three MTB strains: the drug-sensitive H37Rv strain, an isoniazid-resistant strain (H), and a rifampicin-resistant strain (R). Nanoparticles were tested at concentrations corresponding to 8 mg/mL of rifampicin and 8 mg/mL of isoniazid. The bacteriostatic activity of the nanoparticles was determined by evaluating MTB growth on Levenstein-Jensen solid medium [17–19]. Inoculated tubes were incubated for 4 weeks, after which the number of colony forming units (CFUs) was recorded. Antimicrobial activity was assessed by comparing CFU counts between treated samples and controls. Positive cultures were stained using the Ziehl–Neelsen method [20], and the stained smears were subsequently examined with a Leica DMLS microscope.

Statistical Analysis

The research data represent mean \pm standard deviation while statistical analysis through Minitab 19 Statistical Software implemented one-way analysis of variance (ANOVA) to determine group difference significance.

Results and Discussion

The double emulsion method is an effective technique for creating nanoparticles based on polymers, including PLA, according to the literature [9–11]. This encapsulation method provides highly efficient ways to incorporate both hydrophobic and hydrophilic substances into drug delivery systems. Obtaining a double emulsion starts by mixing the active ingredients as an aqueous emulsion with an organic solution protected by stabilizing agents. When the second emulsion is formed, it is converted into stable nanoparticles after evaporation of the solvent [21]. The novelty of this work is the use of ultrasonic homogenizer to enhance emulsion formation by double emulsion method to produce PLA-RIF-INH NPs (Figure 1). The ultrasonic treatment improves dispersing the active ingredient particles in the polymer matrix, resulting in improved distribution uniformity and higher encapsulation standards. This innovative approach allows the production of smaller nanoparticles, contributing to the clarification of their morphological characteristics.

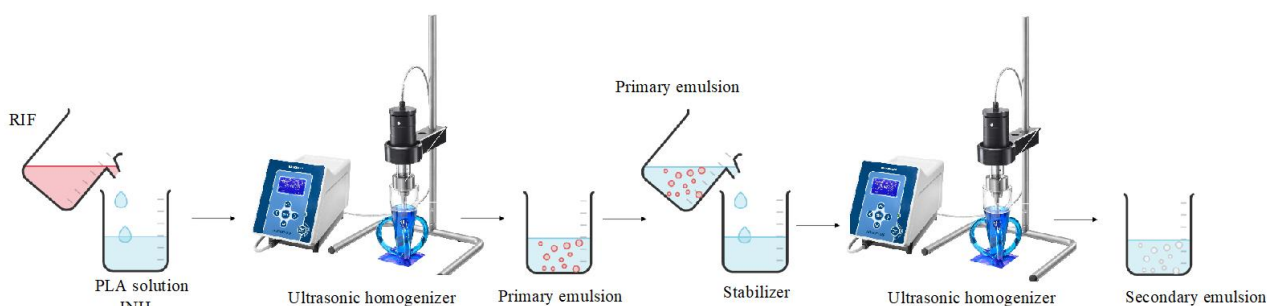


Figure 1. Scheme for producing PLA-RIF-INH NPs by double emulsion method

An appropriate choice of organic solvent stands as a vital component in double emulsion solvent evaporation because it controls nanoparticle formation along with their stability and drug entrapment capacity. For proper drug dispersing within the polymer matrix the solvent needs to demonstrate appropriate solubility toward hydrophilic and hydrophobic elements. The emulsifying capacity must be strong because emulsion stability depends on it, which affects nanoparticle size, dispersity, and drug loading efficiency. The present work investigated the three different organic solvents DCM, DMSO and EA to study their effects on the physicochemical features of PLA-based nanoparticles [16]. The formation process of nanoparticles gets substantially affected by the different physicochemical properties found in three solvents including volatility, solubility and miscibility with aqueous phases. Results on the influence of organic solvents on physical and chemical properties of nanoparticles are presented in Table 1.

Table 1

Effect of organic solvents on physicochemical properties of PLA-RIF-INH NPs

Organic solvent	Average size of NPs, nm	PDI	LE (INH), %	LE (RIF), %	NPs yield, %
DCM	365 \pm 2	0.060 \pm 0.002	26 \pm 4	26 \pm 5	24 \pm 5
DMSO	545 \pm 4	0.422 \pm 0.035	10 \pm 7	10 \pm 7	11 \pm 2
EA	314 \pm 5	1.000 \pm 0.102	19 \pm 5	19 \pm 5	16 \pm 9

Among the solvent systems tested, DCM provided the most favorable results for the formation of nanoparticles. The size of the nanoparticles produced was 365 \pm 2 nm, and the lowest PDI was found to be 0.060 \pm 0.002, indicating a highly homogeneous distribution of nanoparticles, which is a desirable property for drug delivery applications. In fact, not only was DCM found to yield highly uniform sized nanoparticles, but it was also the most efficient solvent system in terms of drug loading: the LE was measured at 26 \pm 4 % for INH and 26 \pm 5 % for RIF, with a yield of 24 \pm 5 % for the nanoparticles themselves. DMSO produced opposite results: the size was large (545 \pm 4 nm), the PDI was high (0.422 \pm 0.035), signifying polydispersity, and

the LE was actually quite low ($10 \pm 7\%$) for both antitubercular medications; the yield of the DMSO nanoparticles was $11 \pm 2\%$, as well. EA had intermediate size results, but it was found to be the least stable solvent system, with the highest sharp distribution of sizes: the PDI registered was 1.000 ± 0.102 . The results demonstrate that DCM represents the optimal solvent for producing PLA-based nanoparticles because it generates uniform tiny particles with better drug loading along with high yield values. Both DMSO and EA do not attain satisfactory laboratory outcomes as nanoparticle formulations and exhibit elevated polydispersity indices because of their limited effectiveness in solvent performance.

Studies on nanoparticle synthesis with organic solvents requires additional attention to surfactants because these molecules are essential for stabilizing nanoparticles while influencing their characteristics. Results provided in Table 2 summarize the obtained data.

Table 2

Effect of different surfactants on the characteristics of PLA-RIF-INH NPs

Surfactant	Average size of NPs, nm	PDI	LE (INH), %	LE (RIF), %	NPs yield, %
PVA	354 ± 2	0.072 ± 0.025	23 ± 4	26 ± 5	54 ± 7
Tween-80	486 ± 3	0.234 ± 0.033	29 ± 5	30 ± 2	40 ± 5
Pluronic F-127	534 ± 2	0.495 ± 0.047	13 ± 6	13 ± 7	8 ± 7

The synthesis process of PLA-RIF-INH nanoparticles is directly influenced by the type of surfactant selected. PVA resulted in creating the nanoparticles with the smallest average size, whereas nanoparticles produced with Pluronic F-127 and Tween-80 became larger in size. The synthesis of PLA-RIF-INH nanoparticles with a PVA-based surfactant results in the most uniform particle size distribution, as indicated by the lowest polydispersity index compared to Pluronic F-127 and Tween-80, which show higher polydispersity. Tween-80 serves as the most effective surfactant for drug loading as it yields in $29 \pm 5\%$ INH and $30 \pm 2\%$ RIF, but Pluronic displays low values of loading (?) at $13 \pm 6\%$ INH and $13 \pm 7\%$ RIF. The drug loading efficiency of INH and RIF using PVA stands at $23 \pm 4\%$ and $26 \pm 5\%$ respectively. The NPs yield reached $54 \pm 7\%$ through the use of PVA which made it the optimal surfactant choice for the manufacturing process. The NPs yield reaches $40 \pm 5\%$ and $8 \pm 7\%$ when using Tween-80 and Pluronic. The selection of surfactant serves as a critical factor during PLA-RIF-INH NPs synthesis, as PVA delivers the best outcomes regarding size control together with uniform distribution and drug loading capacity and particle yield. Our analysis focuses on the impact of PVA concentration on essential features that define the created nanoparticles (Table 3).

Table 3

Effect of PVA concentration on the characteristics of PLA-RIF-INH nanoparticles

PVA concentration, %	Average size of NPs, nm	PDI	LE (INH), %	LE (RIF), %	NPs yield, %
0.3	658 ± 5	0.160 ± 0.015	6 ± 3	5 ± 6	45 ± 3
0.5	367 ± 8	0.127 ± 0.023	23 ± 4	26 ± 5	44 ± 1
1	287 ± 8	0.358 ± 0.054	10 ± 2	10 ± 2	61 ± 5
1.5	190 ± 7	0.219 ± 0.047	25 ± 6	29 ± 8	67 ± 4
3	127 ± 3	0.363 ± 0.046	16 ± 5	17 ± 3	60 ± 8

The particle size of nanoparticles becomes smaller when PVA concentration rises. The size of the nanoparticles decreases from 658 ± 5 nm to 127 ± 3 nm when PVA concentration increases from 0.3 % to 3 %. Nanoparticle Polydispersity Index depends on the concentration of Polyvinyl Alcohol present in the formulation. The best particle size distribution is achieved at a PVA concentration of 0.5 %, where the PDI reaches 0.127 ± 0.023 . PDI shows increased variations at PDI concentrations of 1 % and 3 % because these levels cover a wider range of particle dimensions. The incorporation amounts of INH and RIF in the nanocarriers show a direct relationship with PVA concentration values. At PVA concentration of 1.5 % both INH and RIF achieve their highest loading efficiency to reach $25 \pm 6\%$ and $29 \pm 8\%$ respectively. The optimal stabilization of the emulsion and suitable drug encapsulation conditions within nanoparticles occur at this specific surfactant concentration of 1.5 %. The nanoparticle producing process depends directly on how much PVA solu-

tion is used. The maximum INH and RIF loading efficiency together with the highest nanoparticle yield ($67\pm 4\%$) occur when the PVA concentration reaches 1.5%. The nanoparticle yield decreases slightly at 0.3% and 0.5% PVA concentrations although the size and PDI values remain relatively good. A 1.5% PVA concentration functions as the optimal condition for making PLA-RIF-INH NPs because it produces the most desirable particle size together with the highest drug loading ratio and nanoparticle yields.

Different molecular weights of PLA were used to study the relationship between nanoparticle parameters, such as particle size, polydispersity, drug loading efficiency, and yield (Table 4).

Table 4

Effect of polymer molecular weight on PLA-RIF-INH NPs characteristics

Molecular weight of PLA	Average size of NPs, nm	PDI	LE (INH), %	LE (RIF), %	NPs yield, %
10 000	138±4	0.251±0.017	79±2	1±2	37±5
15 000	197±8	0.287±0.048	23±2	20±8	65±2
20 000	263±4	0.340±0.019	11±4	11±3	43±2

The highest INH loading efficiency of $79\pm 2\%$ was achieved using PLA with MW 10000 for the formation of particles with 138 ± 4 nm dimensions and PDI 0.251 ± 0.017 yet the nanoparticles' yield reached only $37\pm 5\%$. PLA 15,000 produced nanoparticles with 197 ± 8 nm dimensions along with $23\pm 2\%$ INH content but achieved $20\pm 8\%$ RIF content and reached exceptional nanoparticles' yields at $65\pm 2\%$. The increase in molecular weight to 20,000 resulted in nanoparticle sizes of 263 ± 4 nm while the PDI rises to 0.340 ± 0.019 and INH and RIF loading efficiency decreases to $11\pm 4\%$ and $11\pm 3\%$ producing a nanoparticle yield of $43\pm 2\%$ at this molecular weight.

The study evaluated the effect of different concentrations of INH and RIF loaded in polymeric nanoparticles. Optimization of the elements can improve system stability and loading efficiency while maintaining controlled drug release. The selection process for INH and RIF concentrations should focus on optimizing loading efficiency while ensuring both small particles and narrow size distribution. The results are summarized in Table 5.

Table 5

Effect of drug concentration on PLA-RIF-INH NPs characteristics

Concentration of INH, mg/mL	Concentration of RIF, mg/mL	Average size of NPs, nm	PDI	LE (INH), %	LE (RIF), %	NPs yield, %
2	2	263±3	0.224±0.059	9±2	10±2	30±4
4	4	257±4	0.287±0.048	23±2	20±6	37±8
8	8	266±1	0.196±0.061	14±7	15±3	78±4
10	10	259±2	0.146±0.035	2±6	3±4	18±2

When the drug concentration reaches 2 mg/mL the NPs have an average diameter of 263 ± 3 nm and a polydispersity of 0.224 ± 0.059 which points on a uniform particle distribution. The achieved drug loading efficiency percentages were for INH at 9% and for RIF at 10% while the overall NPs' yield reached only 30%. The active ingredient concentration increases to 4 mg/mL reduced NPs sizes down to 257 ± 4 nm while increasing loading efficiency of INH to 23% and RIF to 20% and resulting in a NPs yield of 37%. The encapsulation process shows better performance at this additive concentration. The experimental system exhibits enhanced homogeneity as the concentration reaches 8 mg/mL where it maintains a stable particle size (266 ± 1 nm) with lower polydispersity (0.196 ± 0.061). This technique produces stable systems with high encapsulation by achieving both acceptable loading efficiency (INH 14% and RIF 15%) and maximum yield of NPs at 78%. An increase in INH and RIF concentration to 10 mg/mL leads to reduced encapsulation (INH — 2%, RIF — 3%) along with decreased NP producing (18%) even with small particle size (259 ± 2 nm) and minimal polydispersity values (0.146 ± 0.035). The drug substances tend to escape from the polymer matrix when it reaches saturation levels and leach into the surrounding aqueous solution which results in lower loading efficiency [22]. The formation of stable PLA nanoparticles reaches its optimal condition at INH and RIF concentration of 8 mg/mL since it creates ideal yield rates with suitable particle size distribution and drug loading efficiency.

The optimized nanoparticles exhibited optimal properties consisting of 197 ± 8 nm average size and 0.287 ± 0.048 polydispersity values and 23 ± 2 % isoniazid loading efficiency alongside 20 ± 8 % rifampicin loading efficiency and 65 ± 2 % nanoparticle yield. Analysis of the produced nanoparticles included SEM examinations. Observations of Figure 2 indicate to the formation of round-shaped nanoparticles with a smooth surface. The software imageJ program enabled measurement of PLA-RIF-INH NPs size which amounted to 130 ± 8 nm.

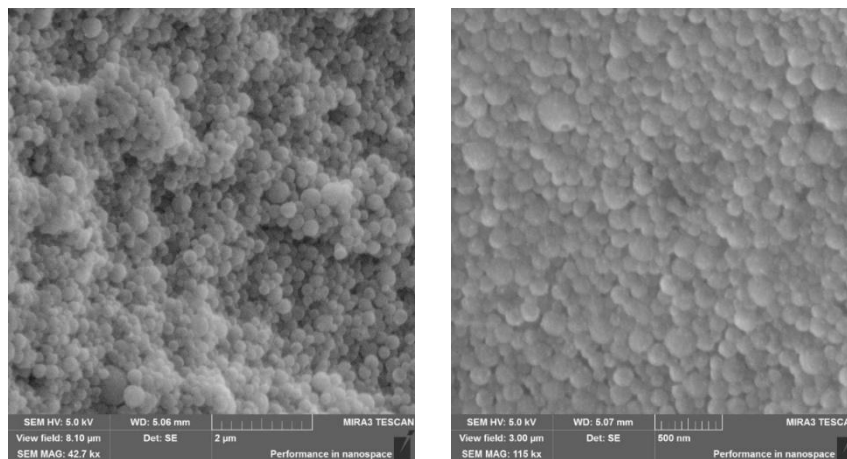


Figure 2. SEM images of PLA-RIF-INH NPs at a 2 μ m and 500 nm scale

A zeta potential of PLA-RIF-INH NPs is $+9.68 \pm 3$ mV suggests that the nanoparticles possess a moderately positive surface charge, which is generally sufficient to maintain colloidal stability through electrostatic repulsion (Figure 3). Although higher absolute values (± 30 mV or more) are typically associated with strongly stable systems, the observed value in this study was adequate to prevent aggregation under experimental conditions [23]. Moreover, the slightly positive charge may facilitate interaction with negatively charged components of bacterial cell walls or mucus layers, potentially enhancing cellular uptake and therapeutic efficacy.

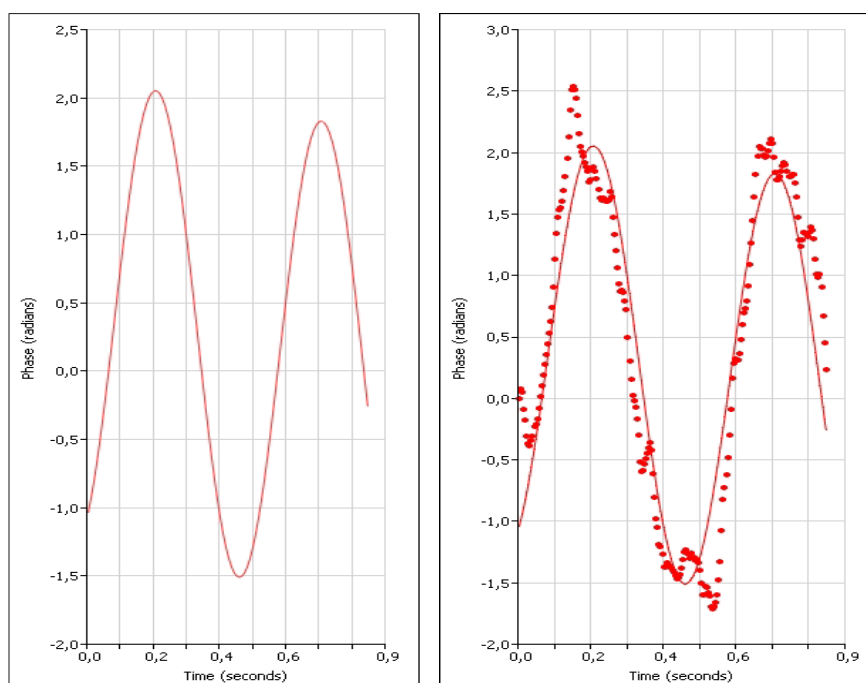


Figure 3. Zeta potential measurement of PLA-RIF-INH nanoparticles by phase analysis light scattering (PALS). The left panel shows the modeled phase shift curve, while the right panel displays experimental data (red dots) overlaid with the fitted curve

TGA and DSC were carried out to better understand the interaction of drugs with the polymer matrix of nanoparticles, and to confirm their effective incorporation into the structure (Figure 4). The study of thermal properties of isoniazid (Figure 4a) by DSC revealed a pronounced endothermic effect at 179.5 °C without mass loss, indicating a phase transition or melting of the substance [24, 25]. Thereafter, according to TGA, a gradual decrease in mass up to 25 % was observed in the temperature range of 250–450 °C, indicating thermal decomposition of the compound. The analysis of DSC and TGA curves of rifampicin (Figure 4b) demonstrates several peaks indicating the multistage character of the thermal decomposition of the drug substance. The first endothermic peak is observed at 188.7 °C and corresponds to the melting process of rifampicin. At this point, the substance passes from solid to liquid phase and no mass loss is recorded, indicating the absence of thermal decomposition. Then follows an exothermic peak at 209 °C, probably associated with the process of recrystallization and change of polymorphic form of rifampicin. This process is accompanied by partial decomposition of rifampicin with a mass loss of 10 %. The next exothermic peak at 253 °C is characterized by an additional 10 % mass loss, indicating the second stage of rifampicin decomposition [26]. The final stage of thermal decomposition is manifested by an exothermic peak at 425 °C, which is accompanied by a significant mass loss. The DSC curve of PLA (Figure 4c) shows a sharp endothermic peak at 330 °C, accompanied by a significant mass loss (up to 90 %), which indicates on intensive thermal decomposition of the polymer [3, 27]. The DSC curve of PLA nanoparticles encapsulated with isoniazid and rifampicin (Figure 4d) shows an endothermic peak at 350 °C, which is accompanied by thermal decomposition of the polymer matrix with a mass loss of 65 %. Compared to the DSC-curve of pure PLA, this peak has a lower intensity and is shifted to higher temperatures. This difference may indicate on a change in the thermal stability of PLA-INH-RIF nanoparticles, which may be the result of successful encapsulation of drugs and their interaction with the polymer matrix.

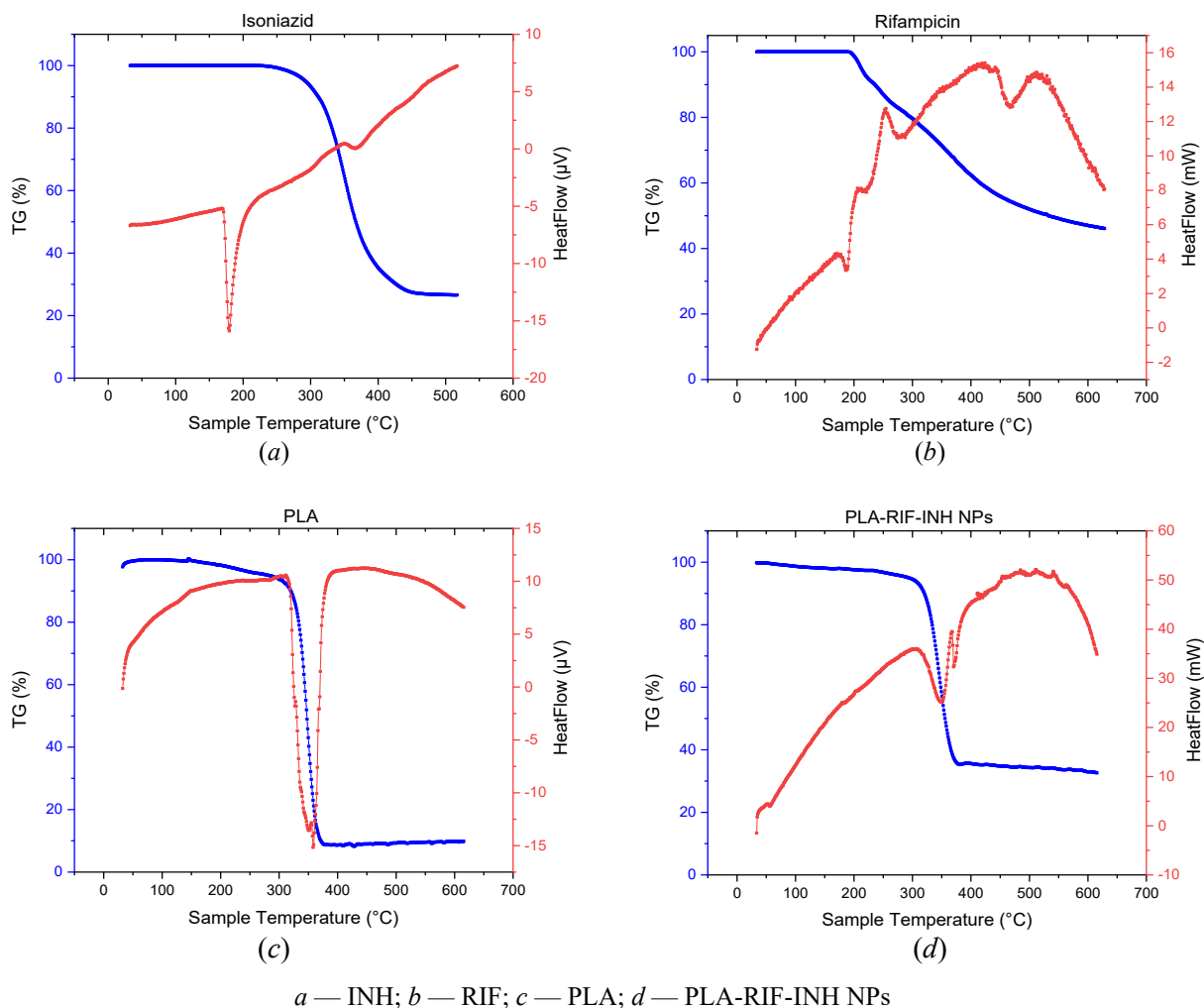


Figure 4. Thermal properties of the system components and the synthesized nanoparticles

In this study, FTIR spectroscopy was used to characterize the individual components, as well as the synthesized PLA-RIF-INH nanoparticles (Figure 5). The FTIR spectrum of PLA shows a characteristic peak at 3395 cm^{-1} , which corresponds to valence vibrations of hydroxyl ($-\text{OH}$) groups present at the end of the polymer chain [28]. The band at 1705 cm^{-1} corresponds to the valence vibrations of the carbonyl group ($\text{C}=\text{O}$). Asymmetric and symmetric vibrations of methyl groups ($-\text{CH}_3$) are observed at 2951 cm^{-1} and 1361 cm^{-1} , respectively. The absorption at 1041 cm^{-1} refers to the C-O bond vibrations. In addition, bending vibrations of $-\text{CH}_3$ asymmetric and symmetric type are identified at 1412 cm^{-1} and 1361 cm^{-1} , respectively [3, 29]. The IR spectrum of INH shows characteristic absorption bands corresponding to its functional groups. The band at 3306 cm^{-1} corresponds to the valence vibrations of the N-H bond. The band at 1670 cm^{-1} indicates the presence of a carbonyl ($\text{C}=\text{O}$) group conjugated to the pyridine ring. The symmetric C=N stretching vibrations of the ring appear at 1554 cm^{-1} while symmetric C=C stretching vibrations give rise to a peak at 1412 cm^{-1} [30, 31]. The IR spectrum of RIF contains peaks which specifically identify the different functional groups within the molecule structure. N-H stretching occurs at 3418 cm^{-1} thus verifying amino functional groups during analysis. The C-H bond shows valence vibrations that produce the signal at 2974 cm^{-1} . The carbonyl ($\text{C}=\text{O}$) group generates a peak at 1616 cm^{-1} while C=C double bond vibrations correspond to the signal at 1454 cm^{-1} . The fundamental vibrational patterns of different rifampicin functional groups can be validated through peaks at 1381 cm^{-1} (CH_2 , C=C) and 1053 cm^{-1} ($-\text{CH}$, CO, C-H) and 978 cm^{-1} ($\equiv\text{C}-\text{H}$, C-H) [32–34].

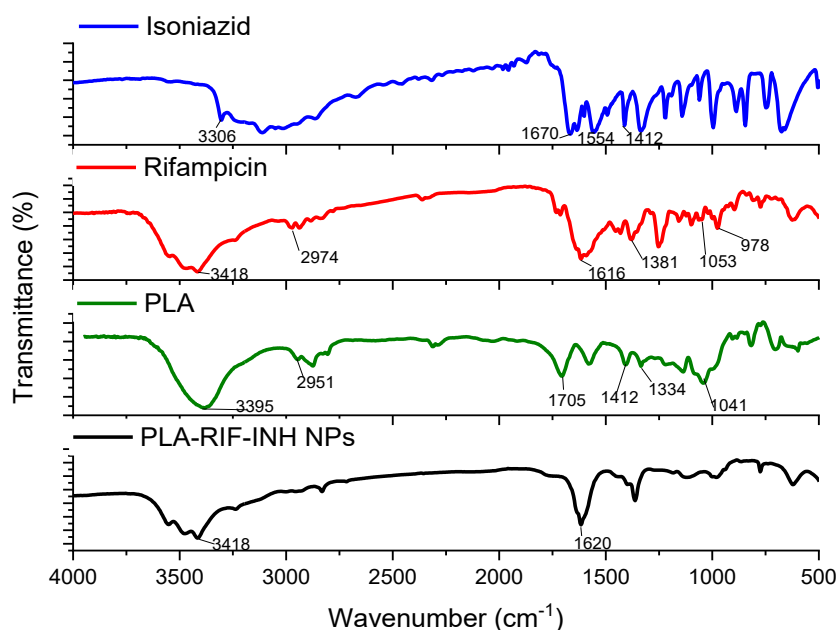


Figure 5. FTIR spectra for the system components and the synthesized nanoparticles

In the spectrum of the PLA-RIF-INH NPs the characteristic peaks of PLA, rifampicin, and isoniazid are still present, but with noticeable shifts and intensity changes. The broadening and slight shifts of the amide (1650 cm^{-1}) and hydroxyl (3400 cm^{-1}) peaks suggest hydrogen bonding interactions between the drugs and the PLA matrix. The ester peak of PLA at 1750 cm^{-1} is retained, indicating that the polymer structure remains intact. However, the reduced intensity of the individual drug peaks suggests successful encapsulation and molecular interactions rather than simple physical mixing.

The release profiles of isoniazid and rifampicin from PLA-based nanoparticles were systematically evaluated *in-vitro* to understand the behavior of the drug under pH changes, which is very important for modeling physiological conditions in different parts of the body (Figure 6, 7). Different buffers were used to assess the impact of digestive tract conditions (acidic stomach pH 1.2 and neutral bloodstream pH 7.4, and slightly basic small intestine pH 6.8) on drug release from nanoparticles [35]. Two proven laboratory methods known as the Flow-Through Cell method (Sotax system) and the Franz diffusion cell method were used to evaluate the release kinetics. Both approaches offer distinct advantages and contribute to a comprehensive

analysis of drug release from PLA nanoparticles. Despite methodological differences, the drug release results demonstrated a 98 % correlation, confirming the reliability of the study and the appropriateness of the selected methods for achieving the research objectives.

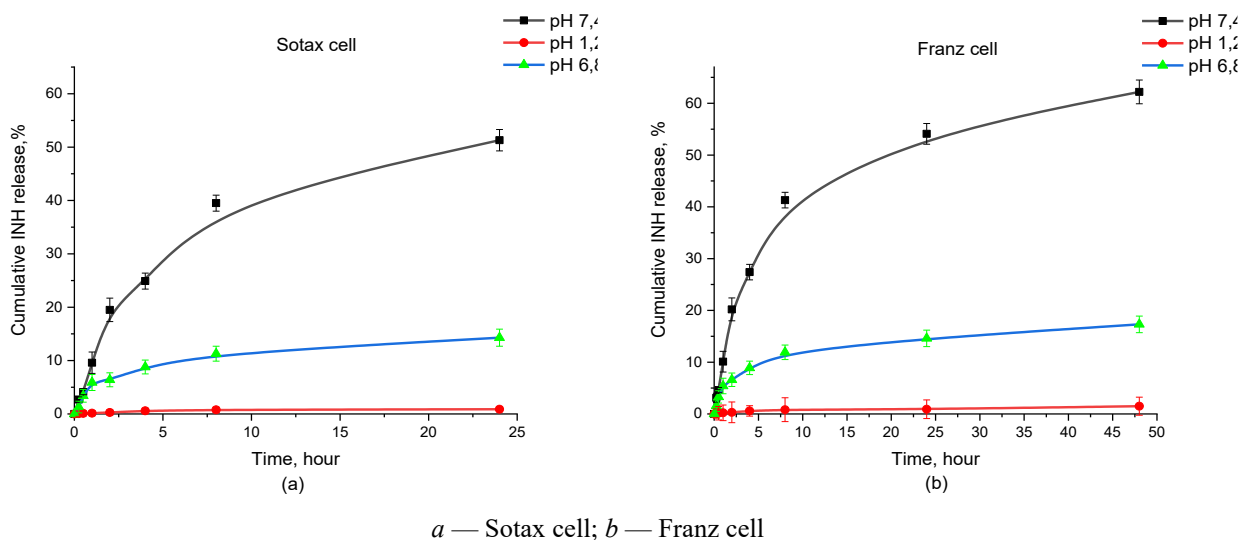


Figure 6. Cumulative release of isoniazid from PLA-RIF-INH nanoparticles under different pH conditions using two release models

The graphs (Figure 6) show that the release of INH is strongly pH dependent. At pH 7.4, a significantly higher release of INH was observed in both dissolution systems. The release profile has a biphasic character, with an initial sharp release during the first few hours, followed by a slower, sustained release over time [36, 37]. This behavior suggests rapid diffusion of drug molecules adsorbed on the surface, followed by a more controlled release from the polymer matrix. The drug release rate showed reduced speed at pH 6.8 which demonstrates lower drug diffusion capability at these conditions. The extended drug release pattern shows that the polymer utilizes either breakdown processes or volume expansion to regulate delivery of medication. Under pH 1.2 conditions the INH release remained low for both nanoparticle systems proving their stability during exposure to strong acidic environments. Stability during oral drug delivery becomes vital since it ensures INH stays properly encapsulated throughout gastric transit towards its targeted site.

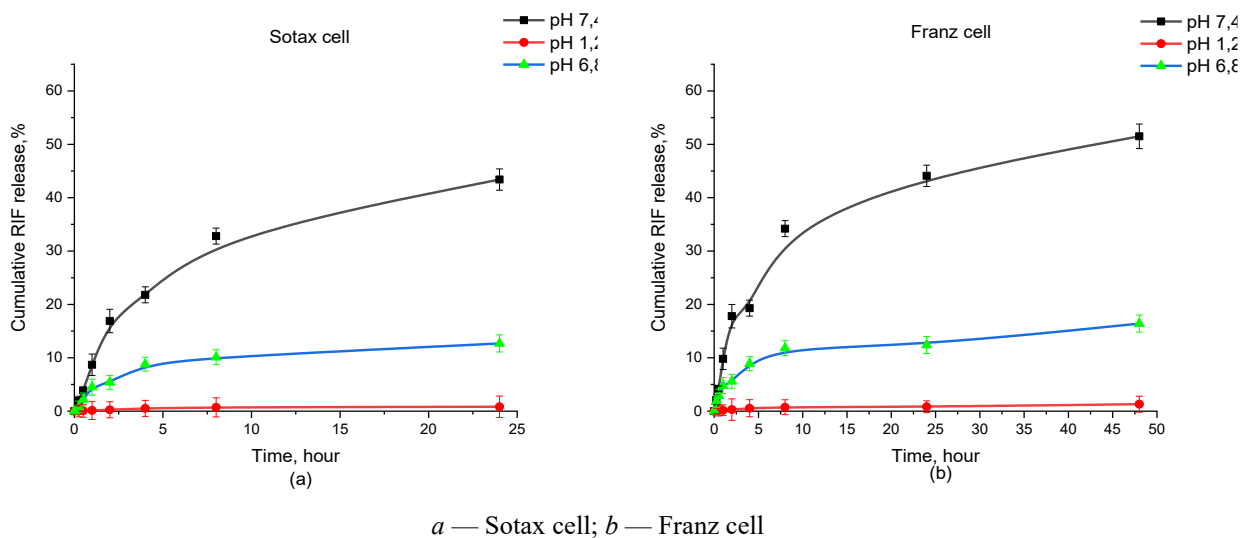


Figure 7. Cumulative release of rifampicin from PLA-RIF-INH nanoparticles under different pH conditions using two release models

Analysis of rifampicin release profiles from PLA nanoparticles in Sotax and Franz cells at different pH values shows a clear dependence of dissolution kinetics on environmental conditions (Figure 7). In neutral medium, which mimics blood flow, the highest drug release is observed, reaching more than 43 % in 24 h in the Sotax system and more than 51.5 % in 48 h in the Franz cell, indicating good solubility of rifampicin under physiological conditions. In a slightly acidic medium (pH 6.8) corresponding to the intestine, the release was markedly lower but had a sustained and gradual pattern, confirming the potential of PLA nanoparticles for prolonged drug delivery. In acidic medium, simulating gastric conditions, rifampicin release was minimal, despite its relatively high solubility at this pH [38, 39].

The results show that PLA nanoparticles create an effective barrier for protected medications in acid environments and prolong their release at normal body pH levels essential for therapeutic effects. The PLA nanoparticle platform has demonstrated potential for tuberculosis treatment improvement through extended drug delivery at controlled rates and increasing bioavailability. This reduces the need for frequent dosing and minimizes side effects.

The antimycobacterial properties were evaluated for the PLA-RIF-INH NPs against PLA NPs without drug incorporation. Tests assessed the drug efficacy for three MTB strains which consisted of the drug-sensitive strain H37Rv in addition to isoniazid-resistant strain H and rifampicin-resistant strain R. The antimycobacterial effectiveness of developed nanoparticles was analyzed through medium Löwenstein-Jensen incubation for three weeks followed by Ziehl-Neelsen staining examination [17–19]. The concentration of the encapsulated drugs used in this study was 8 mg/mL for both rifampicin and isoniazid. Figure 8 shows how the bacterial growth changed after treatment with the nanoparticles. The graphs present the number of colony-forming units (CFU) per 10⁷ cells, comparing placebo PLA NPs with drug-loaded PLA-RIF-INH nanoparticles. In the H37Rv strain group, PLA-RIF-INH NPs markedly decreased the number of CFU compared to PLA NPs used as control, reflecting effective bacteriostatic activity. Similarly, a significant reduction in bacterial growth was observed for the H — strain, although slightly less than the drug-sensitive strain. A moderate reduction in CFU counts was also observed for the R strain group, reflecting the fact that encapsulation of RIF and INH in PLA NPs retains antimicrobial activity even for resistant strains.

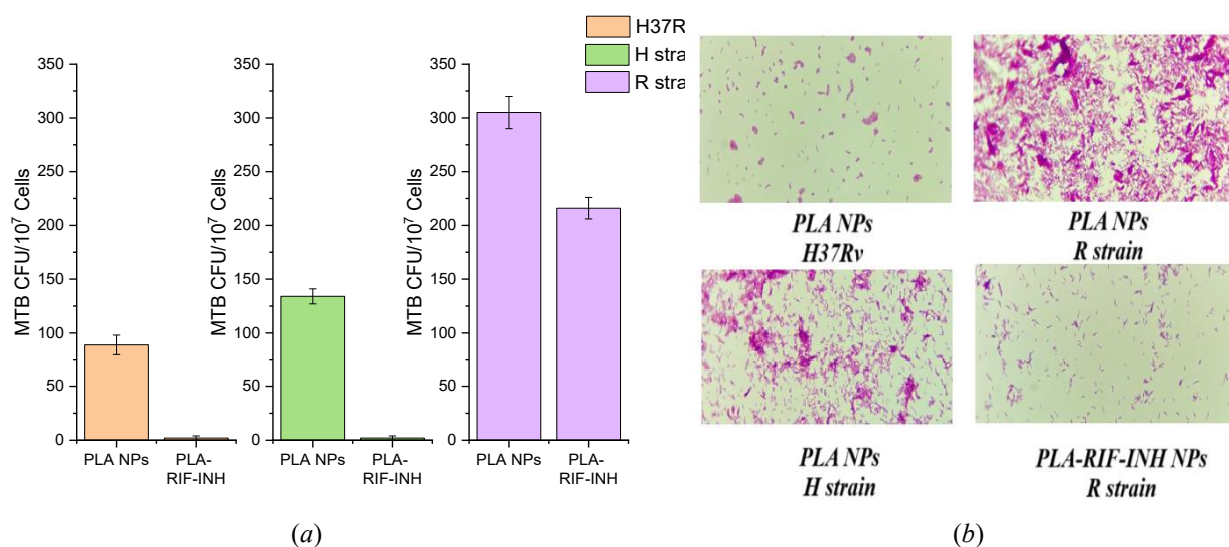


Figure 8. Antimycobacterial activity of PLA-RIF-INH NPs to different strains: H37Rv, H strain — isoniazid-resistant strain, R strain — rifampicin-resistant strain

The microscopic image (Figure 8b) confirms bacterial growth in cultures which contained rifampicin-resistant strains. The nanoparticle formulation demonstrated strong suppression of isoniazid-sensitive MTB strains but showed restricted effectiveness against MTB strains resistant to rifampicin. The developed nanoparticles demonstrate potential for tuberculosis treatment by targeting isoniazid-resistant infections but more approaches are essential to address rifampicin resistance.

Conclusions

The research developed and evaluated PLA NPs as drug carriers to deliver antituberculosis drugs including rifampicin and isoniazid. The optimized preparation method produced uniform PLA-RIF-INH NPs

with a 197 ± 8 nm average diameter, 0.287 ± 0.048 polydispersity index value, drug loading efficiency reaching 23 ± 2 % isoniazid and 20 ± 8 % rifampicin and a 65 ± 2 % NPs yield. The use of the flow cell method and vertical diffusion technique in Franz cells evaluated rifampicin and isoniazid release from PLA NPs at gastrointestinal tract relevant pH values. Drug release shows its highest activity at pH 7.4 making this system suitable for systemic use. Studies using microbiological methods indicated that PLA-RIF-INH NPs exhibited antimycobacterial properties against sensitive Mycobacterium tuberculosis strain H37Rv as well as isoniazid-resistant H strain. The limited impact of the system on rifampicin-resistant strain R demonstrates the requirement to advance the composition and combination therapy strategies further. The developed PLA-RIF-INH NPs demonstrate potential as an effective tuberculosis medication delivery system by offering controlled drug release in conjunction with high effectiveness for both sensitive and isoniazid-resistant MTB strains. The study findings will serve as foundation data to enhance polymeric delivery system methods for tuberculosis treatment research.

Supporting Information

The Supporting Information is available free at <https://ejc.buketov.edu.kz/index.php/ejc/article/view/272/215>

Funding

This research was funded by the Science Committee of the Ministry of Science and Higher Education of the Republic of Kazakhstan under Grant No. AP14871344, titled “Development of colloidal biopolymer-based drug delivery systems for tuberculosis chemotherapy”.

Author Information*

*The authors' names are presented in the following order: First Name, Middle Name and Last Name

Aldana Rymzhanovna Galiyeva (*corresponding author*) — Leading Researcher, Institute of Chemical Problems, Karaganda Buketov University, Universitetskaya street, 28, 100024, Karaganda, Kazakhstan; e-mail: aldana_karaganda@mail.ru; <https://orcid.org/0000-0002-8551-6297>

Nazgul Asylbekkyzy Yessentayeva — 3rd year PhD Student, Department of Organic Chemistry and Polymers, Karaganda Buketov University, Universitetskaya street, 28, 100024, Karaganda, Kazakhstan; e-mail: naz.yessentayeva92@gmail.com; <https://orcid.org/0000-0003-4820-8460>

Dias Temirlanuly Marsel — Master Student, Karaganda Buketov University, Universitetskaya street, 28, 100024, Karaganda, Kazakhstan.; e-mail: marsel.dias@bk.ru; <https://orcid.org/0000-0002-1204-0814>

Arailym Turashkyzy Daribay — Junior Researcher, Karaganda Buketov University, Universitetskaya street, 28, 100024, Karaganda, Kazakhstan; e-mail: arailymdaribay@gmail.com; <https://orcid.org/0000-0001-5675-0351>

Daniyar Tleuzhanovich Sadyrbekov — Candidate of Chemical Sciences, Researcher, Laboratory of the Engineering Profile “Physical and Chemical Methods of Research”, Karaganda Buketov University, Universitetskaya street, 28, 100024, Karaganda, Kazakhstan; e-mail: daniyar81@gmail.com; <https://orcid.org/0000-0002-3047-9142>

Rouslan Ibragimovich Moustafine — Candidate of Science (Pharmacy), Associate Professor, Director of the Institute of Pharmacy, Kazan State Medical University, Fatykh Amirkhan Street, 16, 420126, Kazan, Russia; e-mail: ruslan.mustafin@kazangmu.ru, <https://orcid.org/0000-0002-0916-2853>

Tatyana Valentinovna Kutulutskaya — Head of the Laboratory of the “Regional Center of Phthisiopulmonology” of the Health Department of Karaganda region, Karaganda, Kazakhstan; e-mail: tata_kutul@mail.ru

References

- 1 Adepu, S., & Ramakrishna, S. (2021). Controlled Drug Delivery Systems: Current Status and Future Directions. *Molecules*, 26(19), 5905. <https://doi.org/10.3390/molecules26195905>
- 2 Liu, S., Qin, S., He, M., Zhou, D., Qin, Q., & Wang, H. (2020). Current applications of poly(lactic acid) composites in tissue engineering and drug delivery. *Composites Part B: Engineering*, 199, 108238. <https://doi.org/10.1016/j.compositesb.2020.108238>

- 3 Galiyeva, A., Daribay, A., Tabriz, N., & Tazhbayev, Y. (2024). Production of Polylactide Nanoparticles Loaded With Isoniazid and Vitamin C: A Promising Candidate for the Treatment of Resistant Forms of Tuberculosis. *Journal of Polymer Science. Portico, 1–11*. <https://doi.org/10.1002/pol.20240375>
- 4 Tazhbayev, Y., Burkeyev, M., Zhaparova, L., Zhumagaliyeva, T., & Arystanova. (2018). Nanoparticles on the basis of polylactic acid and polylactic-co-glycolic acids loaded with drugs. *Bulletin of the Karaganda University. "Chemistry" Series, 90(2)*, 31–39. <https://doi.org/10.31489/2018ch2/31-39>
- 5 Bakare, A.A., Moses, V.Y., Beckely, C.T., Oluyemi, T.I., Ogunfeitimi, G.O., Adelaja, A.A., Ayorinde, G.T., Gbadebo, A.M., Fagbenro, O.S., Ogunsuyi, O.I., Ogunsuyi, O.M., & Ige, O.M. (2022). The first-line antituberculosis drugs, and their fixed-dose combination induced abnormal sperm morphology and histological lesions in the testicular cells of male mice. *Frontiers in Cell and Developmental Biology, 10*. <https://doi.org/10.3389/fcell.2022.1023413>
- 6 Srivastava, S., Sherman, C., Meek, C., Leff, R., & Gumbo, T. (2011). Pharmacokinetic Mismatch Does Not Lead to Emergence of Isoniazid- or Rifampin-Resistant Mycobacterium tuberculosis but to Better Antimicrobial Effect: a New Paradigm for Antituberculosis Drug Scheduling. *Antimicrobial Agents and Chemotherapy, 55(11)*, 5085–5089. <https://doi.org/10.1128/aac.00269-11>
- 7 Galiyeva, A., Daribay, A., Zhumagaliyeva, T., Zhaparova, L., Sadyrbekov, D., & Tazhbayev, Y. (2023). Human Serum Albumin Nanoparticles: Synthesis, Optimization and Immobilization with Antituberculosis Drugs. *Polymers, 15(13)*, 2774. <https://doi.org/10.3390/polym15132774>
- 8 Pienaar, E., Linderman, J.J., & Kirschner, D.E. (2018). Emergence and selection of isoniazid and rifampin resistance in tuberculosis granulomas. *PLOS ONE, 13(5)*, e0196322. <https://doi.org/10.1371/journal.pone.0196322>
- 9 Lee, B.K., Yun, Y., & Park, K. (2016). PLA micro- and nano-particles. *Advanced Drug Delivery Reviews, 107*, 176–191. <https://doi.org/10.1016/j.addr.2016.05.020>
- 10 Pulingam, T., Foroozandeh, P., Chuah, J.-A., & Sudesh, K. (2022). Exploring Various Techniques for the Chemical and Biological Synthesis of Polymeric Nanoparticles. *Nanomaterials, 12(3)*, 576. <https://doi.org/10.3390/nano12030576>
- 11 Li, Y., Zhang, L., Tian, R., Pranantyo, D., Chen, L., & Xia, F. (2023). A Double-Emulsion Method for the Fabrication of PLA Single-Hole Hollow Particles. *Current Chinese Science, 3(4)*, 285–292. <https://doi.org/10.2174/2210298103666230428092735>
- 12 Sarsenbekova, A.Zh., Bolatbay, A.N., Morgun, V.V., Havlicek, D., Davrenbekov, S.Zh., & Nasikhately, E. (2022). Study of thermal stability and determination of effective activation energy values during degradation of unsaturated polyester copolymers atmosphere. *Bulletin of the University of Karaganda — Chemistry, 105(1)*, 86–91. <https://doi.org/10.31489/2022Ch1/86-91>
- 13 Burkeyev, M., Tazhbayev, Y., Bolatbay, A., Minayeva, Y., Davrenbekov, S., Nassikhately, Y., Kovaleva, A., Kutzhanova, K., & Kazhmuratova, A. (2022). Study of Thermal Decomposition of the Copolymer Based on Polyethylene Glycol Fumarate with Acrylic Acid. *Journal of Chemistry, 2022*, 514358. <https://doi.org/10.1155/2022/3514358>
- 14 Sarsenbekova, A.Zh., Bolatbay, A.N., Havlicek, D., Issina, Zh.A., Sarsenbek, A.Zh., Kabdenova, N.A., & Kilybay, M.A. (2024). Effect of Heat Treatment on the Supramolecular Structure of Copolymers Based on Poly(propylene glycol fumarate phthalate) with Acrylic Acid. *Eurasian Journal of Chemistry, 29(2)*, 114, 61–73. <https://doi.org/10.31489/2959-0663/2-24-9>
- 15 Borsynbayev, A., Omarov, K., Mustafin, Y., Havlicek, D., Absat, Z., Muratbekova, A., Kaikenov, D., Pudov, A., & Shuyev, N. (2022). A study of copper leaching from the tailings of the Karagaily (Republic of Kazakhstan) concentrating factory using an electric hydropulse discharge. *Journal of the Serbian Chemical Society, 87(7-8)*, 925–937. <https://doi.org/10.2298/JSC2208925B>
- 16 Saranjit, S., Mariappan, T.T., Sharda, N., & Singh, B. (2000). Degradation of Rifampicin, Isoniazid and Pyrazinamide from Prepared Mixtures and Marketed Single and Combination Products Under Acid Conditions. *Pharmacy and Pharmacology Communications, 6(11)*, 491–494. <https://doi.org/10.1211/146080800128735575>
- 17 Hakkimane, S., Shenoy, V.P., Gaonkar, S., Bairy, I., & Guru, B.R. (2018). Antimycobacterial susceptibility evaluation of rifampicin and isoniazid benz-hydrazone in biodegradable polymeric nanoparticles against Mycobacterium tuberculosis H37Rv strain. *International Journal of Nanomedicine, 13*, 4303–4318. <https://doi.org/10.2147/ijn.s163925>
- 18 Heidary, M., Zaker Bostanabad, S., Amini, S.M., Jafari, A., Ghalami Nobar, M., Ghodousi, A., Kamalzadeh, M., & Darban-Sarokhalil, D. (2019). The anti-mycobacterial activity of Ag, ZnO, and Ag-ZnO nanoparticles against MDR- and XDR- Mycobacterium tuberculosis strains. *Infection and Drug Resistance, 12*, 3425–3435. <https://doi.org/10.2147/idr.s221408>
- 19 Van Deun, A., Hossain, M.A., Gumusboga, M., & Rieder, H.L. (2008). Ziehl-Neelsen staining: theory and practice. *The International Journal of Tuberculosis and Lung Disease, 12(1)*, 108–110.
- 20 Dzodanu, E.G., Afrifa, J., Acheampong, D.O., & Dadzie, I. (2019). Diagnostic yield of fluorescence and Ziehl-Neelsen staining techniques in the diagnosis of pulmonary tuberculosis: A comparative study in a district health facility. *Tuberculosis Research and Treatment, 2019*, 4091937. <https://doi.org/10.1155/2019/4091937>
- 21 Lagreca, E., Onesto, V., Di Natale, C., La Manna, S., Netti, P.A., & Vecchione, R. (2020). Recent advances in the formulation of PLGA microparticles for controlled drug delivery. *Progress in Biomaterials, 9(4)*, 153–174. <https://doi.org/10.1007/s40204-020-00139-y>
- 22 Galiyeva, A.R., Tazhbayev, Ye.M., Zhumagaliyeva, T.S., Sadyrbekov, D.T., Kaikenov, D.A., Karimova, B.N., & Shokenova, S.S. (2022). Polylactide-co-glycolide nanoparticles immobilized with isoniazid: optimization using the experimental Taguchi method. *Bulletin of the Karaganda University. "Chemistry" Series, 105(1)*, 69–77. <https://doi.org/10.31489/2022ch1/69-77>
- 23 Basílio, J.A.J., & Shinde, M.D. (2024). Colloidal stability and dielectric behavior of eco-friendly synthesized zinc oxide nanostructures from Moringa seeds. *Scientific Reports, 14*, 2310. <https://doi.org/10.1038/s41598-024-52093-5>

- 24 Galiyeva, A.R., Tazhbayev, Y.M., Yessentayeva, N.A., Daribay, A.T., Marsel, D.T., Sadyrbekov, D.T., Zhaparova, L.Zh., & Arystanova, Z.T. (2023). PEGylation of Albumin Nanoparticles Immobilized with the Anti-Tuberculosis Drug "Isoniazid." *Eurasian Journal of Chemistry*, 110(2), 42–50. <https://doi.org/10.31489/2959-0663/2-23-7>
- 25 Tazhbayev, Ye.M., Galiyeva, A.R., Zhumagaliyeva, T.S., Burkeyev, M.Zh., Kazhmuratova, A.T., Zhakupbekova, E.Zh., Zhaparova, L.Zh., & Bakibayev, A.A. Synthesis and characterization of isoniazid immobilized poly(lactide-co-glycolide) nanoparticles. *Bulletin of the University of Karaganda — Chemistry*, 101(1), 61–70. <https://doi.org/10.31489/2021Ch1/61-70>
- 26 Alves, R., Reis, T.V. da S., Silva, L.C.C. da, Storpirtis, S., Mercuri, L.P., & Matos, J. do R. (2010). Thermal behavior and decomposition kinetics of rifampicin polymorphs under isothermal and non-isothermal conditions. *Brazilian Journal of Pharmaceutical Sciences*, 46(2), 343–351. <https://doi.org/10.1590/s1984-82502010000200022>
- 27 W. Badri, K. Miladi, Q.A. Nazari, H. Fessi, & A. Elaissari (2017). "Effect of Process and Formulation Parameters on Polycaprolactone Nanoparticles Prepared by Solvent Displacement," *Colloids and Surfaces A: Physicochemical and Engineering Aspects*, 516, 238–244. <https://doi.org/10.1016/j.colsu rfa.2016.12.029>
- 28 Symons, A.L., Varanasi, S., Fredericks, P.M., Whittaker, A.K., Hill, D.J.T., & Rasoul, F. (2013). FT-IR characterization and hydrolysis of PLA-PEG-PLA based copolyester hydrogels with short PLA segments and a cytocompatibility study. *Journal of Polymer Science Part A: Polymer Chemistry*, 51(24), 5163–5176. <https://doi.org/10.1002/pola.26930>
- 29 Chieng, B., Ibrahim, N., Yunus, W., & Hussein, M. (2013). Poly(lactic acid)/Poly(ethylene glycol) Polymer Nanocomposites: Effects of Graphene Nanoplatelets. *Polymers*, 6(1), 93–104. <https://doi.org/10.3390/polym6010093>
- 30 Tazhbayev, Y., Galiyeva, A., Zhumagaliyeva, T., Burkeyev, M., & Karimova, B. (2021). Isoniazid—Loaded Albumin Nanoparticles: Taguchi Optimization Method. *Polymers*, 13(21), 3808. <https://doi.org/10.3390/polym13213808>
- 31 Gunasekaran, S., Sailatha, E., Seshadri, S., & Kumaresan, S. (2009). FTIR, FT Raman spectra and molecular structural confirmation of isoniazid. *Indian Journal of Pure & Applied Physics*, 47, 12–18.
- 32 Sharma, A., Puri, V., Kumar, P., Singh, I., & Huanbutta, K. (2021). Development and Evaluation of Rifampicin Loaded Alginate–Gelatin Biocomposite Microfibers. *Polymers*, 13(9), 1514. <https://doi.org/10.3390/polym13091514>
- 33 Ivashchenko, O., Tomila, T., Ulyanchich, N., Yarmola, T., & Uvarova, I. (2014). Fourier-Transform Infrared Spectroscopy of Antibiotic Loaded Ag-Free and Ag-Doped Hydroxyapatites. *Advanced Science, Engineering and Medicine*, 6(2), 193–202. <https://doi.org/10.1166/asem.2014.1473>
- 34 Yessentayeva, N.A., Galiyeva, A.R., Daribay, A.T., Sadyrbekov, D.T., Moustafine, R.I., & Tazhbayev, Y.M. (2024). Optimization of Poly(lactide-Co-Glycolide)-Rifampicin Nanoparticle Synthesis, In Vitro Study of Mucoadhesion and Drug Release. *Polymers*, 16(17), 2466. <https://doi.org/10.3390/polym16172466>
- 35 Galiyeva, A.R., Tazhbayev, Ye.M., Zhumagaliyeva, T.S., & Daribay, A.T. (2022). Encapsulation of Isoniazid in Poly(lactide-Co-Glycolide) Nanoparticles by Nanoprecipitation. *Bulletin of the University of Karaganda — Chemistry*, 107(3), 208–217. <https://doi.org/10.31489/2022Ch3/3-22-17>
- 36 Chorny, M., Fishbein, I., Danenberg, H.D., & Golomb, G. (2002). Lipophilic drug loaded nanospheres prepared by nanoprecipitation: effect of formulation variables on size, drug recovery and release kinetics. *Journal of Controlled Release*, 83(3), 389–400. [https://doi.org/10.1016/s0168-3659\(02\)00211-0](https://doi.org/10.1016/s0168-3659(02)00211-0)
- 37 Loiko, O.P., Herk, A.M. van, Ali, S.I., Burkeyev, M.Zh., Tazhbayev, Y.M., & Zhaparova, L.Zh. (2013). Controlled release of Capreomycin sulfate from pH-responsive nanocapsules. *E-Polymers*, 13(1). <https://doi.org/10.1515/epoly-2013-0118>
- 38 Gao, Y., Zuo, J., Bou-Chacra, N., Pinto, T. de J.A., Clas, S.-D., Walker, R.B., & Löbenberg, R. (2013). In Vitro Release Kinetics of Antituberculosis Drugs from Nanoparticles Assessed Using a Modified Dissolution Apparatus. *BioMed Research International*, 2013, 1–9. <https://doi.org/10.1155/2013/136590>
- 39 Arca, H.Ç., Mosquera-Giraldo, L.I., Pereira, J.M., Sriranganathan, N., Taylor, L.S., & Edgar, K.J. (2018). Rifampin Stability and Solution Concentration Enhancement Through Amorphous Solid Dispersion in Cellulose ω-Carboxyalkanoate Matrices. *Journal of Pharmaceutical Sciences*, 107(1), 127–138. <https://doi.org/10.1016/j.xphs.2017.05.036>

Eyyub S. Mammadov¹, Fuad Sh. Kerimli², Nargiz F. Akhmedova^{2*},
Sabit E. Mammadov², Sakina E. Mirzaliyeva²

¹*Baku Branch of Lomonosov Moscow State University, Baku, Azerbaijan;*

²*Baku State University, Baku, Azerbaijan*

(*Corresponding author's e-mail: nargiz.akhmedova1@gmail.com)

Effect of Solid-Phase Modification of High-Modulus Zeolite TsVM with Cerium Oxide in Conversion of Bioethanol to Hydrocarbons

The catalysts used for the conversion of bioethanol into hydrocarbons were obtained by solid-phase modification of high-modulus zeolite HTsVM ($\text{SiO}_2:\text{Al}_2\text{O}_3 = 40$) of the ZSM-5 type with cerium carbonate followed by heat treatment at 550 °C for 4 hours. The reactions were carried out in a flow reactor with a fixed catalyst bed in the temperature range of 300–450 °C at atmospheric pressure in order to study the effect of cerium oxide concentration in the HTsVM on its selectivity for isomerization and aromatization products. The modification of zeolite HTsVM with cerium oxide was shown to result in a change in its structural and acidic characteristics, as well as its selectivity for cracking, isomerization and aromatization reactions. The isomerisation selectivity of a catalytic system based on zeolite ZSM-5 can be increased by modifying it with rare earth or transition metals, which gives the catalyst a bifunctional character. This increase in isomerisation selectivity and decrease in aromatization selectivity are due to a significant reduction in the density of strong acid sites, the formation of additional Lewis cation sites and a decrease in total pore volume, as well as an increase in mesopore volume. The optimal 3 % $\text{CeO}_2/\text{HTsVM}$ catalyst demonstrates high stability (30 hours) and high selectivity for isomerization products (44.90–46.06 %) within the temperature range of 300–350 °C. The gasoline fraction obtained using the 3 % $\text{CeO}_2/\text{HTsVM}$ catalyst at 300 °C is enriched in isoparaffinic hydrocarbons (48.73 wt.%) and complies with the Euro 5 standard with regard to aromatic hydrocarbon content (21.17 wt.%) and benzene content (<1.0 wt.%).

Keywords: zeolite TsVM, cerium oxide, modification, selectivity, isomerization, aromatization, catalyst, surface, porosity, acid centers, bioethanol

Introduction

In recent years, special attention has been paid to new highly efficient methods for obtaining valuable olefin, aromatic and isoparaffin hydrocarbons from alternative renewable raw materials in the presence of catalytic systems based on high-silica zeolites [1, 2].

One of the methods for obtaining gasoline hydrocarbons and other valuable organic substances is the production of bioethanol from biomass [3].

The possibility of obtaining high-octane components of motor fuels from bioethanol in the presence of various types of zeolite catalysts has been shown in [4–7]. However, achieving high selectivity for isoparaffin hydrocarbons with sufficient selectivity for aromatic hydrocarbons requires the development of new catalytic systems with polyfunctional properties. ZSM-5 zeolite is the most promising candidate among the various types of molecular sieves for the production of high-octane components from bioethanol due to its inherent advantages, such as a high specific surface area, greater resistance to coke formation and the presence of various types of acid sites and systems of interconnected sinusoidal and straight channels [8]. The isomerization selectivity of the catalytic system based on ZSM-5 zeolite can be increased by modifying it with rare earth or transition metals (Pt, Pd, Ni) to impart a bifunctional character to the catalyst [9–12]. Rare earth metals are used as promoting additives to increase the isomerization activity and stability of catalysts in the processes of processing hydrocarbon feedstock from alcohols [3, 13–15]. Zeolite catalysts modified with cerium dioxide nanopowders make it possible to increase the isomerization activity of the catalyst in the process of converting hydrocarbon feedstock into high-octane components [16]. In the process of converting hydrocarbon feedstock and bioethanol, modification of HZSM-5 zeolite with Ga, Fe, Cr, Zn, Pd, Pt [15, 17] increases the yield of aromatic hydrocarbons, while the addition of Zr [18], Co [7] and La, Ce [19, 20] in-

creases the yield of isoparaffin hydrocarbons. Modification of HZSM-5 zeolite with transition and rare earth metals can lead to the formation of Brønsted and Lewis acid sites of varying strength, as well as new active sites capable of directly interacting with intermediates formed during ethanol conversion. This imparts a polyfunctional character to the catalyst, giving it a predominant isomerizing ability [21, 22].

The method of impregnation with aqueous solutions of transition and rare-earth metal compounds is widely used to modify zeolites [4, 10, 13, 14]. However, modification of zeolite catalysts by impregnation followed by oxidative treatment, as a rule, does not lead to a highly dispersed distribution of the modifier on its surface.

Meanwhile, the method of solid-phase modification based on topochemical processes occurring during the interaction of transition metal oxides or salts with zeolites has proved to be very promising [23–25].

This paper presents the results of the influence of the concentration of cerium oxide in the composition of HTsVM zeolite prepared by solid-phase modification method on the selectivity of cracking, isomerisation and aromatization products in the conversion of bioethanol.

Experimental

Commercial high-silica zeolite TsVM (an analogue of zeolite ZSM-5) produced by Nizhny Novgorod Sorbents, Russia, was used for the preparation of catalysts.

The initial zeolite, with a $\text{SiO}_2/\text{Al}_2\text{O}_3$ molar ratio of 40 and a Na_2O content of less than 0.05 wt.%, was calcined in air at 550 °C for four hours prior to modification. Modification of the HTsVM zeolite with cerium carbonate was conducted via a dry mixing process in a vibrating ball mill for two hours. This was followed by calcination at a temperature of 550 °C for a period of four hours. The unmodified and modified samples were subsequently pelletized through a pressing method. For the subsequent studies, particles with a diameter ranging from 0.5 to 1.0 millimetres were utilized.

X-ray diffractograms of the samples were obtained on a RIGAKU MINIFLEX diffractometer (source $\text{CuK}\alpha$, $\lambda = 0.15046$ nm, 40 mA, 45 kV). Measurements were taken over a scanning angles $2\theta = 3\text{--}80^\circ$ at a rate of 2° per minute.

The surface area by BET and pore volume by BJH were determined by adsorption method with liquid nitrogen at -196 °C using ASAP-2010 instrument by Micromeritics. The samples were degassed for 4 h in vacuum ($1\text{--}10^{-3}$ Pa) at 250 °C.

The acid characteristics of the studied samples were determined by ammonia TPD method using sorption analyzer USGA-101 (“Unisit”) according to the method described in [14].

The catalytic activity of the samples under investigation was determined in a quartz reactor with a fixed layer of catalyst (2 g) at atmospheric pressure. Prior to the commencement of the experiments, the samples were activated in a stream of dry air for 2 h at 550 °C. The reaction was carried out within the temperature range of 300–450 °C, with the volumetric rate of ethanol feed equal to 1.0 h^{-1} .

To determine the confidence interval, the experimental results were processed statistically using Microsoft Excel [26, 27]:

$$\text{CI} = \bar{x} \pm z \frac{s}{\sqrt{n}},$$

where CI is the confidence interval, \bar{x} is the sample mean, z is the confidence level value, s is a sample standard deviation, n is a sample size. The confidence level was 95 %. The standard deviation (S) was calculated based on the results of three measurements ($n = 3$).

The data presented in Table 1 were obtained with experiment duration of one hour. Experiments were also performed on the modified catalysts between 1–50 hours. The deactivated catalyst was regenerated in a stream of dry air at a rate of 4 l/hour. Regeneration started at 100 °C, with the temperature rising at a rate of 5 °C/min to reach 500 °C, which was then maintained for one hour. Analysis of the gaseous reaction products was conducted using an Agilent GC 782A gas chromatograph equipped with Porapak Q columns and a “5A” brand molecular sieve. Analysis of the liquid reaction products was performed using a quartz glass capillary column ($100\text{ mm} \times 0.25\text{ mm} \times 0.25\text{ }\mu\text{m}$) with a ZB-1 liquid phase applied to a PerkinElmer Autosystem XL chromatograph [7].

Product selectivity was determined using the following ratio:

$$\text{Selectivity, \%} = \frac{\text{final product, wt.\%}}{\sum \text{products, wt.\%}} \times 100\text{ \%}.$$

Results and Discussion

X-ray diffraction patterns of freshly prepared HTsVM and cerium-modified zeolite catalysts, are shown in Figure 1.

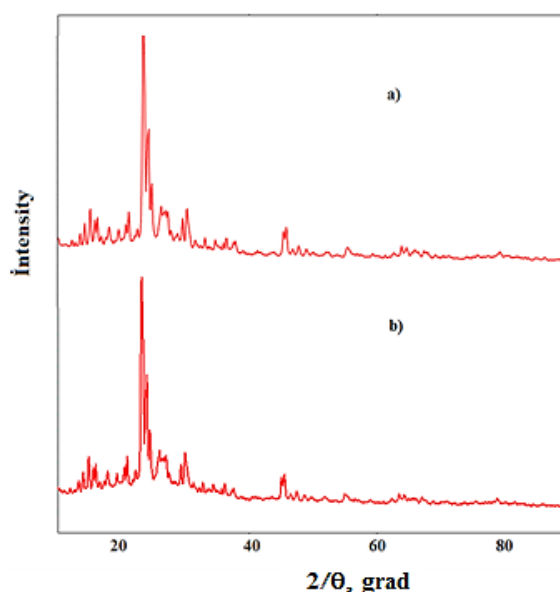


Figure 1. X-ray diffraction patterns of unmodified zeolite HTsVM (a) and modified catalyst 3 % CeO₂/ HTsVM (b)

Peaks at $2\theta = 7.96^\circ, 8.88^\circ, 23.2^\circ$ and 24° are observed for all samples, which are characteristic of zeolite with an MFI framework [28]. This indicates that the HTsVM framework is well preserved after modification. No obvious peaks are found on the modified samples within the investigated angles, which indicates a homogeneous dispersion of cerium oxide in the zeolite

Table 1 shows the results of the effect of temperature on the composition of ethanol conversion products in the presence of HTsVM.

Table 1

**Effect of temperature on the activity of HTsVM catalyst
in the process of ethanol conversion (SiO₂/Al₂O₃=40)**

Products. wt.%	300 °C	350 °C	400 °C	450 °C
H ₂	1.00 ± 0.12	1.42 ± 0.09	1.63 ± 0.10	1.72 ± 0.03
C ₁ -C ₂	0.88 ± 0.03	1.52 ± 0.09	3.14 ± 0.44	3.77 ± 0.29
C ₂ H ₅ OH	1.90 ± 0.04	1.03 ± 0.11	0.96 ± 0.06	–
C ₂ H ₄	6.61 ± 0.15	2.25 ± 0.13	1.15 ± 0.06	0.11 ± 0.05
C ₃ H ₆	2.68 ± 0.09	1.32 ± 0.07	0.34 ± 0.06	–
C ₃ H ₈	12.86 ± 1.26	16.12 ± 0.52	17.39 ± 0.41	19.51 ± 0.69
H-Alkanes C ₄₊	2.38 ± 0.03	2.02 ± 0.12	1.43 ± 0.06	0.74 ± 0.06
iso-C ₄	1.61 ± 0.04	1.53 ± 0.04	1.42 ± 0.08	1.05 ± 0.08
iso-C ₅ -C ₆	8.78 ± 0.07	7.94 ± 0.43	7.15 ± 0.46	3.44 ± 0.13
iso-C ₇ -C ₁₄	1.72 ± 0.07	1.26 ± 0.21	0.727 ± 0.04	0.32 ± 0.02
Σ iso-C ₅ -C ₁₄	10.60 ± 0.29	9.14 ± 0.06	7.87 ± 0.57	4.75 ± 0.17
Alkenes C ₄₊	3.94 ± 0.08	2.42 ± 0.14	1.72 ± 0.08	0.64 ± 0.04
C ₆ H ₆	1.23 ± 0.04	1.71 ± 0.07	1.93 ± 0.09	2.35 ± 0.10
ArC C ₇ -C ₈	12.46 ± 1.38	17.07 ± 5.10	17.37 ± 0.71	11.55 ± 0.36
ArC C ₉₊	3.32 ± 0.36	4.73 ± 0.54	5.20 ± 0.43	8.40 ± 0.32
Σ ArC C ₆ -C ₉₊	17.48 ± 0.56	22.16 ± 0.61	24.30 ± 0.78	26.91 ± 0.68
Naphthalenes C ₅₊	0.84 ± 0.04	0.63 ± 0.08	0.52 ± 0.03	0.31 ± 0.03
H ₂ O	38.12 ± 0.47	38.98 ± 1.04	39.05 ± 0.98	39.87 ± 0.97

Table 2

Effect of temperature on cracking selectivity

Products, wt. %	2 % CeO ₂				3 % CeO ₂				4 % CeO ₂			
	300 °C	350 °C	400 °C	450 °C	300 °C	350 °C	400 °C	450 °C	300 °C	350 °C	400 °C	450 °C
H ₂	0.82±0.03	1.04±0.06	1.14±0.06	1.42±0.03	0.92±0.03	1.13±0.07	1.22±0.041	1.64±0.07	1.12±0.039	1.23±0.05	1.32±0.05	1.54±0.04
C ₁ -C ₂	0.61±0.02	0.82±0.02	1.46±0.17	1.92±0.03	0.71±0.01	0.91±0.01	1.22±0.041	1.82±0.04	0.63±0.001	0.70±0.01	1.04±0.05	1.62±0.05
C ₂ H ₅ OH	2.35±0.17	1.64±0.07	1.21±0.07	-	2.12±0.13	1.53±0.05	1.22±0.041	0.20±0.01	2.40±0.017	1.90±0.02	1.83±0.14	1.13±0.08
C ₂ H ₄	2.96±0.15	1.64±0.06	0.30±0.01	-	2.83±0.08	1.14±0.05	0.42±0.001	0.10±0.01	2.93±0.006	2.23±0.07	1.13±0.08	0.42±0.01
C ₃ H ₆	0.72±0.02	0.41±0.02	0.10±0.01	-	0.61±0.01	0.32±0.01	0.11±0.001	-	0.85±0.005	0.50±0.01	0.30±0.01	-
C ₃ H ₈	8.253±0.16	9.74±0.13	12.98±0.72	14.80±0.52	7.94±0.23	8.84±0.44	11.86±0.141	13.97±0.01	7.47±0.026	8.34±0.15	11.10±0.50	13.59±0.62
n- Alkanes C ₄₊	2.843±0.12	2.44±0.04	2.14±0.07	1.32±0.03	2.24±0.08	2.44±0.05	2.05±0.003	1.50±0.01	3.02±0.019	2.94±0.08	2.34±0.09	2.14±0.07
iso-C ₄	1.82 ±0.03	1.63±0.07	1.02±0.03	0.71±0.01	2.16±0.21	1.93±0.07	1.55±0.002	0.90±0.65	1.95±0.006	1.73±0.07	1.21±0.01	0.80±0.01
iso C ₅ -C ₆	20.54±1.37	19.94±1.19	17.22±1.21	14.49±0.61	22.40±1.06	21.32±1.00	18.23±0.325	15.55±0.08	20.94±0.594	19.57±0.66	17.41±0.77	14.82±0.75
iso C ₇ -C ₁₄	5.45 ±0.08	5.39±0.29	3.74±0.10	2.64±0.08	5.93±0.07	5.73±0.07	4.46±0.013	2.93±1.05	5.70±0.050	5.43±0.14	4.33±0.08	2.63±0.08
Σ iso C ₅ -C ₁₄	26.24±1.38	25.21±1.26	20.93±1.43	17.09±0.73	28.31±1.24	27.03±1.12	22.61±0.374	18.52±0.01	26.41±0.463	25.02±1.06	21.86±1.34	17.40±0.81
Alkenes C ₄₊	0.94 ±0.04	0.60±0.01	0.51±0.01	0.41±0.01	0.61±0.01	0.51±0.01	0.40±0.001	0.30±0.02	0.61±0.015	0.50±0.01	0.41±0.01	0.20±0.01
C ₆ H ₆	0.73±0.02	0.50±0.01	0.41±0.01	0.60±0.01	0.60±0.01	0.41±0.01	0.30±0.001	0.22±0.56	0.61±0.001	0.40±0.01	0.30±0.01	0.23±0.09
ArC C ₇ -C ₈	10.77±0.55	12.39±0.54	15.02±0.69	17.93±0.97	9.99±0.34	11.61±0.66	13.68±0.125	16.76±0.06	9.57±0.056	11.36±0.29	13.41±0.67	16.43±0.89
ArC C ₉₊	1.93 ±0.01	2.33±0.05	2.83±0.04	3.13±0.05	1.73±0.04	1.82±0.05	2.54±0.005	2.83±0.80	1.43±0.003	1.72±0.10	2.33±0.08	2.62±0.11
Σ C ₆ -C ₉₊	13.28±1.25	15.19±0.50	18.17±0.70	21.61±0.96	12.37±0.76	13.81±0.80	16.52±0.255	19.77±0.04	11.56±0.101	14.01±0.64	16.01±0.70	19.20 ±0.96
Naphthalenes C ₅₊	1.64 ±0.08	1.24±0.06	0.91±0.01	0.90±0.01	1.54±0.10	1.13±0.08	0.92±0.009	0.82±1.07	2.10±0.011	1.92±0.08	1.64±0.06	1.52±0.07
H ₂ O	38.25±1.60	38.98±1.31	39.93±1.26	40.3±1.09	38.64±2.33	39.80±1.54	40.73±1.042	40.93±0.07	39.67±0.484	40.12±1.47	40.52±1.26	40.95±1.36

It can be seen that the reaction temperature significantly affects the distribution of products. In the presence of HTsVM, an increase in the reaction temperature from 300 °C to 450 °C was observed, which led to an increase in the yield of C₁–C₃ alkanes. There was also a decrease in the yield of C₂–C₄+ alkenes and C₄–C₁₄ isoparaffinic hydrocarbons, and an increase in the yield of C₆–C₉+ aromatic hydrocarbons.

The highest yields of C₁–C₃ alkanes (23.28 wt.%) and C₆–C₉+ aromatic hydrocarbons (26.91 wt.%) are observed at 450 °C. Figure 2 shows the effect of temperature on selectivity for cracking isomerization and aromatization reactions. High cracking and aromatizing activity of unmodified HTsVM is observed in the temperature range of 400–450 °C. Under these conditions, the selectivity for cracking and aromatization reactions is 33.68–38.71 % and 39.86–44.75 %, respectively.

The isomerization selectivity of the catalyst decreases significantly with increasing temperature. The lowest selectivity (7.90–14.98) for the isomerization reaction is observed in the temperature range 400–450 °C.

Modification of HTsVM zeolite with cerium oxide significantly changes its catalytic properties.

It can be seen from Figure 2 that the highest selectivity for the isomerisation reaction is achieved in the temperature range of 300–350 °C.

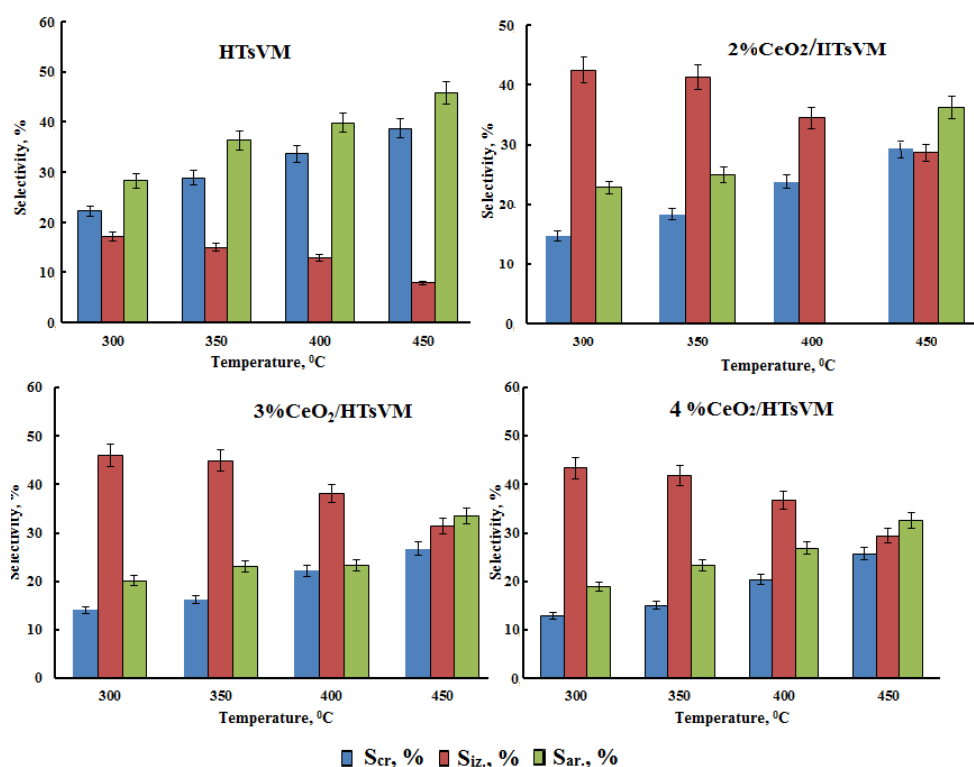


Figure 2. Temperature dependence of selectivity for cracking products (S_{kr}), isomerization (S_{iz}) and aromatization (S_{ar})

The maximum yield of isoparaffinic hydrocarbons iso-C₅–C₆ + iso-C₇H₁₆ (27.12–28.33 wt.%) with selectivity on isomerization reaction equal to 46.11–44.9 % is achieved on the sample modified with 3.0 wt.% cerium oxide. Further increase of reaction temperature up to 450 °C sharply reduces the yield of isoparaffin hydrocarbons (up to 18.52 wt.%) and selectivity for isomerization reaction (31.35 %). An increase in the content of cerium in the HTsVM composition decreases the cracking and aromatizing activity of the catalyst. An increase in selectivity for cracking and aromatization products is observed with increasing reaction temperature (Figure 2).

It is important to note that the modification results in a significant reduction of benzene content in the reaction products. On samples containing 3.0–4.0 wt.% cerium oxide, the benzene content in the reaction products decreases to 0.22–0.61 wt.%.

Thus, the selectivity for isomerization, aromatization and cracking products is determined by the content of cerium oxide in the catalyst and the temperature of the process.

The catalyst 3 % CeO₂/HTsVM shows high isomerization selectivity in the temperature range 300–350 °C (Figure 2), and the obtained liquid hydrocarbons have high octane number (105–110). The liquid products obtained at temperatures of 300–350 °C correspond to modern standards for Euro-4 and Euro-5 motor fuels in terms of isoparaffinic (44.9–46.1 wt.%), aromatic (20.1–22.9 wt.%), olefinic (<1.0 wt.%) and benzene (<1.0 wt.%) content.

Apparently, the change of catalytic properties of HTsVM is connected with the change of its structural and acid characteristics as a result of modification. Unmodified HTsVM zeolite has the highest total pore volume and specific surface area. However, the distribution of micro- and mesopore volume and average pore diameter depends on the concentration of cerium oxide added to HTsVM zeolite (Table 3).

Table 3

Structural characteristics of cerium-containing zeolite catalysts

Catalyst	HTsVM	2 % CeO ₂ / HTsVM	3 % CeO ₂ / HTsVM	4 % CeO ₂ / HTsVM
S _{BET} . m ² /g	265.33±21.31	255.60±22.50	244.90±16.25	236.47±15.12
S _{micro} . m ² /g	125.03±3.65	122.67±5.52	113.97±3.58	107.73±2.42
S _{meso} . m ² /g	142.40±1.46	134.47±0.96	131.27±1.15	129.80±4.10
V _{total} . cm ³ /g	0.24±0.01	0.23±0.01	0.21±0.01	0.19±0.01
V _{meso} . cm ³ /g	0.061±0.001	0.081±0.001	0.091±0.001	0.10±0.001
V _{micro} . cm ³ /g	0.18±0.01	0.15±0.01	0.12±0.01	0.09±0.01
V _{meso} /V _{total} . %	24.96	34.72	42.42	54.53

where S_{BET} is the specific surface area of the catalyst; S_{micro} and S_{meso} are the specific surface area of micro- and mesopores; V_{total} is a total specific pore volume; V_{micro} and V_{meso} are a volume of micro- and mesopores; 4V/Å is an average pore diameter.

Modification of HTsVM with cerium oxide decreases its specific surface area, total pore volume, micropore volume and average pore diameter. The modification of zeolite with cerium oxide also increases the mesopore volume and the V_{meso}/V_{total} ratio. The most noticeable decrease in pore diameter (from 36.21 to 31.41–32.49) is observed in samples containing 3.0–4.0 wt.% cerium oxide. The occurring changes in structural characteristics are obviously associated with the localization of modifier particles in the pores or in the pore mouths, as well as on the surface of zeolite crystals.

Table 4 shows the acid characteristics of unmodified and cerium-containing zeolite catalysts.

Table 4

Acid characteristics of initial and cerium-containing zeolite catalysts

Catalyst	Concentration of weak acid centres, μmol/g (100–300 °C)	Concentration of strong acid centres, μmol/g (300–600 °C)	Total concentration of acid centres, μmol/g
HTsVM	394.67±5.10	235.33±4.22	630.00
2 % CeO ₂ / HTsVM	325.57±2.53	183.67±8.19	509.23
3 % CeO ₂ / HTsVM	275.50±6.65	162.42±3.94	437.92
4 % CeO ₂ / HTsVM	258.33±6.19	139.00±4.05	397.33

All samples have two peaks of acid centres: low-temperature ones with ammonia desorption region from 100 to 300 °C (mainly Lewis acid centres), and high-temperature ones in the region of 300–600 °C (mainly strong Brønsted acid centres). The unmodified HTsVM has the highest concentration of strong acid centres (235.33 μmol/g). The introduction of 2.0–4.0 wt.% of cerium oxide into zeolite HTsVM significantly reduces the concentration of strong acid centres. At the content of cerium oxide in HTsVM up to 4.0 wt.% the concentration of strong acid centres decreases 1.8 times.

The catalytic activity of cerium-containing zeolite catalysts with respect to yield and selectivity for isoparaffin hydrocarbons agrees well with the results of their structural and acid properties.

The changes in the structural and acid characteristics of zeolite catalysts resulting from modification can be explained by the preparation of catalysts with cerium oxide and subsequent calcination at 550 °C in an air environment for 5 hours. The cerium oxide nanoparticles are localized in the zeolite channels and on the zeolite's outer surface, where they form additional Lewis acid sites, including cerium ions and cationic sites (Ce(OH)₂⁺ and Ce(OH)₂⁺), as well as acid-base pairs (Ce⁺–O). These pairs are formed when the cerium

oxide interacts with Brønsted acid sites. The metal-containing sites formed in this process can activate ethanol molecules and intermediates. At the moderate acidic sites of Brønsted, these undergo skeletal rearrangement, predominantly forming isoparaffinic hydrocarbons.

One of the important operational properties of the catalyst is its regenerability and stability of operation.

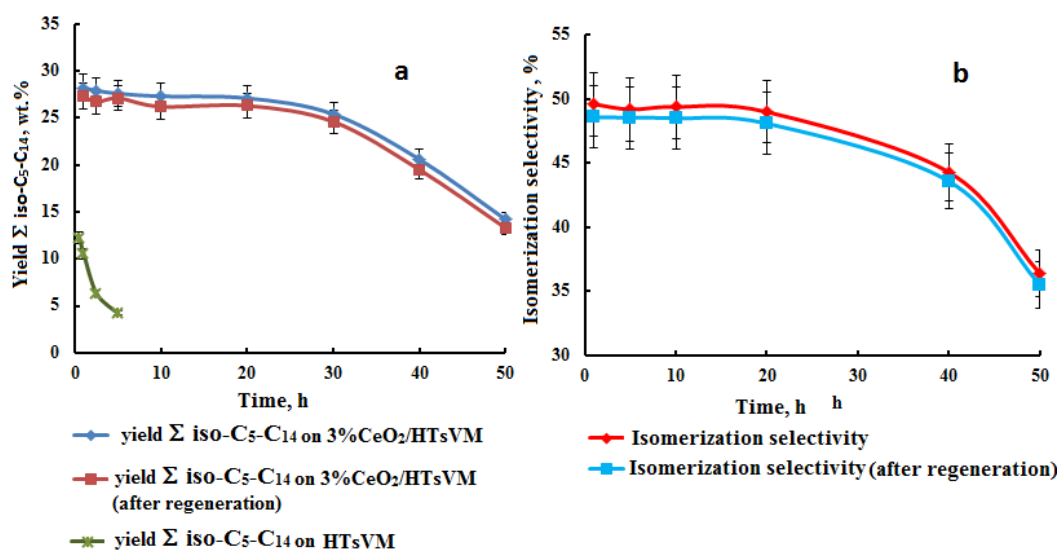


Figure 3. Dependence of yield (a) and selectivity for isoparaffin hydrocarbons ΣC_5-C_{14} (b) on the duration of operation

Figure 3 shows the dependence on the yield of the amount of isoparaffinic hydrocarbons ΣC_5-C_{14} and the selectivity to isomerization products on the running time for unmodified HTsVM and the optimal 3 % CeO₂/ HTsVM. It is evident that the catalyst deactivates rapidly after two hours of operation. This deactivation may be related to the accumulation of coking compounds on the catalyst, which reduces the access of bioethanol to the active sites located in the zeolite pores. Coke deposition on zeolites is strongly correlated with strong acidity, which explains the rapid deactivation of the initial HTsVM, which concentrates strong acidic sites (Table 3). Modification with cerium oxide increases the stability of the catalyst. From Figure 3 it is evident that the optimal catalyst 3 % CeO₂/HTsVM exhibits high stability of operation and practically retains its initial activity for 30 hours of operation. After 30 hours of operation, a noticeable decrease in the catalyst activity is observed. However, after 50 hours of operation, the catalyst fully restores its activity after regeneration. High isomerization activity and stability of the modified catalyst are obviously associated with changes in the acidic and textural characteristics of the HTsVM zeolite because of modification process. The low density of Brønsted acid sites and the higher concentration of various types of cationic Lewis sites (Ce(OH)₂⁺ and Ce(OH)²⁺), which are formed during the interaction of cerium oxide with strong Brønsted acid sites, facilitate the interaction of bioethanol with the active sites of the zeolite, reduce the hydrogen transfer reaction [21, 29], suppress coke deposits and increase the isomerization efficiency and stability of the catalyst. In addition, modification of the HTsVM zeolite with cerium oxide leads to an increase in the mesopore volume, which improves mass transfer during the reaction.

Conclusions

The solid-phase modification method was used to obtain catalysts based on zeolite HTsVM modified with cerium oxide (2.0–4.0 wt.%). As a result of modification and calcination of the zeolite, a dispersed distribution of the modifier occurs on the external surface and in the pores of the zeolite, where the modifier particles interact with both surface and localized in the pores of the zeolite strong Brønsted acid centers. As a result, there is a decrease in the density of strong acid centers, the formation of Brønsted acid centers of moderate strength, cationic Lewis acid centers, acid-base pairs Ce⁺-O- and an increase in the volume of mesopores, which leads to a decrease in the redistribution of hydrogen, isomerizing efficiency and stability of the catalyst. The optimal catalyst of the 3 % CeO₂/HTsVM composition demonstrates regenerability, high stability (30 hours), selectivity for isomerization products (44.90–46.06 %) and provides a high octane number of the catalysate (105–110) in the temperature range of 300–350 °C.

Funding

The study was financially supported by the Ministry of Science and Education of the Azerbaijan Republic.

Author Information*

*The authors' names are presented in the following order: First Name, Middle Name and Last Name

Eyyub Sabit oglu Mammadov — PhD in Chemistry, Head of the Laboratory, Baku Branch of Lomonosov Moscow State University, University street 1, Khojasan settlement, Binagadi district, AZ1146, Baku, Azerbaijan; e-mail: eyyub-84@mail.ru; <http://orcid.org/0000-0003-4122-6391>

Fuad Shamseddin oglu Kerimli — Doctor of Chemical Sciences, Associate Professor, Department of Physical and Colloidal Chemistry, Dean, Faculty of Chemistry, Baku State University, 23 Academician Zahid Khalilov Street, AZ 1148, Baku, Azerbaijan; e-mail: fuad_kerimli80@mail.ru; <http://orcid.org/0000-0001-7772-8583>

Nargiz Firudin qizi Akhmedova (*corresponding author*) — PhD in Chemistry, Researcher, Laboratory of Metal Complex Catalysts, Faculty of Chemistry, Baku State University, 23 Academician Zahid Khalilov Street, AZ 1148, Baku, Azerbaijan; e-mail: nargiz.akhmedova1@gmail.com; <http://orcid.org/0000-0003-0912-8687>

Sabit Eyyub oglu Mammadov — Doctor of Chemical Sciences, Professor, Department of Physical and Colloidal Chemistry, Faculty of Chemistry, Baku State University, 23 Academician Zahid Khalilov Street, AZ 1148, Baku, Azerbaijan; e-mail: sabitmamedov51@mail.ru; <http://orcid.org/0000-0002-8099-9496>

Sakina Eylaz qizi Mirzaliyeva — PhD in Chemistry, Associate Professor, Department of Physical and Colloidal Chemistry, Faculty of Chemistry, Baku State University, 23 Academician Zahid Khalilov Street, AZ 1148, Baku, Azerbaijan; e-mail: mirzaliyeva.s@mail.ru, <https://orcid.org/0009-0009-9908-4112>

Author Contributions

The manuscript was written through contributions of all authors. All authors have given approval to the final version of the manuscript. **CRedit**: **Eyyub Sabit oglu Mammadov** performed XRD and acidity study of the obtained catalysts and analyzed the obtained data; **Fuad Shamseddin oglu Kerimli** participated in the preparation of catalysts and catalytic experiments; **Nargiz Firudin gizi Akhmedova** took part in catalytic experiments and in writing the paper; **Sabit Eyyub oglu Mammadov** took part in setting, formulation and task of the research, in analyzing scientific and technical literature and writing the article; **Sakina Eylaz gizi Mirzaliyeva** participated in the analysis and identification of reaction products and their processing.

Conflicts of Interest

The authors declare no conflict of interest.

References

- 1 Chaipornchalerm, P., Prasertsab, A., Prasanseang, W., & Wattanakit Ch. (2024). Perspectives on Recent Advances in Hierarchical Zeolites for Bioethanol Conversion to Chemicals, Jet Fuels, and Carbon Nanotubes. *Energy & Fuels*, 38(15), 13612–13636. <https://doi.org/10.1021/acs.energyfuels.4c02069>
- 2 Costa, R.S., Cavalcante, R.M., Antunes, M., & Silva P. (2025). Effects of adding metals to Beta zeolite on ethanol conversion to hydrocarbons. *Catalysis Today*, 445, 115048. <https://doi.org/10.1016/j.cattod.2024.115048>
- 3 Anekwe, I.M.S., Isa, Y.M., & Oboirien, B. (2024). Bioethanol as a potential eco-friendlier feedstock for catalytic production of fuels and petrochemicals. *Journal of chemical technology and biotechnology*, 98(9), 2077–2094. <https://doi.org/10.1002/jctb.7399>
- 4 Spennati, E., Iturrate, M., Bogni, S., Cosso, A., Millini, R., Riani, P., Busca, G., & Garbarino G. (2024). Ethanol conversion to hydrocarbons over Sn-doped H-ZSM-5 zeolite catalysts. *Microporous and Mesoporous Materials*, 79, 113284–113291. <https://doi.org/10.1016/j.micromeso.2024.113284>
- 5 Thangaraj, B., Monama, W., Mohiuddin, E., & Mdleleni, M.M. (2024). Recent developments in (bio)ethanol conversion to fuels and chemicals over heterogeneous catalysts. *Bioresource Technology*, 409, 131230–131239. <https://doi.org/10.1016/j.biortech.2024.131230>

- 6 Cordero-Lanzac, T., Aguayo, A.T., Gayubo, A.G., & Bilbao, J. (2021). Influence of HZSM-5-based catalyst deactivation on the performance of different reactor configurations for the conversion of bioethanol into hydrocarbons. *Fuel*, 302, 121061(1–11). <https://doi.org/10.1016/j.fuel.2021.121061>
- 7 Mamedov, E.S., Babayeva, B.A., Akhmedova, N.F., & Mamedov, S.E. (2023). Bioethanol Conversion into High-Octane Components of Motor Fuel in the Presence of Cobalt-Containing HZSM-5 Type Zeolites. *Chemistry for sustainable development*, 31(3), 302–308. <https://doi.org/10.15372/KhUR2023470>
- 8 Sousa, Z.S.B., Veloso, C.O., Henriques, C.A., & Silva, V.T. (2016). Ethanol conversion into olefins and aromatics over HZSM-5 zeolite: Influence of reaction conditions and surface reaction studies. *Journal of Molecular Catalysis A: Chemical*, 422, 266–274. <https://doi.org/10.1016/j.molcata.2016.03.005>
- 9 Eagan, N.M., Kumbhalkar, M.D., Buchanan, J.S., Dumesic, J.A., & Huber, G.W. (2019). Chemistries and processes for the conversion of ethanol into middle-distillate fuels. *Nature reviews chemistry*, 3, 223–249. <https://doi.org/10.1038/s41570-019-0084-4>
- 10 Martins, J.M. Silva, & M.F. Ribeiro (2013). Influence of rare earth elements on the acid and metal sites of Pt/HBEA catalyst for short chain n-alkane hydroisomerization. *Applied Catalysis A: General*, 466, 293–299. <https://doi.org/10.1016/j.apcata.2013.06.043>
- 11 Andreeva, A.V., Baimuratova, R.K., Dorokhov, V.G., Akkuratov, A.V., Shilov, G.V., Kugabaeva, G.D., Golu-beva, N.D., & Dzhardimalieva, G.I. (2024). Rational Synthesis of UiO-66 and its Application in the Hydrogenation Reaction of p-Chloronitrobenzene. *Eurasian Journal of Chemistry*, 29, 3(115), 92–108. <https://doi.org/10.31489/2959-0663/3-24-1092>
- 12 Hasanguliyeva, N.M., Shakunova, N.V., & Litvishkov, Y.N. (2024). Microwave Solid-Phase Synthesis of Ni-Co Ferrites and their Activities in Liquid-Phase Oxidation of m-Xylene. *Eurasian Journal of Chemistry*, 29(3 (115)), 82–91. <https://doi.org/10.31489/2959-0663/3-24-1>
- 13 Mahmudov, K.T., Karimli, F.Sh., Mamedov, E.S., Gurbanov, A.V., Akhmedova, N.F., & Mamedov, S.E. (2022). Catalytic Disproportionation of Ethylbenzene over Ln-Modified HZSM-5 Zeolites. *Petroleum Chemistry*, 4(2), 122–129. <https://doi.org/10.1134/S0965544122060147>
- 14 Mamedov, E.S., Gahramanov, T.O., Akhmedova, N.F., Mamedov, S.E., Mamedova, A.Z., & Akhmedov, E.I. (2024). Effects of the Type and Loading of Rare-Earth Metals (Pr, Yb, Ho) on the para-Selectivity of HTsVM Zeolite in Toluene Ethylation. *Petroleum Chemistry*, 64(2), 258–266. <https://doi.org/10.1134/S0965544124010134>
- 15 Xiang, H., Xin, R., Prasongthum, N., Natewong, P., Sooknoi, T., Wang, J., Reubroycharoen, P., & Fan, X. (2022). Catalytic conversion of bioethanol to value-added chemicals and fuels: A review. *Resources Chemicals and Materials*, 1(1), 47–68. <https://doi.org/10.1016/j.rcm.2021.12.002>
- 16 Khomyakov, I.S., Bozhenkova, G.S., & Bragina, O.O. (2018). Study of catalytic activity of modified high-silica zeolites of the MFI type in the process of conversion of straight-run gasolines. *Theoretical foundations of chemical technology*, 52, 832–836. <https://doi.org/10.1134/S0040579518050342>
- 17 Van der Borcht, K., Galvita, V.V., & Marin, G.B. (2015). Ethanol to higher hydrocarbons over Ni, Ga, Fe-modified ZSM-5: Effect of metal content. *Applied Catalysis A: General*, 492, 117–126. <https://doi.org/10.1016/j.apcata.2014>
- 18 Kuzmina, R.I., & Pilipenko, A.Y. (2015). Effect of temperature on ethanol conversion over the surface of Zr-modified zeolite ZSM-5. *Catalysis for Sustainable Energy*, 2(1), 83. <https://doi.org/10.1515/cse-2015-0006>
- 19 Babayeva, B.A., & Mammadov, S.E. (2021). The conversion of ethanol on the HZSM-5 zeolite modified with lanthanum. *Azerbaijan chemical journal*, 1, 55–60. <https://akj.az/en/journals/856>
- 20 Dossunov K., Churina D.Kh., Yergaziyeva G.Y., Telbayeva M.M., & Tayrabekova S.Zh. (2016). Conversion of Bio-ethanol over Zeolites and Oxide Catalysts. *International Journal of Chemical Engineering and Applications*, 7(2), 128–132. <https://doi.org/10.7763/IJCEA.2016.V7.556>
- 21 Khezri, H., Izadbakhsh, A., & Izadpanah, A.A. (2020). Promotion of the performance of La, Ce and Ca impregnated HZSM-5 nanoparticles in the MTO reaction. *Fuel Processing Technology*, 199, 106253(1–12). <https://doi.org/10.1016/j.fuproc.2019.106253>
- 22 Liu, Ch., Uslamin, E.A., Khramenkova, E., Sireci E., Ouwehand, L.T.L.J., Ganapathy, S., Kapteijn, F., & Pidko, E.A. (2022). High Stability of Methanol to Aromatic Conversion over Bimetallic Ca, Ga-Modified ZSM-5. *ACS Catalysis*, 12(5), 3189–3200. <https://doi.org/10.1021/acscatal.1c05481.s001>
- 23 Velichkina L.M., Barbashin Y.E., & Vosmerikov A.V. (2021). Study of the combined effect of post-synthetic alkaline treatment and nickel modification of MFI zeolite on the dynamics of its deactivation in the process of refining straight-run gasoline. *Izvestiia vysshikh uchebnykh zavedenii khimiiia khimicheskaiia tekhnologiia*, 67(8), 103–112. <https://doi.org/10.6060/ivkkt.20246708.10t>
- 24 Dai, Ch., Du, K., Chen, Zh., Chen, H., Guo, X., & Ma, X. (2020). Synergistic Catalysis of Multi-Stage Pore-Rich H-BZSM-5 and Zn-ZSM-5 for the Production of Aromatic Hydrocarbons from Methanol via Lower Olefins. *Industrial & Engineering Chemistry Research*, 59(47), 20693–20700. <https://doi.org/10.1021/acs.iecr.0c05225>
- 25 Velichkina, L.M., Kanashevich, D.A., Vosmerikova, L.N., & Vosmerikov, A.V. (2014). Effect of Silicate Modulus and Modifying with Metals on the Acidic and Catalytic Properties of ZSM-5 Type Zeolite in the Isomerization of n-Octane. *Chemistry for Sustainable Development*, 22, 237–245.
- 26 Harris, D.C., & Lucy, C.A. (2020). Quantitative Chemical Analysis. 10th Edition, W.H. Freeman & Company, 828. New York.
- 27 Larsson, M., & Nilsson, G. (2023). Consequences of Insufficient Selectivity in Quantitative and Qualitative Chemical Analysis. *Journal of Analytical Sciences, Methods and Instrumentation*, 13(2), 13–25. <https://doi.org/10.4236/jasmi.2023.132002>

28 Ghosal, D., Basu, K.J., & Sengupta, S. (2015). Application of La-ZSM-5 Coated Silicon Carbide Foam Catalyst for Toluene Methylation with Methanol. *Bulletin of Chemical Reaction Engineering & Catalysis*, 10(2), 201–209. <http://dx.doi.org/10.9767/bcrec.10.2.7872.201-209>

29 Jia-bei, SH., Bai-chao, L., Mei, D., Wei-bin, F., Zhang-feng, Q., & Jian-guo, W.G. (2024). The effect of hydrothermal pre-treatment on the catalytic performance of Zn/HZSM-5 catalysts for ethylene aromatization reaction. *Journal of fuel chemistry and technology*, 52(8), 1079–1087. [https://doi.org/10.1016/S1872-5813\(24\)60448-2](https://doi.org/10.1016/S1872-5813(24)60448-2)

Askhat S. Borsynbayev^{1*} , Yedige S. Mustafin¹ , Khylysh B. Omarov² ,
Aigul A. Muratbekova¹ , Daulet A. Kaykenov¹ , Daniyar T. Sadyrbekov¹ ,
Asanali A. Ainabayev¹ , Abylaikhan N. Bolatbay¹ , Milana A. Turovets¹ 

¹Karaganda Buketov University, Karaganda, Kazakhstan;

²Kazakh University of Technology and Business, Astana, Kazakhstan

(*Corresponding author's e-mail: askhat.9@mail.ru)

Study of the Phase Composition and Kinetics of the Metal Leaching Process Using Electrohydropulse Discharge on the Waste from the Zhezkazgan Concentrating Plants

This work involved conducting X-ray phase analysis and energy-dispersive spectroscopy (EDS), for the first time, as well as examining the kinetics of metal extraction processes from the tailings of the Zhezkazgan Concentration Plant (ZhCP) before and after their treatment. Based on the results of X-ray diffraction results, the main diffraction peaks have been found to corresponded to silicon-containing or silicate minerals, as well as phases characteristic of Cu₂S, CuFe₂S₃, and ZnS. Following electrohydropulse discharge leaching, the silicates (SiO₂) were partially destroyed, releasing metal oxides. The elemental composition of the tailings was analyzed using electron probe X-ray microanalysis. The EDS analysis revealed the presence of 13 elements, the most intense lines of which were silicon, oxygen, and aluminum, while the remaining elements were found in minor quantities. The activation energy was determined graphically using the Arrhenius equation based on the rate constants (lnK) at various temperatures and exposure times to electrohydropulse discharge. To determine the kinetics of the leaching process, a high-temperature thermometer was installed on the reactor to record the temperature of the slurry, including the solution reaction mixture. During the hydropulse discharge process, the temperature of the reaction medium rose to 60 °C over 30 minutes.

Keywords: hydropulse discharge, pulp, laboratory cell, ammonium bifluoride, tailings samples, metals, acid, copper

Introduction

The metallurgical industry produces large quantities of waste, including tailings and process residues that present significant environmental and economic challenges. Efficiently recycling and repurposing of these materials is essential in order to reduce ecological impact and recover valuable components. Without proper management, these industrial by-products can contribute to soil and water contamination, disrupting ecosystems, and leading to the loss of potentially useful raw materials. Processing metallurgical tailings and waste using physical and chemical methods has attached considerable attention due to growing environmental concerns and the potential for resource recovery. Metallurgical processes produce a various types of waste, such as slags, dusts, and sludges, which can be repurposed using innovative recycling techniques.

Metallurgical waste, such as slag and tailings, often contains valuable metals and minerals. For instance, that mining and metallurgical waste can be effectively repurposed as construction materials, emphasizing the importance of physical beneficiation processes alongside hydrometallurgical and pyrometallurgical methods for recycling these materials [1, 2]. The evaluation of sulphation baking and autogenous leaching of Turkish metallurgical slag flotation tailings further illustrates the potential of these wastes as valuable raw materials, particularly in the context of declining ore grades and increasing metal prices [3]. These findings align with those of other authors, who discuss the transformation of hazardous metallurgical waste into resources and showcase various harmless treatment and utilization methods [4, 5].

The utilization of metallurgical waste in construction materials is also a prominent theme in the literature. For example, the use of metallurgical waste slag as a cementitious material, which not only contributes to sustainable construction practices and addresses the environmental impact of waste disposal [6]. Similarly,

other research emphasizes the role of metallurgical wastes in promoting sustainability within the steel industry, highlighting the diverse types of waste generated and their potential applications [7, 8].

Environmental considerations are paramount in the processing of metallurgical wastes. A review emphasizes the marketability of blast furnace and steelmaking slag, which can be utilized in various applications, thereby reducing landfill waste and promoting resource conservation [9]. Furthermore, the environmental impacts of copper slag are discussed with the highlighting of the need for effective management strategies to mitigate the risks associated with waste accumulation [10].

Chemical methods for processing metallurgical waste are also crucial for recovering resources. For instance, metals can be recovered from waste-derived copper-lead electrocatalysts, demonstrating the potential to convert waste into valuable products through chemical processes [11, 12]. Another study explores the extraction of valuable metals such as lead, zinc, and copper from metallurgical waste using chloride distillation, showcasing the effectiveness of chemical approaches in waste management [13, 14]. The importance of understanding the properties of metallurgical waste in order to determine suitable recycling methods is also emphasized, as are the challenges that arise from insufficient knowledge of waste characteristics during the recycling process [15, 16].

A comprehensive understanding of the characteristics of metallurgical waste informs suitable recycling methods and highlights the need to advance processing technologies. While established methods for handling depleted ore and mining waste, particularly tailings from processing plants, provide a foundation, further innovation is necessary to improve the recovery of resources.

In hydrometallurgical industries, efficient leaching techniques, such as those utilizing ammonium salts, have proven effective for extracting copper from processing plant waste [17]. Fluorine-containing components are widely used as additives and fluxes in the processing of various ores, in the separation of some rare and rare-earth metals, as well as in electrolysis. Ammonium hydrodifluoride is an effective reagent for processing mineral raw materials containing non-ferrous and noble metals resistant to simple fluorination. It facilitates the separation of valuable components by converting raw materials into a mixture of simple and complex fluorides. Up to 90 % of the ammonium fluoride used in fluorination can be recovered for NH_4HF_2 regeneration, supporting a closed technological cycle.

The regeneration of NH_4HF_2 enables a closed, environmentally friendly production cycle. Ammonium hydrodifluoride can process polymetallic raw materials effectively at temperatures below 200 °C, and the resulting fluorination by-products ensure environmental safety [18]. Copper leaching from chalcopyrite has been demonstrated using aqueous ammonia and glycine, with ceramic chips aiding particle breakdown [19]. NH_4HF_2 facilitates the extraction of valuable metals, including gold and silver, using closed-loop bifluoride processes. Compared to chlorine metallurgy, these methods operate at lower temperatures with greater environmental safety and simpler reagent regeneration. Ammonium bifluoride is a promising reagent for processing rare metal and technogenic raw materials. Studies confirm its effectiveness in isolating rare earth elements and calcium fluoride CaF_2 [20, 21].

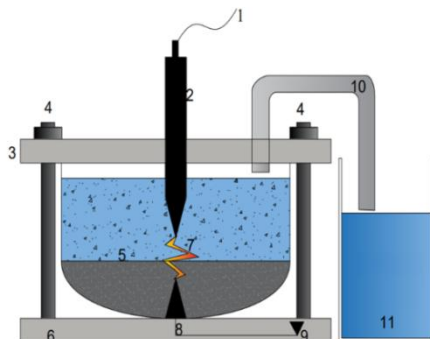
Experimental

Effective extraction of valuable metals from metallurgical waste requires optimized treatment methods that facilitate the breakdown of mineral structures and promote metal solubility. In this study, electrohydropulse (EHP) processing was applied to waste samples from the Zhezkazgan concentrating plant to assess its efficiency in metal recovery. The process involved high-voltage discharge in a liquid medium to induce structural disruption and enhance leaching. For each experiment, 300 g of tailing samples (stale ZhCP No. 1.2, current ZhCP No. 1.2, and stale ZhCP No. 3) were placed in a stainless steel reaction cell with a total volume of 1 liter. To establish the required reaction conditions, 500 ml of water was added along with 15 ml of H_3PO_4 , adjusting the medium's acidity to pH 1–2. Additionally, 4 g of NH_4HF_2 was introduced as an activator to promote the decomposition of silicate structures and enhance metal release. The prepared pulp was then subjected to an electrohydropulse discharge for 30 minutes to facilitate the transfer of metals into solution. Following treatment, the solution was filtered to remove solid residues.

The electrohydropulse discharge was generated using a high-voltage charged capacitor, which was discharged into water within a controlled laboratory cell [22]. The electrohydropulse treatment setup included a system capable of accumulating and releasing high-voltage energy, generating powerful pulsed discharges. The anode had a conical shape with an insulated tip, while the cathode was a cylindrical reaction cell with a central protrusion at its base. The energy stored in the system allowed for effective disruption of mineral structures. The parameters of the high voltage were optimized to ensure a stable and efficient process. The

operating parameters were as follows: switch operating voltage — 30 kV; pulse frequency — 0.6 Hz; pulse energy — 200 J; voltage amplitude — 30 kV; voltage rise rate — 0.005–5 μs ; type of electric discharge — spark discharge in liquid; pulse duration — 100 μs .

The reaction medium was acidified to enhance the efficiency of metal leaching. A schematic of the experimental setup is shown in Figure 1.



1 — wire connected to a spark gap; 2, 8 — electrodes; 3, 6 — retaining plates made of textolite; 4 — anchor bolts; 5 — pulp; 7 — plasma cord; 9 — grounding; 10 — gas outlet tube; 11 — glass with a solution

Figure 1. Scheme of a laboratory cell for studying the effect of electrohydropulse discharge

Dried tailing samples — stale ZhCP No. 1.2, current ZhCP No. 1.2, and stale ZhCP No. 3, both before and after treatment — were analyzed using X-ray phase analysis conducted on a powder diffractometer. This investigation revealed the phase composition and structural changes resulting from electrohydropulse treatment. This method provided a comprehensive evaluation of the mineralogical transformations and the efficiency of the processing technique. In order to understand how the metals are distributed in the samples, X-ray phase studies were carried out using a powder diffractometer D8 AdvanceEco, Bruker. Recording mode Bragg-Brentano geometry, angular range from 15 to 75°, with a step of 0.03°, spectrum acquisition time 2 s X-rays were generated using a copper tube with a wavelength $\text{Cu-k}\lambda = 1.5406 \text{ \AA}$. DiffracEVA v.4.2 Decryption Software, PDF-2 Matching Phase Search Database (2016). The weight ratio of the phases was assessed using the standard equation (1), which is based on determining the values of the integral intensities and estimating their contributions.

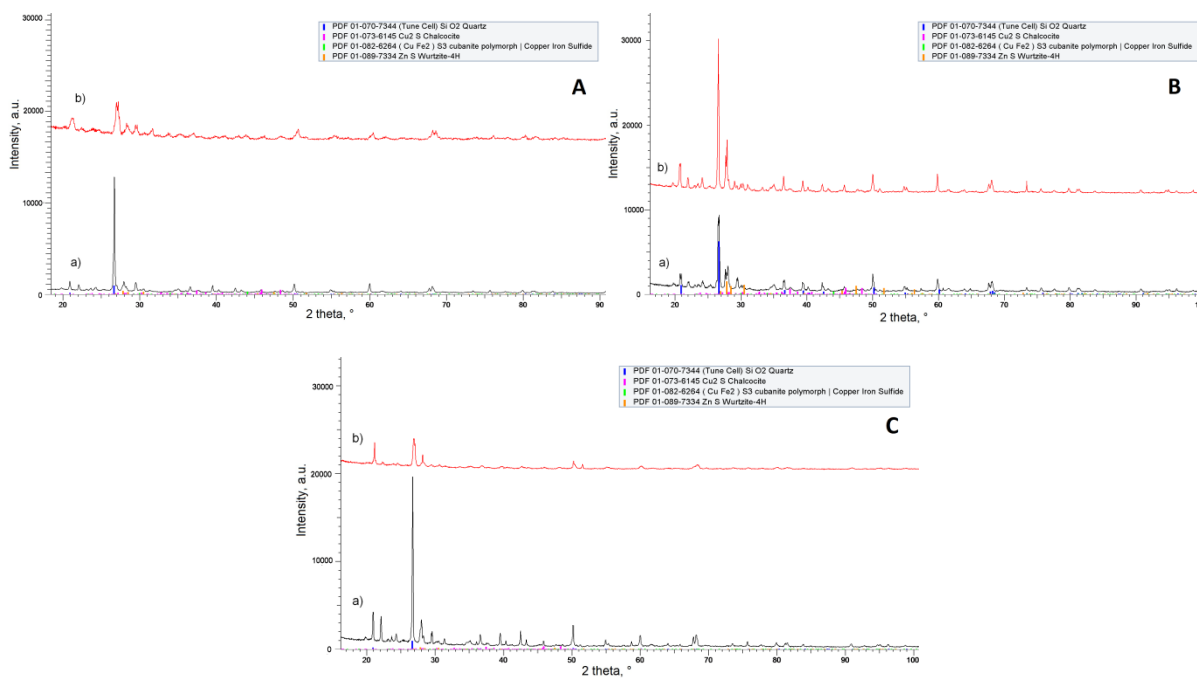
$$V_{\text{admixture}} = \frac{RI_{\text{phase}}}{I_{\text{admixture}} + RI_{\text{phase}}}, \quad (1)$$

where I_{phase} is the average integrated intensity of the main phase of the diffraction line, $I_{\text{admixture}}$ is the average integrated intensity of the additional phase, R is the structural coefficient equal to 1.45.

In order to study the thermodynamic aspects of the leaching process, a setup was arranged to precise monitoring temperature changes. A high-temperature thermometer integrated into the reactor enabled the temperature increase of the pulp and reaction mixture solution to be recorded. During the electrohydropulse treatment, which lasted 30 minutes, the temperature of the reaction medium gradually increased to 60 °C, indicating the active progression of chemical processes. Furthermore, the activation energy of the reactions was determined using a graphical method based on the Arrhenius equation, which enabled a quantitative evaluation of the kinetic parameters.

Results and Discussion

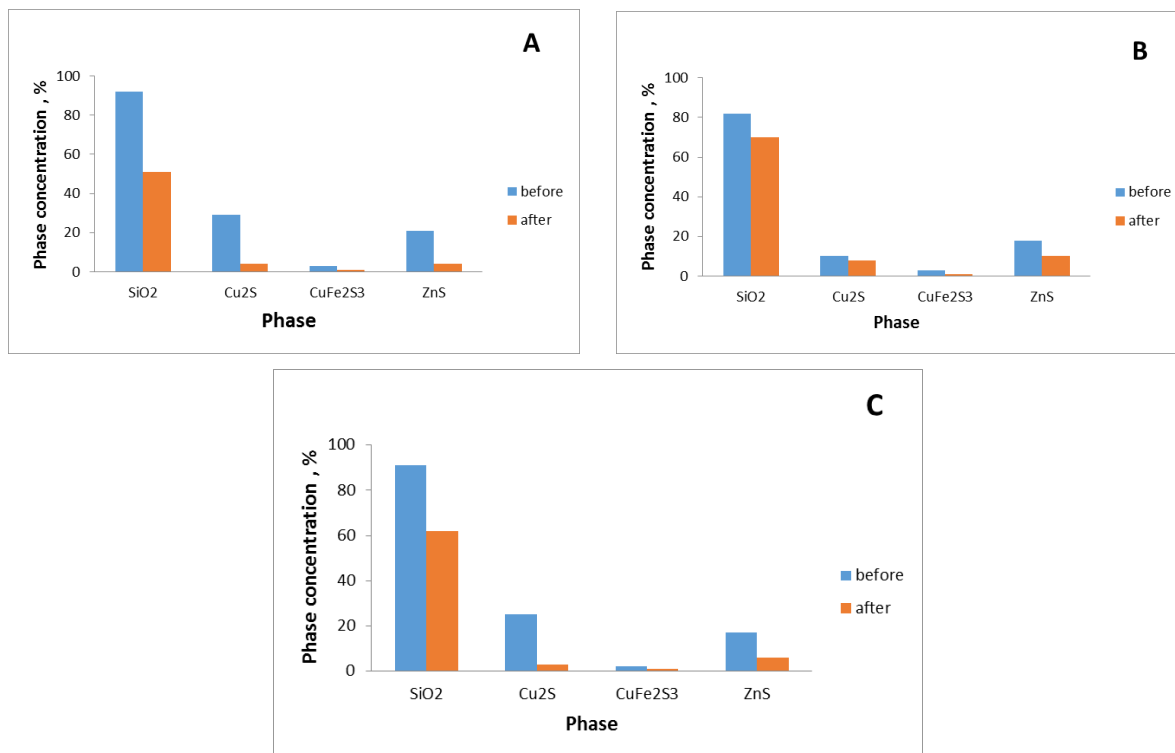
Figure 2 shows the results of X-ray diffraction of the studied samples before and after leaching of ZhCP No. 1, 2, 3. According to the results of X-ray diffraction, it was found the main reflections, with the highest intensity, are characteristic of silicon dioxide (SiO_2 — quartz) appropriate to most silicon-containing or silicate rocks. Diffraction reflections typical to the Cu_2S , CuFe_2S_3 and ZnS phases have also been established. No reflections characteristic of CaSiO_3 phases were found. The determination of the phase composition, as well as the concentration of the phases, was carried out using the equation (1).



A — ZhCP No. 1.2 stale; B — ZhCP No. 1.2 current; C — ZhCP No. 3 stale

Figure 2. X-Ray diffraction patterns of ZhCP tailings before (a) and after leaching (b)

As a result of treatment with ammonium bifluoride, the X-ray spectra show that SiO₂ silicates were partially destroyed and released the metal oxides, which is clearly visible in terms of the height of the peaks. Additionally, the spectra show that the amount of metals decreases in those particles of impurities of metal oxides after treatment with HPD.



A — ZhCP No. 1.2 stale; B — ZhCP No. 1.2 current; C — ZhCP No. 3 stale

Figure 3. Results of changes in the phase composition

The presented diagrams (Figure 3) show that in the dried sediment after leaching, a decrease in the content of phases characteristic of the ZhCP 1,2 (A) SiO_2 from 94 % to 50 %, Cu_2S from 30 % to 5 % and CuFe_2S from 5.1 % to 0.3 %. ZnS from 18.7 % to 4.1 %. is observed. The diagram also shows a depletion of the metals content in the sediment after leaching, which characterizes their transition into solution.

One method of studying sediment composition is electron probe X-ray spectral microanalysis (EP-XRSMA). In this study, we present the results obtained using a JXA8200 microanalyser (JEOL, Japan) in the X-ray methods of analysis laboratory.

Based on phase composition data, samples of the ZhCP and KCP tails were subjected to X-ray spectral EMF analysis. Thirteen elements (Cu, Fe, Si, Al, Mn, Cr, Mg, Ca, Ba, O, Na, K and S) were recorded in the energy dispersive spectra of the studied sample sections prior to HPD treatment (Figure 4).

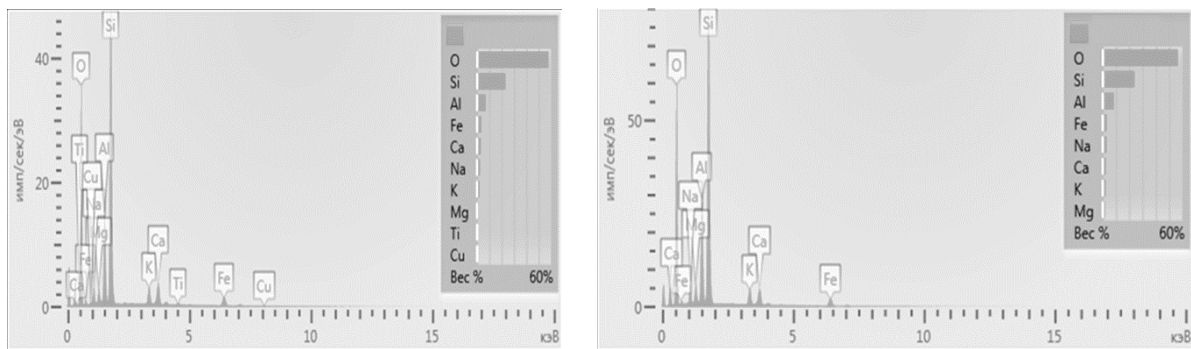


Figure 4. X-ray spectral EMF analysis of the dried sediment before and after HPD ZhCP No. 1.2 Current

The spectra showed the presence of silicon, oxygen and aluminium in varying intensities. The remaining elements are present in small quantities.

The spectrum before HPD (Fig. 5) shows the intensities of the lines of sulphur, oxygen, magnesium, iron, copper and zinc, as well as a significant number of other elements.

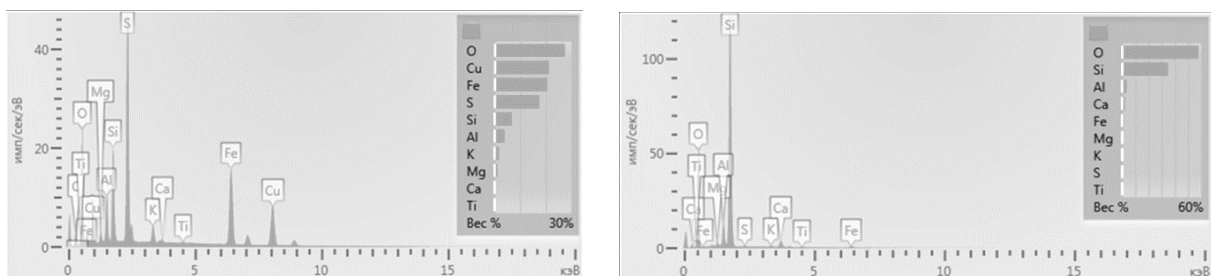


Figure 5. X-ray spectral EMF analysis of the dried sediment before and after HPD ZhCP No. 1.2 stale

The spectrum after HPD (Fig. 5) shows the intensity of the silicon, aluminium and oxygen lines, with the remaining elements present in small amounts. The spectrum (Fig. 6) before HPD treatment shows the intensities of the copper, carbon, oxygen and sulfur lines.

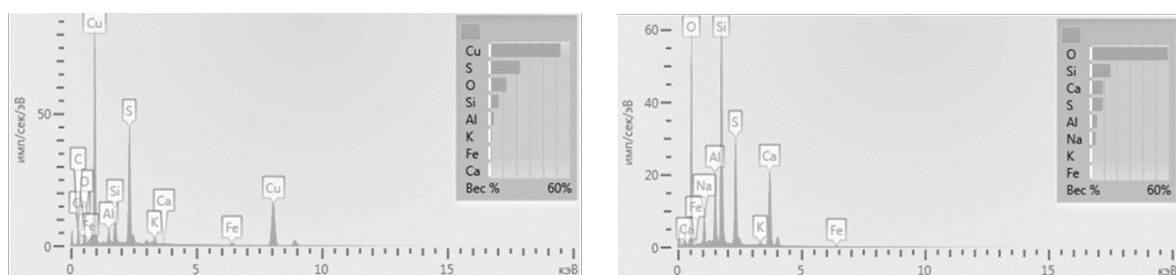
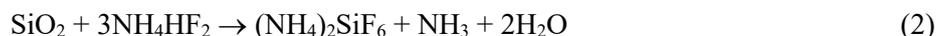


Figure 6. X-ray spectral EMF analysis of the dried sediment before and after HPD ZhCP No. 3 stale

The EMF spectra show that the concentration of copper and other elements decreases after the leaching and processing of HPD. The elements detected in the spectra transition into solution. These elements are all in solution in the form of complexes, which must be precipitated using reagents to keep the copper ions in solution. The process by which copper transitions into solution is complex and staged, beginning with the opening of the silicate surface under the influence of ammonium hydrodifluoride [23]:



The remaining sediment consists of complex conglomerates of particles of various sizes and compositions. The concentrations of all the studied elements (Fe, Zn, Pb, Cu, S, Si, Al, Na, Mg, K, Ca, Ti, Cr and Mn) fluctuate significantly. Spectra obtained from different particles at different points all contain lines of carbon and oxygen. Rather than forming compounds, these elements form mechanical mixtures bonded in the form of complexes containing oxygen and carbon.

The experiment results on duration of the experiments in minutes and on the temperature dependence have been processed mathematically to obtain the rate constant of copper leaching. This rate constant has been converted the logarithmic form in order to determine the activation energy using the Arrhenius equation.

Table 2

Copper leaching rate constants at different temperatures

Copper leaching rate constants	Temperature, °C				
	36	42	48	54	60
K	0,05204	0,05973	0,06353	0,066439	0,073857
$1/T$	0,003236	0,003174	0,003115	0,003058	0,003003
$\ln K$	-2,9556	-2,8178	-2,7562	-2,7114	-2,6056

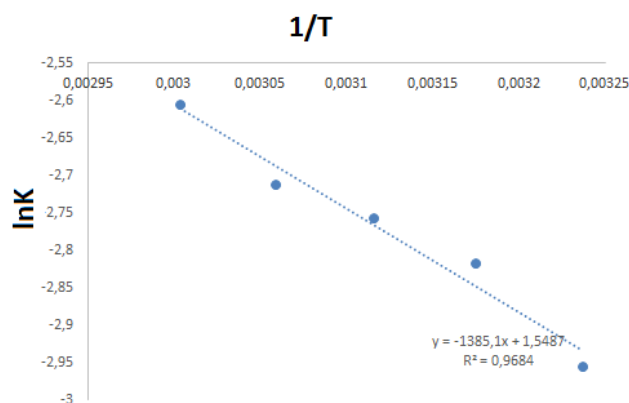


Figure 7. Rate constant versus reciprocal temperature

The activation energy is determined using a graphical method. Knowing the rate constants ($\ln K$) at different temperatures from the HPD time can be used to calculate the activation energy (E_A). The Arrhenius function was built using the table data (Fig. 7), according to which the activation energy was determined. The activation energy was calculated using the Arrhenius equation:

$$\ln K = A_0 e^{-E_A/RT}, \quad (3)$$

where A_0 is the pre-exponential factor (does not depend on temperature); R is the universal gas constant; $R = 8.314 \text{ J/(K}\cdot\text{mol)}$; K — rate constant s^{-1} , E_A — activation energy, $E_A = 1385.1 \cdot 8.314 = 11515.72 \text{ J/mol} = 11.52 \text{ kJ/mol}$.

The process of copper leaching from the tailings of the ZhCP proceeds in a mixed region with a predominance of diffusion factors, as evidenced by the obtained value of the activation energy. When extracting copper from the tailings of the ZhCP, it is necessary to carry out intensive mixing of the feedstock for the best extraction.

Conclusions

For the first time, the tailings of the Zhezkazgan Concentrating Plant were studied using X-ray phase analysis and energy-dispersive spectroscopy (EDS) analysis, as well as the kinetics of the leaching process. The conducted research allowed us to determine changes in the phase composition of the minerals in the tailings, which occurred as a result of electrohydropulse treatment. The applied method provided a comprehensive assessment of mineralogical changes and the effectiveness of the treatment.

Based on the obtained data, the following conclusions were made:

The combined application of electrohydropulse discharge and the ammonium biftrate activator demonstrated the destruction of silicon-containing rocks.

Energy-dispersive spectroscopy (EDS) revealed the presence of thirteen elements, the most intense lines being those of silicon, oxygen, aluminium and various non-ferrous metals. Following electrohydropulse discharge (EGIR) treatment, a significant decrease in copper concentration in the tailings minerals was observed, indicating a transition of copper ions into solution.

This study investigated the kinetics of copper leaching at low temperatures (up to 60 °C) over a 30-minute treatment period. Graphical analysis based on the Arrhenius equation was used to determine the activation energy value from the Zhezkazgan Concentrating Plant tailings, which amounted to 11.52 kJ/mol. It was established that this process occurs in the diffusion region and can be effectively carried out at relatively low temperatures.

Author Information*

**The authors' names are presented in the following order: First Name, Middle Name and Last Name*

Askhat Sakenovich Borsynbayev (*corresponding author*) — PhD, Researcher of the LEP “Physical-chemical methods of investigation”, Karaganda Buketov University, 28, Universitetskaya street, 100024, Karaganda, Kazakhstan; e-mail: askhat.9@mail.ru; <https://orcid.org/0000-0001-7709-5552>

Yedige Suindikovich Mustafin — Full Professor, Doctor of Chemical Sciences, Karaganda Buketov University, 28, Universitetskaya street, 100024, Karaganda, Kazakhstan; e-mail: edigemus@mail.ru; <https://orcid.org/0000-0001-9450-9227>

Khylysh Beysenovich Omarov — Full Professor, Doctor of Technical Sciences, Professor, Department of Chemistry, Chemical Technology and Ecology, Kazakh University of Technology and Business, building 37 A, Kayym Mukhamedkhanov str., 010000, Astana, Kazakhstan, e-mail: homarov1963@mail.ru; <https://orcid.org/0000-0003-2931-652X>

Aigul Akizhanovna Muratbekova — Candidate of Chemical Sciences, Associate Professor, Department of Chemical Technology and Petrochemistry, Karaganda Buketov University, 28, Universitetskaya street, 100024, Karaganda, Kazakhstan; e-mail: aigulmuratbekova@mail.ru; <https://orcid.org/0000-0002-2156-9306>

Daulet Asanovich Kaykenov — PhD, Lead Researcher of the LEP “Physical-chemical methods of investigation”, Universitetskaya street, 28, 100024, Karaganda, Kazakhstan; e-mail: kr.daykai@mail.ru; <https://orcid.org/0000-0003-4621-7603>

Daniyar Tleuzhanovich Sadyrbekov — Candidate of Chemical Sciences, Lead Researcher of the LEP “Physical-chemical methods of investigation”, Universitetskaya street, 28, 100024, Karaganda, Kazakhstan; e-mail: daniyar81@gmail.com; <https://orcid.org/0000-0002-3047-9142>

Asanali Anuarovich Ainabayev — Candidate of Chemical Sciences, Senior Researcher of the LEP “Physical-chemical methods of investigation”, Universitetskaya street, 28, 100028, Karaganda, Kazakhstan; e-mail: aliopel_82t@mail.ru; <https://orcid.org/0000-0002-3443-446X>

Abylaikhan Nurlanuly Bolatbay — PhD, Senior Lecturer, Department of Physical and Analytical Chemistry, Karaganda Buketov University, 28, Universitetskaya street, 100024, Karaganda, Kazakhstan; e-mail: abylai_bolatabai@mail.ru; <https://orcid.org/0000-0001-5047-3066>

Milana Alexandrovna Turovets — Master of Technical Sciences, 1st year PhD student, Engineer, LEP “Physical-chemical methods of investigation”, Karaganda Buketov University, 28, Universitetskaya

street, 100024, Karaganda, Kazakhstan; e-mail: turovec26.07@mail.ru; <https://orcid.org/0000-0002-0493-6426>

Author Contributions

The manuscript was written through contributions of all authors. All authors have given approval to the final version of the manuscript. **CRedit**: **Askhat Sakenovich Borsynbayev** conceptualization, investigation, data curation, investigation, validation, visualization, writing-review & editing; **Yedige Suindikovich Mustafin** conceptualization, methodology, data curation, supervision; **Khylysh Beysenovich Omarov** conceptualization, methodology, data curation, supervision; **Aigul Akizhanovna Muratbekova** writing-review & editing, resources; **Dauletkhan Asanovich Kaykenov** formal analysis, validation, data curation; **Daniyar Tleuzhanovich Sadyrbekov** formal analysis, data curation; **Asanali Anuarovich Ainabayev** formal analysis, investigation, data curation; **Abylaikhan Nurlanuly Bolatbay** data curation, formal analysis; **Milana Aleksandrovna Turovets** data curation, writing-review & editing.

Conflicts of Interest

The authors declare no conflict of interest.

References

- Guo, F., Chen, Q., Liu, Z., Cheng, D., Han, N., & Chen, Z. (2023). Repurposing mining and metallurgical waste as electroactive materials for advanced energy applications: advances and perspectives. *Catalysts*, 13(9), 1241. <https://doi.org/10.3390/catal13091241>
- Wang, W.W., Liu, C., Qin, B., Liu, Z.B., Li, X.Y., Li, M.C., & Chen, S.X. (2025). Comprehensive recovery of valuable metals from laterite via neutralization sludge. *Separation and Purification Technology*, 368, 133006. <https://doi.org/10.1016/j.seppur.2025.133006>
- Kart, E. (2021). Evaluation of sulphation baking and autogenous leaching behaviour of turkish metallurgical slag flotation tailings. *Physicochemical Problems of Mineral Processing*, 57(4), 107–116. <https://doi.org/10.37190/ppmp/138839>
- Xavier, L.H., Ottoni, M., & Abreu, L.P.P. (2023). A Comprehensive Review of Urban Mining and the Value Recovery from E-Waste Materials. *Resources, Conservation and Recycling*, 190(9), 106840. <https://doi.org/10.1016/j.resconrec.2022.106840>
- Wang, Y., Zhao, H., Wang, X., Chong, J., Huo, X., Guo, M., & Zhang, M. (2024). Transformation and detoxification of typical metallurgical hazardous waste into a resource: a review of the development of harmless treatment and utilization in china. *Materials*, 17(4), 931. <https://doi.org/10.3390/ma17040931>
- Liu, Y., Su, Y., Xu, G., Chen, Y., & You, G. (2022). Research progress on controlled low-strength materials: metallurgical waste slag as cementitious materials. *Materials*, 15(3), 727. <https://doi.org/10.3390/ma15030727>
- Iluțiu-Varvara, D. and Aciu, C. (2022). Metallurgical wastes as resources for sustainability of the steel industry. *Sustainability*, 14(9), 5488. <https://doi.org/10.3390/su14095488>
- Tileuberdi, A.N., Misiuchenka, V., Tleuov, A., Shingisbayeva, Z., Anarbayev, A., Ulbekova, M., & Tleuova, S. (2023). Studies of Physicochemical Bases and Optimization of Environmentally Safe Technology of Lead Production Waste Recycling. *Journal of Ecological Engineering*, 24(9), 293–301. <https://doi.org/10.12911/22998993/169183>
- Ghisman, V., Mureșan, A., Buruiană, D., & Axente, E. (2022). Waste slag benefits for correction of soil acidity. *Scientific Reports*, 12(1). <https://doi.org/10.1038/s41598-022-20528-6>
- Gabasiane, T., Danha, G., Mamvura, T., Mashifana, T., & Dzinomwa, G. (2021). Environmental and socioeconomic impact of copper slag — a review. *Crystals*, 11(12), 1504. <https://doi.org/10.3390/cryst11121504>
- Yang, S., An, H., Anastasiadou, D., Xu, W., Wu, L., Wang, H., & Weckhuysen, B. (2022). Waste-derived copper-lead electrocatalysts for CO₂ reduction. *Chemcatchem*, 14(18). <https://doi.org/10.1002/cctc.202200754>
- Liu, C., Xu, J., & Zhao, J. (2025). Copper deposit development potential on the Qinghai-Xizang Plateau in China based on the pressure-state-response framework. *Sci Rep*, 15, 4589. <https://doi.org/10.1038/s41598-025-89046-5>
- Tileuberdi, A., Zhaksylyk, A., Pazylova, D., Sagyndykova, N., Tleuov, A., & Tleuova, S. (2024). Mathematical approach to solving the problem of waste-free processing of metallurgical wastes. *Polish Journal of Environmental Studies*, 33(5), 5887–5892. <https://doi.org/10.15244/pjoes/183431>
- Chicardi, E.; Lopez-Paneque, A.; García-Orta, V.H.G.; Sepúlveda-Ferrer, R.E.; & Gallardo, J.M. (2025). Enrichment Methods for Metal Recovery from Waste from Electrical and Electronic Equipment: A Brief Review. *Metals*, 15(2), 140. <https://doi.org/10.3390/met15020140>
- Omran, M., Fabritius, T., & Abdelrahim, A. (2020). Effect of metallurgical waste properties on determining suitable recycling method. *Key Engineering Materials*, 835, 297–305. <https://doi.org/10.4028/www.scientific.net/kem.835.297>
- Karimi, S., Mohammadpour, P., Esmailzadeh, M., & Izadi, M. (2025). Sustainable synthesis and application of green deep eutectic solvent in chalcopyrite leaching: A combined experimental and molecular dynamic simulation approach. *Nano-Structures & Nano-Objects*, 42, 101481. <https://doi.org/10.1016/j.nanoso.2025.101481>

- 17 Maslennikova, I.G. (2009). Influence of the amount of ammonium hydrogen difluoride on the degree of fluorination of mineral raw materials. *Russian Journal of Applied Chemistry*, 82, 1333–1337. <https://doi.org/10.1134/S1070427209080023>
- 18 Mel'nichenko, E.I., Krysenko, G.F., & Mel'nichenko, M.N. (2006). $(\text{NH}_4)_2\text{SiF}_6$ evaporation in the presence of SiO_2 . *Russian Journal of Inorganic Chemistry*, 51(1), 27–31. <https://doi.org/10.1134/s0036023606010050>
- 19 Deng, Z., Oraby E., Li, H., & Eksteen J. (2022). Extraction of Copper from Chalcopyrite Using Alkaline Glycine–Ammonia Solutions. *Minerals*, 12, 1507. <https://doi.org/10.3390/min12121507>
- 20 Krysenko, G.F., Epov, D.G., Medkov, M.A. et al. (2018). Extraction of Rare-Earth Elements in Hydrofluoride Decomposition of Loparite Concentrate. *Russ. J. Appl. Chem.*, 91, 1665–1670. <https://doi.org/10.1134/S1070427218100142>
- 21 Review: Mel'nichenko, E.I., Ftoridnaia pererabotka redkometalnykh rud Dalnego Vostoka (Fluoride Processing of Rare-Metal Ores from the Far East), Vladivostok: Dalnauka, 2002, 268 p. *Russian Journal of Applied Chemistry*, 75, 2033–2034 (2002). <https://doi.org/10.1023/A:1023372406496>
- 22 Mustafin, Ye.S., Omarov, Kh.B., Borsynbaev, A.S., Havlichek, D., Pudov, A.M., & Shuyev, N.V. (2021). Production of electrolytic copper from Zhezkazgan Processing Plant tailings leaching solutions using a hydro-impulse discharge. *Bulletin of the Karaganda University. "Chemistry" Series*, 104(4), 128–137. <https://doi.org/10.31489/2021ch4/128-137>
- 23 Borsynbayev A.S., Omarov, Kh.B., Mustafin, Ye.S., Havlichek, D., Absat, Z.B., Muratbekova, A.A., & Pudov A.M. Study of copper leaching from the tailings of the Karagaily (Republic of Kazakhstan) concentrating factory using an electric hydro-pulse discharge. *J. Serb. Chem. Soc.*, 87, 7–8, 925–937. <https://doi.org/10.2298/JSC210622005B>